STRUCTURAL STUDIES
OF
VARIOUS ß-ALUMINAS

Amanda Karen Petford

St. Cross College
Oxford

Thesis submitted for the degree of
Doctor of Philosophy in the University of Oxford

October 1984

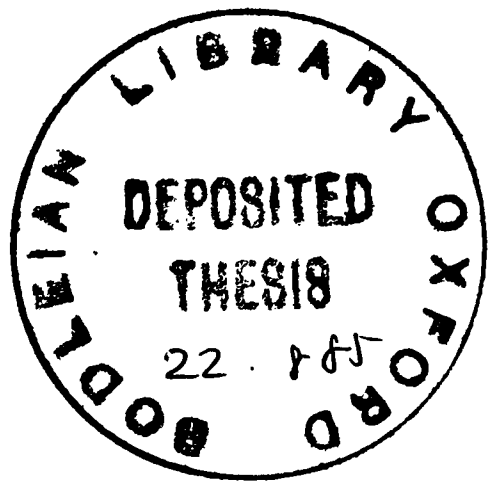

To my Parents

Abstract

STRUCTURAL STUDIES OF VARIOUS ß-ALUMINAS.

Amanda Karen Petford, St. Cross College, Oxford.

A thesis submitted for the degree of D.Phil. in the University of Oxford.

Michaelmas Term, 1984.

This thesis describes results obtained using high resolution electron microscopy, acoustic microscopy and chemical analysis to study the structure and properties of the superionic ß-aluminas.

The acoustic microscopy and chemical analysis results relate solely to sodium ß- and ß"-alumina, which are used as the solid state electrolyte in the sodium/sulphur cell.

The high resolution electron microscopy results cover sodium ß- and ß"-alumina as well as a number of ion-exchanged ß"-aluminas.

The ß-alumina structure consists of spinel-like blocks separated by the so-called conduction planes. The conduction planes have a low density, and contain all the mobile cations. Lattice images of sodium ß- and ß"-alumina, silver ß-alumina, ammonium/hydronium ß"-alumina, gadolinium ß"-alumina and divalent and trivalent europium ß"-alumina are presented and discussed.

A hitherto unreported long-period structure in sodium ß-alumina is shown, as is superlattice ordering in the divalent and trivalent ß"-aluminas.

Defects in these materials are also discussed. The most common damage mode in the ß"-aluminas, due to electron beam irradiation, is the loss of the mobile-ion containing planes, and the subsequent collapse and shear of the structure to form broad defect spinel blocks. It is shown that collapse vectors determined for sodium ß"-alumina can also be applied to ammonium/hydronium ß"-alumina. Two further damage modes observed in this ß"-alumina are also discussed. A damage mode has been observed in sodium ß-alumina and silver ß-alumina which involves the extrusion of material to the crystal surface. Electron diffraction patterns from the extruded material have been indexed.

The acoustic microscope has been used to examine bulk sodium ß/ß"-alumina electrolyte tube specimens. Images of rectangular features present in the tubes (approximately 40µm in length) are presented and the possible nature of the features is discussed.

INDEX

ACKNOWLEDGEMENTS

The production of this thesis, and the research described in it, has been made possible with the help of a large number of people.

Firstly I should like to thank my academic supervisor Dr Colin J. Humphreys for excellent supervision and in particular for his care in reading this thesis.

I should like to thank Dr J.L. Hutchison for instructing me in the use of the Jeol 200CX high resolution electron microscope.

Grateful thanks are also due to :

Dr G.A.D. Briggs and Chris Ilett for help in using the acoustic microscope.

Dr C.J. Salter for operating the CAMECA electron microprobe analysis system.

Mr A. McKnight and Mr S. Lee for photographic work during the past three years, and in particular for printing the photographic figures in the thesis.

Mr G. Dixon-Brown, Mr R. Doole and Mr P. Duncan for maintenance of the Jeol 200CX.

Dr Robert Hull, Dr Jeff Butler, Dr Iain Salisbury, Dan Johnson, Joe Ngo, Crispin Hetherington, Dr Graeme Waddington, Dr John Barry and Dr J.C.H. Spence for encouragement, advice and useful discussion.

I should also like to thank Professor Sir Peter Hirsch, F.R.S., for providing laboratory facilities, the Science and Engineering Research Council for financial support, Chloride Silent Power Ltd. (in particular my

industrial supervisor Dr Steven Heavens) for providing advice, specimens and financial support, and Dr Josh Thomas for providing ion-exchanged ß"-alumina specimens and for useful discussions.

I am very grateful to Nigel Lashbrook for preparation of certain of the figures.

Finally, I would like to thank my parents for their help and support over the last three years, and in particular my father for his sterling support in the preparation of this thesis.

Preface

The research to be described in this thesis, a study of the structures and properties of various ß-aluminas, was motivated by the potential value of these materials for, among other uses, the electrolyte separating the electrodes of one type of high-temperature advanced battery system. The thesis is divided into three parts. Part I (chapter 1) gives a brief survey of the prospects for electric vehicles and the advanced battery systems under development - including the sodium/sulphur cell. Part II is concerned with a high resolution study of several ß-aluminas. This section covers the theory of lattice imaging, the structures and properties of ß-alumina materials, and the results obtained in this study using the lattice imaging technique. Part III is concerned with a larger scale study of sodium ß/ß"-alumina electrolyte tubes, and includes a review of the various damage modes observed, and presents results obtained in this study from the electrolyte specimens using acoustic and optical microscopy and chemical analysis.

Conclusions reached and suggestions for further work are presented in the final chapter.

The research was carried out in the Department of Metallurgy and Science of Materials. at the University of Oxford over the period 1981 - 1984. None of the work has been submitted previously for a degree at this or any other university. The work reported is original and has been carried out independently by the author under the supervision of Dr. C.J.Humphreys. The work of others has been freely drawn upon and is acknowledged in the text. References used

are listed in alphabetical order at the end of the thesis.

Some of the results presented in this thesis have previously been published in the following publications:

1 Hull R., Petford A.K., Humphreys C.J. and Smith D.J. - "High resolution electron microscopy of silver ß and ß"-aluminas" - Solid State Ionics 9 and 10, 1983 p.181.

2 Petford A.K., Briggs G.A.D., Hull R., Humphreys C.J. and Ilett C. - "Examination of cracks and other defects in Na ß and ß"-alumina using acoustic, optical and scanning electron microscopy" - Solid State Ionics 9 and 10, 1983 p.173.

Chapter 1. Electric vehicles and advanced battery systems.

1.1 Electric vehicles.

Electric vehicles have been in existence for many years, the first one probably being built in Aberdeen in 1837. However, with the discovery of oil in Texas and the Middle East resulting in plentiful, cheap petrol, the electric vehicle (EV) gave way to the internal combustion engine (ICE) vehicle. By the 1960s EVs had virtually disappeared in this country, with the exception of milk floats, fork lift trucks and a few electric trams. By 1979 the number of EVs registered in this country was 45,350 compared with a total of over 17 million vehicles. Most of these electric vehicles were milk floats with a maximum speed of about 25 mph.

The vast increase in the price of oil, problems of supply, and the realisation that oil reserves are shrinking rapidly, have led to a renewed interest in research into the feasibility of producing a range of EVs to replace ICE vehicles.

For an electric vehicle to be a viable alternative to an ICE vehicle, it must have an acceptable range and maximum speed. These parameters will depend on the use to which the EV is to be put; for example, a private passenger vehicle and a delivery vehicle would have quite different needs.

EVs would be powered by motors driven by rechargeable batteries. The batteries could be charged overnight using off-peak power which would improve load levelling in power

stations, particularily in nuclear power stations which cannot be shut down overnight. If electricity produced overnight can be sold or stored in large battery banks at the power station, the need would no longer exist for extra generators which are only switched on during peak periods - a costly and wasteful requirement. This constant rate of flow of electricity is known as load levelling.

The main advantages of EVs are the following: i) fuel economy, ii) low whole-life costs, iii) quietness, iv) reduced exhaust fumes, v) mechanical simplicity.

i) The first of these has been mentioned above, but one must also consider the fact that an EV only uses fuel when the vehicle is moving, which makes it ideal for stop-start driving in towns, and for delivery vehicles with frequent stops for delivery (such as milk floats).

ii) The cost of running a vehicle on electricity is at present much lower than that of running one on petrol although one should remember that the cost of battery purchase and replacement would increase the effective fuel price. However the running costs (repairs, lifetime) are likely in the future to be lower than in an ICE vehicle, resulting in an overall reduction in price.

iii) and iv) Both these reasons make EVs popular with environmentalists, as they result in a substantial decrease in noise and air pollution.

v) In an EV, the engine, gearbox,clutch, ignition and cooling systems are replaced by an electric motor and controller. The fuel tank is replaced by batteries and a charger.

The next section deals with a more detailed analysis

of the problems involved in the production of a battery suitable for powering an EV.

1.2 Batteries for Electric Vehicles

Batteries can be divided into two classes - primary and secondary. Primary batteries generate power by chemical reactions which are irreversible, leading to the need to replace components which are used up during discharge; frequently the whole battery will be discarded. Secondary batteries generate power by reversible chemical reactions. The reactants are restored to their original form by applying a reverse current - charging. Primary batteries tend to have higher energy densities than secondary cells, but they have a limited lifetime, have much higher running costs, and require frequent maintenance. The secondary batteries include the lead-acid, nickel-zinc, zinc-chlorine, lithium intercalation, and sodium-sulphur systems.

See table in figure 1.1 for a comparison of these systems.

At present almost all EVs run off lead-acid cells, but these have a limited use and are likely to be superceded by one of the "advanced" battery systems described in sections 2B) and 2C) below. The three main problems associated with EVs all relate to the battery; these are: performance and range, rate of recharge and initial cost. Performance and range are limited by the energy density (energy per unit weight) and the number of cycles which a battery can undergo during its lifetime. For a battery of a given energy density and size, the maximum speed can be raised by reducing the range, and vice versa. There is a

	Advanced battery systems				
	Lead/acid	Ni/Zn	Zn/Cl_2	Li/TiS_2	Na/S
Operating voltage (V)	1.9	1.6	1.7	3.0 - 1.7	1.65 - 1.35
Temperature range (C)	-20 - +50	-30 - +40	-10 - +9	room temp.	+300 - +400
Energy Efficiency (%)	80	75	70	30	70 - 75
Energy density (Wh/kg)	30	70	70 - 120	132	120
(theoretical)	-	-	-	480	180
Maximum sustained power density (W/kg)	50	200	100	100	120
Self-discharge time to 50% (days)	200	200	-	-	n.a.
Deep cycles (80% d.o.d)	1500	300 - 400	-	1000	few x 1000
Cost ($/kWh)	50	approx 50	-	-	approx 50

Fig. 1.1 Characteristics of various advanced battery systems.

limit on the size and weight of battery which can be used in any vehicle, and thus increases in speed and range must be obtained by using batteries with a high energy density.

A battery must be able to support a reasonable number of charge/discharge cycles (about 1000 is the target aimed at by most companies) in order to keep down the cost of an EV. The initial cost of a battery for an EV will be high, but running costs can be kept below those of an ICE vehicle provided replacement batteries are not required too frequently.

Recharging must be done over a few hours and this could present some problems. Vehicles which are only used during the daytime can be recharged overnight and fleets of EVs could be used on a rota system if they were required for use on strict schedules. EVs would not be suitable for operators who needed constant access to a vehicle for use at random times (such as ambulances). The problem of access to recharging points also has to be considered, and in areas where cars are parked in the road overnight this is not a trivial consideration.

The next section discusses each possible battery system in turn with reference to advantages, cost and modes of failure.

1.2a The Lead/acid storage cell.

At present this is the most widely used type of storage cell. It can be manufactured to fulfill a variety of uses such as: starter batteries, traction batteries and stationary storage batteries.

Cell construction and cell reactions.

The lead/acid cell consists of an anode containing sponge lead, a cathode containing lead dioxide (PbO_2) and an electrolyte of sulphuric acid solution.

The electrode construction varies according to the uses to which the cell will be put: in the case of batteries for use in electric vehicles, the electrodes can be of the tubular plate or grid type.

The electrolyte consists of high purity sulphuric acid solution of between 28% - 40% acid in the charged cell. The solution has to be strong enough to give reasonably high specific parameters and to prevent freezing at low temperatures, whilst remaining weak enough to prevent excessive passivation and sulphuration of the electrodes, as this would decrease the lifetime of the cell. The positive and negative electrodes are held apart by porous separators.

The cell reactions are:

cathode $PbO_2 + 2H^+ + H_2SO_4 + 2e^- \rightarrow PbSO_4 + 2H_2O$

anode $Pb + H_2SO_4 \rightarrow PbSO_4 + 2H^+ + 2e^-$

overall $PbO_2 + Pb + 2H_2SO_4 \rightarrow 2PbSO_4 + 2H_2O$

Advantages

The lead acid cell operates over a wide temperature range and is composed of relatively cheap, readily available materials.

The specific capacity is not as high as that of some of the advanced batteries, but the lead-acid cell has the advantage of being reliable and easy to maintain. At medium specific energies of 30 - 35 Wh/kg, lifetimes of 700 - 800

cycles have been achieved (see figure 1.1 for parameters).

Disadvantages and failure modes.

Lead/acid cells tend to be heavy due to the amount of lead used although it is hoped that the use of heat-resistant plastic containers will reduce the weight.

Self-discharge can be a major problem in the lead-acid cell, and tends to increase with number of cycles. The addition of certain organic materials can help reduce this problem. A covering layer of PbO_2 on the positive electrode should prevent further anodic oxidation; however separation of this layer from the grid can occur, leading to corrosion of the grid to form various lead oxides and sulphates. Corrosion can be reduced by adding cobalt sulphate to the electrolyte, although the reason for this is not fully understood.

Dendritic growth on the electrodes can lead to short-circuiting but this can be controlled by the correct choice of separator.

Passivation can cause a decrease in the discharge voltage, but the addition of a mixture of barium sulphate with various organic materials is used to promote the production of a loose layer of large $PbSO_4$ grains which do not inhibit the reactions of the active lead and lead oxide.

Uses of lead/acid cells.

Lead/acid storage cells are in use at present as traction batteries in electric vehicles such as milk floats. They are also used as starter batteries and in various electronic and telecommunication devices.

Summary

The lead/acid cell can be used as a traction battery in commercial electric vehicles - but not in electric cars due to its weight -although its low energy density limits the range and speed of the vehicle (the charge time is approximately 6 hours). The cell has the advantage of operating at ambient temperatures and being easy to maintain.

1.2bi The Nickel-Zinc Battery

Cell Construction and reactions

The Ni/Zn cell consists of a nickel cathode and a zinc anode, with aqueous KOH as the electrolyte. The nickel cathode can be either of the sintered or pressed variety, of which the pressed electrode is cheaper but has a shorter life, whilst the sintered electrode costs more to produce but has a longer life.

The zinc on the anode is obtained via chemical conversion of ZnO (in the form of a paste). A microporous separator is present at the anode to prevent dendritic growth of the zinc, which would lead to a cell short-circuit.

The cell reactions are:

cathode $NiOOH + H_2O + e^- \rightarrow Ni(OH)_2 + OH^-$

anode $Zn + 2OH^- \rightarrow Zn(OH)_2 + 2e^-$

followed by $Zn(OH)_2 \rightarrow ZnO + H_2O$

overall $2NiOOH + Zn + H_2O \rightarrow 2Ni(OH)_2 + ZnO$

Advantages

As can be seen from figure 1.1 the Ni/Zn cell

operates at ambient temperatures and has a good low temperature performance. This is obviously an advantage as the cost of insulating the cells can be kept low.

The Ni/Zn cell compares favourably, as regards energy and power densities, with other possible EV batteries and has a comparable efficiency (75%).

The production of a sealed system, with low maintenance requirements, seems possible and would reduce the cost of a Ni/Zn cell.

Disadvantages and modes of failure

At present the Ni/Zn cells have not achieved lifetimes of more than about 300 cycles; this would have to be increased to about 1000 or more before the cell would become commerciably viable.

The high cost of nickel means that Ni/Zn cells are expensive, although it may be possible to set up a reclamation plant to obtain nickel from the chrome on scrapped motor vehicles.

In most cells which fail, the failure is due to deterioration of the zinc electrode. Three distinct modes of failure can be observed:

i) dendritic growth on the Zn electrode leading to a short-circuit between the anode and cathode,

ii) Shape change effects due to the movement of active material from the edge to the centre of the electrode. This can lead to loss of capacity and possible shorting,

iii) A loss of capacity due to passivity of the electrode.

The insertion of the separator limits the growth of dendrites on the anode whilst the use of excess anode

material (in the form of ZnO) can help reduce shape change effects. Various additives such as organic binders or various metallic compounds can also be helpful in reducing both dendritic growth and shape change effects.

Possible uses for Ni/Zn cells

A major use for Ni/Zn cells would be as traction batteries both in commercial and private vehicles. The Ni/Zn cell is also suited for use in power storage, for example in computers and telecommunication, and it seems likely that the cell could take over part of the market at present held by the Ni/Cd cell - calculators, radios and the like, due to the improved energy density of the Ni/Zn cell over the Ni/Cd cell.

Summary

Providing the problems of sealing, cost and short lifetime can be overcome, the Ni/Zn battery seems a likely candidate for use in EVs due to it operating at ambient temperatures, using a simple aqueous electrolyte and being manufactured using well understood techniques, such as electrochemical conversion.

1.2bii The Zinc/chlorine cell.

Cell construction and cell reactions.

Due to the fact that chlorine is a very powerful oxidant, in the presence of an aqueous electrolyte, it reacts very corrosively towards most metals, and so most power sources involving chlorine used anhydrous molten electrolytes. Over the last ten years a new type of Zn/Cl_2

cell with an aqueous electrolyte has been developed. This involves the accumulation of the chlorine produced on charging as solid $Cl_2.6H_2O$. The chlorine hydrate is precipitated from aqueous chlorine solution below 9°C. It is approximately non-corrosive and can therefore be stored safely at low temperatures.

The overall cell reaction is:

$$Cl_2.6H_2O + Zn \rightarrow ZnCl_2 + 6H_2O$$

See figure 1.2 for cell design.

The negative electrode consists of a thin copper substrate which becomes coated in metallic zinc during charging due to the deposition of zinc ions from solution. The anode is formed from a corrosion resistant conductor such as graphite in a porous form to allow maximum electrolytic contact. During charging, chlorine is produced at the anode, dissolves in the aqueous electrolyte and is carried to the cooled container where it is deposited as $Cl_2.6H_2O$. During discharge the metallic zinc is dissolved and recombines with the reduced chlorine ions. The concentration of chlorine in the electrolyte is kept nearly constant by the partial dissolution of the hydrate.

Advantages

The active materials in the cell are cheap and, at present, readily available, and the specific parameters compare reasonably well with those of other medium power cells, having a lifetime of several hundred cycles.

Disadvantages and modes of failure.

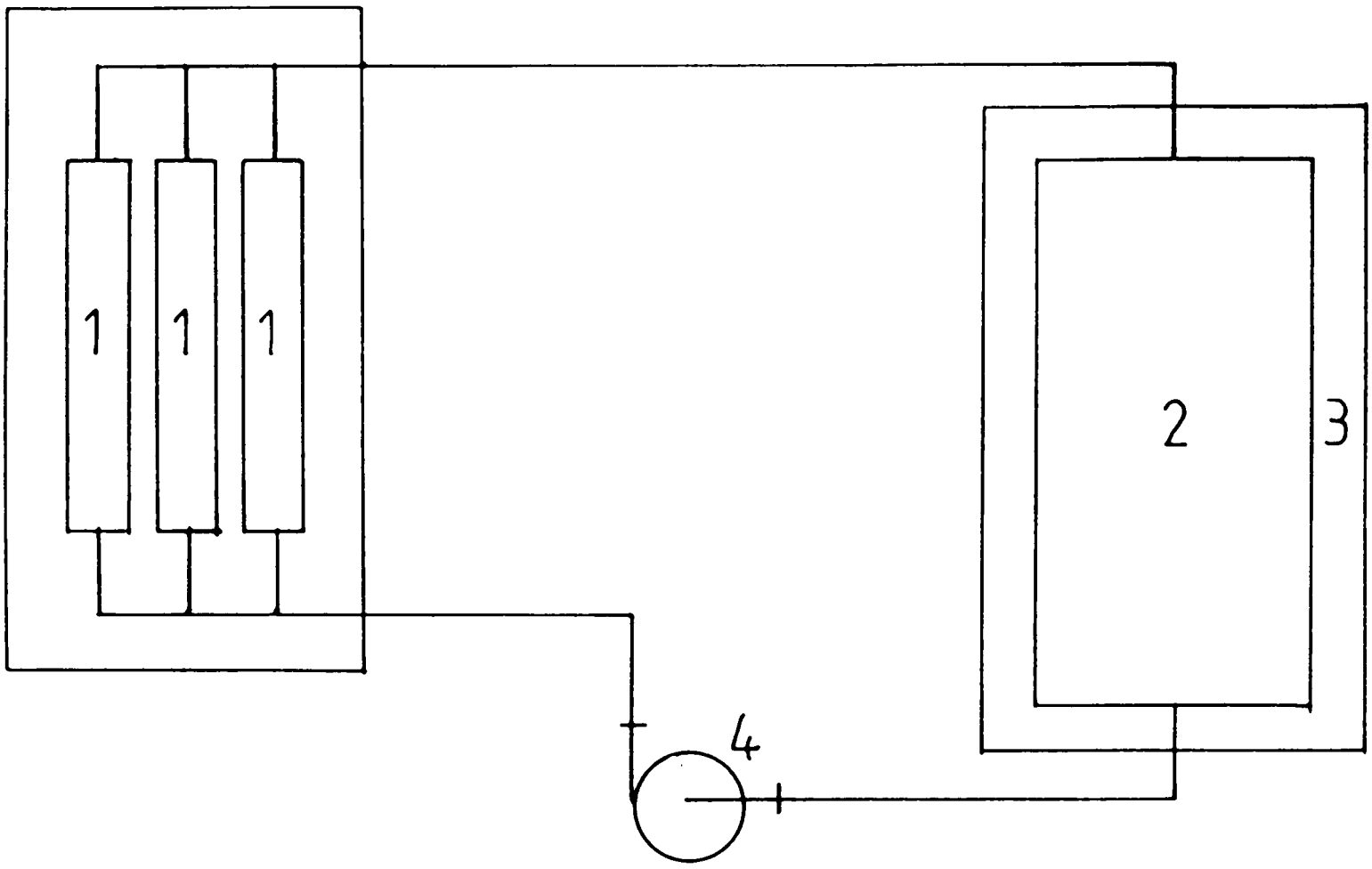

1 - cell
2 - container for $Cl_2 \cdot 6H_2O$
3 - cooler for precipitation and storage of $Cl_2 \cdot 6H_2O$
4 - pump for recirculation of aqueous electrolyte ($ZnCl_2$ solution)

Fig. 1.2 Design for the Zinc / Chlorine Cell

The Zn/Cl_2 battery system has to be kept cooled to prevent the solid $Cl_2.6H_2O$ from forming chlorine in the liquid or gas phase. The operable temperature range is quite narrow - from -10°C to +9°C, the lower limit being the freezing point of the aqueous electrolyte. This presents obvious safety risks, as in an accident the chlorine hydrate might well heat up and produce dangerous chlorine fumes.

The deposition of zinc from solution in the aqueous electrolyte can lead to dendritic growth on the cathode, causing cell short-circuiting. The use of additives such as chlorine - resistant surface reactants, can decrease the dendritic growth rate.

Possible uses for Zinc/chlorine battery systems.

The Zn/Cl_2 cell has been suggested for use as a traction battery in electric vehicles, but the cells might be more suitable as large-scale power storage units such as those required for load-levelling in power stations.

Summary

Although the Zn/Cl_2 cell is cheap, the safety risks involved in the possible evolution of chlorine gas limit its use as a traction battery for electric vehicles. However, if this problem can be solved, the energy storage capacity and efficiency (70%) are comparable with other battery systems under consideration. A test car (Volkswagen Golf) has been fitted with a Zn/Cl cell and has a range of 150 miles at 55mph.

1.2biii The Lithium intercalation cell.

Cell construction and reactions.

The lithium intercalation cell is distinct from the other batteries discussed in that its charge - discharge reaction does not involve the formation of any new phases - phases which can often reduce the overall current and power density of the cell.

A lithium intercalation cell, such as the Li/TiS_2 system, contains the anode from which lithium ions can be produced, a lithium ion solid electrolyte and ~~and~~ the intercalation electrode consisting of a lamellar structure such as TiS_2 (see figure 1.3). The structure of TiS_2 consists of sheets of tightly bound TiS_6 octahedra held together by weak van der Waals forces. The lithium ions can be inserted (intercalated) in the van der Waals gaps between the chalcogen (sulphur) layers to form Li_xTiS_2 with an increase in the c lattice parameter of 9%. The maximum value of x appears to be 1.6 at room temperature, although in a cell the maximum value of x is 1.0, as the intercalation of further lithium ions results in a structure in which there is an excess of lithium ions over the number of available octahedral sites.

During discharge, lithium ions produced at the anode migrate through the electrolyte and are intercalated in the TiS_2 to form Li_xTiS_2. At the same time charge balancing occurs by the flow of electrons through the external circuit to the Li_xTiS_2 (see figure 1.4). During charging the reaction is reversed, and if the cell is to have a lifetime of more than one cycle, the intercalation reaction must be fully reversible. The cell reaction is thus:

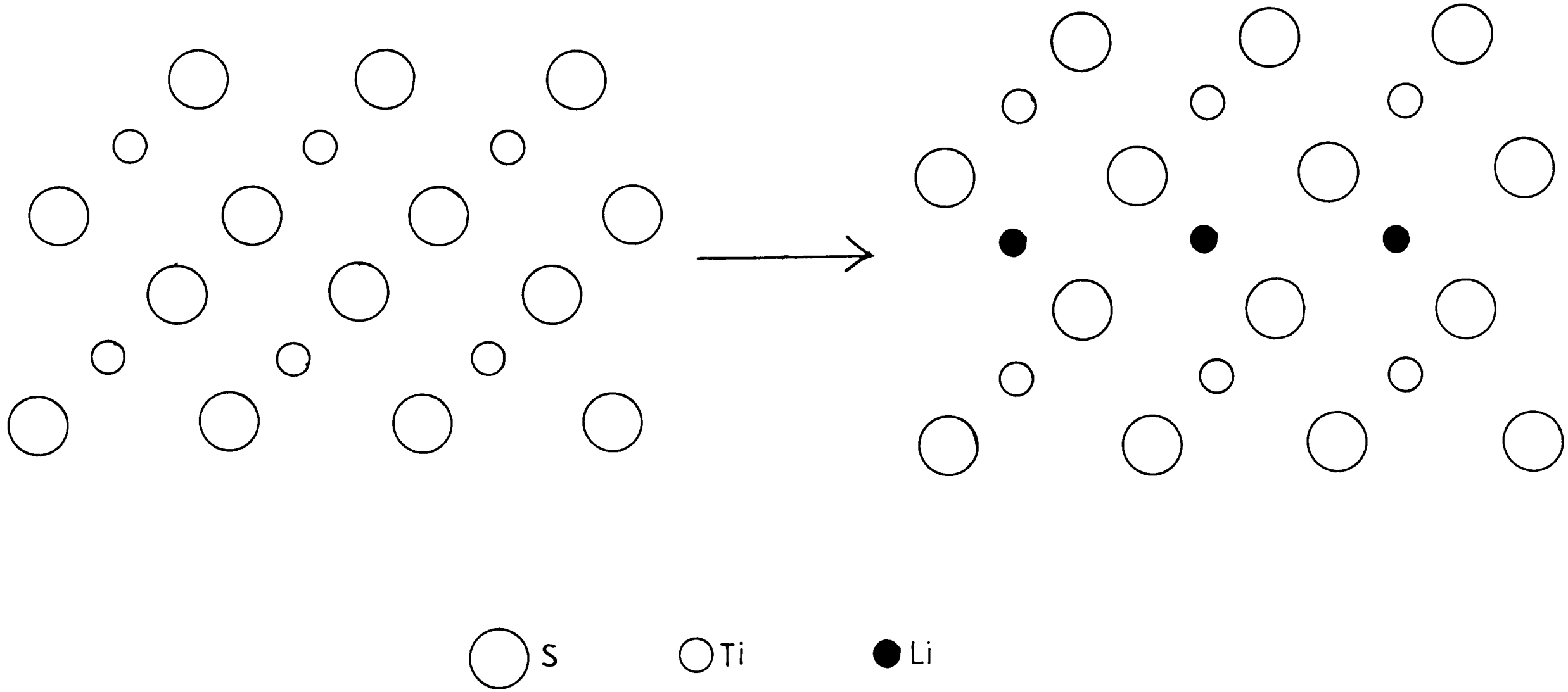

Fig. 1.3 Structure of TiS_2 before and after Li intercalation

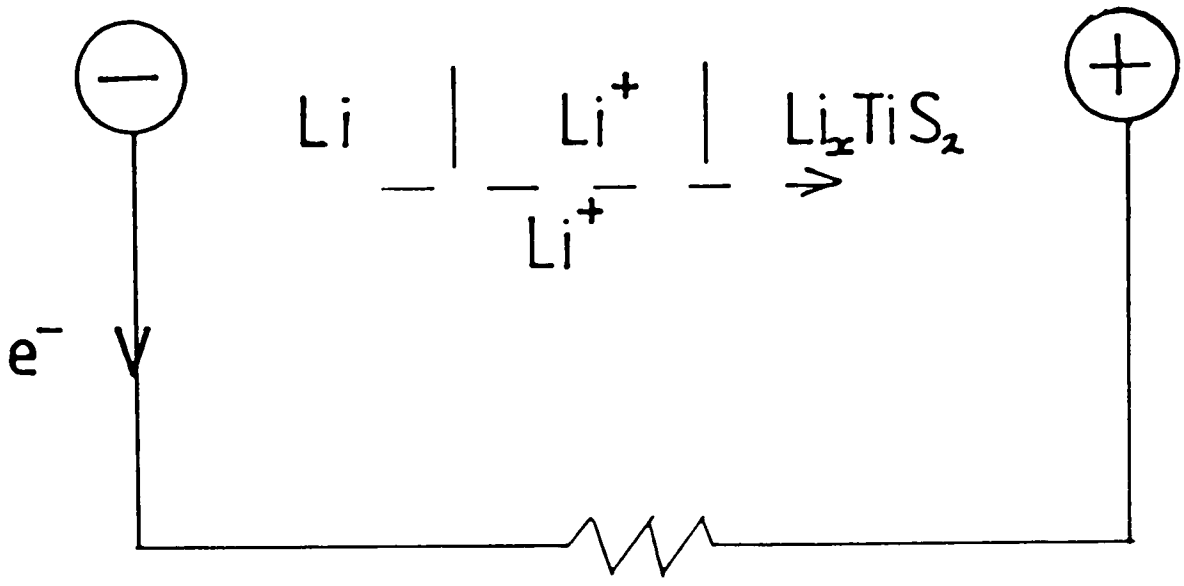

Fig.1.4 Schematic Representation of the Lithium Intercalation Cell

$$xe^- + xLi^+ + TiS_2 \rightarrow Li_xTiS_2$$

The intercalation electrode must thus be a material with both high electronic and ionic conductivities. It is also important that the discharge voltage does not vary too considerably with variation in the value of x (in Li_xTiS_2). (At present from ~3V at x=0 to ~1.7V at x=1)

Other intercalation electrode materials have been tried, but the most research has been done on TiS_2 as this is the lightest of the dichalcogenides, and also the most economical, due to high reversibility of the lithium intercalation reaction.

Advantages

The Li/TiS_2 cell operates at room temperature and involves only solid materials. This reduces the problems of insulation and corrosion.

The cells are capable of a very high energy density - comparing favourably with that of other secondary battery systems.

Disadvantages and modes of failure.

The change in cell emf during discharge of the cell means that, although the cell would be suitable as a traction battery in an electric vehicle, it would not be very suitable for use as an energy storage device (for example in power stations).

Another problem is the change in size (~9%) of the intercalation electrode during discharge. It has been suggested that holding the TiS_2 electrode in contact with the electrolyte by means of a spring might solve this difficulty.

The cell can suffer a resistance rise due to the growth of electrolyte/lithium complexes on the lithium electrodes, if these complexes are impervious to lithium. The most recent electrolyte materials under test form complexes which are porous to lithium.

Uses of the Lithium intercalation cell.

The Li/TiS_2 cell would not be suitable as an energy storage device, but would be ideal for use as a traction battery.

Summary

The lithium intercalation cell is still undergoing extensive research to try to solve the problems mentioned above. The aim is to produce a cell with a porous lithium/electrolyte interface, an electrolyte of high lithium ion conductivity, and a titanium disulphide intercalation electrode with perfect stoichiometry. This last criterion is not easy to achieve - it has been reported that the sulphur content of the titanium disulphide can vary by as much as 25% - in which case lithium intercalation can not occur.

1.2c The sodium-sulphur cell.

Cell construction and cell reactions.

The sodium-sulphur (Na/S) cell consists of a sodium anode, a solid electrolyte, and a sulphur and carbon-felt cathode. The cell operates at approximately 350°C to keep both the electrodes (sodium and sulphur) in the liquid state. The solid electrolyte usually used in this cell is a ceramic - sodium ß-alumina. ß-alumina is a generic term for a number

of sodium polyaluminates which have a two-dimensional layer structure which results in a very high sodium ion conductivity (see chapter 3 for detailed description of the structure of the ß-aluminas).

The two crystallographic variants of ß-alumina most widely used as the solid electrolyte of the Na/S cell are ß and ß". ß"-alumina has a higher conductivity but is more difficult to process and must be stabilised by the addition of magnesium or lithium. A mixture of ß and ß" is usually used.

Sodium ß-alumina is impermeable to liquid sodium and liquid sulphur and is an electronic insulator. It can thus function as separator as well as electrolyte in the Na/S cell.

The electrolyte is produced (in the form of a thin-walled tube, with dimensions of the order of: length >300mm, diameter ~30mm, wall thickness ~2mm) by various manufacturing techniques conventionally used for oxide ceramics. The sintered tubes can have densities close to the theoretical maximum. Magnesia or lithia is added to encourage the growth of ß"-alumina crystals.

The "green" ß-alumina tubes can be zone sintered or batch sintered. The first is a continuous process in which tubes are passed through a furnace at a high temperature (1700°C) in a soda-rich atmosphere The second involves stacking the green tubes in a furnace, and heating and cooling following a preset cycle. It has been suggested that a "double-peak" firing cycle increases the strength and lowers the resistivity of the ß-alumina.

The possibility also exists of using a

sodium-conducting glass as the solid electrolyte. The glass is formed into small (80μm diameter) hollow tubes which are packed together to lower the electrolyte impedance. The disadvantage of this electrolyte is that it is complex to produce and therefore more expensive than sodium ß-alumina. Thus nearly all Na/S cells use ß-alumina as the solid electrolyte.

Since liquid sulphur is highly corrosive to metals, the most common arrangement of the Na/S cell is that seen in figure 1.5 - the central sulphur cell, although some groups in America still use the central sodium cell.

The graphite current collector and sulphur cathode fit closely together, and are usually of a segmented form to allow maximum surface area contact (see fig 1.6). The cell reactions are summarised in fig. 1.7.

Advantages.

The starting materials used in the manufacture of the sodium-sulphur cell are cheap and readily available, and the processes by which the electrolyte is manufactured are well understood. The system has the highest energy density of the long lifetime cells, and can support up to a few thousand cycles.

Disadvantages and modes of failure.

The main disadvantage of the Na/S cell is that it operates at around 350°C. This means that the conditions inside the cell are very extreme and liable to promote corrosion. Also, if the electrolyte tube were to crack, liquid sulphur and sodium would meet and react in a highly

Fig. 1.5 The Sodium - Sulphur Cell.

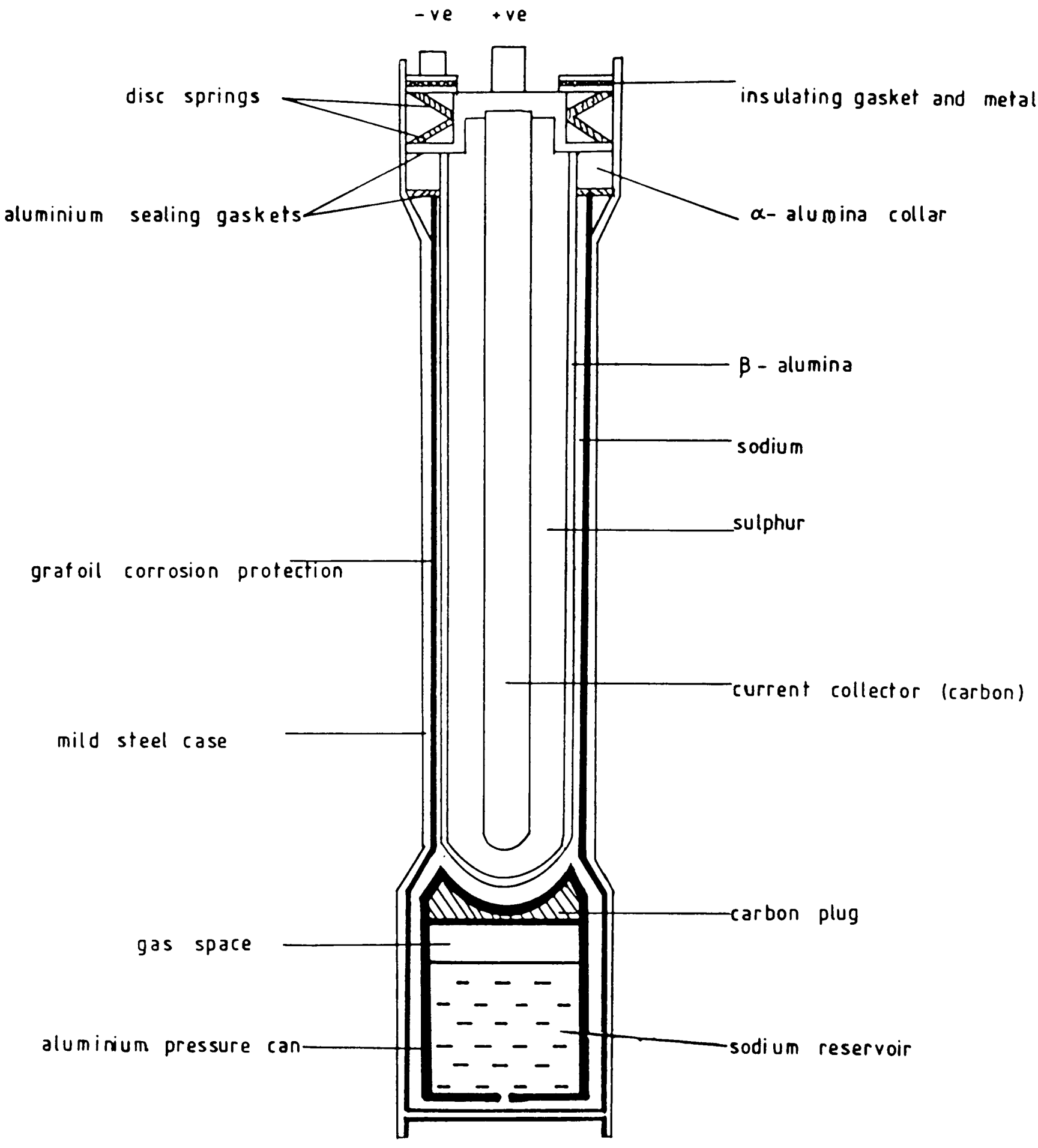

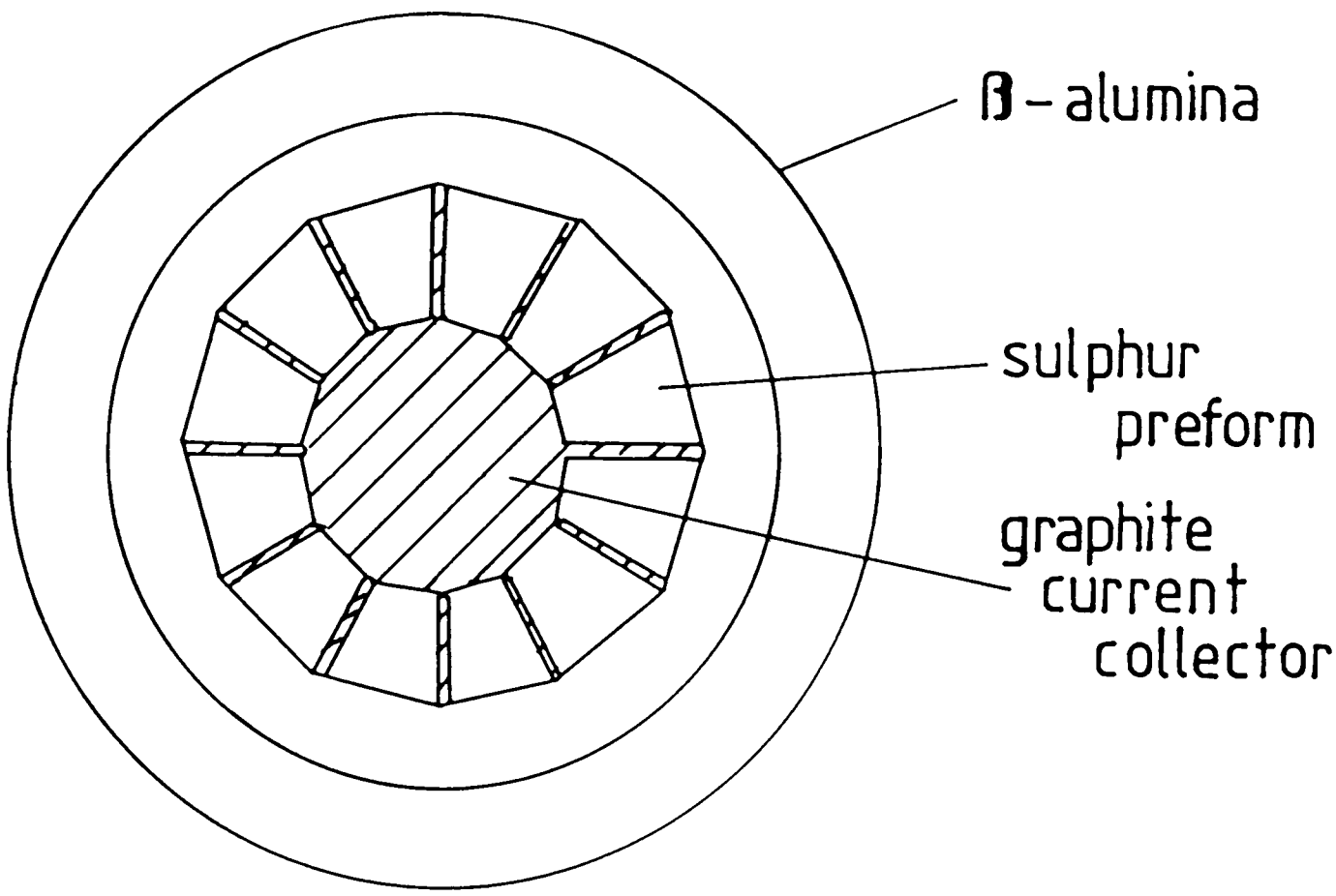

Fig. 1.6 Schematic Representation showing arrangement of multi-segmented preform in cell

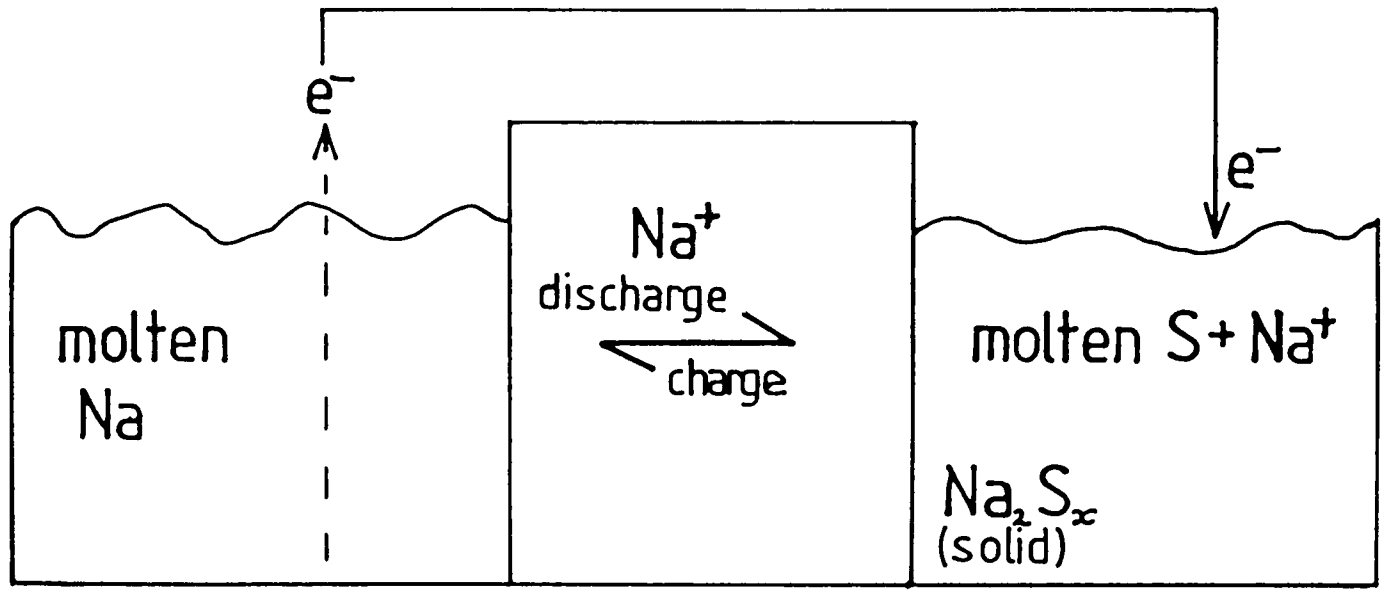

ANODE

$$2Na \longrightarrow 2Na^{+} + 2e^{-}$$

CATHODE

$$2e^{-} + S_x \longrightarrow S_x^{2-}$$

OVERALL

$$2Na + S_x \longrightarrow Na_2S_x$$

Fig.1·7 Schematic Representation of the Sodium / Sulphur Cell and Cell Reactions

exothermic manner. The corrosion problem has been partially solved by putting the sulphur electrode at the centre of the cell so that it does not come into contact with the cell casing. As can be seen from fig. 1.5, the casing is lined with a sodium-corrosion-proof material.

Failure of the Na/S cell is usually due to a breakdown of the ß-alumina electrolyte. This can occur for a number of reasons:

1. Rapid crack propagation - this occurs when an electrolyte surface flaw becomes filled with sodium. A Poiseuille pressure gradient is generated at the tip of the crack due to the flow of sodium into the crack, out of the ß-alumina. This pressure causes the crack to propagate slowly, until a critical length is achieved, after which propagation is rapid. The exact parameters necessary for crack propagation (eg. critical current density) are difficult to establish due to the complexity of the problem. However the situation has an analogue in the dendritic growth of electrode material through the electrolyte, for example in the nickel-zinc cell.

2. Cracking or fracture at a weak point of the tube due either to an intrinsic defector to an external shock.

3. Slow degradation (Mode II degradation). This is observed as a darkening of the electrolyte. This darkening starts at the sodium face of the ß-alumina and gradually builds up into the bulk of the tube. This slow degradation cannot be accounted for if one considers a Poiseuille pressure argument, but appears to be due to the creation of point defects. It is proposed that the chemical colouration due to contact with molten sodium involves reduction of the electrolyte, followed by charge compensation of the oxygen

vacancies with electrons.

This theory agrees with the experimentally observed fact that electron conductivity increases with darkening; and that heating a darkened crystal in air for a few hours will result in bleaching (due to reoxidation of the ß-alumina).

The increase in electron conductivity results in a lowering of ion conductivity and hence a rise in cell resistance, leading to a decrease in the Faradaic efficiency. This can ultimately lead to cell failure.

A resistance polarisation effect can occur due to the build-up of non-conducting species at grain boundaries. This is illustrated in figure 1.8.

Uses of the sodium-sulphur cell.

The Na/S cell cannot be manufactured on a very small scale and is thus not suited for use in household appliances such as radios, watches etc. Its main uses will be as a traction battery in electric vehicles, and as a load-levelling energy storage device in power stations.

Summary

The Na/S cell has one of the highest energy densities, and withstands one of the largest number of cycles of all the systems considered here. It is ideally suited for use in electric vehicles, provided that the safety risks involved in having molten sodium and sulphur present are considered and kept acceptably low, and that the materials problems of the breakdown of the ß-alumina electrolyte can be overcome.

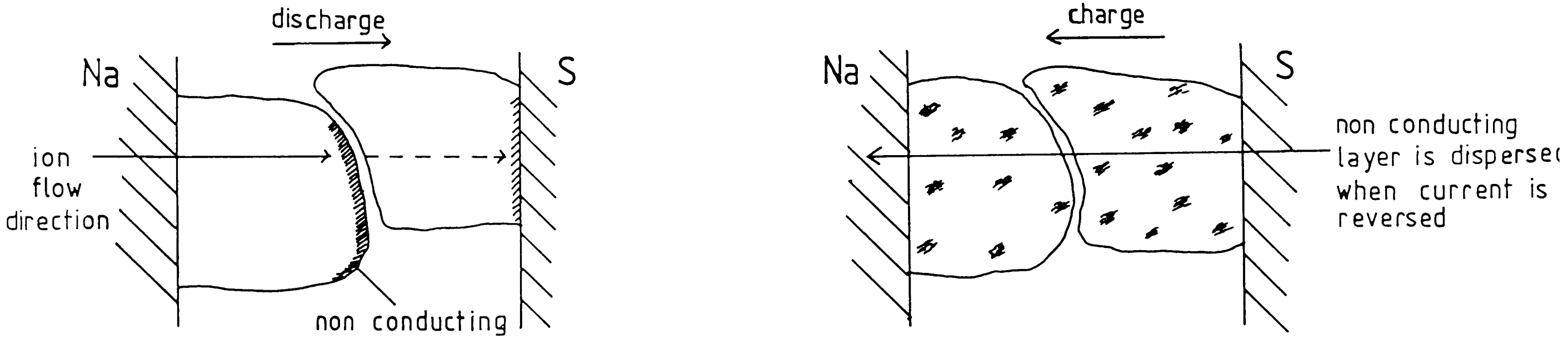

Fig. 1·8 Schematic Representation of the resistance polarisation effect in β-alumina.

Chapter 2. High resolution electron microscopy.

2.1 The transmission electron microscope (TEM).

a) Introduction

The idea of using electron beams to produce enlarged images with the aid of electromagnetic lenses was first evolved in 1932 by Knoll and Ruska (Technical University of Berlin) and by Bruche and Johannson (AEG Research Institute of Berlin).

The resolution of the best light microscope was soon exceeded by Krause and from then on development of the EM progressed steadily, mainly in the direction of better resolution and higher accelerating voltage.

In the late 1950s Hirsch et al. first looked at electrolytically thinned films using a transmitted beam.

The electron microscope basically consists of an electron gun and a series of lenses - divided into the illuminating and magnifying systems. The lenses are nowadays almost always magnetic rather than electrostatic because magnetic lenses have smaller aberrations and are more stable at high voltages. By altering the excitation (focal length of the post-specimen lenses) one can image either the specimen or the primary diffraction pattern (see fig. 2.1).

b) Magnetic lenses.

The main difference between optical lenses and magnetic lenses is that there is no magnetic equivalent of a concave lens; thus electron beams are always convergent and the aberrations due to the lenses are additive.

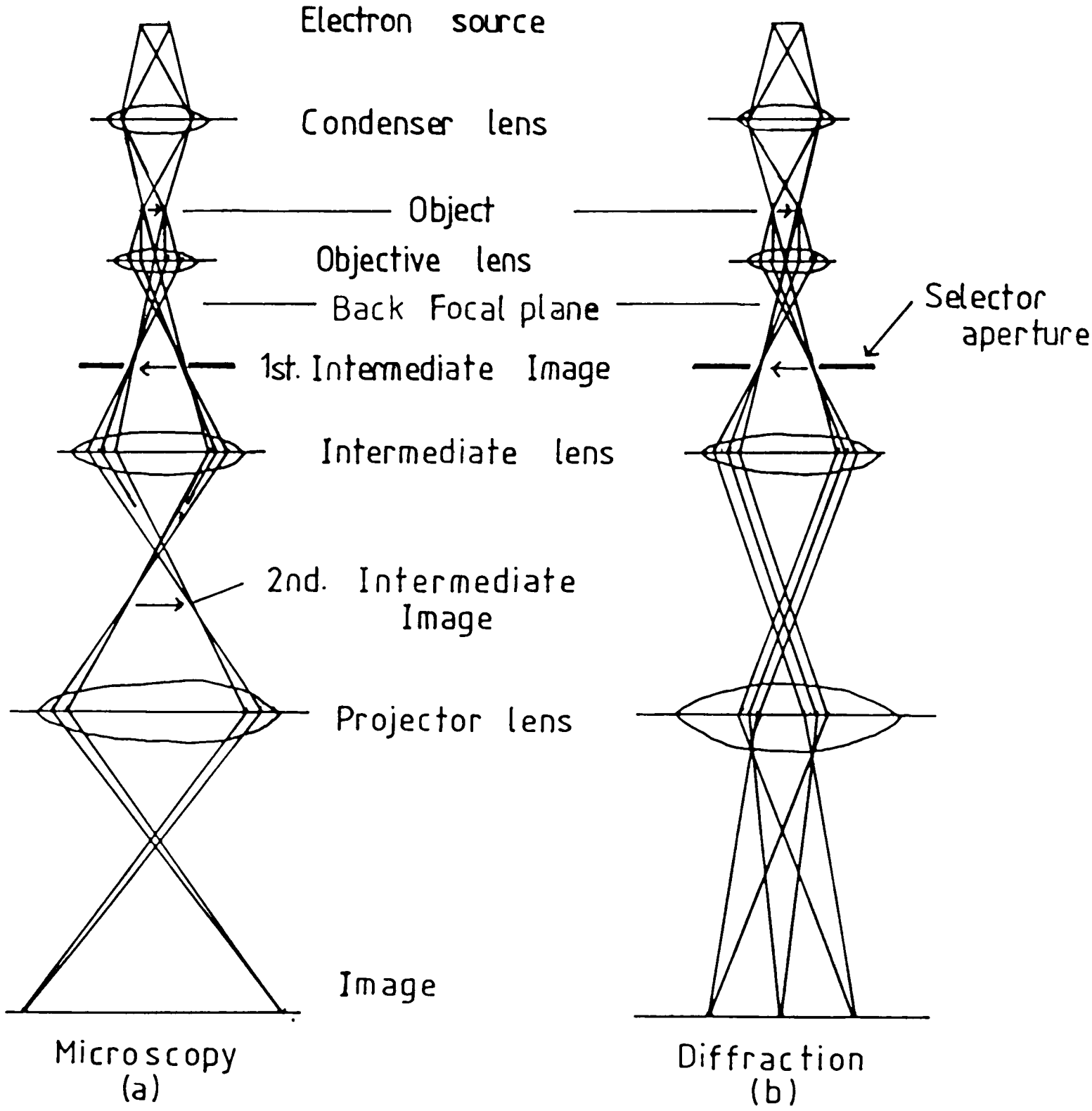

Fig. 2.1 Ray Paths in the Electron Microscope under (a) microscopy conditions and (b) diffraction conditions

The performance of a magnetic lens depends on its pole pieces, and a simplified diagram of an objective lens is shown in fig. 2.2 with the shape of its associated magnetic fields.

To obtain the paraxial ray equations, one assumes that a) only electron "rays" close to, and nearly parallel to the optic axis are significant, and that b) inside the lens Laplace's equation for free space holds.

1 $$\nabla^2 \phi_m = 0 \qquad \phi_m = \text{magnetic potential}$$

An equation for the forces on an electron in the lens can then be obtained, which can be divided into two parts - one which describes the lens action and one which describes the rotational motion.

2 $$\underline{F} = \frac{-e}{c}\left[(v_\theta H_z)\hat{i}_r + (v_z H_r - v_r H_z)\hat{i}_\theta - (v_\theta H_r)\hat{i}_z\right]$$

lens action — rotational motion — ignore as $v_z \approx v$

From this one can obtain paraxial equations for the rotation angle in radians

3 $$\theta = \sqrt{\frac{e}{8mc^2 V_r}} \int_{z=0}^{z=l} H_z\,dz \qquad V_r = \text{relative potential}$$

and for r as a function of z

4 $$\frac{d^2r}{dz^2} = \frac{-e}{8mc^2 V_r} H_z^2 r$$

Integrating (4), assuming that the focal length (f) is long compared with the axial extent of the field (l), the thin magnetic lens approximation is obtained

5 $$\frac{1}{f} = \frac{-e}{8mc^2 V_r} \int_0^l H_z^2\,dz$$

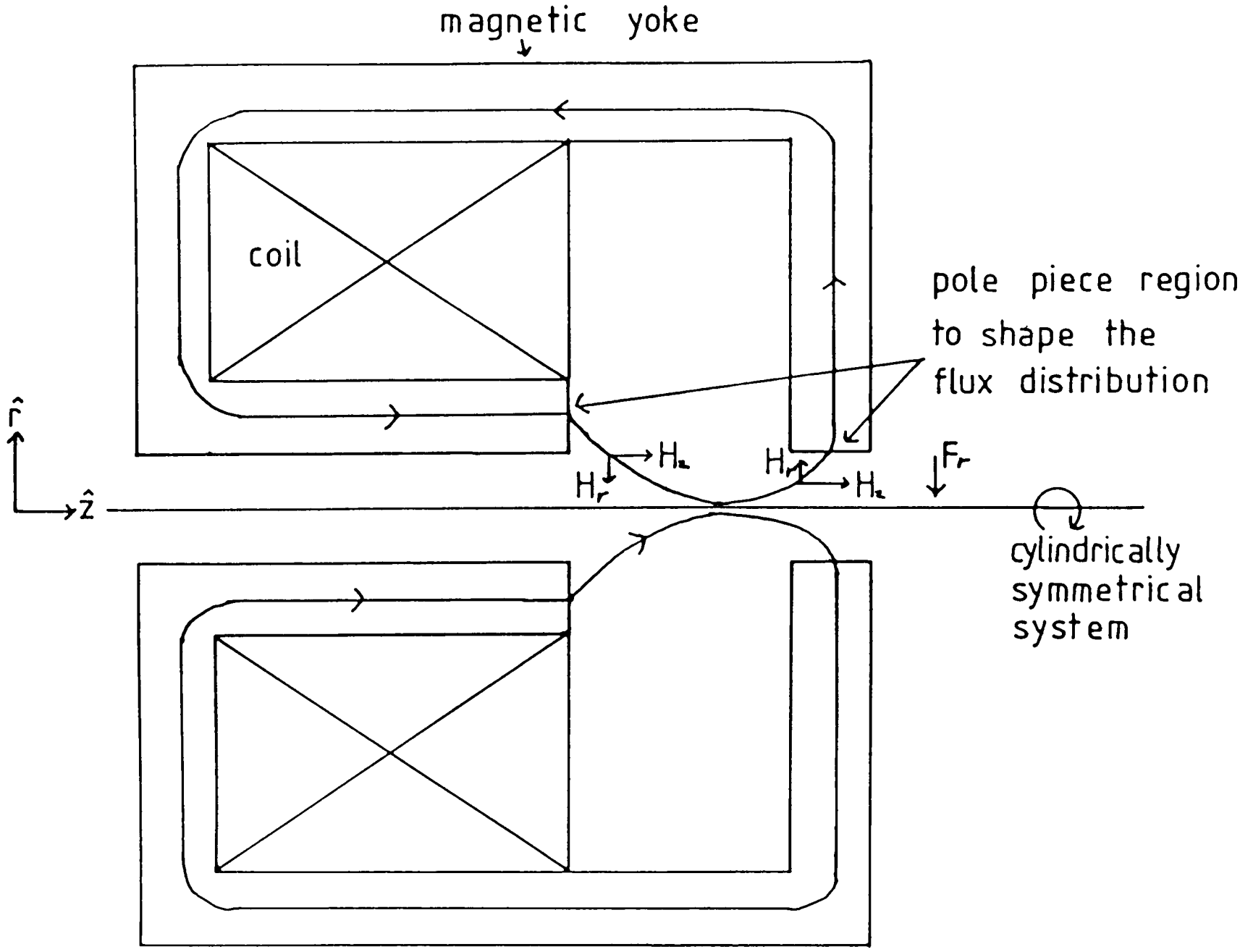

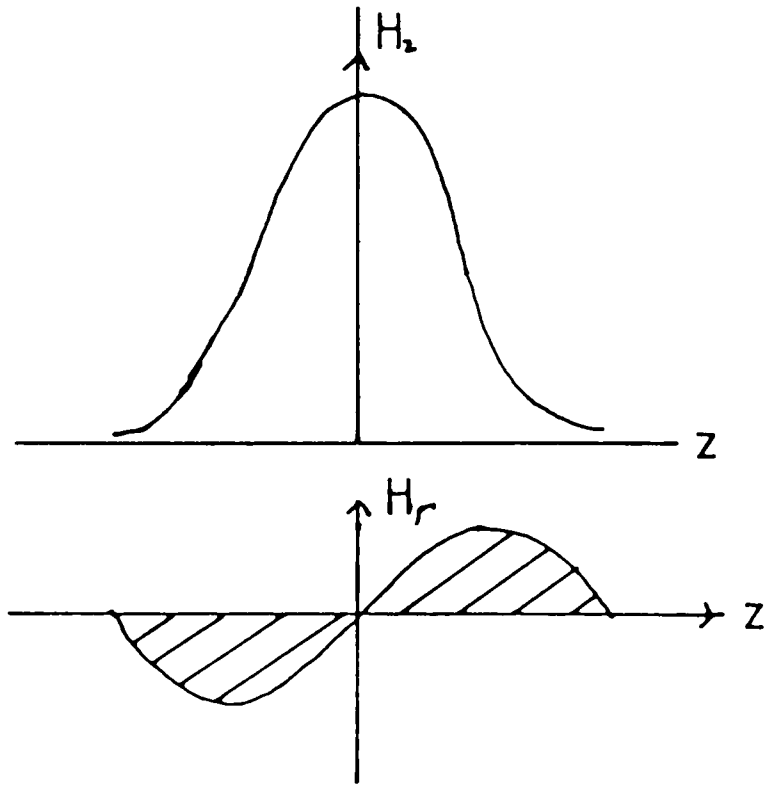

Fig. 2.2 Simplified diagram of a magnetic lens showing the shape of its associated magnetic fields.

The three aberrations of magnetic lenses which present the major limiting factor on lens resolution are the following:

1. Astigmatism - due to the non-circular symmetry of the lens field. This causes a spot to be imaged as a line. In practice, an auxilliary system of coils around the lens (stigmators) can be used to correct astigmatism.

2. Spherical aberration - due to the focal length near the axis being greater than that further from the axis. This gives rise to a disc of confusion (see fig. 2.3a). Spherical aberration cannot be compensated for by the use of concave lenses (as mentioned above) and is therefore the limiting factor on the attainable resolution.

6 $g_s = C_s \alpha^3$ g_s = resolution limit due only to spherical aberration

(= radius of disc of confusion)

C_s = spherical aberration constant

α = semi-angle of illumination

3. Chromatic aberration - due to the lens having a different focal length for electrons of different wavelength. Chromatic aberration arises if there is a spread in energy of the electrons in the illuminating beam. This can be reduced dramatically by suitable stabilisation of the high voltage such that the electron beam is approximately monoenergetic. In addition, chromatic aberration arises from energy losses of the electron beam within the specimen. In thick specimens, this is the dominant mechanism limiting the resolution.

The radius of the disc of confusion due to chromatic aberration is:

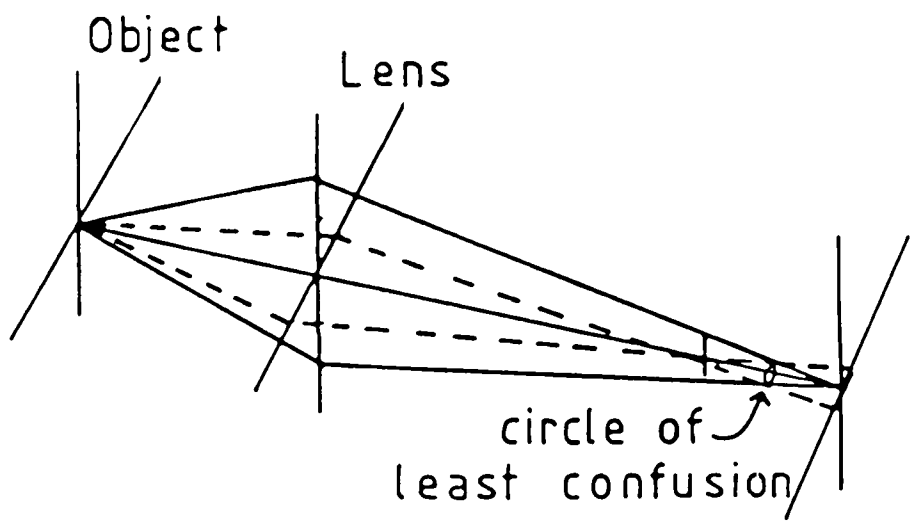

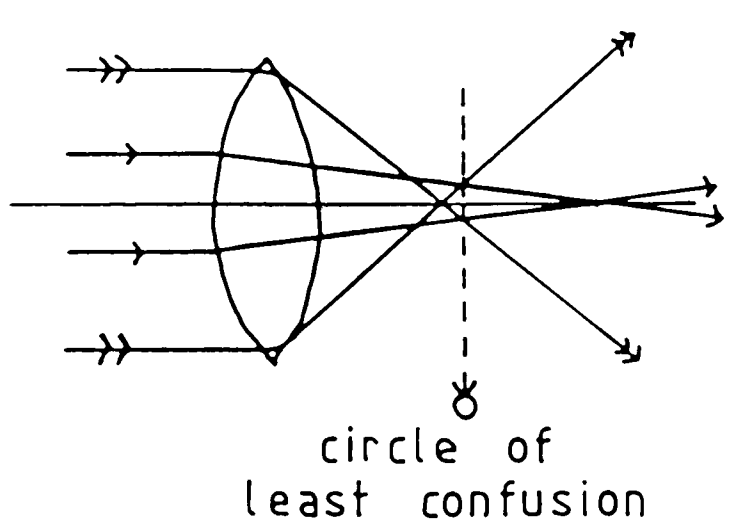

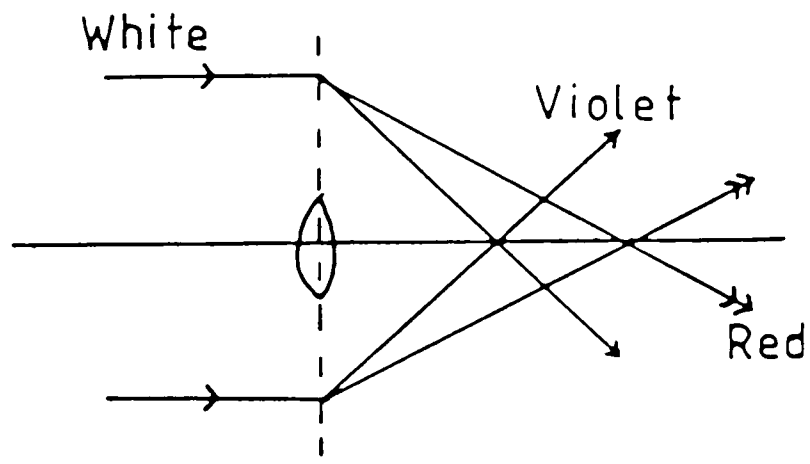

(a) Astigmatism (b) Spherical aberration (c) Chromatic aberration

Fig. 2·3 Aberrations in Magnetic Lenses

7 $g_c = C_c \alpha \frac{\Delta E}{E}$

C_c = chromatic aberration coefficient

α as above

E = energy of the electron beam

C_s and C_c are of the order of a few millimetres for modern microscopes (1.2mm and 1.4mm respectively for the Jeol 200CX HREM).

c) Electron sources

For high resolution electron microscopy (HREM) a bright source is needed so that at high magnification the image can be seen. The most common electron gun is a LaB_6 thermionic emmission source. A field emission gun produces a brighter image but requires a much higher vacuum (4 orders of magnitude better) and so some brightness is sacrificed to keep down the cost of the microscope.

2.2 Imaging in an HREM - phase contrast microscopy.

a) The phase object approximation

When the electron beam passes through a specimen it interacts with the electrostatic potential distribution - thus electrons are accelerated more when close to an atom where the potential is greater (positive). This acceleration reduces the wavelength of the electron and puts its phase ahead of that of a similar electron outside the specimen. The specimen thus affects only the phase, not the amplitude, of the electron wave if the specimen is very thin. Thus a thin specimen is said to act as (or be) a phase object.

If the incident electron beam is $\psi_o(x,y)$ then the wave leaving the specimen is $\psi_E = \psi_o q(x,y)$ where

8 $q(x,y) = \exp[-i\frac{\pi}{\lambda_E}\phi(x,y)]$ ϕ= projected potential in direction of beam

q = transmission function

$(\frac{\pi}{\lambda_E} = \sigma)$

or: $q(x,y)=\cos\sigma\phi(x,y) - i\sin\sigma\phi(x,y)$. For small fluctuations in ϕ, the potential, (ie. a very thin specimen such that $\sigma\phi_0 H<<1$), one can assume :

$\cos\sigma\phi \approx 1$ and $\sin\sigma\phi \approx \sigma\phi$ H = specimen thickness

$\phi_0 H = \phi$

9 $q(x,y) \tilde{} 1 - i\sigma\phi(x,y)$

This is known as the weak phase object approximation and it assumes kinematical scattering within the specimen.

Equation 9 can also be written in the form:

10 $q(x,y) = 1 - i\sigma\{\phi(x,y) - \bar{\phi}(x,y)\}$

where $\bar{\phi}(x,y)$ is the average value of the potential and is constant over a given region of the specimen.

Figure 2.4 indicates the way in which the projected potential (and hence the weak phase object approximation) depends on the atom arrangement within the specimen.

The coherence width C_w is the extent over which the incident illumination is coherent. This is given by:

11 $C_w \approx \frac{\lambda}{\alpha}$ α= convergence angle

and gives a measure of the region over which $\bar{\phi}$ can sensibly be averaged. In the following treatment, it is assumed that the specimen considered is thin, and acts as a weak phase object.

The intensity of the exit face of the specimen is

12 $I = |\psi_E(x,y)|^2 = 1$

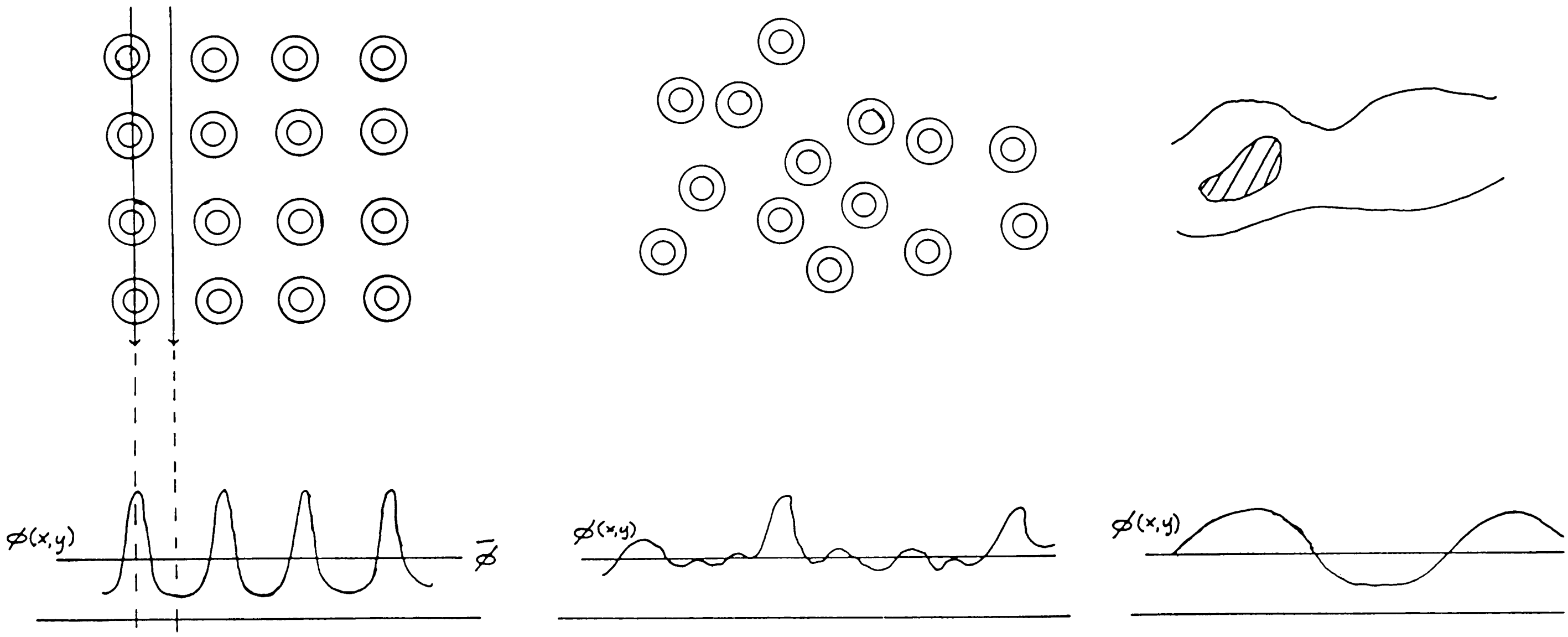

Fig. 2·4 Showing the phase object approximation for (a) a crystal with the incident beam parallel to a principal axis, (b) an amorphous material with a near-random arrangement of atoms, and (c) an amorphous specimen in which the arrangement of atoms is not distinguished, but $\phi(xy)$ depends on the variations on specimen thickness and atom density.

Thus the microscope must be imperfect or defocused to allow information about the specimen to be obtained.

The specimen does in fact absorb some energy due to inelastic collisions with the incident electrons. If the electrons lose sufficient energy that they cannot pass through the specimen or are scattered outside the objective aperture, one can include an absorption term in equation 12:

$\exp(-\mu(x,y))$ where μ is the absorption function. Thus:

13 $I(x,y) = |\exp(-i\sigma\phi(x,y,t) - \mu(x,y,t)|^2 = \exp(-2\mu(x,y,t))$ t=thickness

This does contain information on the specimen structure, as different regions of the specimen, eg. different elements, will absorb electrons by different amounts. However $\mu(x,y)$ is very small compared with $\sigma\phi(x,y)$ and so if the specimen is thin, absorption does not contribute greatly to the contrast in the image.

b) Abbé Theory for Ideal Imaging.

The Abbé theory treats the microscope as a perfect imaging system, and it considers how a plane wave, incident on the specimen, is altered at each point in the microscope. Figure 2.5 shows a geometrical analogue of the Abbe theory, and the following section will refer to this figure.

If a plane parallel wave (ψ_o) of unit amplitude is incident on the specimen surface, it is scattered in a way which depends on the transmission function q(x,y). All radiation scattered at a given angle in the specimen is brought to a point in the back-focal plane of the objective lens. The amplitude at a given point is a measure of the content of q(x,y) at a particular spatial frequency ,u, where

14 $u = 1/d$ Å^{-1}

Ray diagram for a Transmission Electron Microscope.

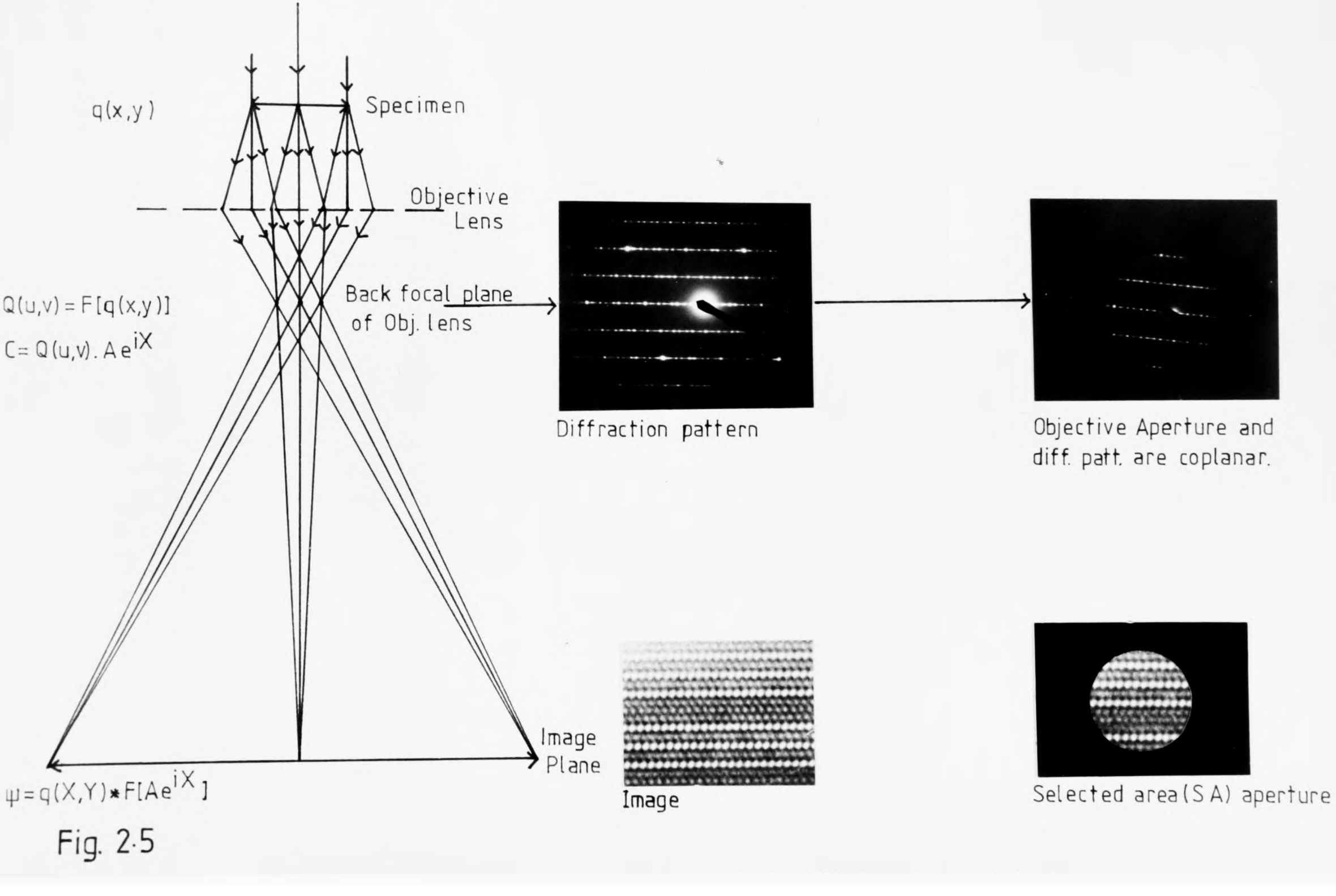

Fig. 2.5

where d is the repeat distance of a set of Bragg planes in the object. A map of these amplitudes is known as the diffraction pattern. A point near the centre of the diffraction pattern (u small) corresponds to a large repeat distance in the specimen (d large). Thus the further out a point is in the diffraction pattern, the higher its corresponding spatial frequency.

Mathematically, the diffraction pattern is the Fourier transform of the exit face wave

15 $$Q(u,v) = F[\, q(x,y)]$$

By referring to figure 2.1 one can see that by imaging the back focal plane of the objective lens one can image the intensity distribution $|\, Q(u,v)|^2$.

From the back focal plane the wave passes to the image plane, undergoing another diffraction process to form an image. This is represented by a second Fourier transform

16 $\psi(x,y) = F[\, Fq] = q(X,Y)$ X,Y are magnified x,y coordinates.

c) Inclusion of the contrast transfer function, optimum defocus

At Gaussian focus, very little contrast is obtained in the image as can be seen if one considers equation 11, and so the objective lens is defocused to add in phase factors which change the relative phases of different spatial frequencies in the specimen. This modifies the intensity distribution in the image (see equation 13) and thus increases the amount of structural information obtainable from the image.

The spherical aberration also introduces a phase factor dependent on the distance of a diffraction spot from

the centre of the diffraction pattern (ie. on the spatial frequency) and the combination of these two effects leads to a multiplication of the electron wave amplitude by

17 $T(u) = \exp[i\chi(u)]$ the contrast transfer function

where: $\chi(u) = \frac{\pi C_s \lambda^3 u^4}{2} + \pi D \lambda u^2$ D=defocus

This is further modified by two exponential damping terms such that

18 $T(u) = \exp(i\chi)\exp(-A)\exp(-B)$ where A depends on Cc and the defocus spread, and B depends on Cs and the beam divergence.

Figure 2.5 shows how the CTF affects the electron wave mathematically.

The optimum defocus is that for which $\sin\chi$ is close to -1 for as large a range of spatial frequencies (u) as possible. This can be calculated if the values of C_s and λ for a particular microscope are known. This condition implies that as large a range of u as possible is transferred to the image without relative contrast.

Contrast transfer functions for the Jeol 200CX HREM at optimum defocus and at a greater underfocus are shown in figure 2.6. An objective aperture is inserted in the diffraction pattern plane to cut out contributions from all scattered beams with spatial frequencies higher than that at which the first zero in $\sin\chi$ occurs. This prevents confusing information from reaching the image plane. In some HREMs the chromatic aberration damping term cuts off the spatial frequencies close to the value of u at which the first zero of $\sin\chi$ occurs, but this is not the case for the Jeol 200CX

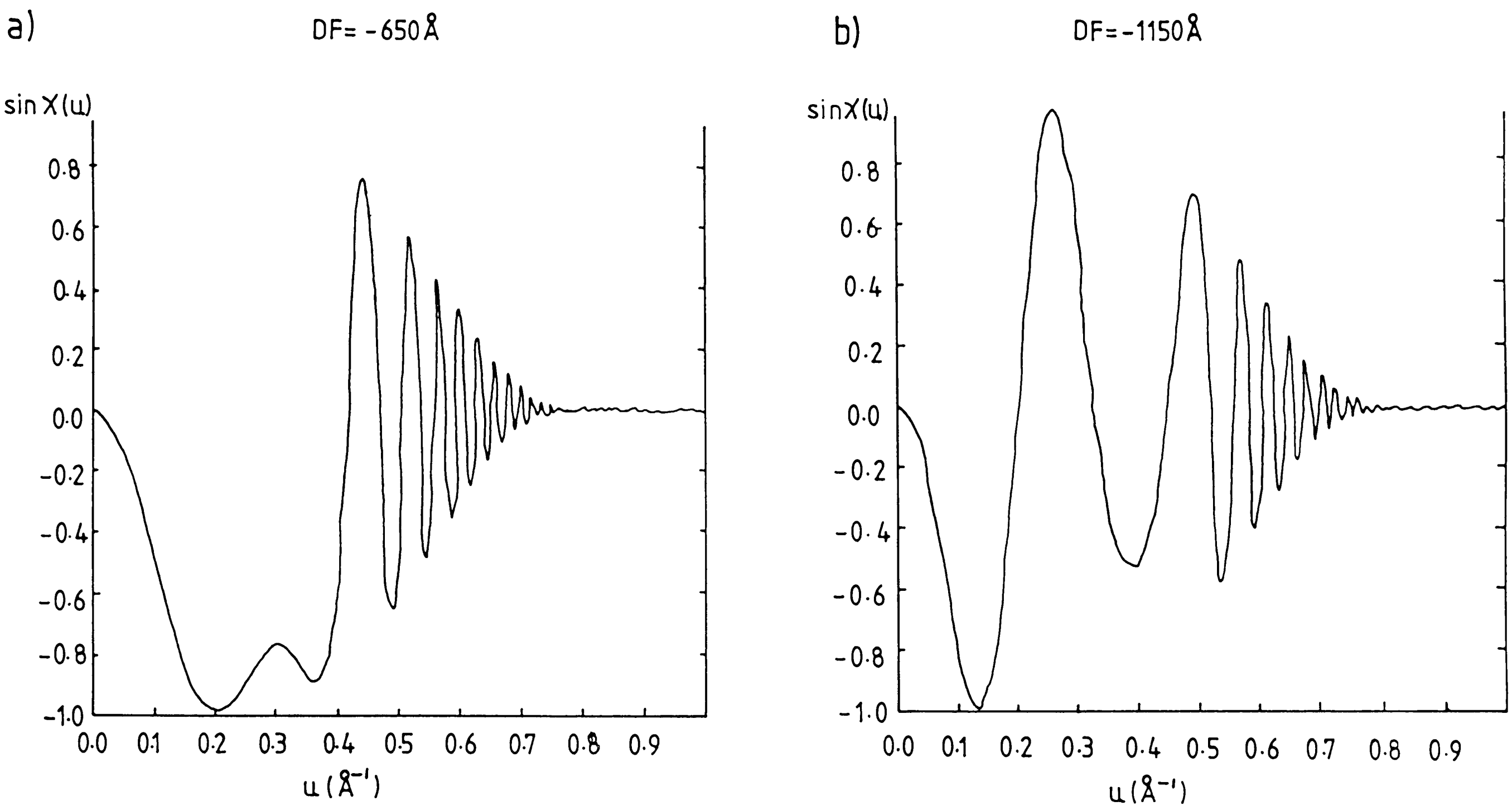

Fig.2·6 Contrast transfer functions for the Jeol 200 CX a) near Scherzer defocus & b) at a greater negative defocus.

for which information extends out to 1.8Å .

The optimum defocus is known as Scherzer defocus and can be calculated from:

19 $$D_s = \sqrt{C_s \lambda}\,\sqrt{3/2}$$

Higher spatial frequencies than those obtained at Scherzer defocus can be imaged. This is done by increasing the defocus so that the plateau of the CTF falls further out in reciprocal space. An annular aperture must then be used to cut out spatial freqencies above and below the plateau region. These defoci are known as passbands, and are given by:

20 $D_n = \sqrt{C_s \lambda}\sqrt{(8n+3)/2}$ (zero passband is Scherzer defocus)

If one considers the equation: $\chi(u) = \frac{\pi}{2} C_s \lambda^3 u^4 + \pi D \lambda u^2$

A B

and considers terms A and B separately, one can see that the shape of $\chi(u)$ is made up of a term in u^2 superimposed on a term in u^4. The term in u^4 will always be positive since C_s is always positive in an electron microscope (see section 2.1b). However, term B (in u^2) can be positive or negative. As can be seen from figure 2.7, only a negative value of D_s will allow the shape of $\chi(u)$ to be such that $\sin\chi(u)$ will have the desired shape (ie. a flat plateau region with $\sin\chi \approx -1$).

If the microscope is defocused at Scherzer defocus such that $\sin\chi(u) \approx -1$, and the weak phase object approximation holds, than in the image plane:

21 $\psi = F[Q(u,v)\ T(u)]$ (From equns. 14,15,17)

Giving:

22 $I = |\psi\psi^*| = 1 + 2\sigma\phi * F[\sin\chi(u)]$

If an aperture is inserted such that $\sin\chi$ is cut off

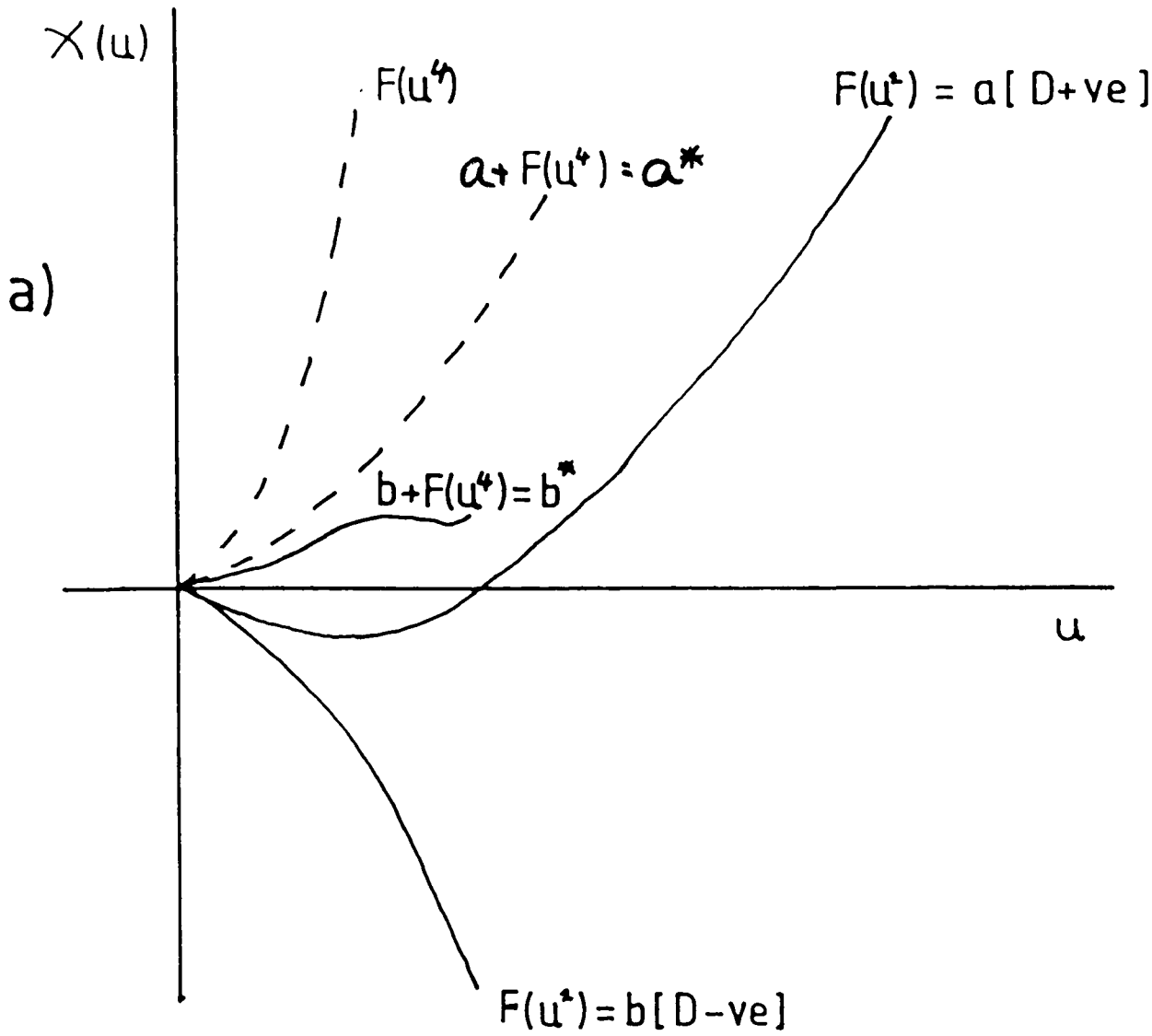

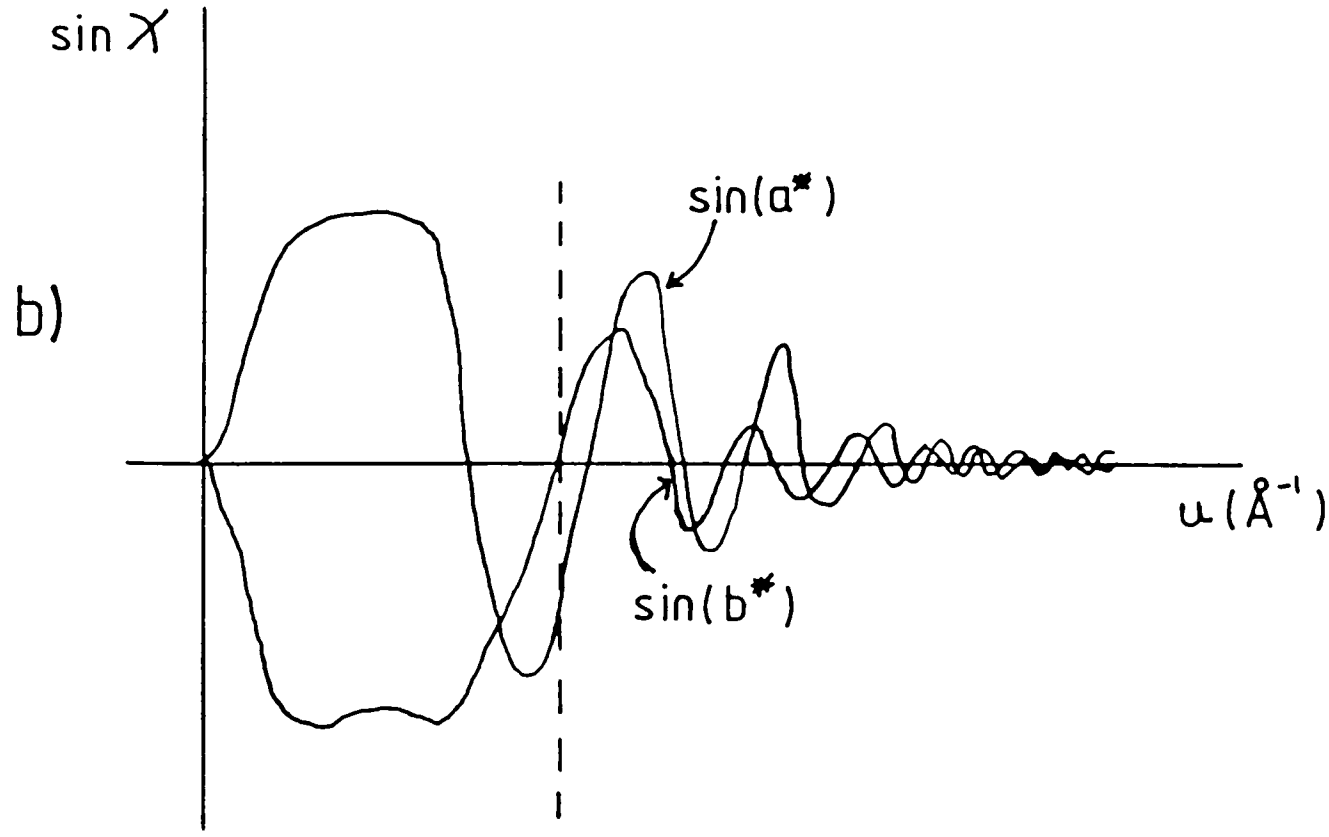

Fig. 2·7 a) χ(u) for positive & negative defocus
(a*, b* = χ)
b) sin χ for positive & negative defocus.

at the first zero, and the remaining part of $\sin\chi$ is flat (see fig.2.6 at Scherzer defocus), then

23 $F[\sin\chi(u)] \Rightarrow \delta(u)$ - a delta function

and thus the final image is a directly interpretable representation of the projected potential of the specimen.

2.3 Practical high resolution electron microscopy.

a) Conditions necessary for obtaining HREM images.

i) The specimen should be thin enough for the weak phase object approximation to hold. - This condition makes interpretation of images easier, but is not necessary for an image to be obtained.

ii) An objective aperture must be inserted to cut off all spatial frequencies above the Scherzer limit.

iii) The objective lens current must be altered to obtain optimum defocus.

iv) The illuminating system must be aligned as perfectly as possible.

v) It must be possible to tilt the specimen so that an image can be obtained down the required projection. In the Jeol 200CX HREM, a stage with dual tilts of +/-10° is used. The best contrast is obtained with the specimen tilted such that the beam is directly down a zone axis. For HREM this condition is very important.

b) Recording the images.

i) The specimen stage must be well constructed so that minimum drift occurs. If the stage drifts, a sharp image will not be obtained.

ii) In the case of beam sensitive materials, the specimen

must be oriented, and the optimum microscope conditions obtained as quickly as possible. The beam can cause severe radiation damage - loss of crystallinity, etching, structural changes. To try to minimise radiation damage, the beam should be aligned and the stigmators adjusted away from the area of interest, and the specimen should be oriented with the beam defocused (lower current density).

The next section discusses the way in which computer simulated HREM images can be generated, and the way in which they can be invaluable in helping to interpret high resolution images.

2.4 Computer simulation of HREM images and diffraction patterns.

Either the thickness of a specimen, or the microscope defocus is usually not known accurately enough to allow direct interpretation of an HREM image. In order to relate features visible in the image to the structure of the object, one must calculate the way in which the electrons will propagate through the specimen, and hence what an image should look like. In practice, one must postulate an object structure and thickness, calculate the image for a particular set of imaging conditions (microscope defocus, aperture size, etc.) and then compare the calculated and experimental images. The structure model and the suggested imaging conditions can then be changed if necessary, and new computed images produced until a good match is seen between the computed and experimental images.

This matching process can be very time consuming, and so various interactive systems have been developed which take

input structure data and imaging conditions and produce computed images and diffraction patterns.

The computer matching process is of special importance where images of defects are concerned, as the exact structure of the defect is usually unknown and is to be found. In this case the only method of determining the defect structure is to compare computed and experimental images for different defect models for known defocus and thickness.

The program system at present in use at Oxford is that developed by Dr.A.J.Skarnulis - known as EMSYS. The multislice technique is employed, in which the crystal is considered to consist of a number of thin slices (5Å thick was used for ß-alumina) perpendicular to the beam. The program calculates the amplitude of each diffracted beam after passing through each successive slice.

The EMSYS system contains the following programs:

1. PLOT - This program uses as input the atomic coordinates, occupancy, atom type and Debye-Waller factor for each atom in the unit cell, plus the unit cell volume and the desired projection. The output is a plotted projection of the crystal structure along the required input direction. The plot is done in real time. A cursor can be used to add, subtract or move atoms.

2. FCOEFF - This program takes the PLOT file as input, plus the maximum required spatial frequency. It calculates structure factors and Fourier coefficients of the crystal potential for use in later programs.

3. MULSLI - This program uses the FCOEFF output to calculate the projected potential of the crystal after each slice, and

finally at the exit face of the crystal. Slices of different potentials (such as defect blocks) can be used sequentially. The output is a computer simulation of the projected potential after one slice.

4. IMAGE - This program uses the exit face wave function calculated in MULSLI and applies chromatic and spherical aberrations, defocus and aperture effects. An image is calculated and displayed on the screen in real time.

5. DIFFPAT - This program uses the PLOT file as input and applies microscope and specimen parameters. It plots a kinematical diffraction pattern on the screen down the required zone axis. The spots can be scaled in size to their calculated intensities.

The normal procedure is to calculate images for either through-focal or through-thickness series and then choose the best match to the experimental image.

Chapter 3. The structure of the ß-aluminas.

3.1 General Structure

The ß-aluminas are a family of polyaluminates of which the first to be characterised was sodium ß-alumina. This was characterised in 1927 (Hendricks and Pauling) and then more fully in 1931 (Bragg et al.). The proposed structure has hexagonal unit cells consisting of spinel-like blocks of close packed oxygen and aluminium layers 11Å thick perpendicular to the c-axis, separated by loosely packed layers containing sodium and oxygen. The spinel blocks are held together across the so-called conduction plane by Al-O-Al bridges. The bridging oxygen ions have large ionic radii, hence the conduction planes are quite wide, so that the sodium ions are not tightly bonded, giving rise to the high ionic conductivity of the ß-aluminas. The structure of ß-alumina and three of its polymorphs - ß", ß"' and ß"" are shown in figure 3.1.

In ß and ß"-alumina the spinel blocks contain four close packed oxygen layers, and in ß"' and ß"" they contain six layers.

Figure 3.2 shows the atomic arrangement in a single spinel block.

3.2 Sodium ß-alumina.

As mentioned above, Na ß-alumina was first characterised fully in 1931 by Bragg et al. They prepared the material by slow cooling of molten alumina in the presence of small amounts of MgO and Na_2O. X-ray diffraction

Sodium β - alumina

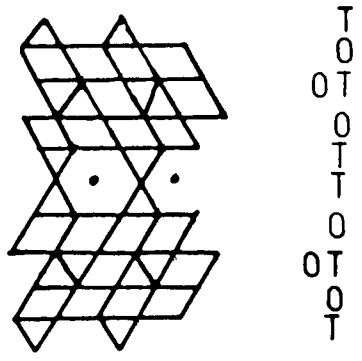

a = b = 5·6Å; c = 22·6Å

Sodium β'' - alumina

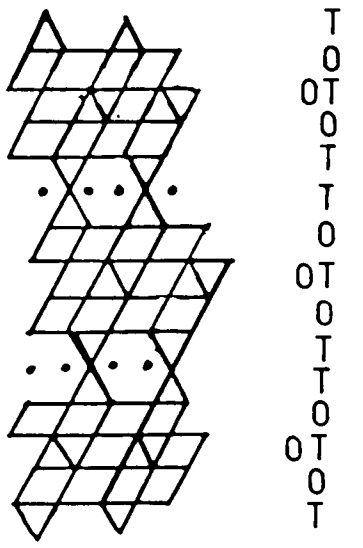

a = b = 5·6Å; c = 33·9Å

Sodium β''' - alumina

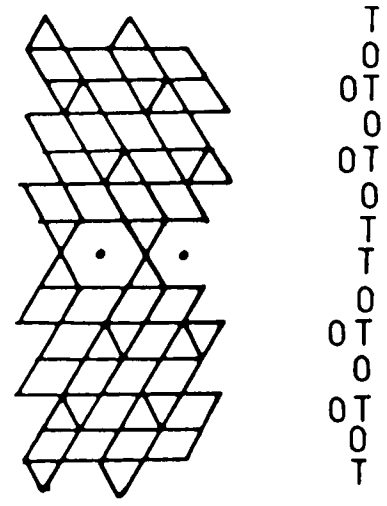

a = b = 5·6Å; c = 31·8Å

Sodium β'''' - alumina

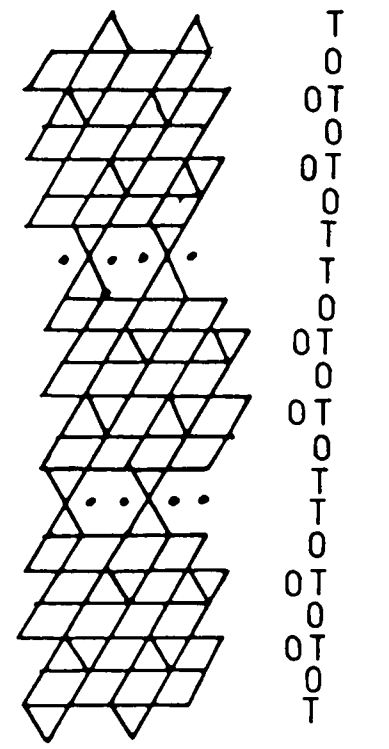

a = b = 5·6Å; c = 48·0Å

O = Al(or Mg) atoms in octahedral coordination

T = Al(or Mg) atoms in tetrahedral coordination

OT = Al(or Mg) atoms in mixed coordination (one octahedral & two tetrahedral sites per unit cell)

• = Sodium ions between bridging tetrahedra

Fig. 3·1 Schematic polyhedral diagrams of the four β-alumina polytypes. The diagrams show one unit cell along the c-axis in each case; all structures are hexagonal with $\alpha = \beta = 90^\circ$, $\gamma = 120^\circ$.

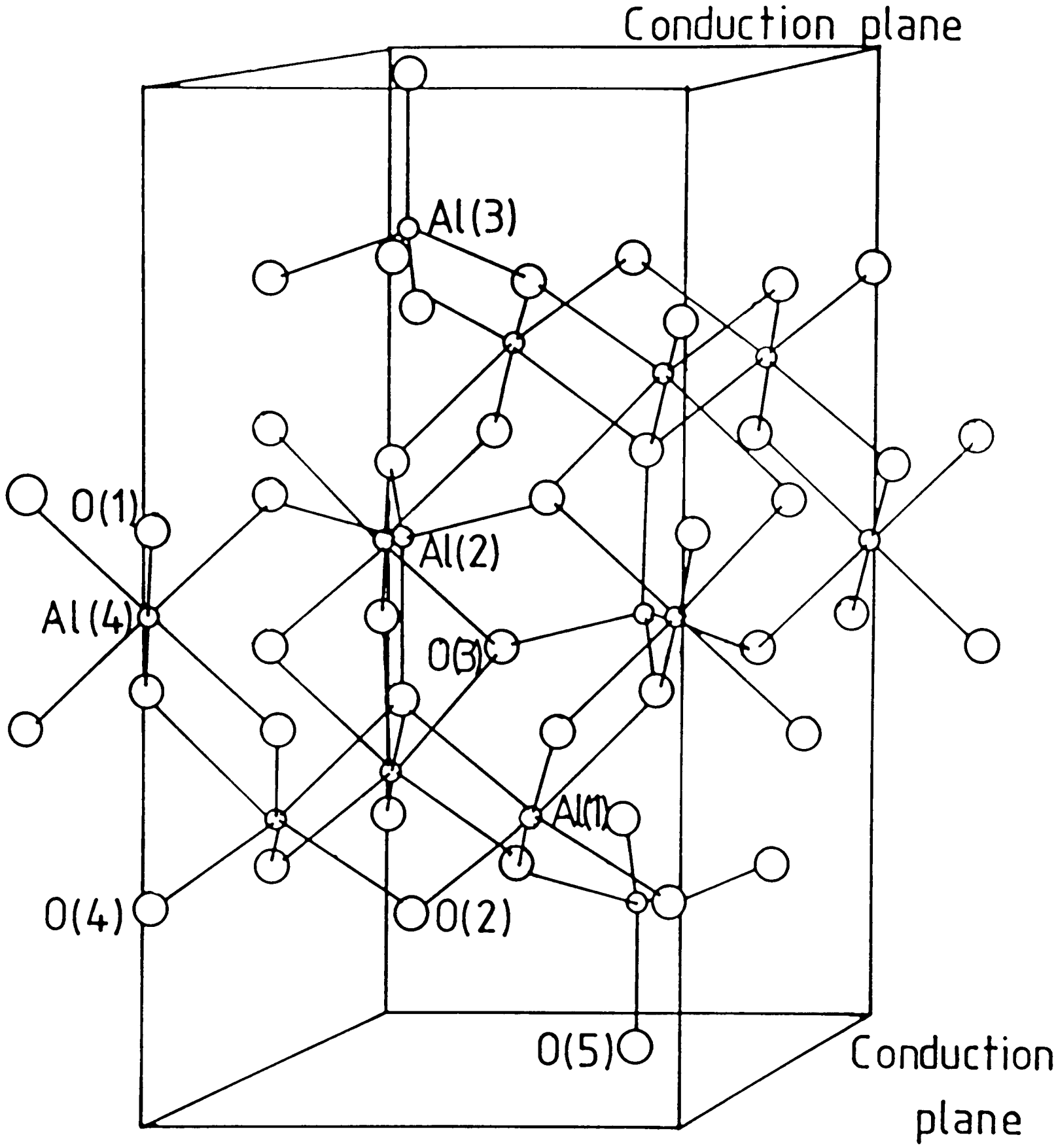

Fig. 3.2 Atomic arrangement in a single spinel-like block in sodium ß-alumina.

o = aluminium

○ = oxygen

methods were used to determine the space group - D_{6h}^{4}(c6/mmc) - giving rise to a hexagonal unit cell with lattice parameters a=5.56Å, c=22.55Å. They also correctly determined the positions of the aluminium and oxygen atoms in the spinel blocks, but wrongly positioned the sodium ions in the conduction planes. In ß-alumina the two spinel blocks in the unit cell are related to one another by a mirror plane passing through the centre of the conduction plane perpendicular to the c-axis. The bonding in the spinel blocks is partially ionic , partially covalent.

In 1937 Beevers and Ross carried out further work, based on ß-alumina specimens of ideal formula $Na_2O.11Al_2O_3$, with lattice parameters a=5.58Å, c=22.45Å, and proposed that the sodium ions were in the (2/3,1/3,1/4) positions - the Beevers-Ross sites.

The structure was refined by Peters, Bettman et al. in 1968 using the space group $P6_3/mmc$, with a=5.59Å and c=22.53Å. It was suggested that ß-alumina is normally in the form $(Na_2O)_{1+x}.11Al_2O_3$ where x ranges from 0.15 to 0.3 giving rise to a non-stoichiometric structure. See table of atomic positions in figure 3.3.

Three possible sodium sites were suggested: the (2/3,1/3,1/4) sites - the BR sites, the (0,0,1/4) sites - anti Beevers-Ross (aBR) sites, and the mid-oxygen (mO) sites in which the excess sodium was found. The mO sites are so named as they lie midway between the O(5) sites (see fig. 3.2) in the conduction planes. These sites are shown in figure 3.4.

A detailed x-ray diffraction analysis of the sodium distribution in the conduction plane leads to the following

Atom type	Point group (Wyckoff notation)	Occupancy per site (standard deviation)	Coordinates x	z	Temperature factors 11	33	12	13
O(1)	12(k)	0.996 (9)	0.1571	0.0501	51	2.3	37	0.1
O(2)	12(k)	0.998 (9)	0.5032	0.1468	38	3.4	16	0.2
O(3)	4(f)	0.993 (12)	0.6667	0.0555	53	1.1	$\beta_{11}/2$	0
O(4)	4(e)	1.014 (11)	0	0.1425	45	2.2	$\beta_{11}/2$	0
O(5)	2(c)	1.018 (21)	0.3333	0.2500	548	2.3	$\beta_{1}/2$	0
Al(1)	12(k)	0.989 (6)	0.8322	0.1063	49	2.6	28	0.1
Al(2)	4(f)	1.028 (8)	0.3333	0.0248	38	2.3	$\beta_{11}/2$	0
Al(3)	4(f)	1.006 (8)	0.3333	0.1756	53	1.5	$\beta_{11}/2$	0
Al(4)	2(a)	1.025 (10)	0	0	39	2.4	$\beta_{11}/2$	0
Na(1) BR	6(h)	0.250 (12)	0.7062	0.2500	668	12	147	0
Na(2) mO	6(h)	0.174 (15)	0.8731	0.2500	858	12	-396	0

Temperature factor of the form: $\exp\{-[(h^2 + k^2) + l^2 + 2hk + (2hl - 2kl)] \times 10^{-4}\}$

Lattice parameters in Angstroms: a = 5.594 c = 22.53

Fig. 3.3 Atomic positions and thermal parameters for sodium β-alumina. (Peters et al., 1971)

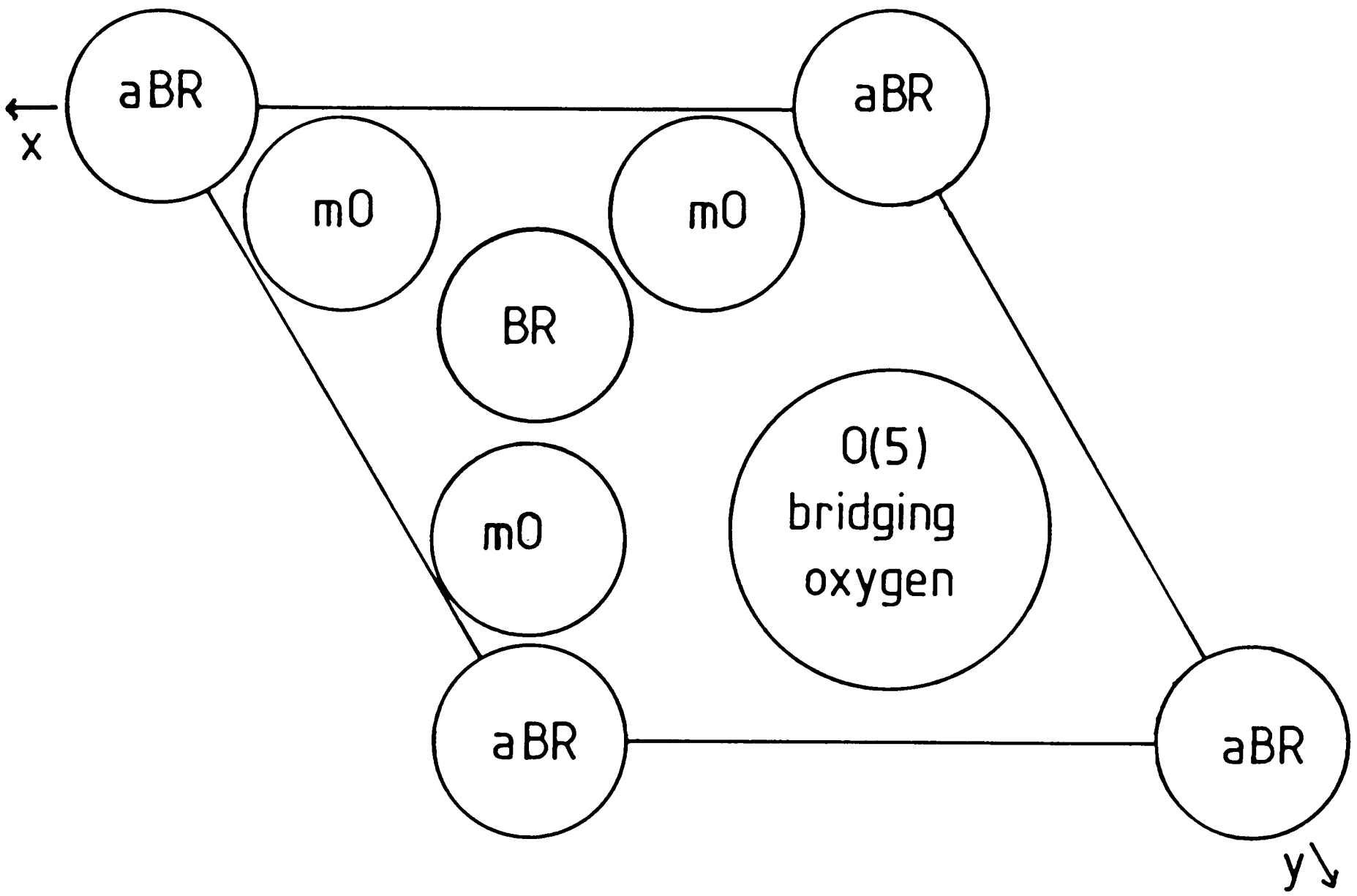

Fig. 3.4 Structure of the conduction plane in sodium β-alumina showing the sodium ion sites.

points (Peters et al., 1971):

a) The BR site is at the centre of a triangular spread of electron density - produced either by large thermal motion of the sodium ions or by a random distortion from the BR site due to the presence of charge-compensation defects (see later). These sites are only approximately 75% filled, again due to the effect of charge-compensation defects.

b) The aBR sites show practically no electron density.

c) The mO sites are sixfold coordinated (6h sites) and contain the sodium lost from the BR sites plus any sodium excess due to non-stoichiometry.

This excess of sodium provides a need for some sort of charge-compensation mechanism to preserve local electroneutrality. Peters et al. (1971) and West (1979) have proposed three possible mechanisms:-

1. The presence of aluminium vacancies in the spinel block giving rise to ß-alumina of formula $2(Na_{1+3x}Al_{11-x}O_{17})$, for which electroneutrality would be achieved for $x=2/3$.

2. The substitution of Al^{3+} in the spinel block by Mg^{2+} leading to ß-alumina of formula $2(Na_{1+x}Al_{11-x}Mg_xO_{17})$. In this case electroneutrality would be achieved for $x=2$.

3. The presence of Al Frenkel defects in the conduction plane with associated bridging oxygens. Two aluminium ions are displaced from the spinel block into the conduction plane. An extra O^{2-} bridge must be created to give rise to two tetrahedral sites for Al^{3+} Frenkel defects. The extra O^{2-} is available due to an excess of Na_2O in the structure. The bridging oxygen has a sodium ion interstitial pair associated with it to preserve overall charge neutrality.

Mechanism 1 has not been seen experimentally so far.

Mechanism 2 has been observed experimentally (but it should be noted that a maximum divalent ion concentration exists above which ß" forms), as has mechanism 3, for which neutron diffraction (Roth et al., 1977) has shown that the interstitial oxygens (with associated Al and Na ions) occupy the mO sites. Mechanism 2 appears to be the only source of charge compensation observed in doped materials.

Electrostatic considerations such as that of Newsam (1982) give rise to a maximum sodium excess in the conduction plane of 57% for undoped materials, and 67% for magnesium doped materials. Bourke (Bourke et al., 1980) prepared undoped samples with a sodium excess greater than 57%, and found them to have a much lower ionic conductivity than that of the ß-alumina usually considered (15% - 30% excess).It has also been noted by Bourke (Bourke et al., 1980) that as the sodium content increased so the c lattice parameter decreased. With an increase in sodium content from 5.00wt% to 7.4wt%, c decreased from 22.54Å to 22.38Å probably due to a decrease in electrostatic repulsion between adjacent spinel blocks as a result of the presence of excess positive ions in the conduction planes. The excess Na does not fill all the extra available sites in the conduction planes and so a degree of cation disorder is present in the non-stoichiometric structure (Sato and Hirotsu, 1976). This disorder is responsible for the high conductivity of sodium ß-alumina (see later for fuller discussion), and hence the stoichiometric material ($Na_2O.11(Al_2O_3)$) does not have high ionic conductivity.

The conductivity is also a function of the correlation between the mobile ions in the conduction planes;

and in non-stoichiometric ß-alumina of the positional correlation ie. ordering, between the charge compensation defects and the mobile ions. The concentration of Na in the conduction planes determines the number of defects. and their correlation, and thus the conductivity is affected by ion concentration . Long range order (LRO) exists between normal unit cells, those containing an interstitial oxygen bridge (McWhan et al., 1978) and those containing excess sodium (see fig. 3.5) at low temperature, in non-stoichiometric ß-alumina. It has been observed that as the LRO due to 'frozen in' interstital oxygens increases so the conductivity decreases, due to the fact that these interstitials present local barriers to the mobile ions.

As mentioned above, as the mobile ion concentration increases so the $\bar{c}$ lattice parameter, and hence the conduction plane height, decreases. This results in the mobile ion becoming more strongly coupled to the lattice, which again decreases conductivity. Maximum conductivity seems to occur for a composition with approx. 25% excess sodium.

Boilot (Boilot et al., 1979) has observed the formation of a 2-dimensional superlattice in stoichiometric ß-alumina on cooling to low temperature. The superlattice has lattice constants $a\sqrt{3}$ x $a\sqrt{3}$ and exists within the conduction planes (see fig. 3.6). For Mg^{2+} doped Na ß-alumina Boilot (Boilot et al., 1977; Collin et al., 1979) has observed two types of ordering - one for x=0, [in $(Na_2O)_{1+x}(MgO)_{2-x}(Al_2O_3)_{11-x}$] ie. undoped material, and one for x=.66 (the maximum value for x before the ß" phase is preferred). The ordering for x between these two values is a

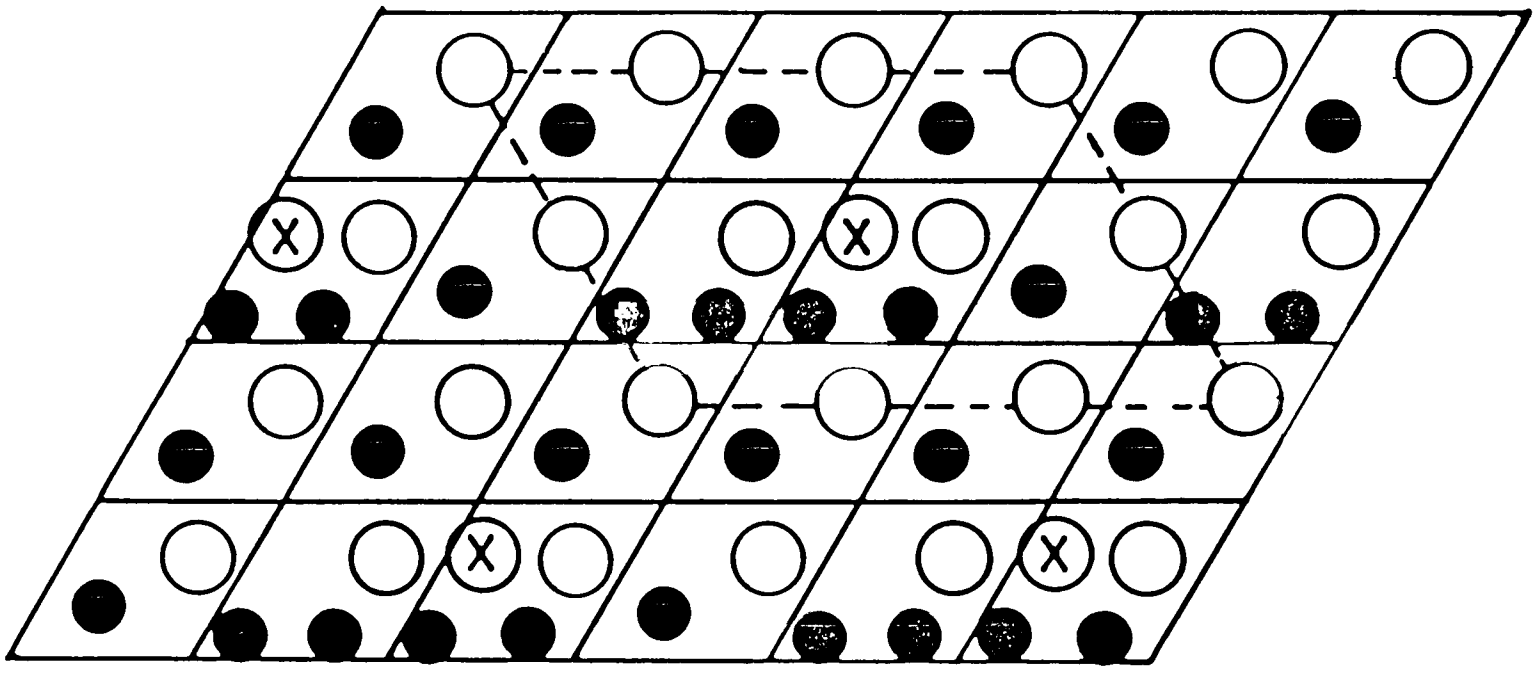

○ Bridging oxygen

⊗ Interstitial oxygen

● Sodium ion

--- Superlattice cell

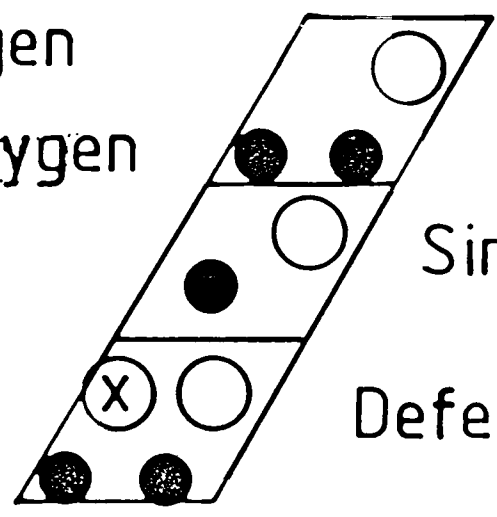

Doubly occupied cell

Singly occupied cell

Defect cell

Fig. 3.5 A possible model for superlattice ordering between singly occupied, doubly occupied, and defect cells in nonstoichiometric sodium ß-alumina at low temperature. (undoped material)

Fig. 3·6 Superlattice ordering of the sodium ions a) in non-stoichiometric Na β-alumina of formula $(Na_2O)_{1.67}(MgO)_{1.33}10{\cdot}33(Al_2O_3)$, and b) in stoichiometric Na β-alumina.

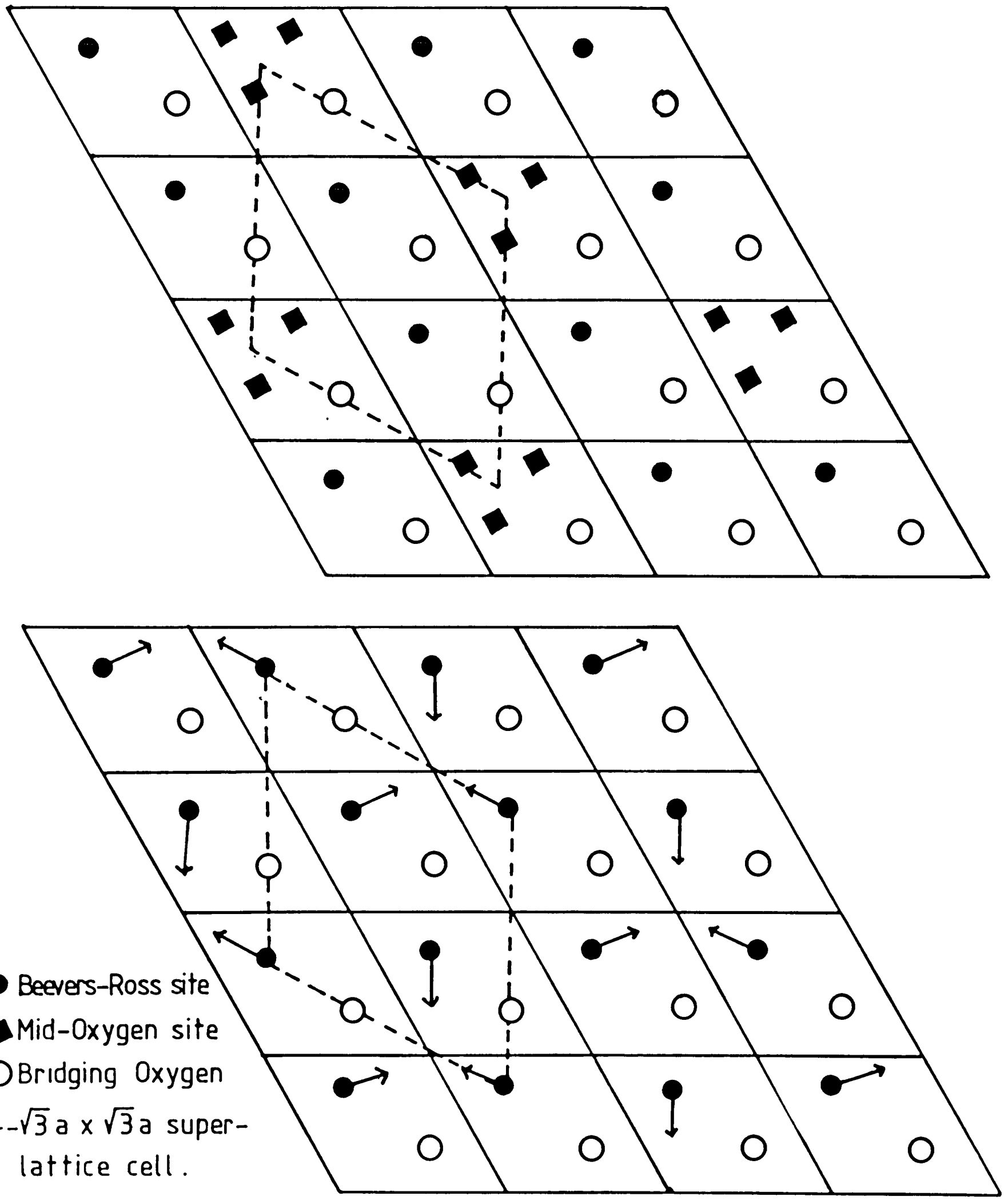

mixture of the two models.

3.3 The structure of sodium ß"-alumina.

A new compound in the ß-alumina system with formula $Na_2O.5Al_2O_3$ and c lattice parameter of value three-halves that of ß was first reported in 1962 (Thery and Briancon). It was formed by the reaction of dry $NaAlO_2$ and Al_2O_3. It was later noted that the compound was only stable in dry conditions and decomposed in the presence of solvents. A stable compound was formed with the addition of small amounts of MgO or Li_2O.

In 1968 Yamaguchi reported the binary compound $Na_2O.5Al_2O_3$ and designated it Na ß"-alumina. The structure has space group $R\bar{3}m$, amd consists, like ß, of spinel blocks separated by conduction planes.

In 1969, Bettman and Peters analysed a crystal of ternary ß"-alumina of ideal formula $Na_2O.MgO.5Al_2O_3$. The unit cell was rhombohedral, of space group $R\bar{3}m$, with lattice parameters a=5.614Å and c=33.85Å. The unit cell usually considered is a hexagonal cell composed of three of the primitive rhombohedral cells.

The hexagonal cell of ß"-alumina consists of three spinel blocks of thickness 11.3Å separated by two conduction planes (see fig.3.1). The aluminium and oxygen arrangement in a spinel block is identical to that of ß-alumina, but the spinel blocks are rotated by 120° with respect to each other in the plane perpendicular to the c-axis. Hence the presence of three spinel blocks per unit cell as opposed to two per unit cell for ß-alumina. Figure 3.7 gives a table of the atomic positions and thermal factors for Na ß"-alumina. As

Atom type	Point group (Wyckoff notation)	Occupancy per site	Coordinates x	z	Temperature factors 11	22	33	12	23	13
O(1)	18(h)	1	0.1562	0.0339	92	81	1.8	81	0.2	0.1
O(2)	18(h)	1	0.1657	0.2357	36	74	2.2	74	0.4	0.2
O(3)	6(c)	1	0	0.0961	70	70	1.5	70	0	0
O(4)	6(c)	1	0	0.2955	38	38	2.5	38	0	0
O(5)	3(b)	1	0	0.5000	309	309	3.3	309	0	0
Al(1)	18(h)	1	0.3362	0.0708	92	107	1.3	92	-0.3	-0.6
Al(2)	6(c)	1	0	0.3501	100	100	1.2	100	0	0
Al(3)	6(c)	1	0	0.4498	73	73	1.3	73	0	0
Al(4)	3(a)	1	0	0	101	101	0.9	101	0	0
Na(1)	6(c)	1	0	0.1719	2222	2222	7.5	2222	0	0

Temperature factor of the form: $\exp\{-[h^2 + k^2 + l^2 + hk + kl + hl] \times 10^{-4}\}$

Lattice parameters in Angstroms: a = 5.614 c = 33.85

Fig. 3.7 Atomic positions and thermal parameters for sodium β"-alumina. (Bettman & Peters, 1969)

for ß-alumina, the thermal vibration factors for the Na ions are large, due to their weak bonding.

The rotation of the spinel blocks by 120° relative to one another makes the BR and aBR sites equivalent. This results in a hexagonal arrangement of mobile ion sites - the 6c sites. Jorgensen (Jorgensen et al., 1981) and Reidinger (Reidinger et al., 1979) and others have also reported the presence of sodium ions in 18-fold mO sites (18h sites) - see fig.3.8 for sites. The cation sublattice is disordered, as each sodium ion can occupy one of the three equivalent 18h sites centred on a 6c site. Reidinger gives an occupancy of 0.88 to each 6c site (the BR and aBR sites) with an overall sodium ion deficiency in the structure of 12%. It is now thought that the 6c and 18h sites are occupied in a ratio of approximately 2:3.

The sodium ions are displaced slightly from the centre of the conduction planes due to the arrangement of the spinel blocks. Equivalent oxygens on either side of the conduction plane do not lie opposite one another, but are staggered, giving rise to an arrangement as seen in figure 3.8.

The ß" structure contains excess sodium relative to the ß structure and so some sort of charge compensation is achieved by the substitution of Mg^{2+} or Li^{+} for some of the Al^{3+} in the spinel blocks. Harbach (1983) has used x-ray diffraction to show that charge compensation can also take place by the addition of interstitial oxygens in the conduction plane. Different concentrations of sodium ion vacancies can be accommodated in the conduction plane by changing the number of Mg or Li ion substitutions in the

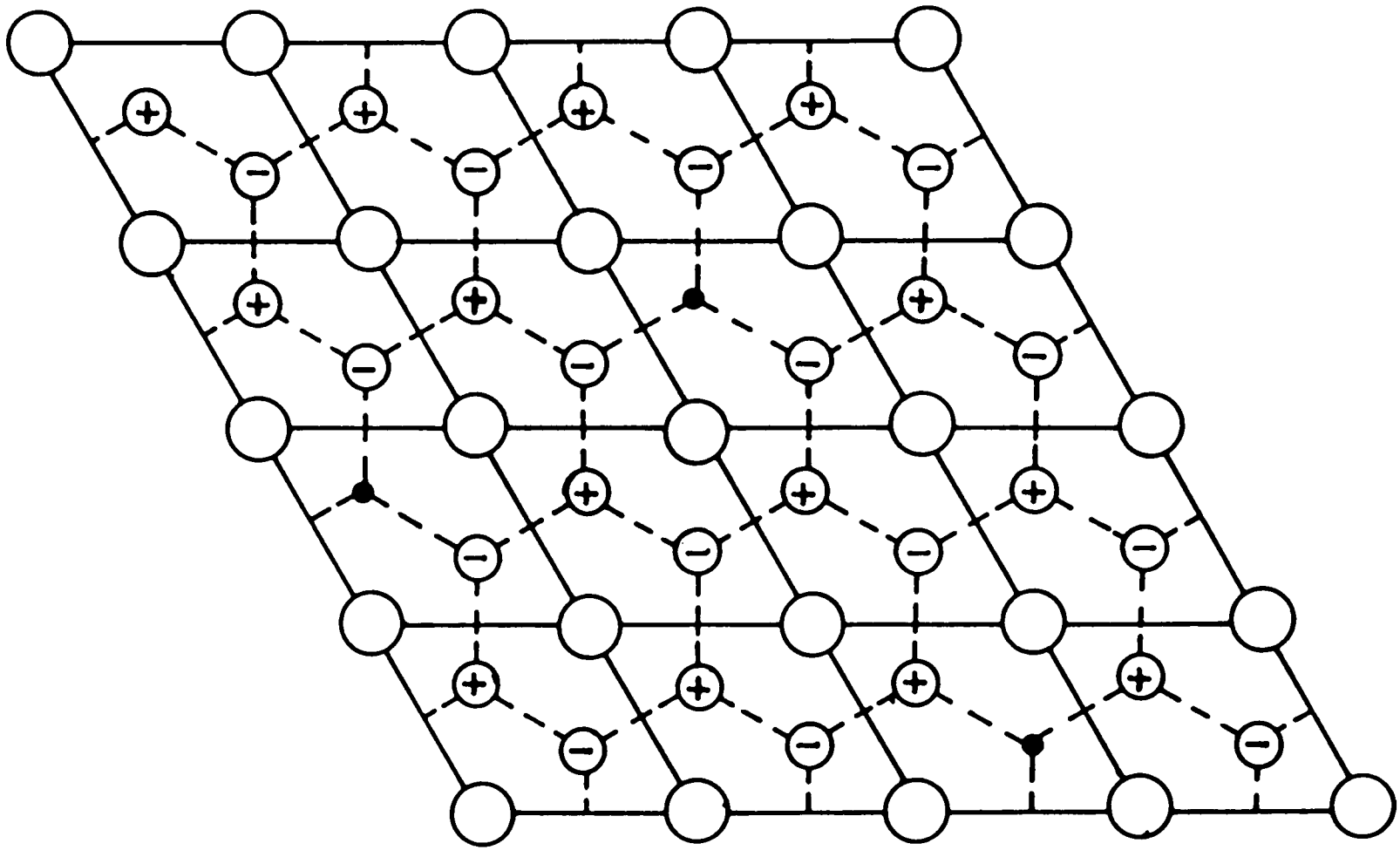

○ Bridging oxygen • Sodium vacancy

⊕ Sodium ion above centre of conduction plane

⊖ Sodium ion below centre of conduction plane

– – – Sodium ion diffusion network

Fig. 3·8 Atomic arrangement in the conduction plane in sodium β″-alumina.

spinel blocks. A minimum Mg ion content exists, below which ß-alumina rather than ß" will form (see section 3.2). Harbach (1983) also reported that the c lattice parameter decreases with increasing sodium concentration, due to an increasing polarization of the negative O(5) ions towards the positive sodium ions. The limiting factor on the possible reduction in conduction plane thickness is the minimum diameter of the bridging oxygen ion (approx. 2.76Å).

The charge compensating Mg^{2+} ions appear randomly to replace aluminium ions in the tetrahedral Al(2) sites in the spinel blocks (Roth et al., 1979), thus reducing the charge and increasing the interatomic distances in the AlO_4 tetrahedra - increasing the a lattice parameter. In Li stabilised Na ß"-alumina (Jorgensen et al., 1981) the Li ions occupy the same Al(2) sites as the Mg ions, and an occupancy of 0.29 was found - close to the ideal occupancy of 0.333. More recently (White et al., 1983) Ni^{2+} has been used to stabilise Na ß"-alumina. The Ni ions appear to occupy the same tetrahedral spinel block sites as the Mg^{2+} and Li^{+} ions. Binary ß"-alumina (Yamaguchi, 1968) is charge compensated by the presence of extra aluminium vacancies in the spinel block. Figure 3.9 compares the structures of binary and ternary Na ß"-alumina.

Studies of Mg^{2+} stabilised ß"-alumina (Frase et al., 1983) have shown that charge compensation is achieved by the presence of Al vacancies in the Al(2) sites. These sites are alternately fully occupied by Mg ions, and partially occupied by Al ions. This study also suggests that a small number of oxygen vacancies exist.

Collin (Collin et al., 1979) has observed

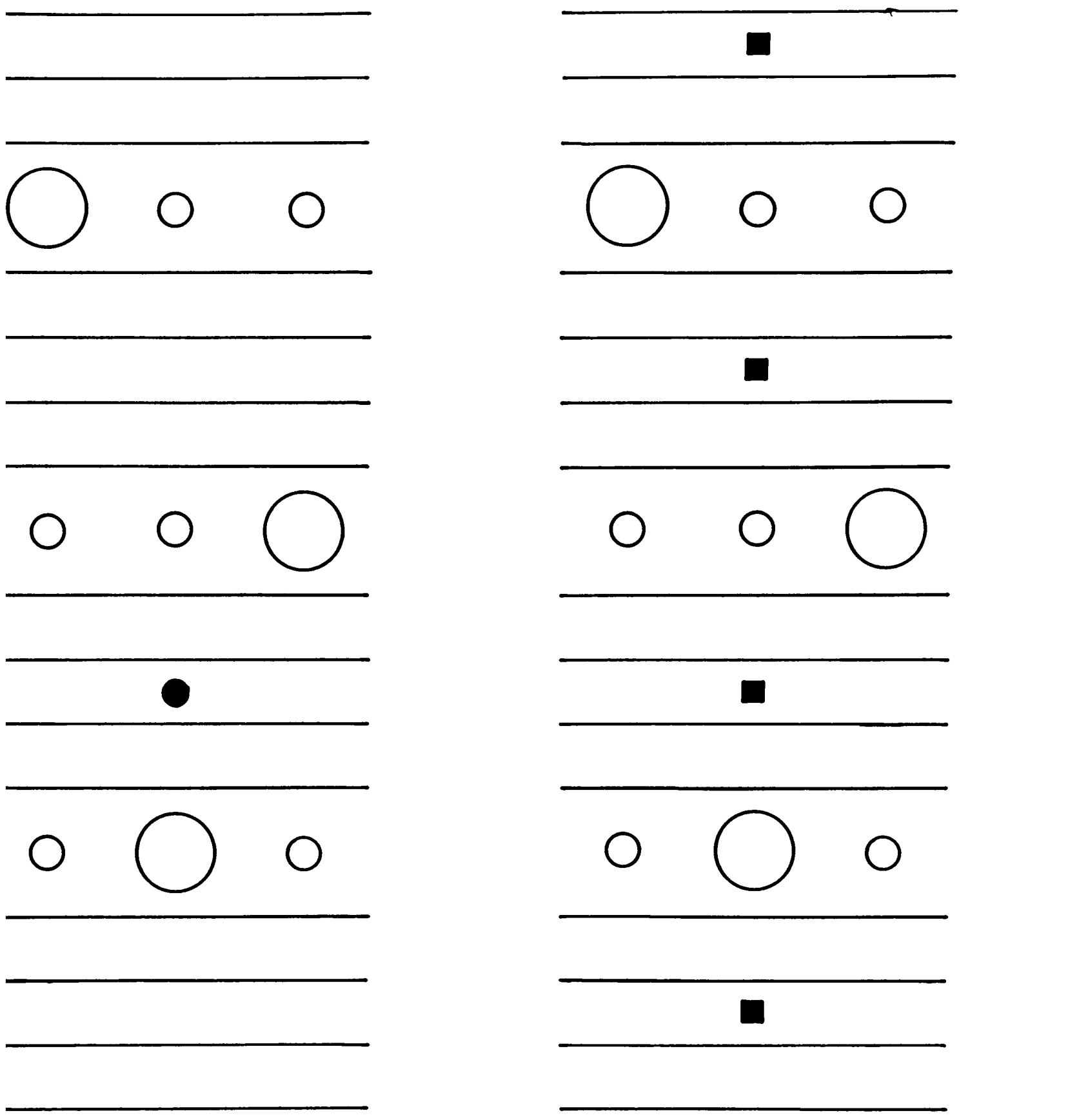

ig. 3·9 Schematic structure of a) binary, and b) ternary ß"-alumina.

2-dimensional ordering of the cation sublattice in Na ß"-alumina, with ordering corresponding to an $a\sqrt{3}$x $a\sqrt{3}$ type superlattice. The superlattice is present at room temperature and lower, but at 300°C the structure disorders. Figure 3.10 shows a microdomain in a conduction plane of Na ß"-alumina (Roth et al., 1979).

3.4 Long period ß-alumina-like structures.

Bovin (Bovin and O'Keeffe, 1980) has observed forms of ß-alumina in which the spinel blocks are stacked in a regular disordered manner.

The structure of ß- (or ß") alumina can be described in terms of the close packed oxygen layers, with the conduction planes being low density close packed oxygen layers. In ß-alumina the conduction plane is a mirror plane and so the packing along the c-axis is: C(ABCA)B(ACBA)C... with the spinel block layers shown in parentheses. In ß"-alumina the packing is: C(ABCA)B(CABC)A(BCAB)... due to the rotation of 120° about the c-axis between spinel blocks. The stacking in both cases can more simply be described just in terms of the conduction planes. For example in the case of ß"-alumina the stacking order would be CBAC...

Bovin has observed structures with stacking of the type ACBACAB, and we have observed other long period structures of this type (see later in this chapter).

Another notation used by Bovin and O'Keeffe is to denote a spinel block with ordering -ABCA- by (-) and a spinel block with ordering -ACBA- by (+). This notation will be used later in this chapter.

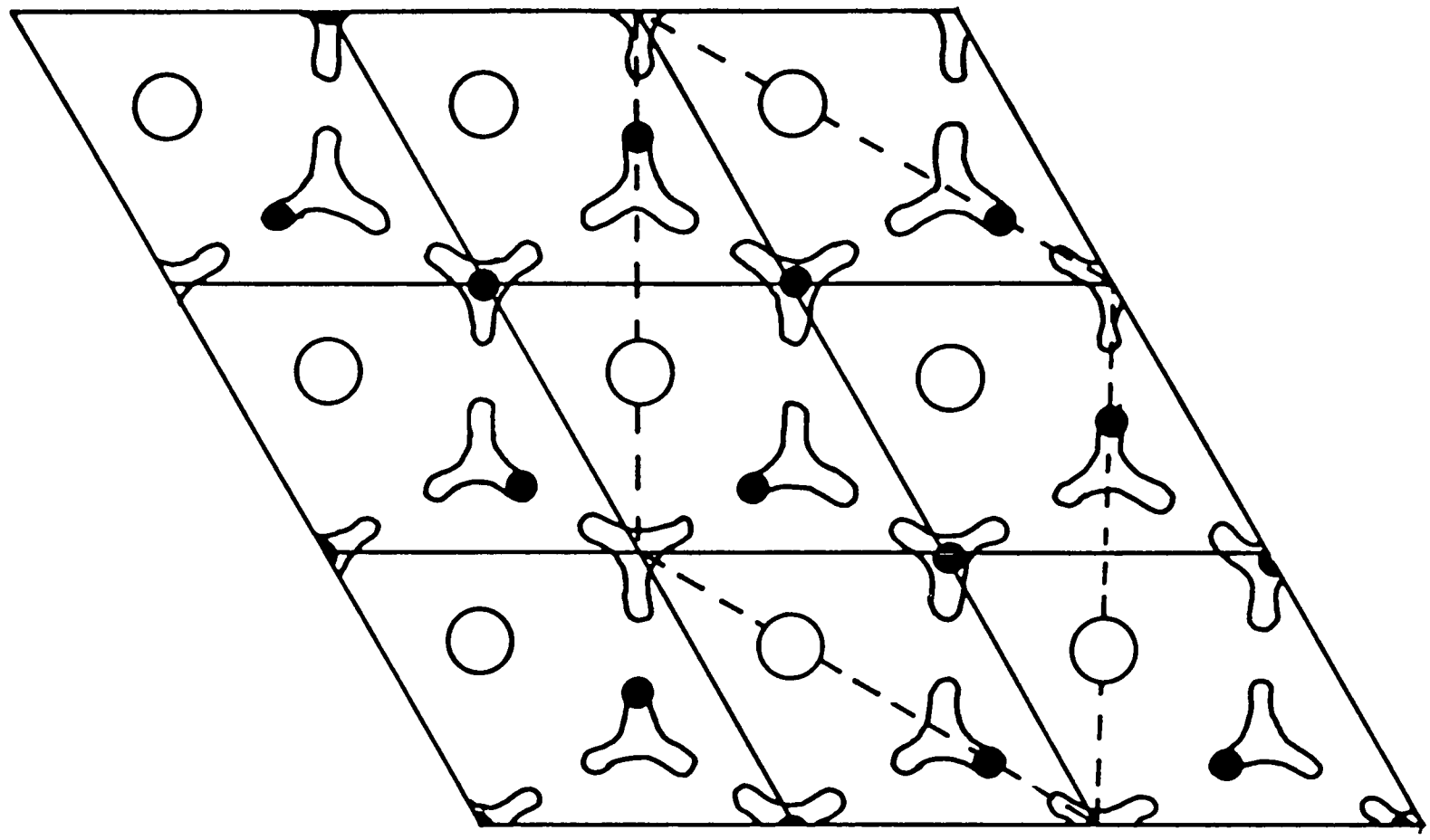

○ Bridging oxygen

● Sodium ion

– – – Microdomain boundary

Fig. 3.10 Microdomain structure in Na ß''-alumina projected on the sodium density of the average structure.

3.5 Preparation of sodium ß and ß"-alumina.

Non-stoichiometric ß-alumina can be prepared by the sintering of Al_2O_3 and Na_2O. Ternary ß"-alumina can be prepared in the same way, with the addition of a small amount of some stabilising oxide such as MgO or Li_2O.

The phase diagram for the ß-aluminas has not been studied extensively although one is shown for the ternary $LiAlO_2$-$NaAlO_2$-Al_2O_3 system at 1300°C in figure 3.11a (from Duncan and West, 1983). This system is being studied prior to analysis of the quaternary Li_2O-Na_2O-MgO-Al_2O_3 system. As can be seen from the phase diagram a substantial region exists in which ß and ß"-alumina alone are present. Duncan and West also noted that as the lithia content increased so the percentage of ß"-alumina present decreased.

At 1500°C a region exists in which pure ß"-alumina is formed (at a lithia content of 0.8-1.4 wt%) - see figure 3.11b.

3.6 High resolution electron microscopy of sodium ß and ß"-alumina.

The theory involved in HREM was described in chapter 2. The specimens of sodium ß and ß"-alumina examined were all taken from commercial electrolyte tubes provided by Chloride Silent Power Ltd. (CSPL).

The specimens were prepared for microscopy by crushing of the ceramic tube under chloroform to a powder. A 2.3mm grid (for the Jeol 200CX) or a 3mm grid (for the Cambridge HREM) coated in a holey carbon film was used to pick up a small amount of the powder. The specimens were kept in a vacuum dessicator between analyses in the

a)

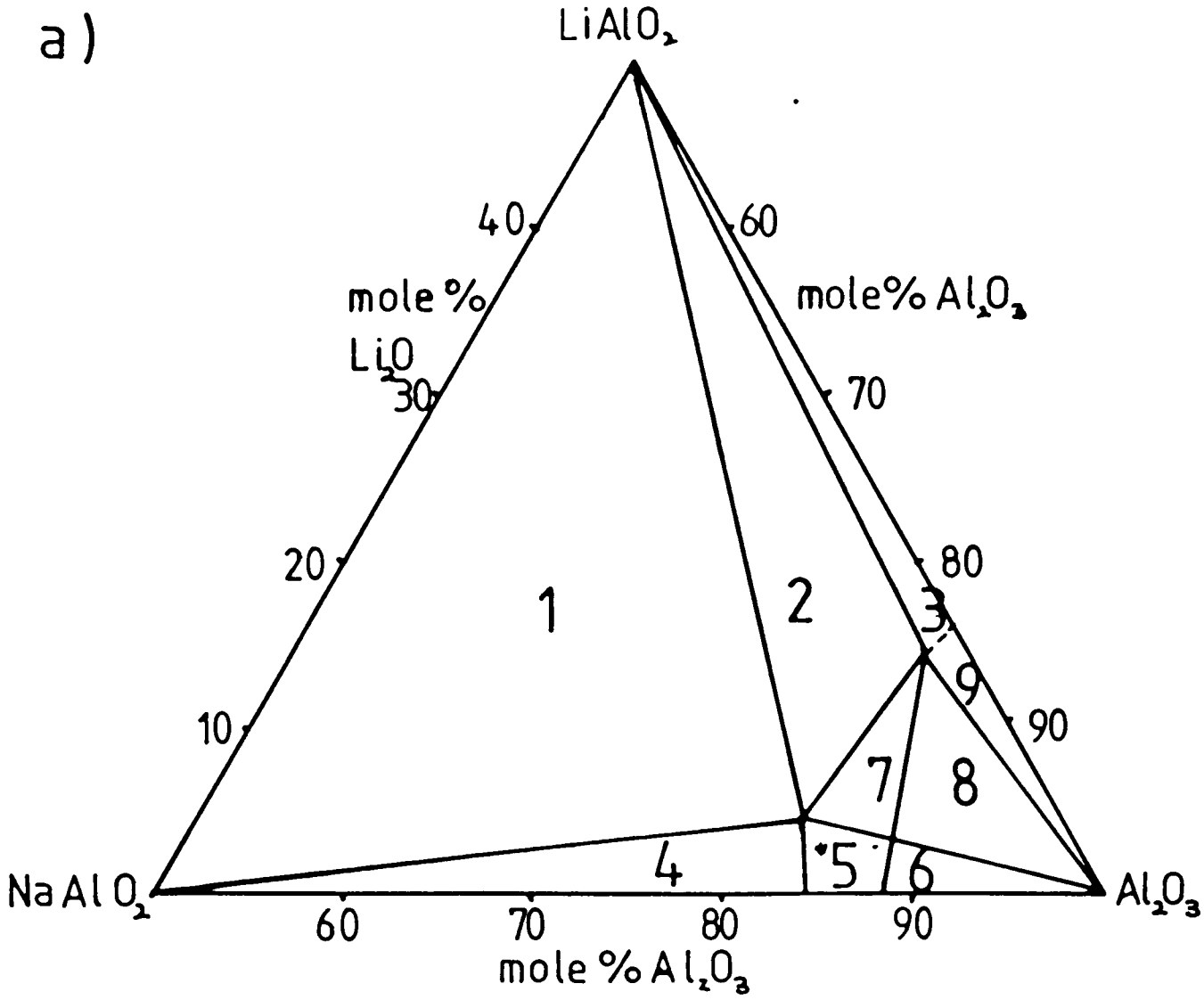

1 - $LiAlO_2$ + $NaAlO_2$ + β/β'' ss
2 - $LiAlO_2$ + $LiAl_5O_8$ ss + β/β''ss
3 - $LiAlO_2$ $LiAl_5O_8$ ss
4 - $NaAlO_2$ + β/β''ss
*5 - β/β''ss
6 - β/β''ss + Al_2O_3
7 - $LiAl_5O_8$ ss + β/β''ss
8 - Al_2O_3 + β/βss + $LiAl_5O_8$ ss
9 - $LiAl_5O_8$ ss + Al_2O_3

b)

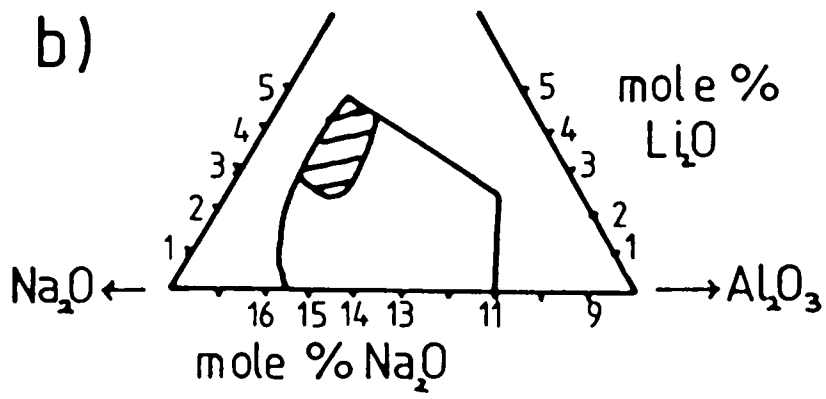

- Region of pure β''

Fig. 3·11 a) The $NaAlO_2$ - $LiAlO_2$ - Al_2O_3 phase diagram at 1300°C, and b) the β β'' region at 1500°C.

microscope.

Figure 3.12 lists the operating parameters of the Jeol 200CX and the Cambridge 600kV HREM.

The orientation most frequently used was [11$\bar{2}$0], as this shows the conduction planes end on, and the O(5) bridging oxygens aligned parallel to the beam with tunnels in between in which the sodium ions sit. Columns of sodium ions appear light in micrograph prints as their projected potential is lower than that of the surrounding columns of aluminium and oxygen ions, since these are packed more closely. In this orientation the unit cell repeat distance perpendicular is

$$a\sin 60° = 4.86\text{Å}$$

Most of the images shown in this thesis were taken by the author on the Jeol 200CX HREM at Oxford, with some images taken with the help of Dr. David Smith on the 600kV HREM at Cambridge. All images are at or close to Scherzer defocus unless otherwise stated.

i) HREM of sodium ß-alumina.

Figure 3.13b) shows an HREM image of sodium ß-alumina taken down the [11$\bar{2}$0] direction, and its associated diffraction pattern. Fig. 3.13a) shows an image of Na ß-al. down the [31$\bar{4}$0] direction The rows of bright spots correspond to the conduction planes - 11.3Å apart - with the O(5) bridging oxygens visible as dark lines between the spots. The darker bands on either side of the conduction planes are the spinel blocks.

If the incident electron beam is exactly parallel to [11$\bar{2}$0] and also exactly parallel to the optic axis of the microscope, the spinel blocks will all show similar contrast since each conduction plane is a mirror plane in ß-alumina.

	Jeol 200CX	Cambridge 600kV HREM
Operating voltage(kV)	200	500*
Electron wavelength(nm) (relativistically corrected)	2.507×10^{-3}	1.421×10^{-3}
C_s (mm)	1.2	2.7
Spread of focus (Å)	40	150
Beam divergence (semiangle, mrads)	0.2	0.2
Specimen holder	Top entry Tilt +/- 10°	Side entry Tilt +/- 30°
No. of lenses	6	6
Type of electron gun	LaB_6 filament	LaB_6 filament
Extended Scherzer defocus $(1.5C_s)^{1/2}$ (Å)	-672	-759

* Usual operating voltage.

Fig.3.12 Operating parameters for the Jeol 200CX and Cambridge 600kV HREM.

a)

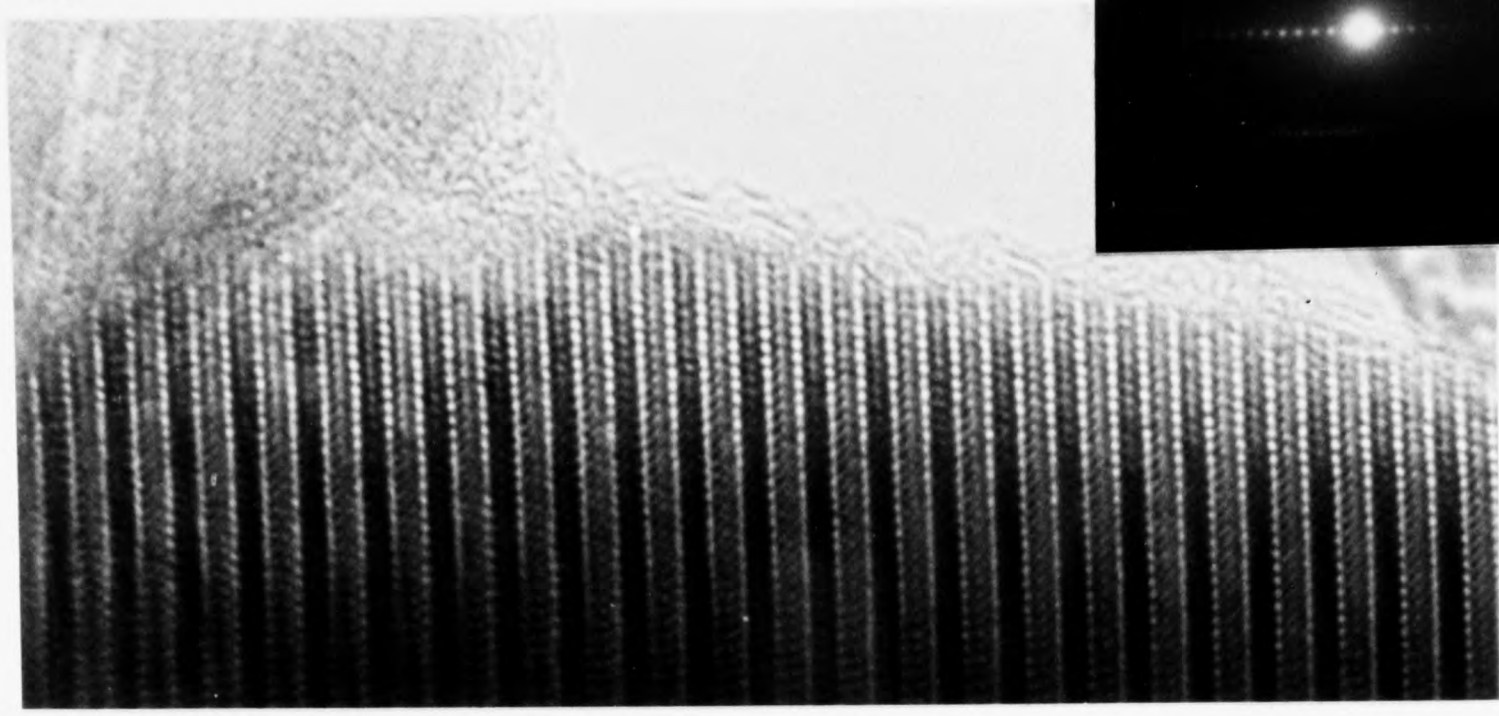

50·0 Å

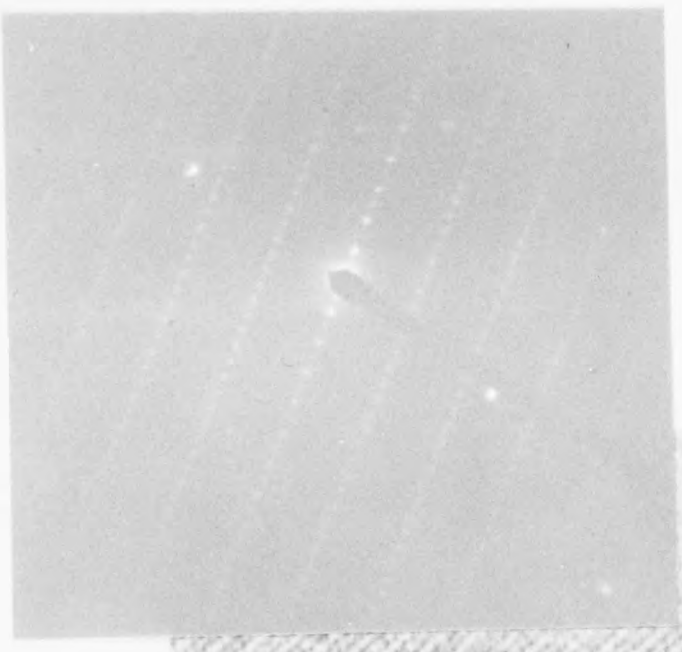

b)

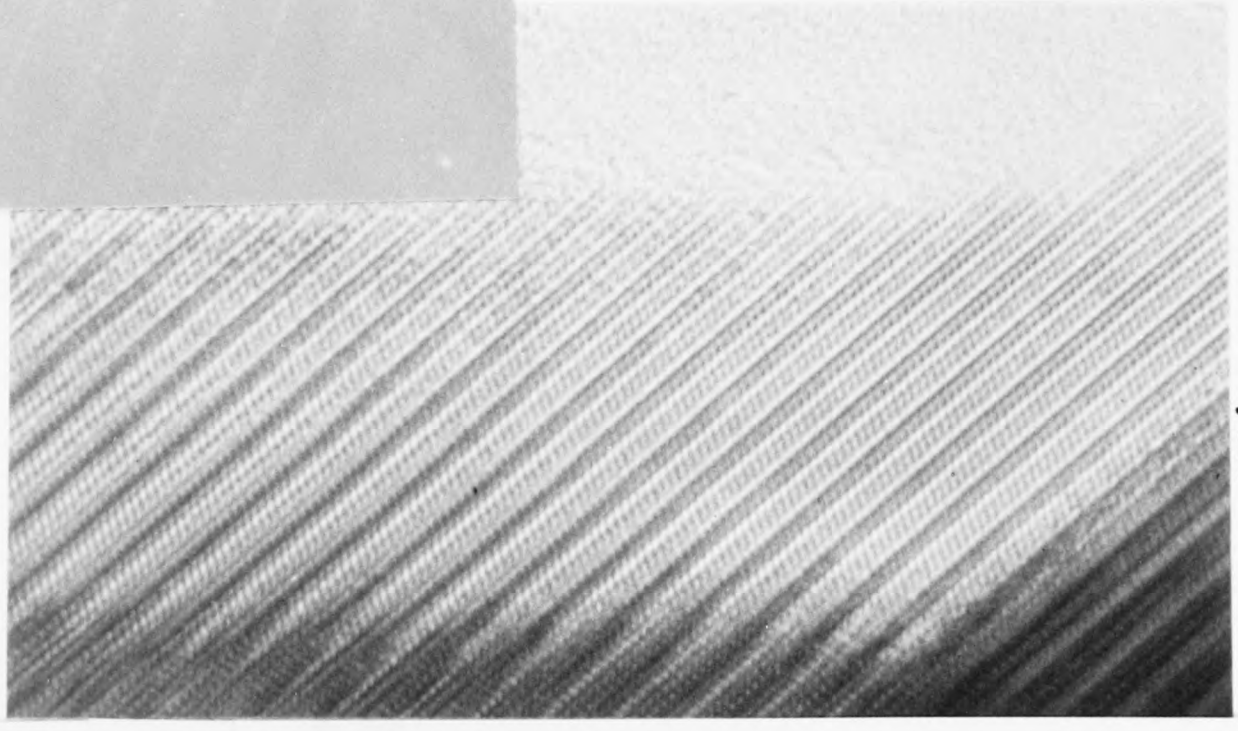

50·0Å

Fig.3·13 200kV lattice images of sodium β-alumina and corresponding diffraction patterns

a) Electron beam close to <310> & b) Beam close to <1 1 0>.

However only a very slight crystal tilt or beam misalignment is required to break the mirror plane symmetry of the (incident beam plus crystal) system. This results in a characteristic alternate light and dark contrast of neighbouring spinel blocks. This can be seen in figure 3.13. Figure 3.14 shows the relation between the conduction plane and the $[11\bar{2}0]$ direction.

Na ß-alumina is found in the Mg doped CSPL electrolyte tubes in small quantities. Although its conductivity is not as high as that of Na ß"-alumina it is more stable. It is also easier to produce mixed material than to produce pure ß"-alumina.. In most of the samples examined the stated percentage of ß" present was around 90%.

ii) HREM of Na ß"-alumina.

The specimens of Na ß"-alumina were also prepared from CSPL samples, which had been doped with MgO.

An HREM image of sodium ß"-alumina and its associated diffraction pattern are shown in figure 3.15. The image is in the $[11\bar{2}0]$ direction. As for ß-alumina, this direction was chosen as it provides the greatest amount of structural information consistent with the microscope resolution. The small white spots at the centre of the spinel blocks correspond to the Al(2) sites. The aluminium ions in these sites are tetrahedrally bonded and give rise to a lower projected potential than the surrounding octahedrally bonded oxygens. All the spinel blocks in ß"-alumina have a similar stacking sequence and therefore show the same contrast even when slightly off tilt.

From the diffraction pattern it can be seen that the

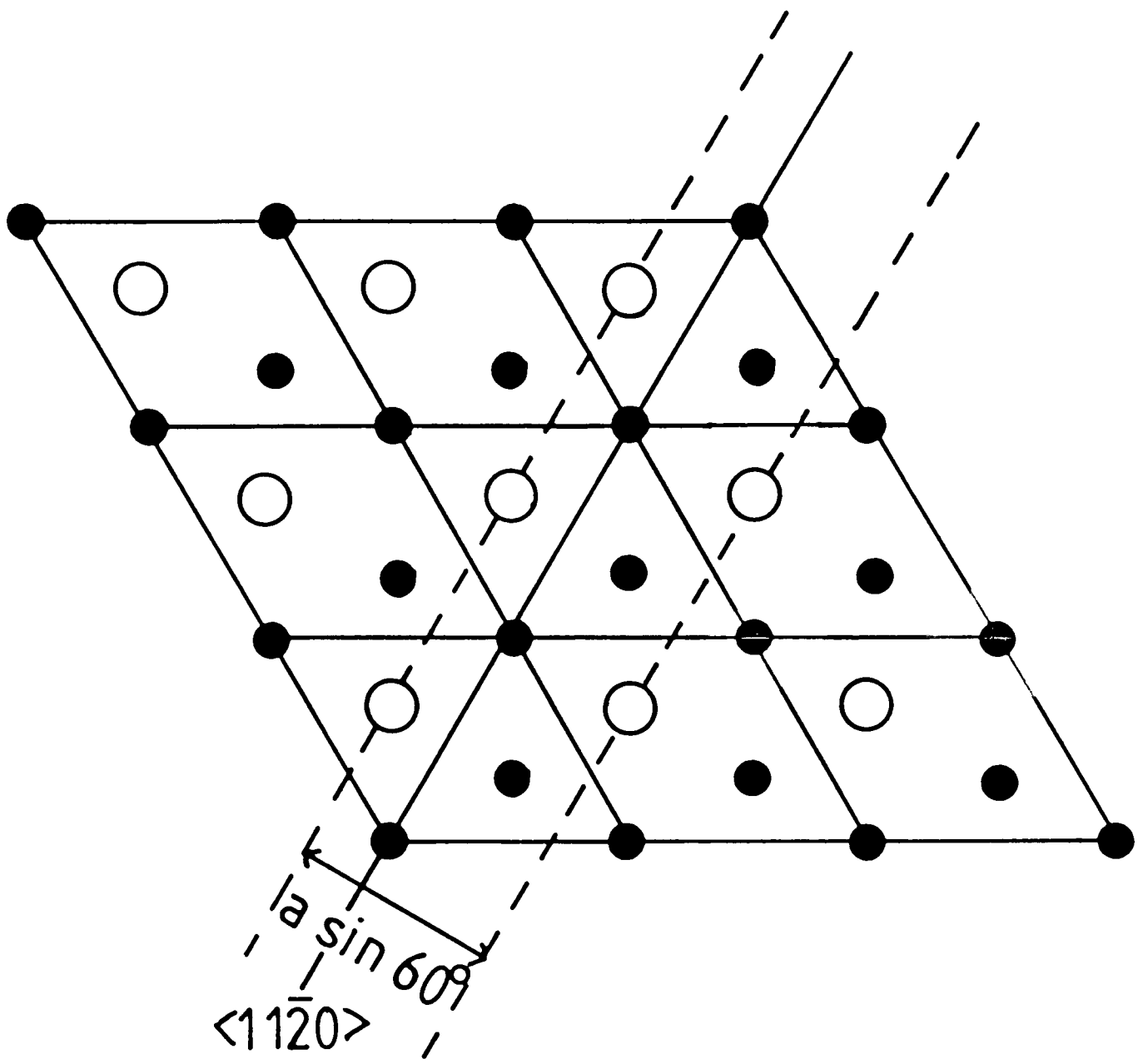

● Sodium ion

○ Bridging oxygen

Fig. 3·14 Schematic diagram showing the relationship between the $\langle 11\bar{2}0 \rangle$ direction and the conduction plane structure in sodium β″-alumina.

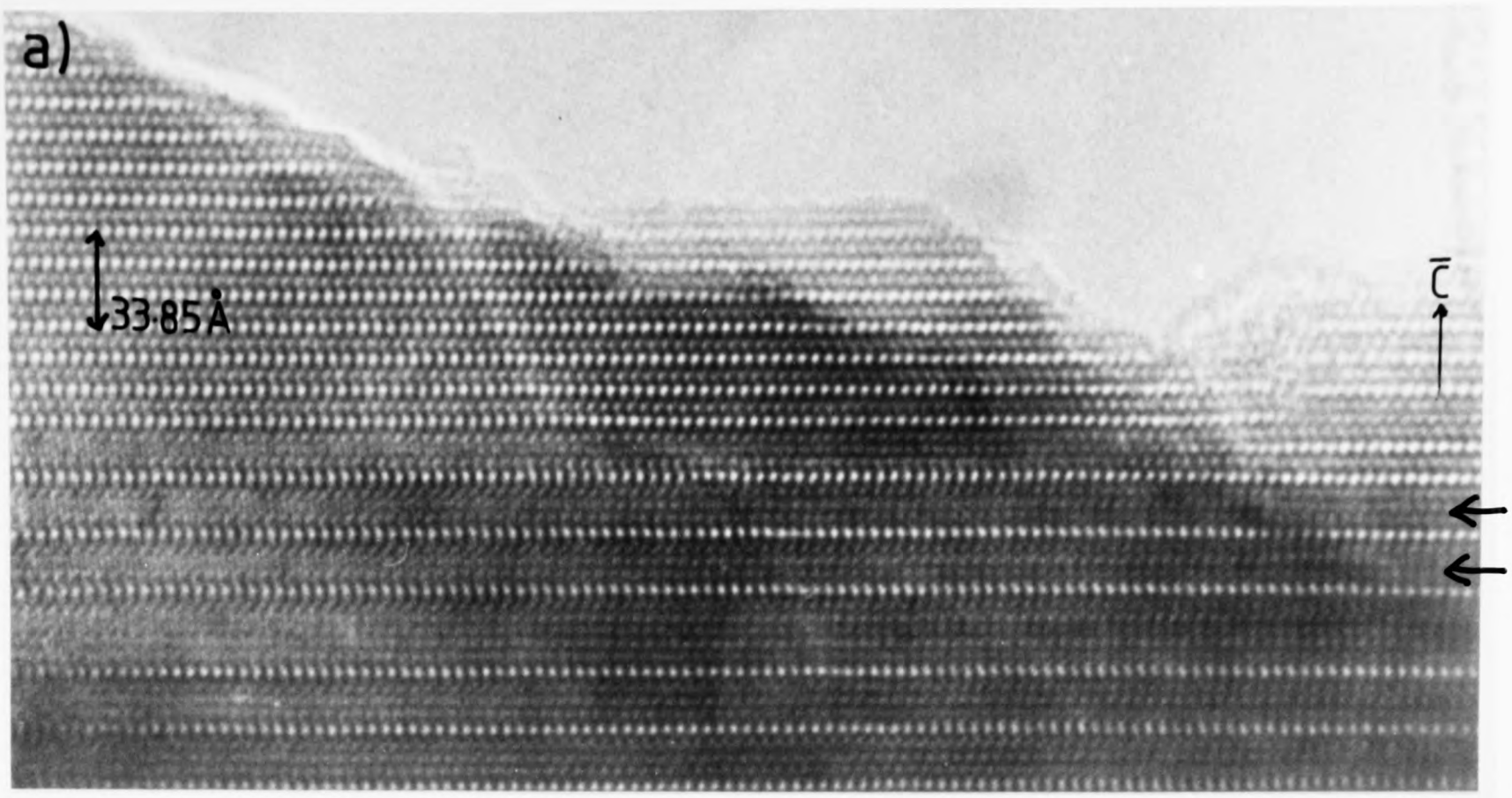

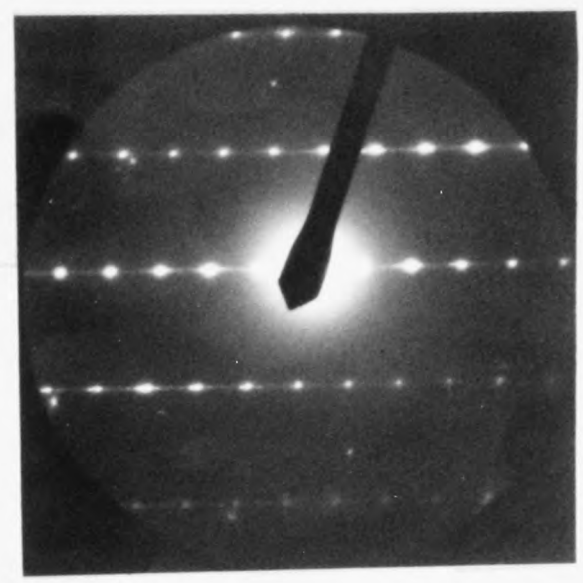

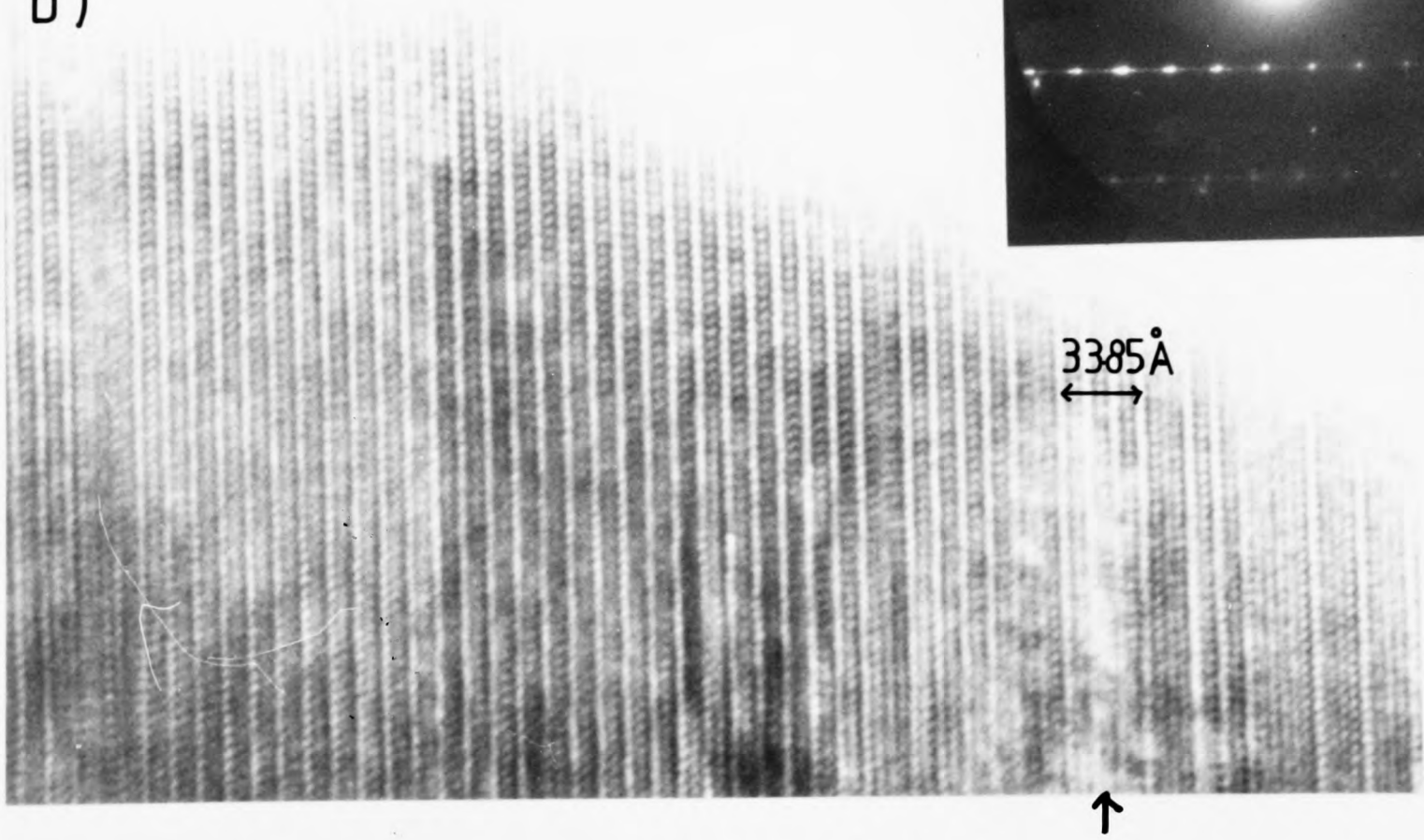

Fig. 3.15 Lattice images of sodium β"-alumina; b) with corresponding electron diffraction pattern. Electron beam in a) and b) along $\langle 11\bar{2}0 \rangle$.

spots line up on every third row (perpendicular to the c* direction), whereas in ß the spots in every row line up. This provides an obvious method for distinguishing between ß and ß"-alumina when looking at crystals from mixed Na ß/ß" material.

In the lattice image of sodium ß"-alumina (figure 3.15) broad spinel blocks can be seen (arrowed). These result from the collapse of a conduction plane. This occurs very easily in ß"-alumina on exposure to the electron beam in an HREM, but in some of the electrolyte tube specimens examined such defect blocks were present before exposure to the beam.

Conduction plane collapse results from the loss of the sodium ions and the bridging oxygens from the conduction layer. A more detailed analysis of conduction plane collapse is given in the next chapter.

iii) HREM of long period structures.

These have been observed as intergrowths in the Na ß and ß"-alumina crystals examined. They have been discussed in section 3.4 of this chapter. Figure 3.16 shows an example of such a long-period structure. Unlike ß-alumina (alternate light and dark spinel contrast when slightly misaligned) or ß" (all spinel blocks of same contrast) the structure imaged has a more complex 'unit cell' containing six spinel blocks (c=67.68Å). In the Bovin and O'Keeffe notation the repeat unit is of the type ++--+- where a (+) spinel block appears light, and a (-) block appears dark. Figure 3.16 also shows the stacking sequence of the entire unit cell which shows a conduction plane oxygen stacking sequence -CACBCB-.

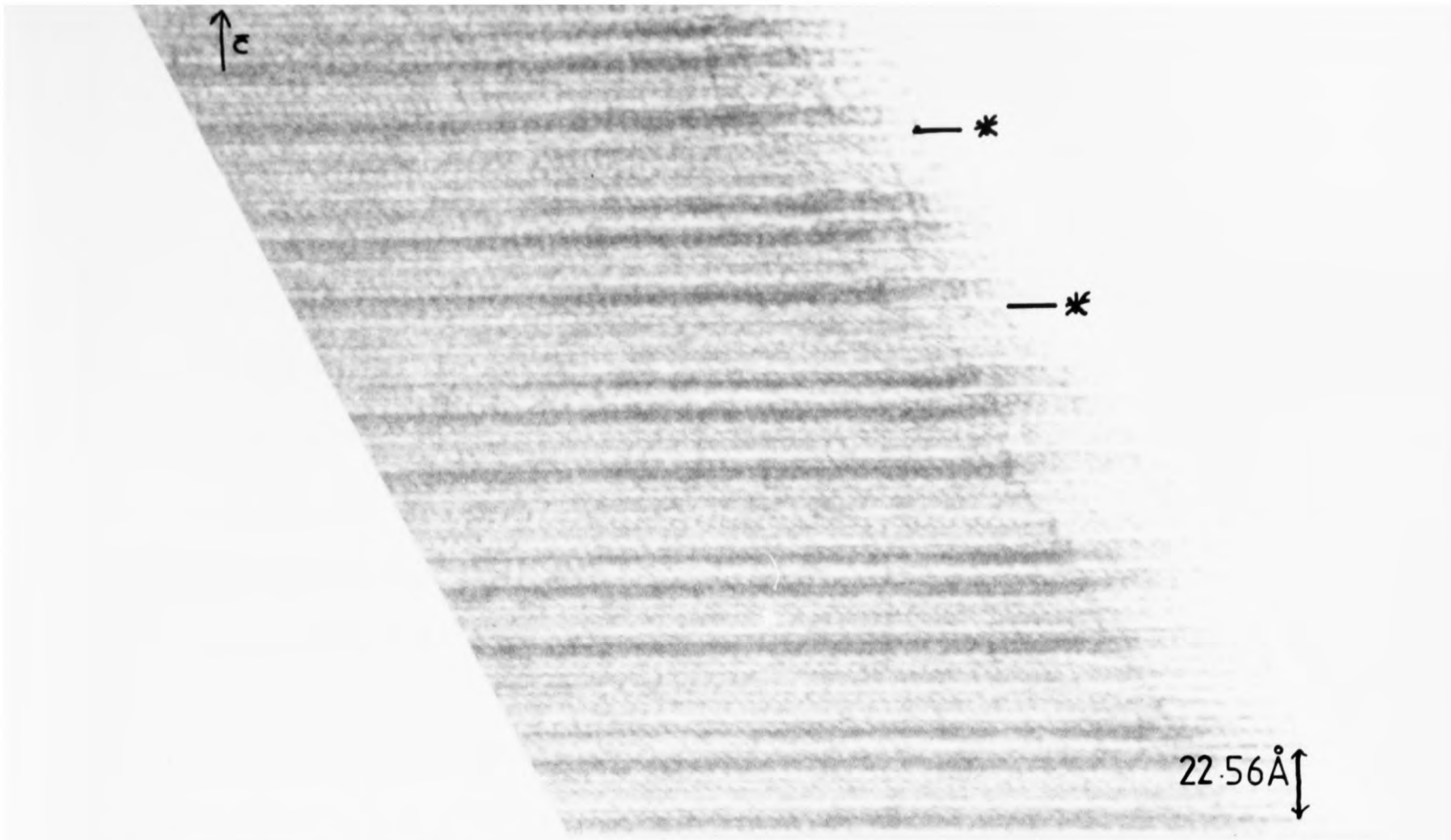

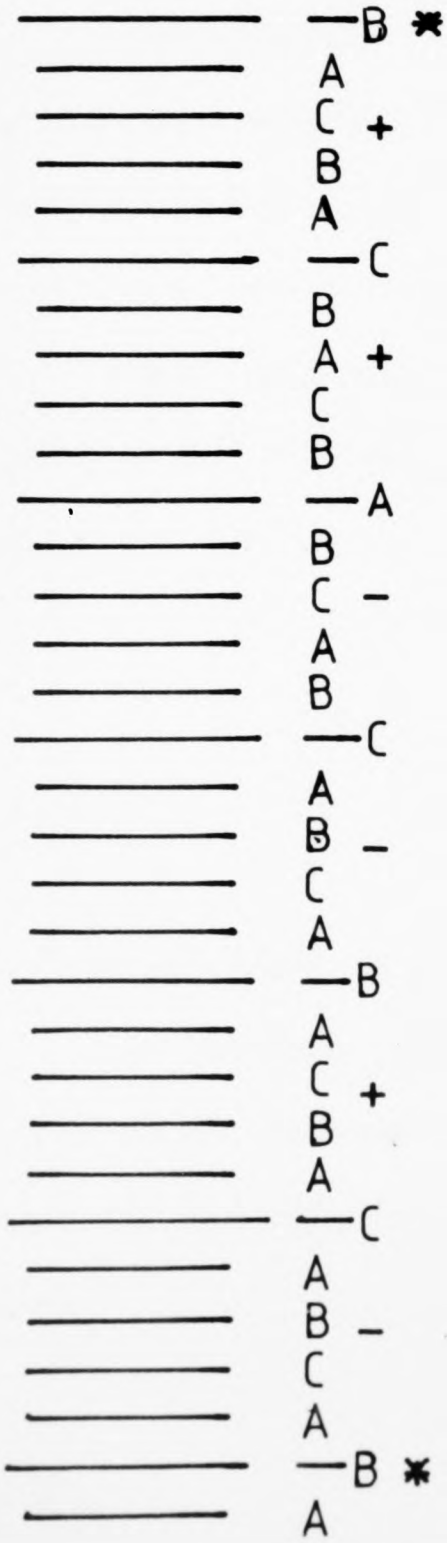

Fig. 3.16 Long period structure in Na ß-alumina. Asterisks mark one repeat of the structure. Spinel blocks denoted (+) are imaged light, and those denoted (–) appear dark. For further explanation of notation please see text.

3.7 Stacking faults and microscopic intergrowths.

Partial dislocations have been observed in ß-alumina by e.g. Stevens (1974) and De Jonghe (1975). The associated stacking faults normally lie in the conduction planes and De Jonghe observed planar faults extending over large areas due to the low stacking fault energy in the conduction plane.

Stevens observed dislocations with $b=a/3[11\bar{2}0]$ which can split into partials by one of two routes:

1 $a/3[11\bar{2}0] \rightarrow a/6[11\bar{2}0] + a/6[11\bar{2}0]$ $(b^2 = a^2/2)$

2 $a/3[11\bar{2}0] \rightarrow a/6[10\bar{1}0] + a/6[01\bar{1}0] + a/6[10\bar{1}0] + a/6[01\bar{1}0]$ $(b^2 = a^2/3)$

The second dissociation is preferred energetically as the overall energy (proportional to b^2) is lower. De Jonghe observed dislocations of $b=a/6[2\bar{1}\bar{1}0]$ and $b=a/2[10\bar{1}0]$, with the first type preferred as a lower energy is involved.

The energy of stacking faults has been measured (Stevens and Miles, 1976) from dislocation nodes using the following formula:

3 $$\gamma = \frac{0.3Gb^2}{W}$$

γ - stacking fault energy

G - shear modulus

b - Burgers vector

W - width of dislocation node

giving a value of $\gamma = 1.65 \times 10^{-3} Jm^{-2}$.

A second method involving the determination of the equilibrium separation 'd' of two partial dislocations gave a value of $\gamma = 6 \times 10^{-3} Jm^{-2}$ in reasonable agreement with the above value.

For example, the passage of an $a/6[1\bar{1}00]$ partial can cause the following stacking fault:

```
                              *                 *
ABCA/ACBA          —>     ABCA/CBAC/CABC          - stacking fault
ß-alumina  a/6[1$\bar{1}$00]      *                 *
```

It is not possible (Stevens and Miles, 1976) to transform ß to ß" or vice versa with partial dislocations alone.

De Jonghe (1977) reported both stacking faults and ß/ß" intergrowths, believed to be introduced in the sintering stage of the electrolyte tube production process. Bevan (Bevan et al., 1974) also observed intergrowths of ß" in ß in Mg doped electrolyte tubes. These may occur when excess sodium or magnesium in small regions preferentially causes ß"-alumina to grow.

Figure 3.17 shows regions of ß-alumina in which various stacking faults are present. In a) a region of ß is shown with stacking faults across two or three spinel blocks, and in b) an intergrowth of ß in a ß" crystal.

3.8. The structure of substituted ß-aluminas.

Both ß and ß"-alumina can be formed by sintering Al_2O_3 and an alkali carbonate other than sodium. Yamaguchi (1968) reported on the structures of Na ß"-alumina and K ß"-alumina and found them to be very similar, with c_{Na}= 33.62Å, and c_K=33.67Å.

A method of substituting the sodium ions in ß-alumina for other monovalent ions was described by Yao and Kummer in 1967.

A table comparing various parameters for Na, Li, K, Ag and NH_4^+ ß-aluminas is shown in fig. 3.18a.

The sodium ions can also be substituted by divalent ions such as Pb^{2+} and Ca^{2+}, and by trivalent ions such as Gd^{3+} and

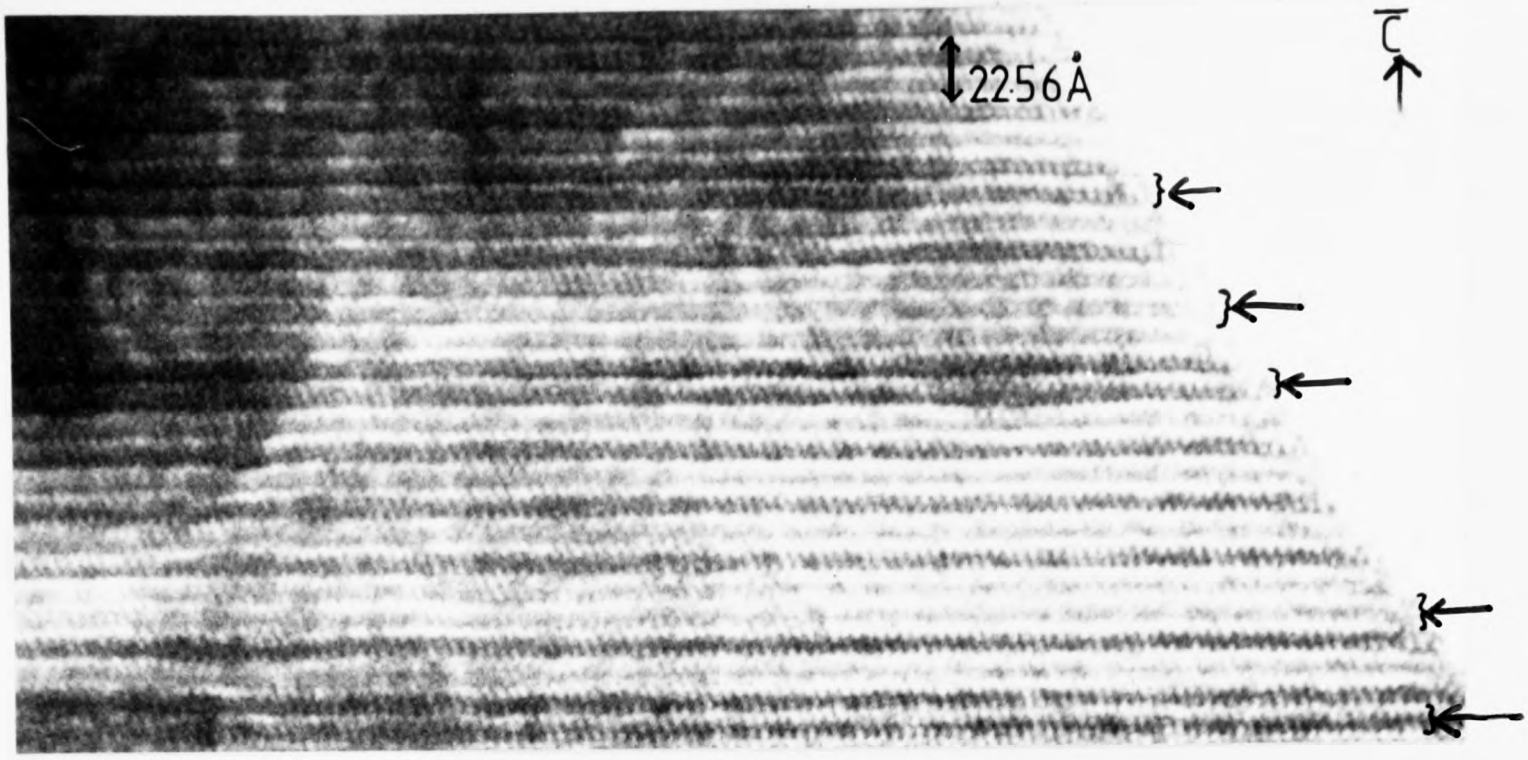

Fig. 3·17a) Spinel block stacking faults in sodium β-alumina (arrowed).

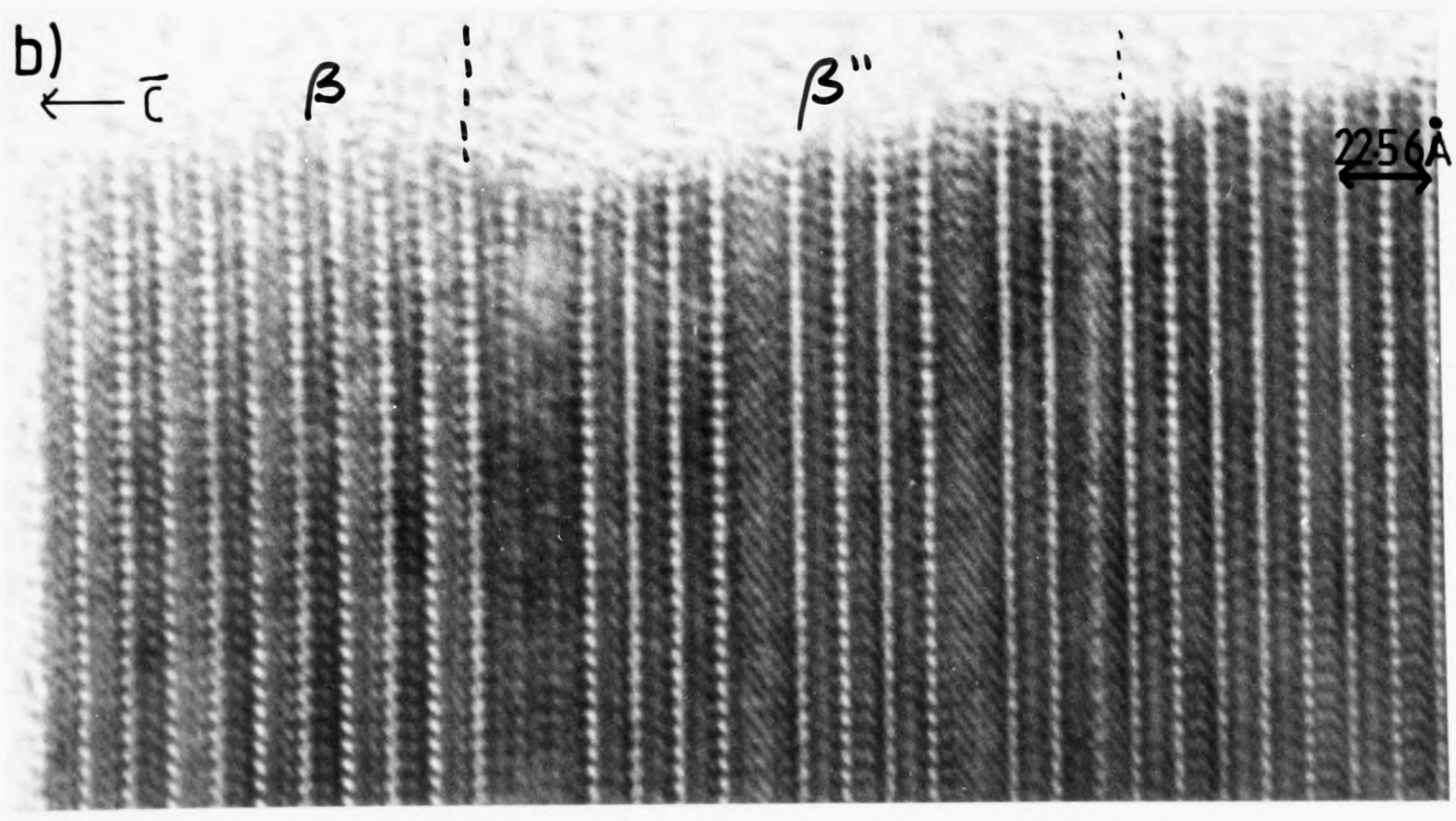

Fig. 3·17b) Intergrowths of sodium β and β''-alumina.

(a) ß-alumina

Cation	Cation radius (Å)	c-lattice parameter (Å)	ref
Li	0.60	22.642	a)
Na	0.95	22.560	f)
Ag	1.26	22.498	c)
NH_4^+	1.48	22.888	b)

(b) ß"-alumina

Li	0.60	-	c)
Na	0.95	33.850	g)
Ag	1.26	33.420	c)
NH_4^+/H_3O^+	1.48/-	34.378	b)
Eu^{2+}	1.10	33.25	e)
Gd^{3+}	0.94	33.134	d)
Eu^{3+}	0.95	33.50	e)

References a)Briant & Farrington, 1981 b)Thomas & Farrington, 1983 c)Bates et al., 1982 d)Dunn & Farrington, 1983 e)Ghosal et al., 1983 f)Whittingham & Huggins, 1971 g)Farrington & Briant, 1979.

Fig.3.18 Cation radii and c-lattice parameters for various ion exchanged a) ß-aluminas and b) ß"-aluminas.

Nd^{3+}. A straight substitution by ion exchange is not always possible for trivalent ions, and a series of ion exchanges must sometimes be made.

There is interest in substituting sodium for other ions as these materials have many useful properties. Na ß"-alumina can similarly be substituted using the same techniques as for ß-alumina, and a table comparing va rious parameters for monovalent Na, K, Ag and NH^{4+}/H_3O^+ ß"-aluminas is shown in figure 3.18b. A study has been made of monovalent silver ß and ß"-alumina, ammonium-hydronium ß"-alumina, trivalent gadolinium ß"-alumina and divalent and trivalent europium ß"-alumina. These materials all show interesting properties, amd their structures are discussed in greater detail later in this chapter.

3.9 Silver ß and ß"-aluminas

Silver ß-alumina can be made by ion exchanging in molten silver nitrate (Yao and Kummer, 1967). Roth (1972) carried out a detailed study of silver ß-alumina and found it to be very similar in structure to sodium ß-alumina but with a different ion arrangement in the conduction plane. Roth (1972) gives three possible Ag sites:- Ag(1) - a threefold site centred on the BR site found in sodium ß-alumina, Ag(2) equivalent to the aBR site for sodium ß-alumina, and Ag(3) equivalent to the mO sites in sodium ß-alumina (see fig. 3.19). All the sites are 6h sites. The O(5) ions sit very close to the 2(c) sites occupied by the equivalent ions in sodium ß-alumina. Figure 3.20 gives the atomic coordinates for non-stoichiometric Ag ß-alumina as calculated by Roth, along with occupancies for each site, plus coordinates for

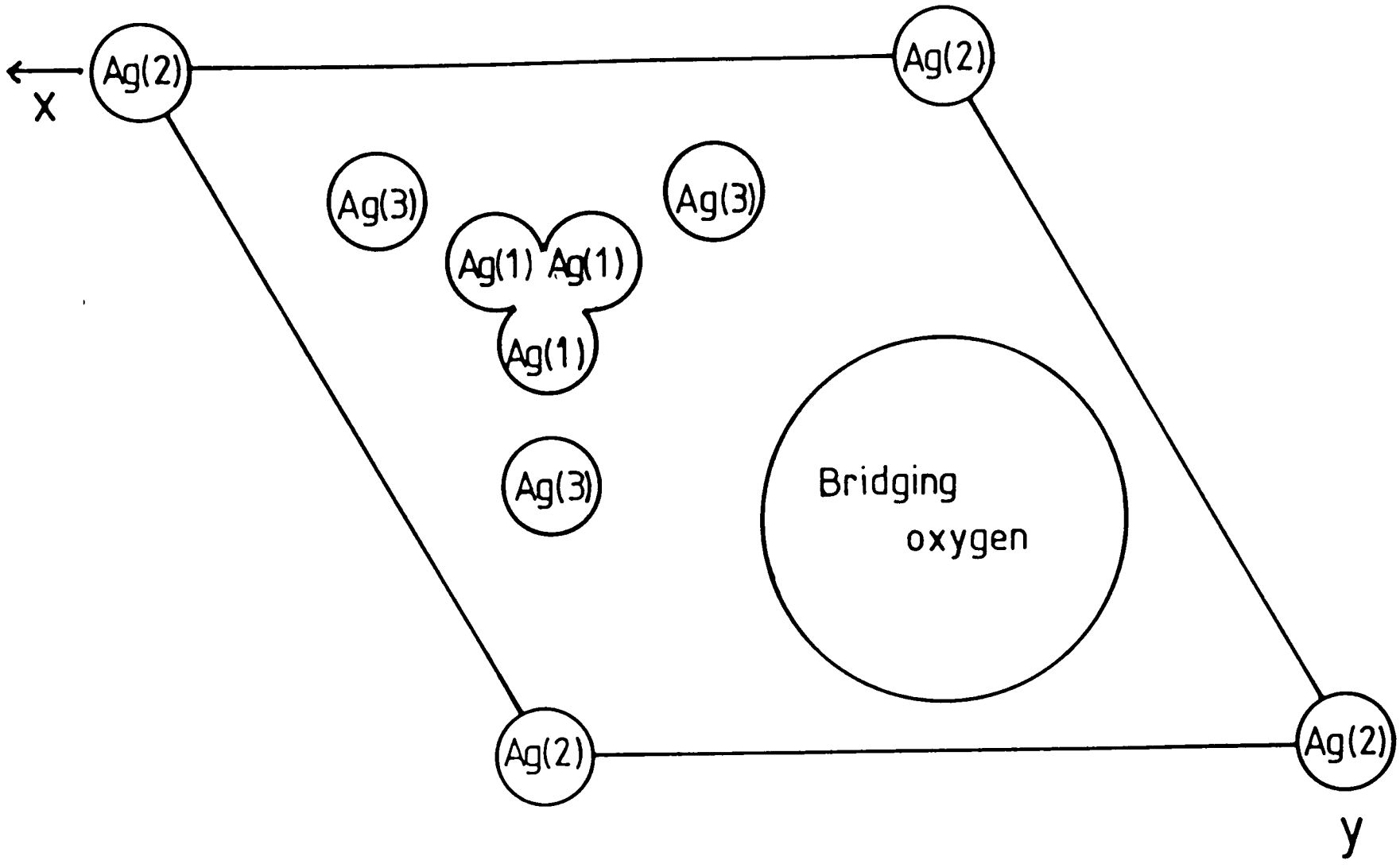

Fig. 3.19 Structure of the conduction plane in silver ß-alumina showing possible silver ion sites.

	S/NS	T(K)	x	Occupancy	ref.
Ag(1) 6(h)	S	4.2	-	-	
	S	300	0.7111	0.74	b)
	NS	300	0.7009	0.79	b)
	NS	300	0.7097	1.34	c)
Ag(2) 6(h)	S	4.2	-	-	
	S	300	0.9709	0.33	b)
	NS	300	0.9758	0.87	b)
	NS	300	0.9753	0.87	c)
Ag(3) 6(h)	S	4.2	0.7773	2.04	a)
	S	300	0.7717	0.82	b)
	NS	300	0.7727	0.84	b)
	NS	300	0.8072	0.34	c)
O(5) 6(h)	S	4.2	0.2972	2.00	a)
	S	300	0.3011	2.00	b)
	NS	300	0.2981	2.00	b)
	NS	300	0.3074	1.91	c)

S/NS = Stoichiometric/non-stoichiometric

References a)Newsam and Tofield (1981). b) Boilot J.P., Colomban Ph., Collin G. and Comes R., J. Phys. Chem.Sol. 41, 1980, p. 47. c) Roth (1972).

Fig. 3.20 Conduction plane sites in silver ß-alumina.

stoichiometric Ag ß-alumina (Newsam and Tofield, 1981). For stoichiometric ß-alumina at 4.2K, only one silver site exists - a threefold site centred on the BR site, with the circle joining the centres of the cation sites midway between the mO and BR sites.

Charge compensation for excess silver in non-stoichiometric Ag ß-alumina involves the presence of aluminium vacancies in the spinel block, according to Whittingham and Huggins (1971). However Roth (1972) found no aluminium vacancies, but found oxygen interstitials in the conduction planes.

Microdomains due to cation ordering have been observed at low temperature in Ag ß-alumina (Boilot et al., 1976). Partial ordering into superstructure domains is high at low temperature and decreases as the temperature increases to a disordered average structure at room temperature amd above. The supercell has lattice parameters $\sqrt{3}a \times \sqrt{3}a$. Newsam and Tofield (1981) have observed a similar dimensioned supercell in stoichiometric silver ß-alumina, again with the O(5) ions occupying one of three possible sites slightly displaced from that in sodium ß-alumina.

Figure 3.21 shows an HREM image of Ag ß-alumina. The specimen preparation technique was the same as that used for sodium ß-alumina. The specimen was obtained from the Clarendon Laboratory, Oxford.

Silver ß"-alumina can be prepared by the same technique used for silver ß-alumina - ion exchange in molten silver nitrate. As for silver ß-alumina, the structure of the ß" material is very similar to that of the sodium material. The spinel block arrangements are the same, with

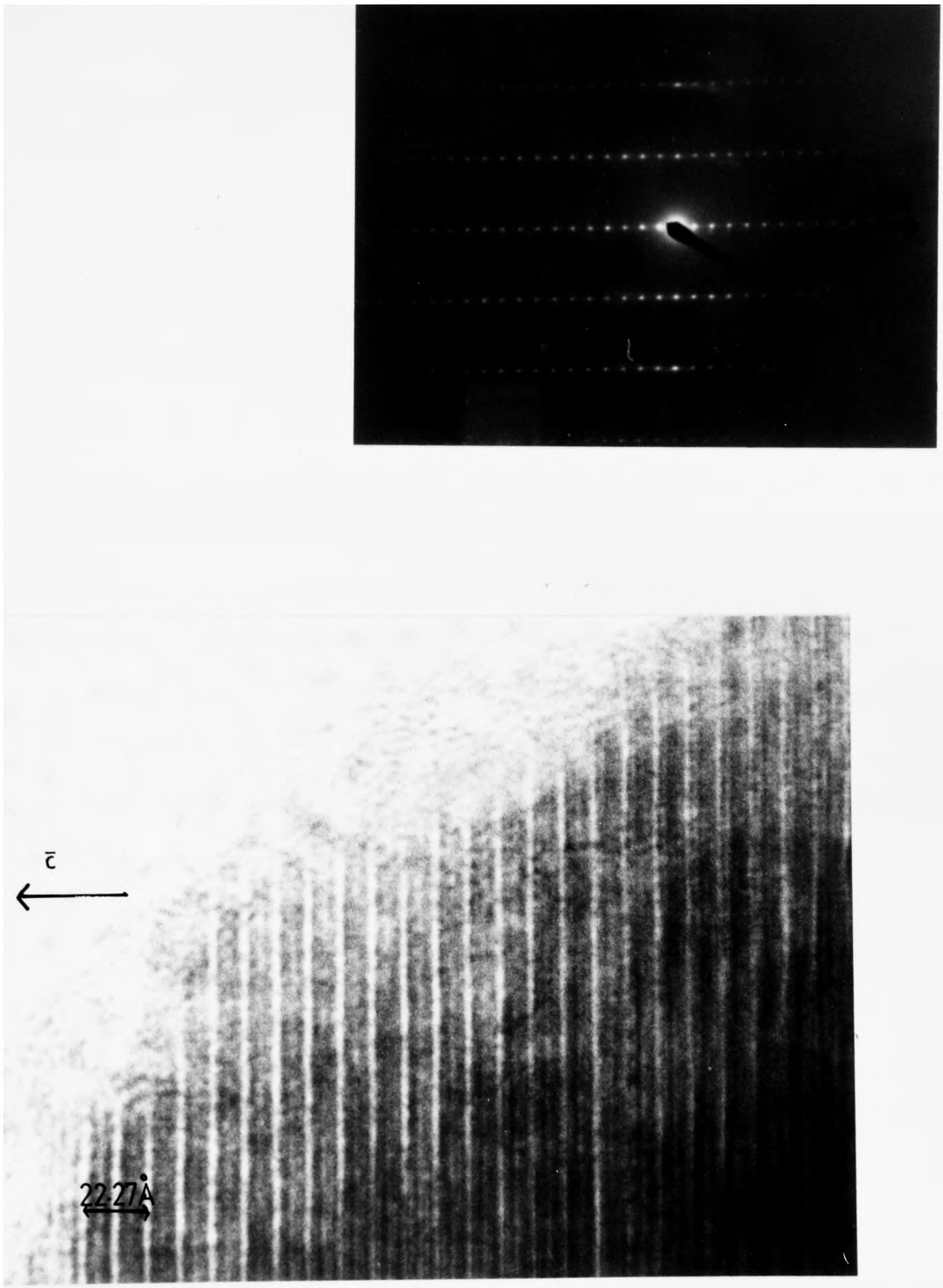

Fig. 3.21 Lattice image of silver ß-alumina with associated electron diffraction pattern. Electron beam along <210>.

possible differences in the silver cation positions.

Defects due to beam damage in these ß-aluminas will be discussed in the next chapter.

3.10 Ammonium/hydronium ß"-alumina.

Ammonium/hydronium ß"-alumina is of interest as it has a very high protonic conductivity. Solid proton conductors are rare as protons easily become trapped in crystalline solids. A Grotthus-like network (one in which the proton donor/acceptor groups form a continuous hydrogen-bonded network in the plane of proton motion) is required so that proton hopping can occur, giving rise to a high proton conductivity. The protonic ß-aluminas are the only class of proton conductors which are stable up to 500K - which makes them useful as electrolytes in fuel cells. The material examined had been prepared by ion exchange of sodium ß"-alumina in ammonium nitrate (Thomas and Farrington, 1983) and has composition

$$(NH_4)_{1.67-y}(H_3O)_yMg_{0.67}Al_{10.33}O_{17}$$

with the Mg ions substituted at ≈37% of the Al(2) sites. (It is not fully understood why ion exchange in ammonium nitrate should give a mixed ß"-alumina.) As for sodium ß"-alumina the mobile ions in the conduction layer do not lie in a plane perpendicular to the c-axis, but are displaced up and down away from the centre of the conduction plane by ≈0.1Å.

The ammonium ions are present on the 6(c) sites (the equivalent BR and aBR sites) with an occupancy of 78%. An ammonium ion at a 6(c) site with an N-H(1) bond upwards along the c-axis and three N-H(2) bonds in the plane of a and b

will be surrounded by three ammonium ions with N-H(1) bonds downwards along the c-axis. The 22% vacant sites are filled by H_3O^+/H_2O ions (see figure 3.22) with O-H bonds directed towards the O(5) bridging oxygens.

On heating the ammonium/hydronium ß"-alumina was found to decompose with the evolution of ammonia (Thomas et al., 1983). On heating to 450°C and cooling again, the ammonium content was decreased to 42%, with the loss of ammonia formed from the nitrogen ion and the three H(2) protons, leaving the H(1) proton forming a hydroxyl ion with the O(2) spinel block oxygen (see figure 3.2 for spinel block notation). When the ammonium content decreased, a third oxygen site (the mO 9(d) site) became discernible, and on cooling again this became the only site occupied by the oxygen in the H_3O^+/H_2O ion.

Neutron diffraction work on single crystal specimens (Thomas et al., 1983) revealed the presence of 001 peaks corresponding to c=20.6Å in the heat-treated sample (those with a lower ammonium content). On examining these specimens using the Jeol 200CX HREM it was found that alternate conduction planes had collapsed during the heat treatment, leaving a dominant 20.6Å spacing - confirming the neutron diffraction studies. Figure 3.23 shows a lattice image and diffraction pattern from such a sample. As can be seen, the normal conduction plane spacing of 11.43Å has almost completely disappeared, although the neutron diffraction spectrum still showed this spacing as expected for the ß" structure. The material examined was taken from the outside of the neutron diffraction specimen, which suggests that the heat treatment causes conduction plane collapse but that this damage has not

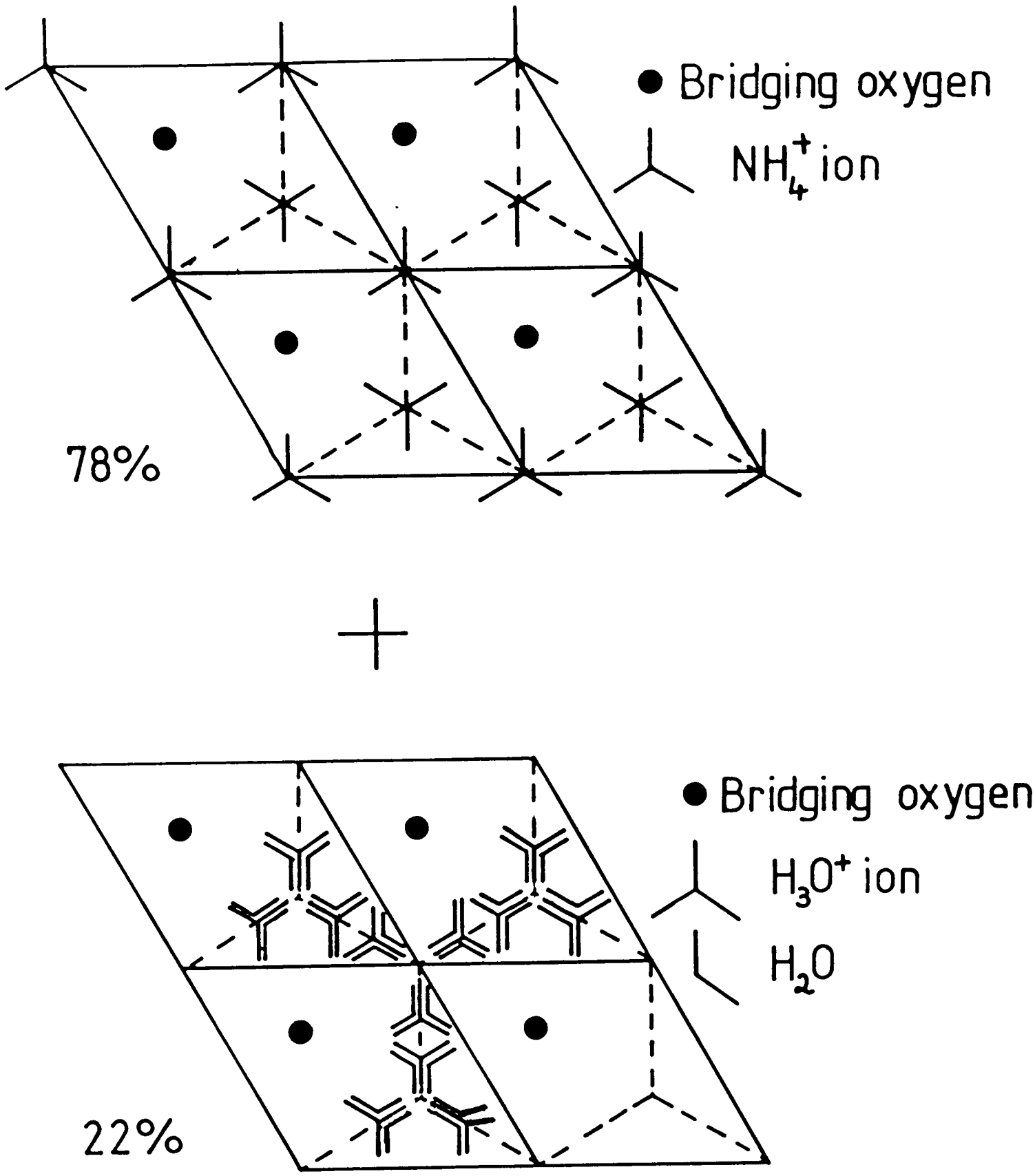

Fig. 3.22 Schematic diagram showing the cation arrangement in the conduction plane in ammonium/hydronium β″-alumina involving the superposition of a 78% NH_4^+ network and a 22% H_3O^+/H_2O network.

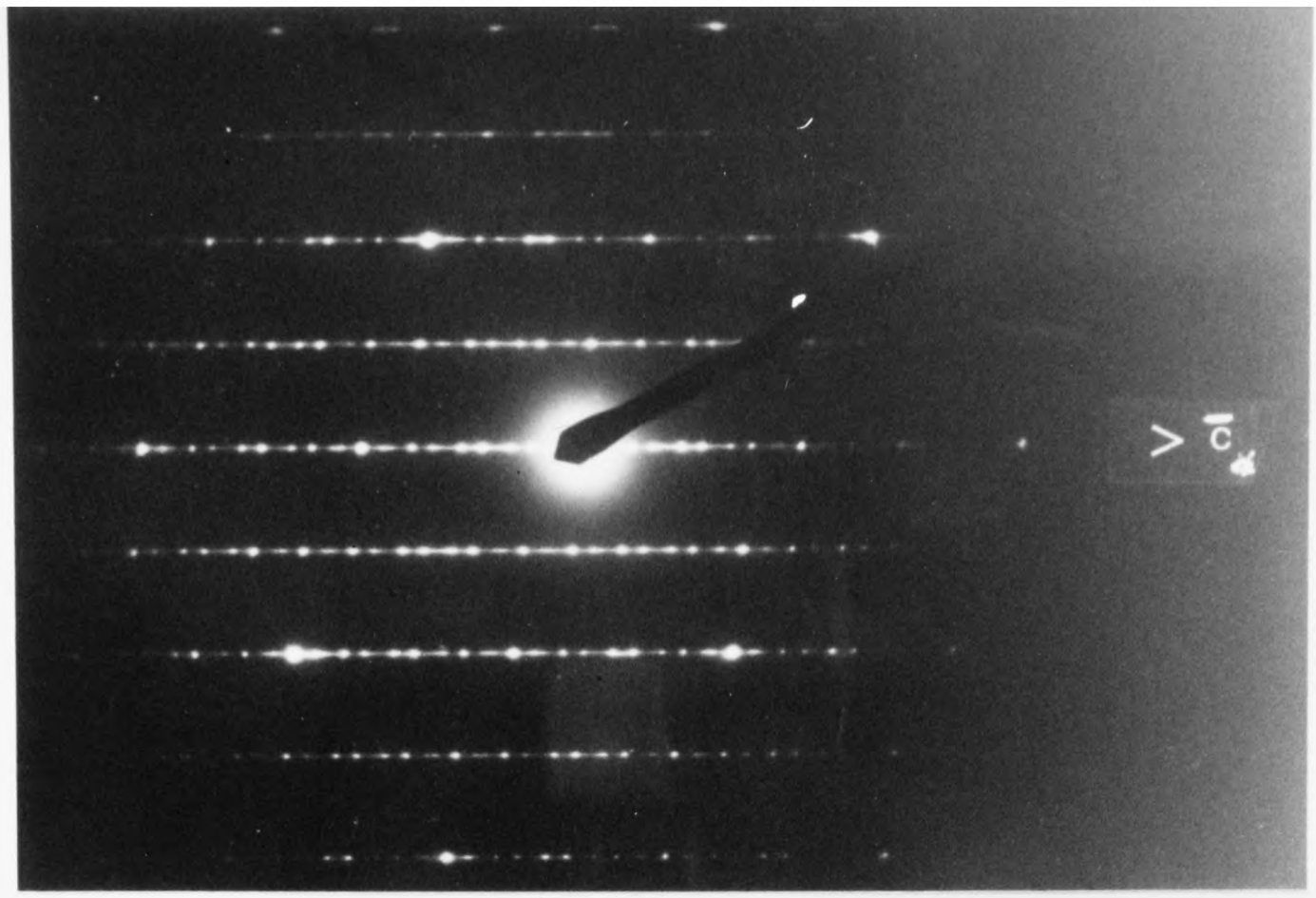

Fig. 3·23 Ammonium/hydronium β''-alumina.

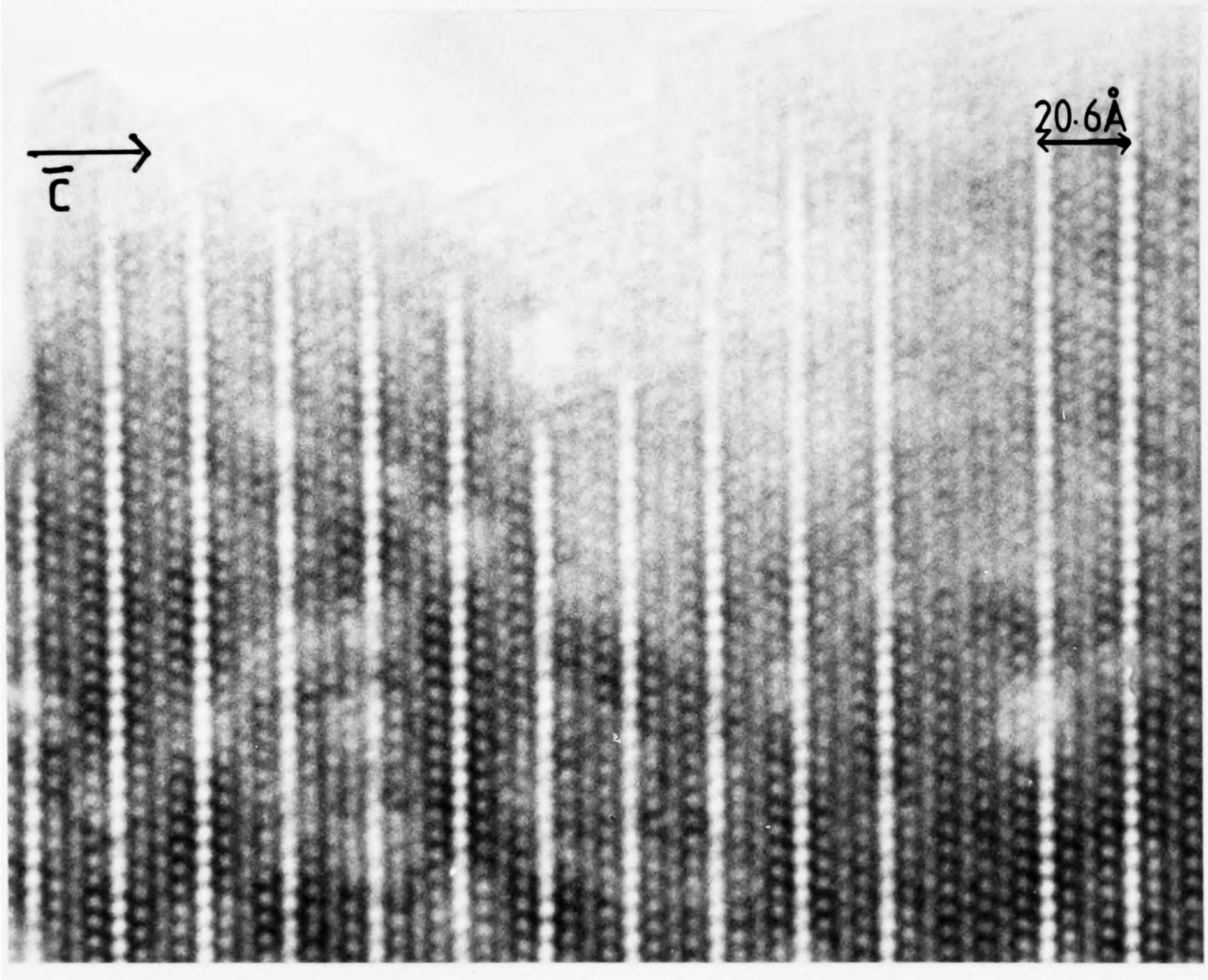

Fig. 3·23 Lattice image and corresponding electron diffraction pattern (electron beam along ⟨11$\bar{2}$0⟩). The dominant conduction plane separation is 20·6Å, with none of the 11·43Å spacings visible. The diffraction pattern spot separation was used to confirm this result.

reached the centre of the specimen. As can be seen the specimen has remained crystalline and does not appear to be distorted.

Non heat—treated specimens have also been examined and no evidence of the 20.6Å spacing is seen. This suggests that the loss of ammonia leads to conduction plane collapse. The next chapter deals in more detail with the mechanism of conduction plane collapse and beam damage effects in this material.

3.11 Gadolinium ß"-alumina.

Various trivalent ß"-aluminas have been prepared by ion exchange of single crystals of Na ß"-alumina (Dunn and Farrington, 1983) in the relevant molten ion halide. These trivalent ß"-aluminas seem to be the first trivalent solid electrolytes, with rapid cation motion at moderate temperatures. Gadolinium ß"-alumina was prepared using molten $GdCl_3$ heated to 615°C and left for 5 hours. A 100% exchange was found leading to $Gd_{0.56}Mg_{0.67}Al_{10.33}O_{17}$.

Gd ß"-alumina is of special interest as it has been found to act as a laser host material. At room temperature the Gd ions are trapped in the conduction plane in well separated sites, although at high temperatures the ions do become mobile and a conductivity of $10^{-3}\Omega^{-1}cm^{-1}$ at 600°C has been reported (Farrington et al., 1983) - thus allowing direct ion exchange at these temperatures by cation diffusion.

The ionic distribution of the gadolinium in the conduction planes has been studied using single crystal x-ray diffraction (Carrillo-Cabrera et al., 1983) and the Gd ions

are found to occupy only the mO sites (9d sites) with an average occupancy of 18.8% and some spreading in the electron distribution towards the BR/aBR sites. Figure 3.24 lists the Gd ion positions and occupancies.

The bridging O(5) oxygens are also disordered, sitting in one of six 18(f) sites displaced by 0.5Å from the normal O(5) site found in sodium ß"-alumina. The oxygens are displaced towards the gadolinium ions (see figure 3.25) and this displacement binds the Gd ions into the lattice, making the material an insulator at room temperature and a conductor at high temperature.

A degree of LRO has been observed in the cation sublattice of Gd ß"-alumina, by neutron diffraction, and high resolution electron microscopy has been used to provide more detailed information. Figure 3.26 shows an HREM image of Gd ß"-alumina and its associated diffraction pattern. A region within the crystal is visible in which ordering in the conduction plane is apparent. Computer simulation was used to obtain a model for the structure.

A 3a x 3a x c supercell was used for the calculation.

The gadolinium ions in the 9d sites were arranged so that some sites were fully occupied and others completely empty - rather than having an average occupancy in each site. (as in fig. 3.25). The overall Gd occupancy was kept constant. Figure 3.27 shows a computer calculated plot of the projected atom positions for the normal material and the superlattice (in the $[11\bar{2}0]$ direction). The EMSYS program suite was used to calculate through-focal and through-thickness series of HREM images of the superlattice structure and to calculate a superlattice electron

Atom type	Point group (Wyckoff notation)	Atomic positions x	y	z	Occupancy (%)
O(1)	18(h)	0.1537	2x	0.0350	100
O(2)	6(c)	0	0	0.2944	100
O(3)	6(c)	0	0	0.0992	100
O(4)	18(h)	0.1631	2x	0.2338	100
O(5)	18(f)	0.4226	0.6667	0.1667	16.67
Al(1)	3(a)	0	0	0	100
Al(2)	6(c)	0	0	0.3503	99.2
				(0.6497	96.4)
Al(3)	18(h)	0.3345	x/2	0.0723	100
Al(4)	6(c)	0	0	0.4504	100
Gd(1)	* 6(c)	0	0	0.1773	1.4
Gd(2)	9(d)	0.3333	0.1667	0.1667	18.8

* only alternate 6(c) sites occupied.

Disordered structure

Fig 3.24 Atomic positions and occupancies for gadolinium ß"-alumina. (Carrillo-Cabrera et al., 1983)

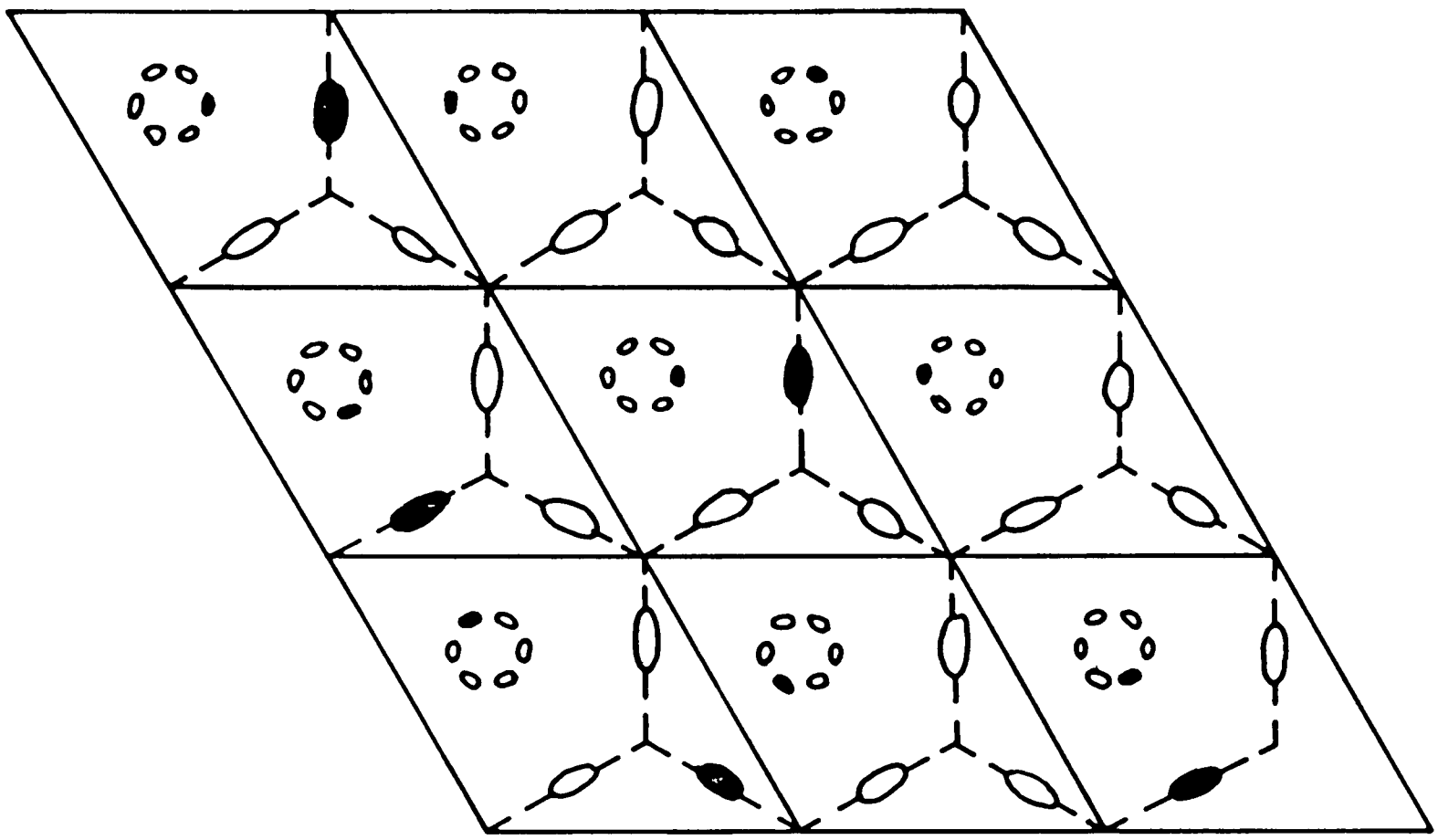

○ Vacant Gd^{3+} site

● Fully occupied Gd^{3+} site

o Vacant bridging oxygen site

• Fully occupied bridging oxygen site

Fig. 3·25 Schematic representation of a possible ordering in gadolinium β′-alumina.

Note: this superstructure has not been completely characterised, & further work is being done.

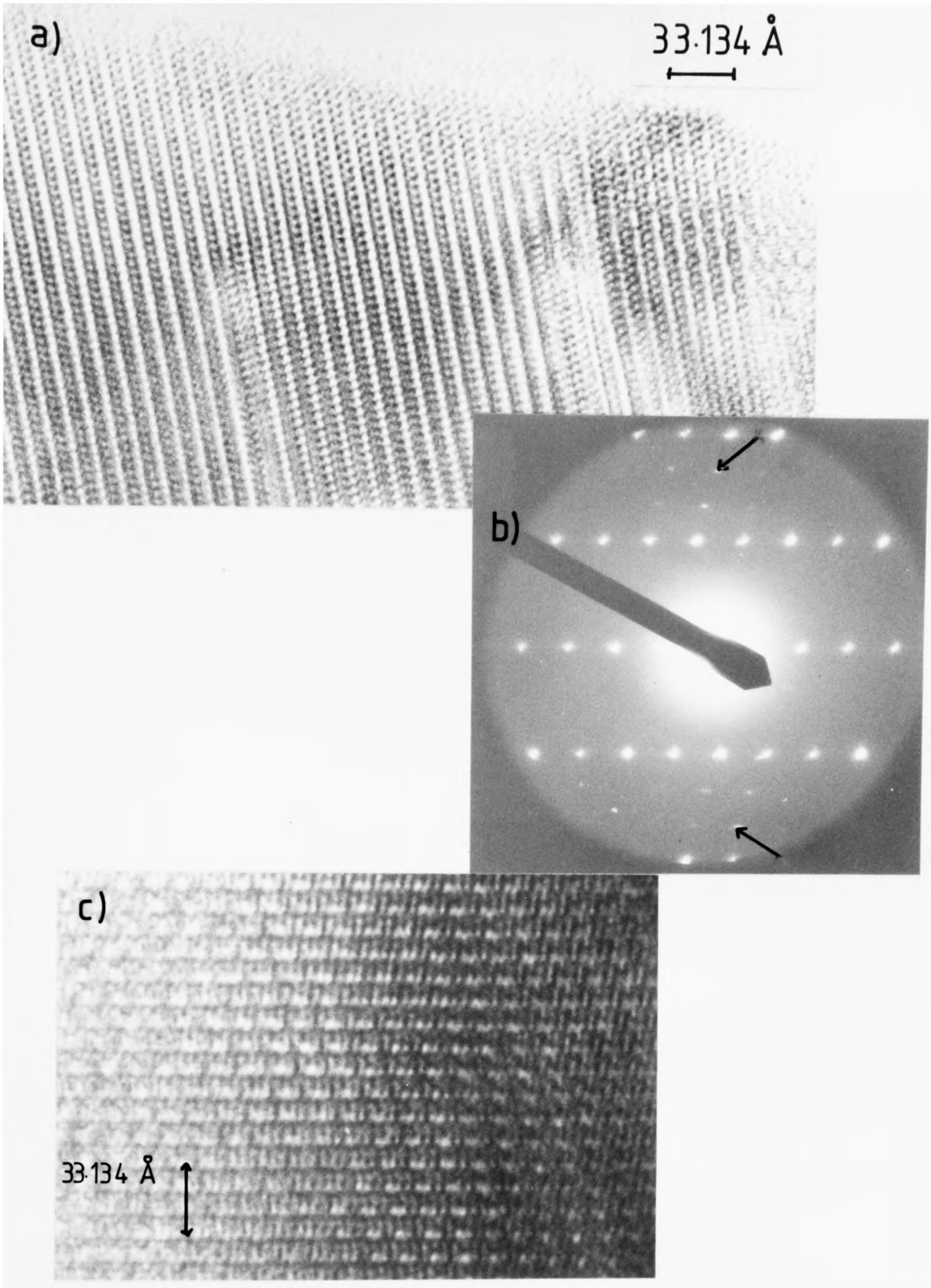

Fig. 3·26 a) and c) Lattice images of gadolinium ß''-alumina showing superlattice ordering along the conduction planes.
b) Electron diffraction pattern from gadolinium ß''-alumina showing superlattice spots (arrowed).
Electron beam along $\langle 11\bar{2}0 \rangle$.

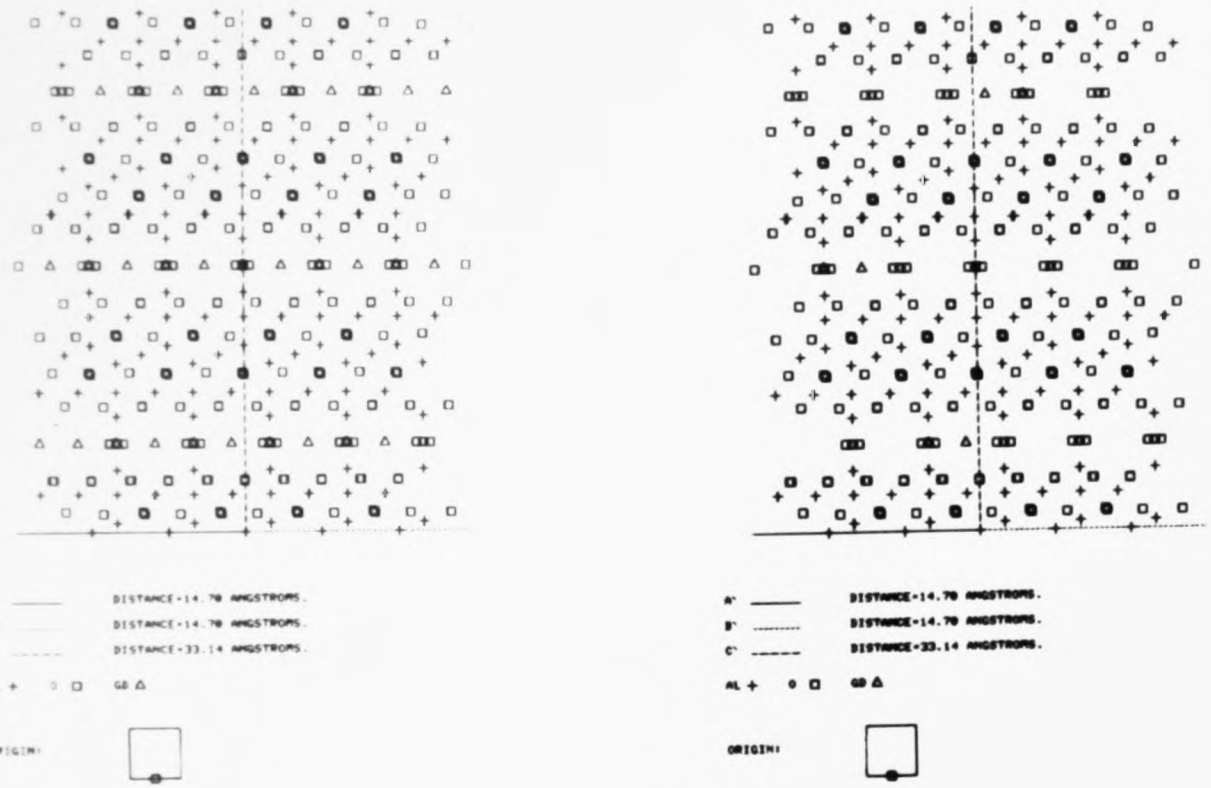

Normal lattice positions

Superlattice positions

Fig. 3.27 Computed projection of atomic positions in gadolinium β''-alumina. [<1$\bar{1}$20>projection]

Computer simulations of the projected potential due to Gadolinium β''-alumina.

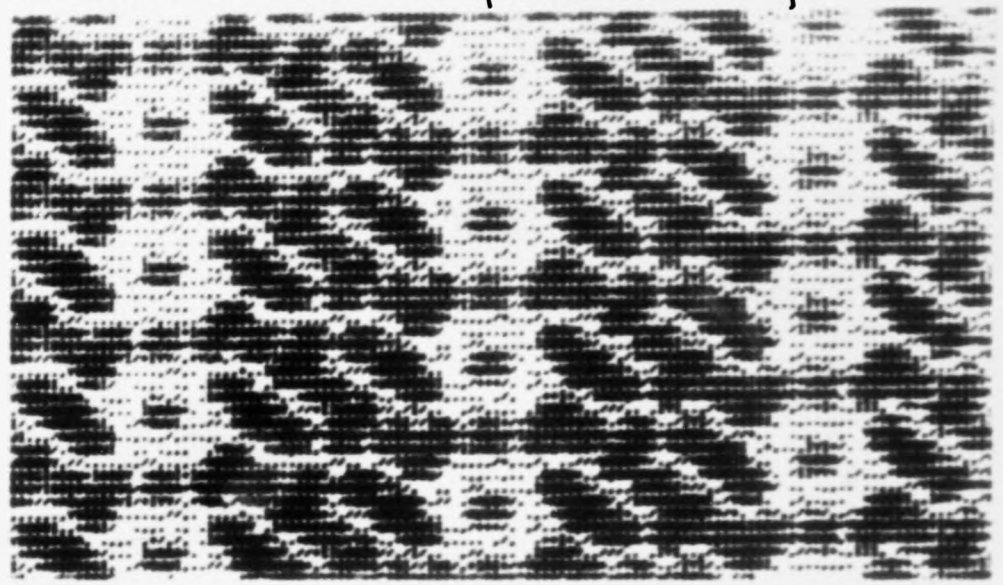

a) Normal lattice atomic positions (all Gd sites partially filled).

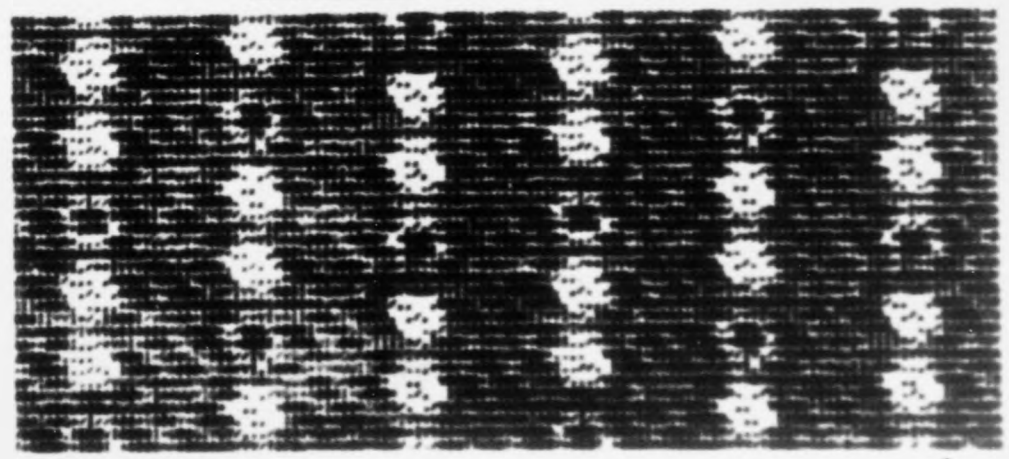

b) Superlattice atomic positions (some Gd sites empty).

Fig. 3.28

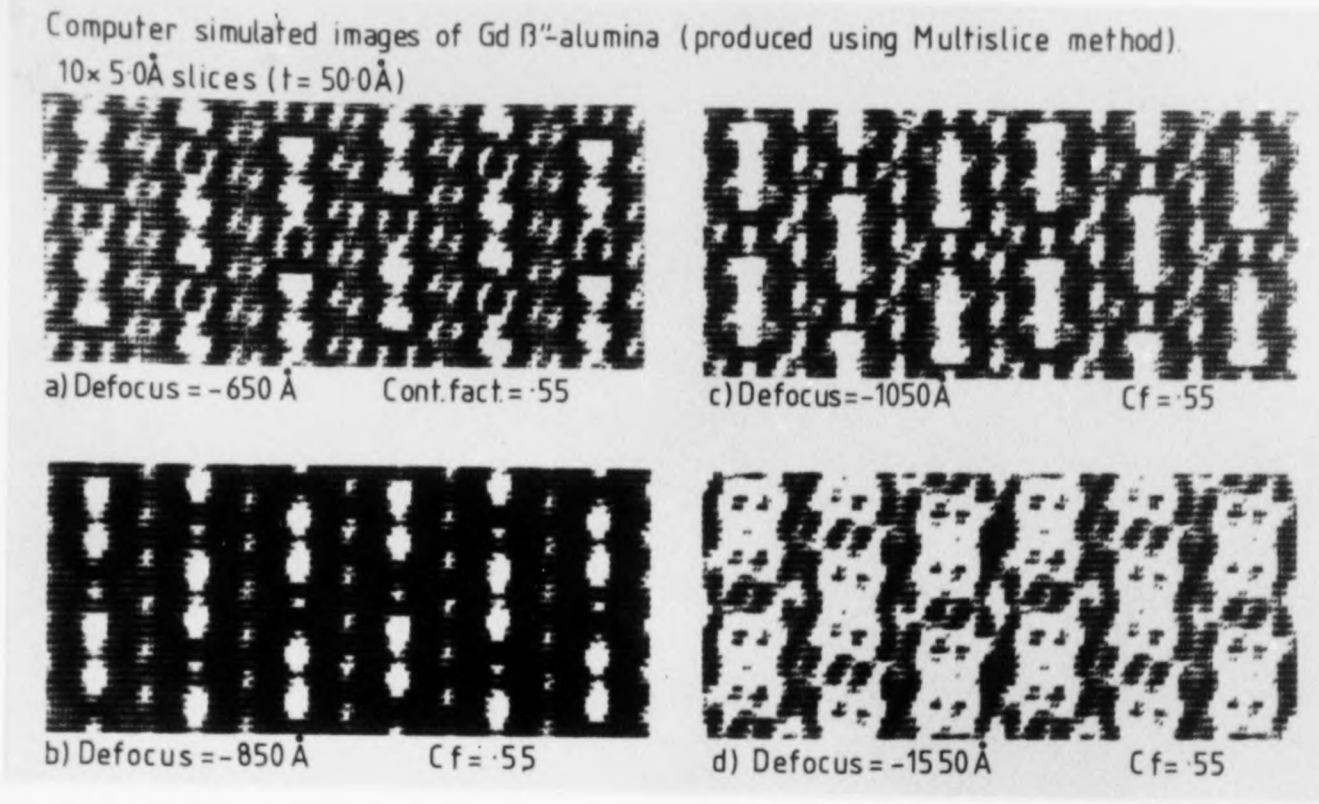

Fig. 3·29 a) Through-focal series for 50·0Å thick Gd β''-alumina superlattice crystal.

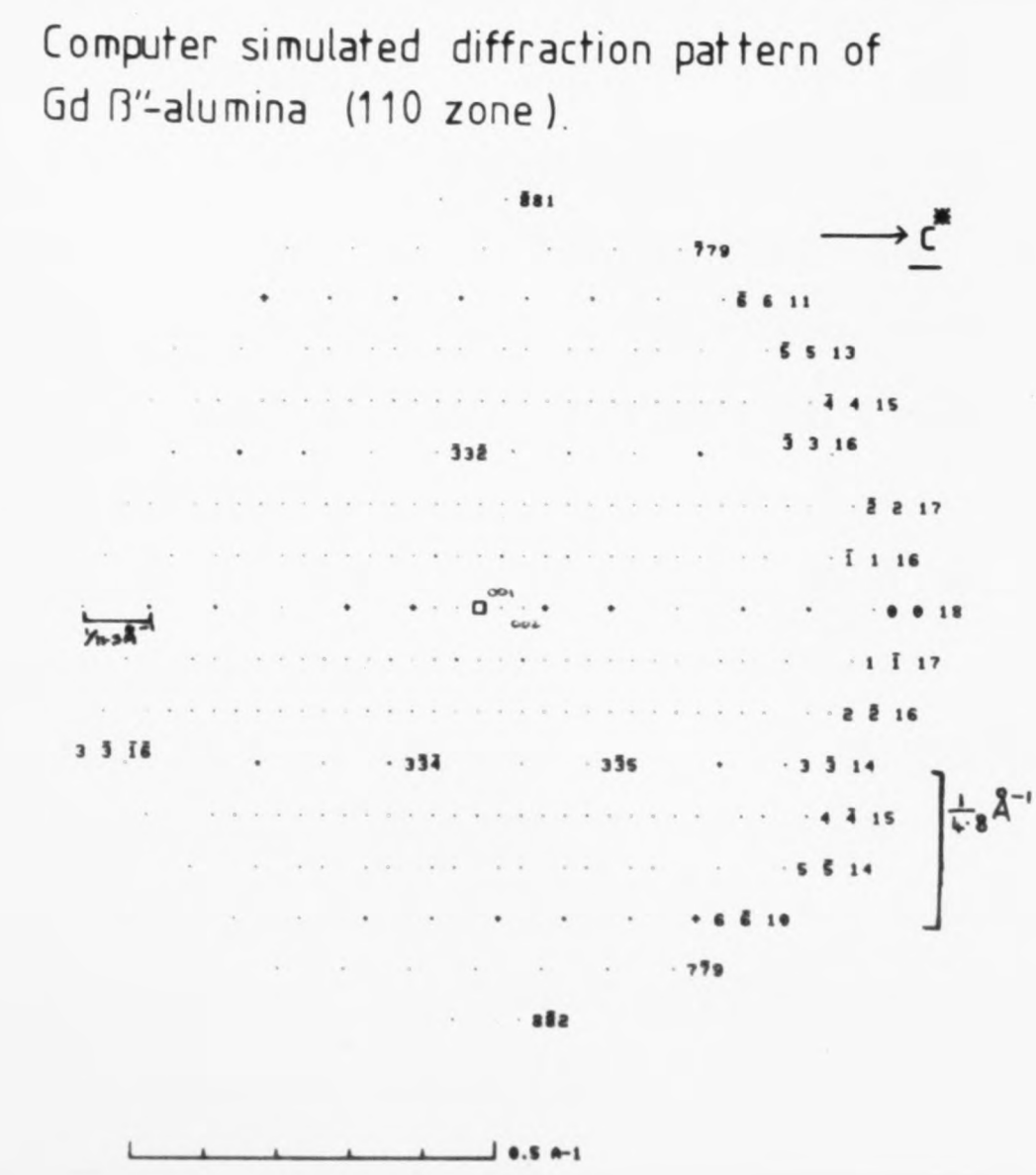

3·29 b) Computed electron diffraction pattern for Gd β''-alumina superlattice crystal.

diffraction pattern. Figure 3.28 shows a comparison between the projected potentials for the normal and superlattice structures, and figure 3.29 shows a through-focal series of images of the superstructure for a crystal thickness of 50Å, and a superlattice electron diffraction pattern.

3.12 Europium ß"-alumina.

A preliminary study has been made of various europium ß"-aluminas. The specimens examined were Eu^{2+} ß"-alumina and mixed Eu^{2+}/Eu^{3+} ß"-alumina - prepared by heating pure Eu^{2+} material. In both cases the specimens were prepared by ion-exchange of the sodium ß"-alumina in the relevant halide ($EuCl_2$ or $EuCl_3$).

Figure 3.30 shows an HREM image and associated electron diffraction pattern of Eu^{2+} ß"-alumina. Superlattice ordering is present and can clearly be seen in the diffraction pattern. The superlattice cell appears to have dimensions 2a x 2a x c. The material is very stable to beam damage and appears very regular with few missing conduction planes.

Figure 3.31a) shows an image of a crystal of Eu^{3+} ß"-alumina from the mixed material, and its associated electron diffraction pattern. A similar model to that used for the gadolinium was used to simulate the superlattice ordering, and figure 3.31 also shows the computer calculated image. As can be seen the match between experimental and calculated images along a single conduction plane is good, but the angle between the conduction plane and a line of gadolinium sites of high occupancy (arrowed) is greater for the computed image than for the experimental image (the angle

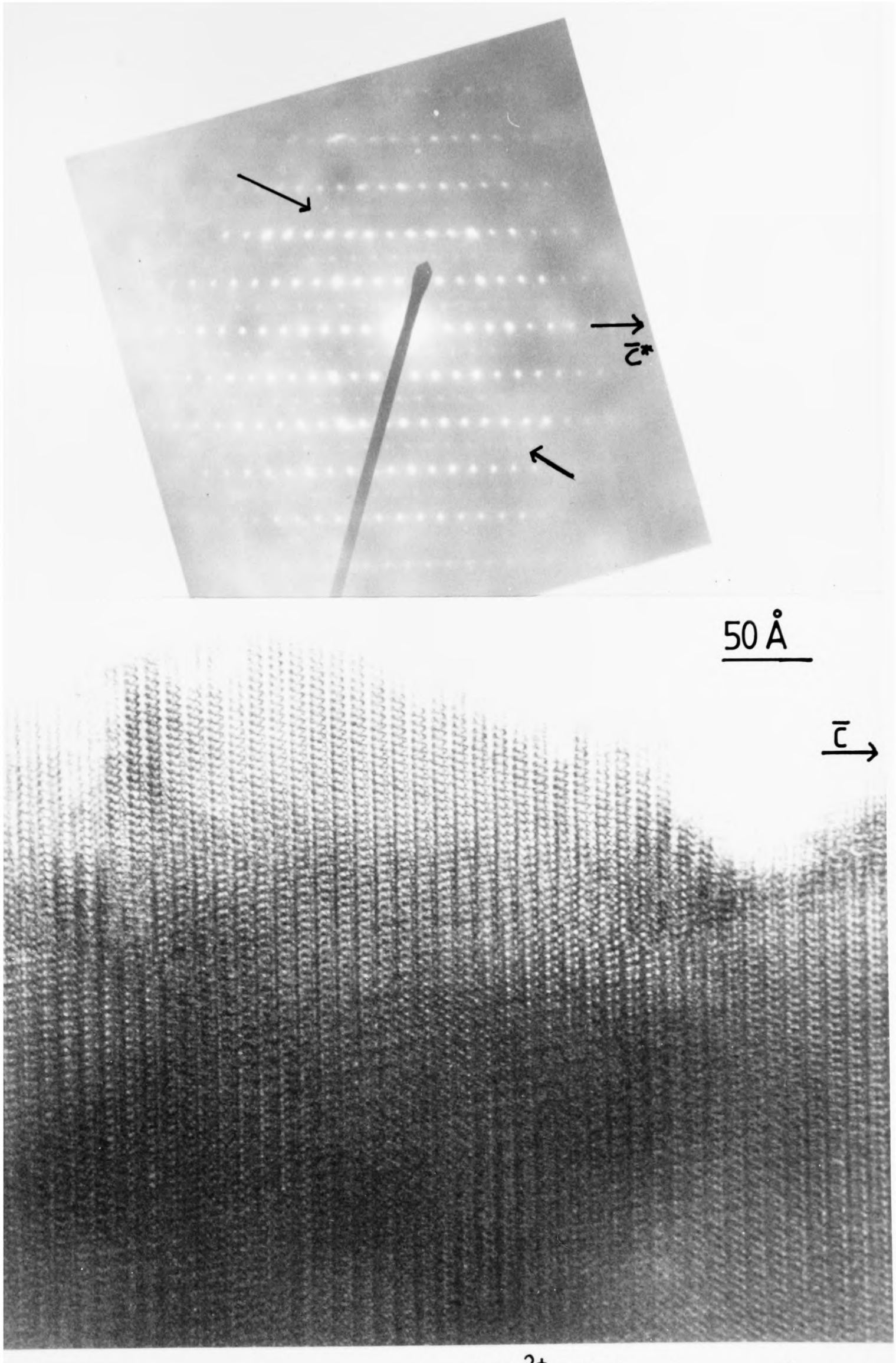

Fig. 3.30 Lattice image of Eu^{2+} β''-alumina and corresponding electron diffraction pattern showing superlattice reflections (arrowed). Electron beam along $\langle 11\bar{2}0 \rangle$.

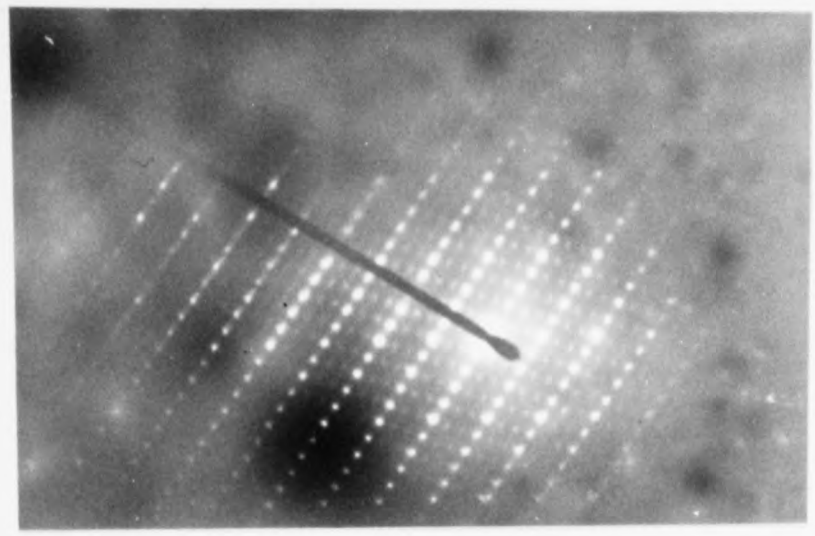

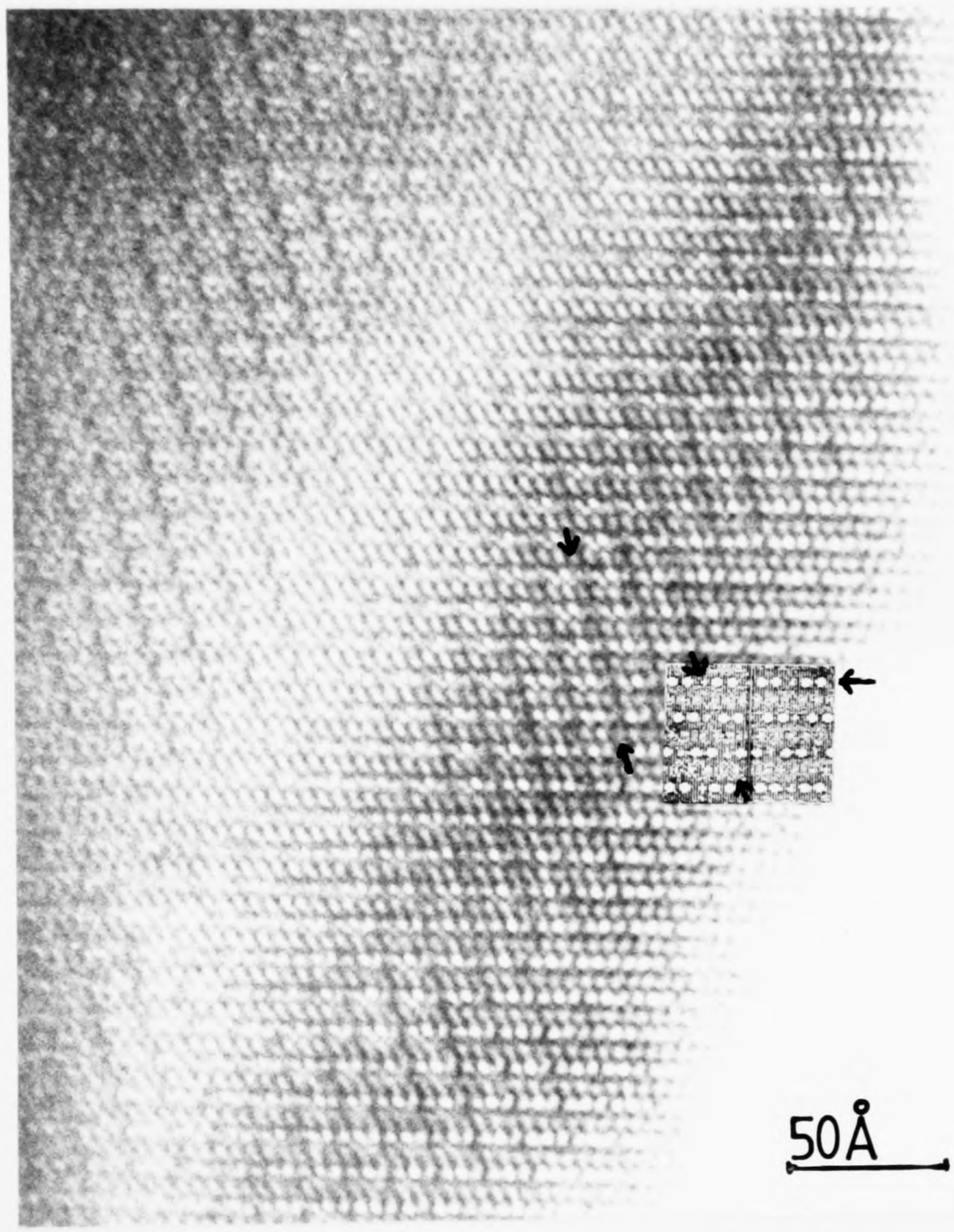

Fig. 3.31 Lattice image of Eu^{3+} β″-alumina with corresponding electron diffraction pattern showing the presence of superlattice ordering. See text for explanation of the computed image.

Electron beam along $\langle 11\bar{2}0 \rangle$.

for the experimental image is 15° and the angle for the computed image is 25°).

Figure 3.32 shows a highly disordered crystal of mixed Eu^{2+}/Eu^{3+} ß"-alumina with many missing conduction planes. This would be expected in material which has been transformed from Eu^{3+} ß"-alumina to the Eu^{2+} phase, as the number of Eu^{2+} cations needed per unit cell in the stoichiometric material is greater than the number of Eu^{3+} cations needed:

$$n_{Eu2+} = 5/6 \qquad n_{Eu3+} = 5/9$$

Thus to produce any conduction planes with the correct Eu^{2+} occupancy, other planes must be lost.

The superlattice cell dimension perpendicular to the c-axis is 2a in Eu^{2+} ß"-alumina and 3a in the Eu^{3+} material; ie. every second tunnel in the Eu^{2+} material is filled, and every third one in the Eu^{3+} material. This is perhaps to be expected as Eu^{2+} should contain half as many cations as the sodium material whilst the Eu^{3+} ß"-alumina should contain only one third as many cations.

Fig. 3.32 Lattice image of highly disordered crystal from a specimen of mixed Eu^{2+}/Eu^{3+} β''-alumina. No determination of the relative amounts of the Eu^{2+} and Eu^{3+} phases present could be made due to the degree of disorder. Electron beam along $\langle 11\bar{2}0 \rangle$.

Chapter 4. Electron beam damage in the ß-aluminas.

4.1 Introduction

Due to the high mobility of the cations in the ß-aluminas, these materials are very sensitive to radiation damage when exposed to an electron beam. ß"-alumina has the higher conductivity and appears to damage much more readily than the ß phase. The major damage mode observed in ß"-alumina is the loss of conduction planes. Other damage modes observed in both ß and ß" are the loss of bulk material to the surface, amorphisation, and the total loss of material under the beam, leading to electron beam 'hole-drilling'. These will be discussed in more detail below.

4.2 Loss of conduction planes in ß"-alumina.

i) Introduction

The loss of sodium and bridging oxygens from conduction planes with subsequent collapse to form broad spinel blocks in sodium ß"-alumina on exposure to an electron beam has been observed by De Jonghe (1977), Bovin (1979) and Matsui and Horiuchi (1981). Figure 4.1 shows a region of sodium ß"-alumina with such broad spinel blocks (arrowed). The material damages rapidly in the beam, and care must be taken to distinguish between beam-induced defects and those already present in the material due to manufacturing techniques.

ii) Analysis of shear vectors and defect block structure.

Figure 4.2a shows the two types of defect formed when a conduction plane is lost and the adjacent spinel blocks

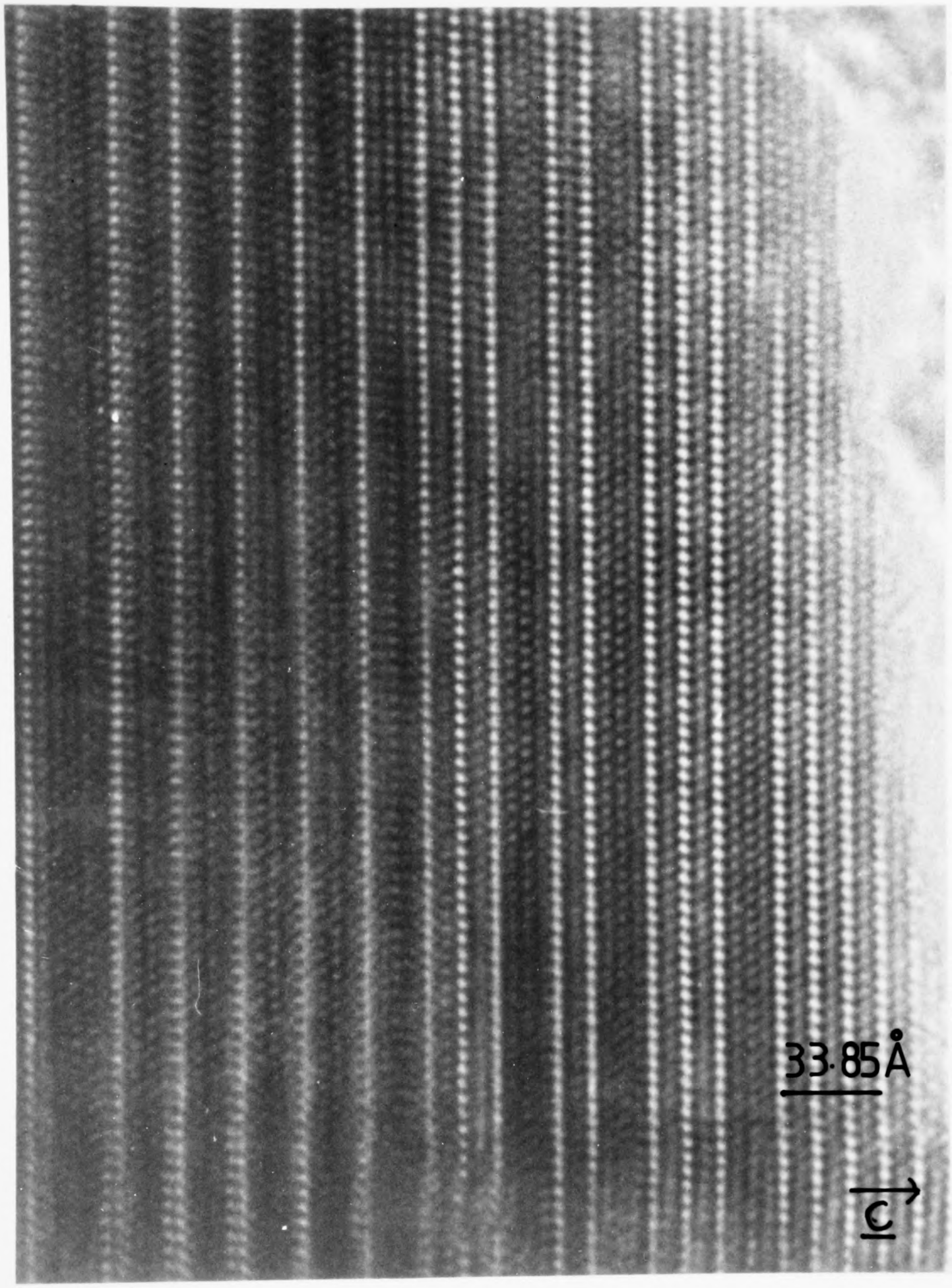

Fig. 4.1 Lattice image of sodium β''-alumina showing broad spinel blocks due to conduction plane loss.

a)

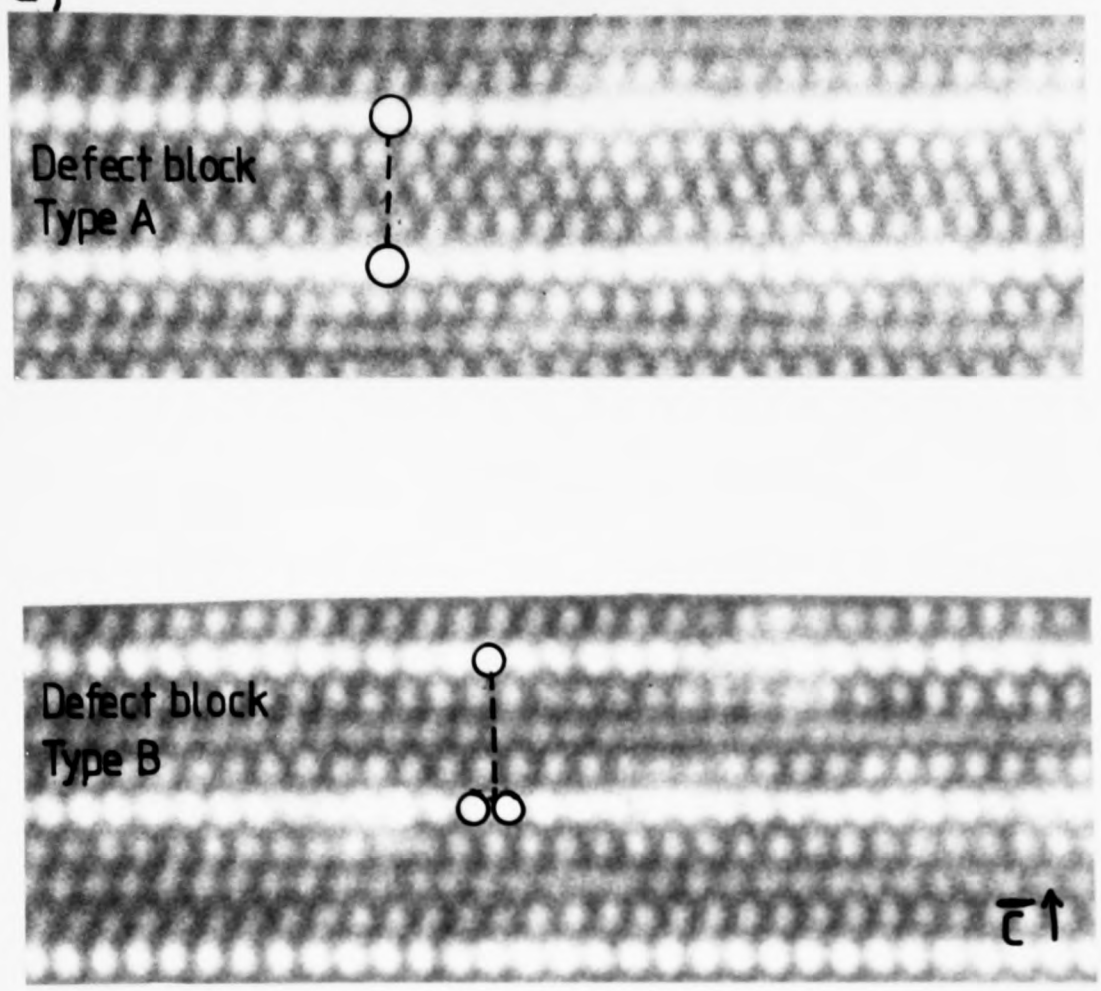

b)

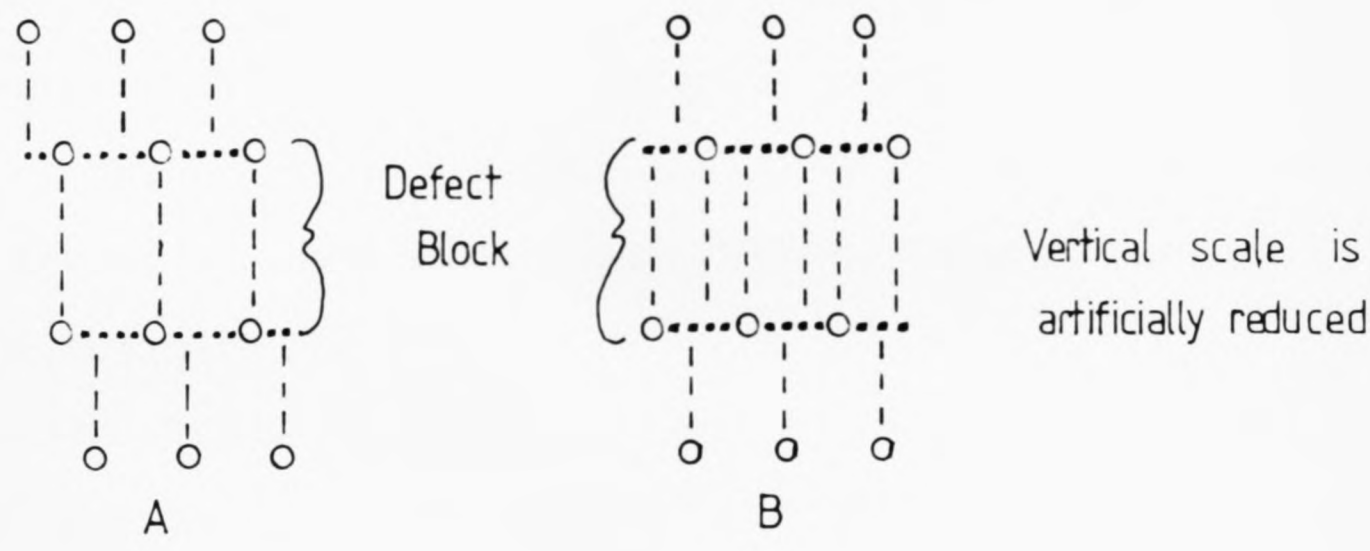

Fig. 4·2 a) HREM images of irradiation induced defects showing A&B type defects.

b) Schematic representation of the arrays of white dots on either side of the irradiation-induced defect blocks expected from the Matsui & Horiuchi model.

collapse and shear (defects arrowed A and B). Not only do the defect blocks give rise to different images, but the alignment of the tunnels on either side of the defects are different. This is shown schematically in figure 4.2b. Matsui and Horiuchi (1981) observed both types of defect and determined the slide vectors giving rise to the defects by examining the relative positions of the white dots on either side of a plane before and after collapse. They arrived at three slide vectors, V_i, composed of a collapse in the c-axis direction, V_c, plus a shear vector. These are listed below:

$$V_1 \approx \frac{1a}{6} + \frac{1b}{3} + V_c$$

$$V_2 \approx -\frac{1a}{3} - \frac{1b}{6} + V_c$$

$$V_3 \approx \frac{1a}{6} - \frac{1b}{6} + V_c$$

a,b are lattice parameters of β"-alumina

V_c = collapse in c-axis direction

$V_{1,2,3}$ are mutually related by 120° rotations around the c-axis and in β"-alumina are therefore crystallographically equivalent. Thus the defect blocks created in each case are structurally the same except for their orientation with respect to the host lattice.

The two types of defect imaged (A and B) can be explained by this model. Imaged in the (110) projection plane, V_1 gives rise to image A, and V_2 and V_3 give rise to image B.

The shear vectors proposed by Matsui and Horiuchi correspond to the bridging AlO_4 tetrahedra losing the bridging O(5) oxygen and sliding together to become

edge-sharing rather than corner-sharing. A polyhedral layer of mixed tetrahedral type, equivalent to that found in the centre of the spinel blocks in the perfect structure, is then formed. This is shown in figure 4.3. Three equivalent shear vectors are found due to the fact that each pair of bridging tetrahedra can slide together along one of three edges.

iii) Secondary damage mechanisms.

When the bridging oxygens are lost from a conduction plane and the bridging tetrahedra collapse, a crystallographic shear (CS) plane is formed. Hull (Hull et al., 1981) has examined the growth of the CS plane by electron microscopy, and has shown that the mechanism for growth is similar to that proposed by Anderson and Hyde (1967) for CS planes in complex oxides: when a number of oxygen vacancies have formed in a conduction plane, they aggregate to form a disc, by a partial dislocation loop (of Burgers vector $b=1/30[5\bar{5}0\bar{2}]$).

In the case of ß"-alumina conduction plane collapse, a crescent (as opposed to a loop) dislocation is observed due to the fact that the collapse always starts at a surface of the crystal. Elastic strain at the dislocation makes it a sink for further vacancies, and the crescent expands by dislocation climb as it absorbs vacancies. The line energy of a half loop at the surface is lower than that of a complete loop in the bulk, thus favouring surface nucleation.

iv) Possible primary damage mechanisms.

In this study (and that of Hull (1983)) a series of experiments was performed in which crystals of Na ß"-alumina were irradiated at different incident electron beam energies. The experiments showed that as the incident electron energy

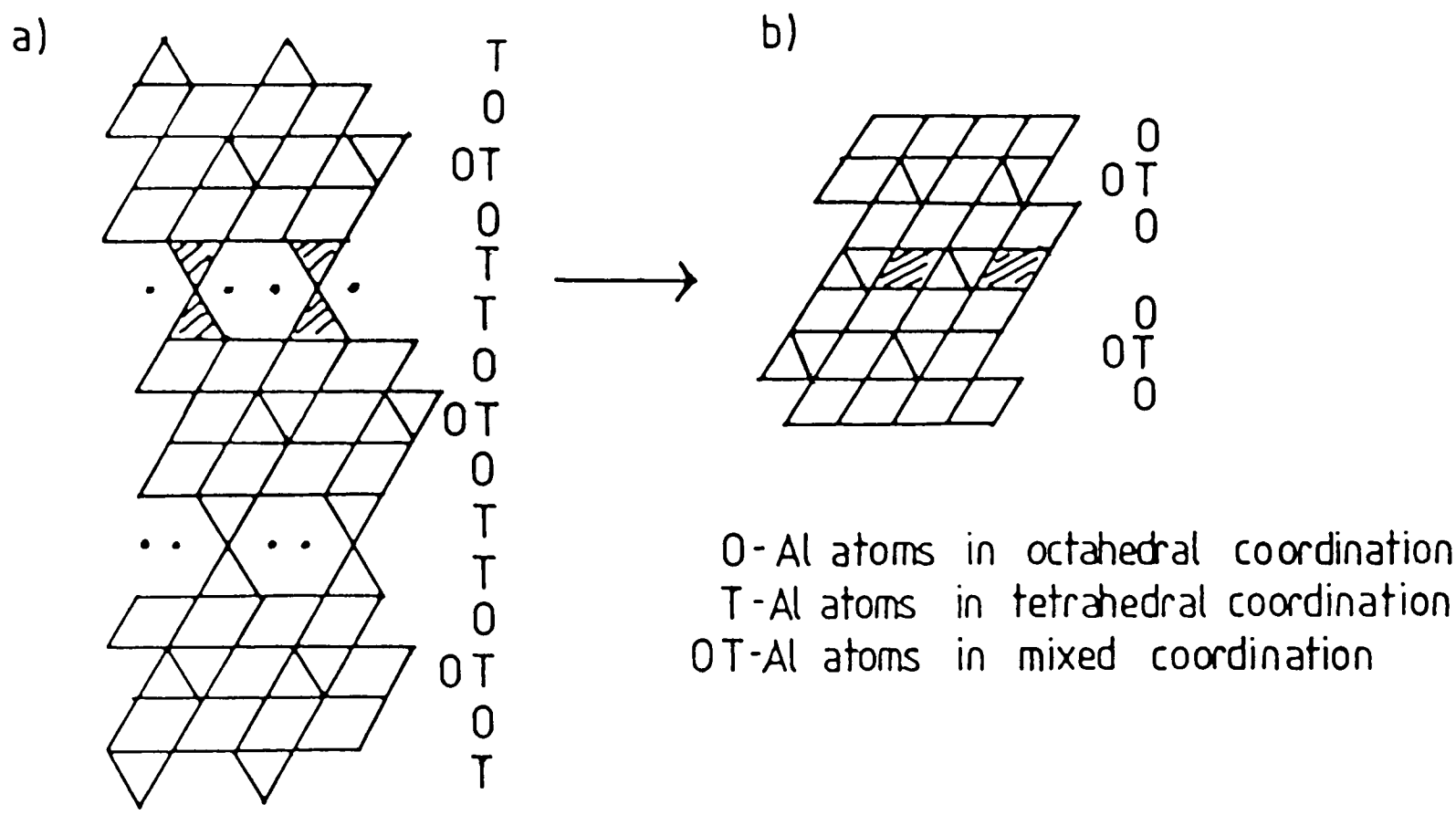

Fig. 4.3 Polyhedral structure of β''-alumina a) before conduction plane collapse and b) after collapse.

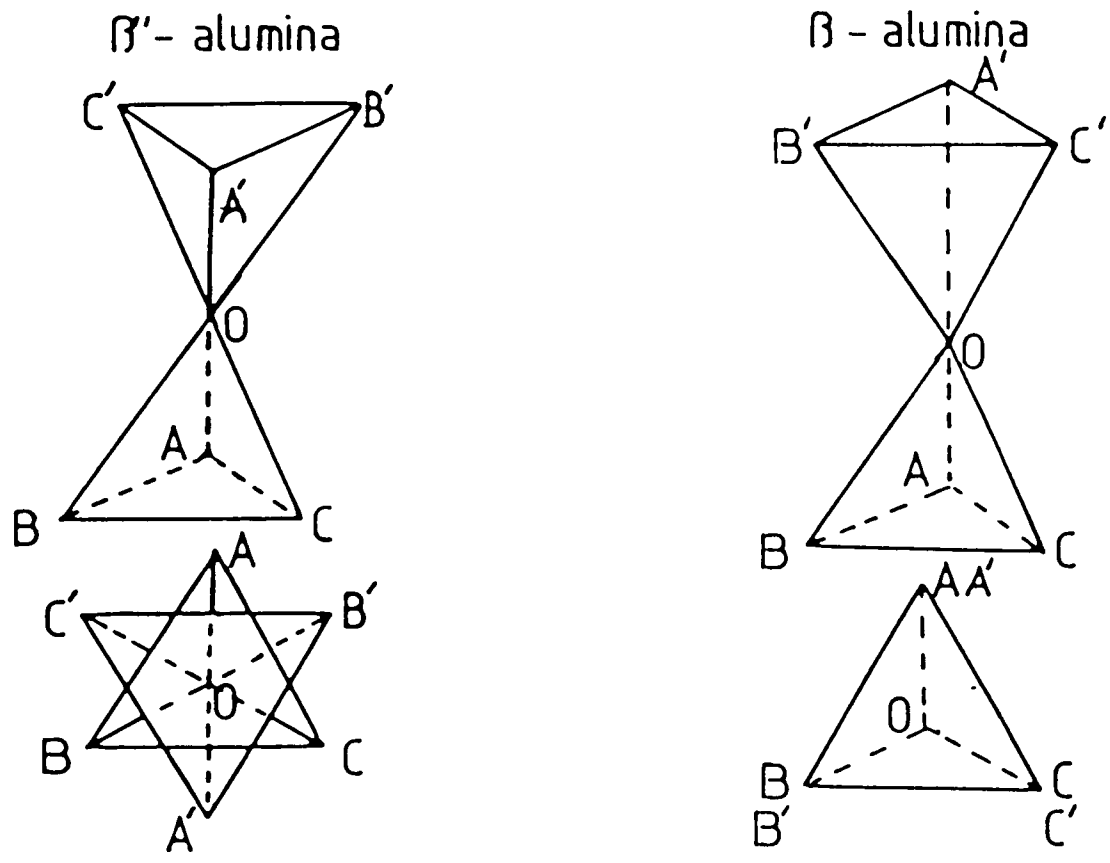

Fig. 4.4 Schematic representation showing the relative orientations of pairs of bridging tetrahedra in mirror plane- and screw axis-related β-aluminas.

increases so the damage rate decreases. This suggests that the primary damage mechanism is ionisation damage rather than displacement damage, as the cross-section for displacement damage increases as the incident electron energy increases. It should however be noted that the damage rate in the Cambridge 600kV HREM was lower than expected by a simple damage cross-section analysis, suggesting that the damage rate also depends on the microscope vacuum. Collapse was also found to occur more rapidly at higher beam currents, as expected.

Although ionisation damage appears to be the most likely primary damage mechanism, the mechanism is still not fully understood.

v) Comparison between cycled and uncycled electrolyte tube material.

Conduction plane collapse occurs very rapidly for Na ß"-alumina in the electron beam at 200kV (in the Jeol 200CX HREM). The use of low beam current densities when orienting the specimen can lower the damage rate sufficiently to enable a distinction to be made between collapsed planes initially present in the structure and those due to the electron beam.

It appears that cycled Na ß"-alumina contains more collapsed planes than the uncycled material, suggesting that cell cycling can lead to plane collapse.

If enough planes collapse within a crystal (each with an associated decrease in crystal size in the c-axis direction of ~2.3Å), the resulting strain can lead to the formation of atomic scale cracks. If this occurs in a cell, the cracks will extend (see chapter 6) possibly leading to cell breakdown.

vi) Conduction plane collapse in other ß-aluminas.

Although conduction plane collapse is very common in Na ß"-alumina it is hardly ever observed in Na ß-alumina. This is thought to be due to the different arrangements of the bridging tetrahedra in ß and ß "-aluminas (see figure 4.4). In ß-alumina the tetrahedra sit on either side of a mirror plane and so cannot slide together to become edge-sharing.

The aggregation of oxygen vacancies to form a crescent as described in section ii) above is also less likely to occur in ß than in ß" due to the large number of interstitial bridging oxygens present in ß-alumina. These are mobile (De Jonghe et al., 1983) and will tend to diffuse into vacant O(5) sites in the lattice. They will also pin any dislocations in the crystal, making ß-alumina much less sensitive to damage than ß".

Conduction plane collapse has been observed in all of the ß"-aluminas examined in this study (Na, NH_4^+/H_3O^+, Ag, Gd, Eu^{2+}, Eu^{3+}). The collapse rate does not appear to depend on the cation mobility which suggests that cation loss is not the rate limiting factor. Of the ß"-aluminas examined, the unannealed ammonium/hydronium material damaged most rapidly, with the Eu^{2+} material being the most stable.

vii) Blocking defects

If two adjacent conduction planes collapse from opposite sides of the crystal, a blocking defect is formed where the two broad defect spinel blocks meet. The blocking defect prevents further collapse of either plane. Bovin (1979) has postulated a possible structure for such a defect. A blocking defect in ammonium/hydronium ß"-alumina is shown

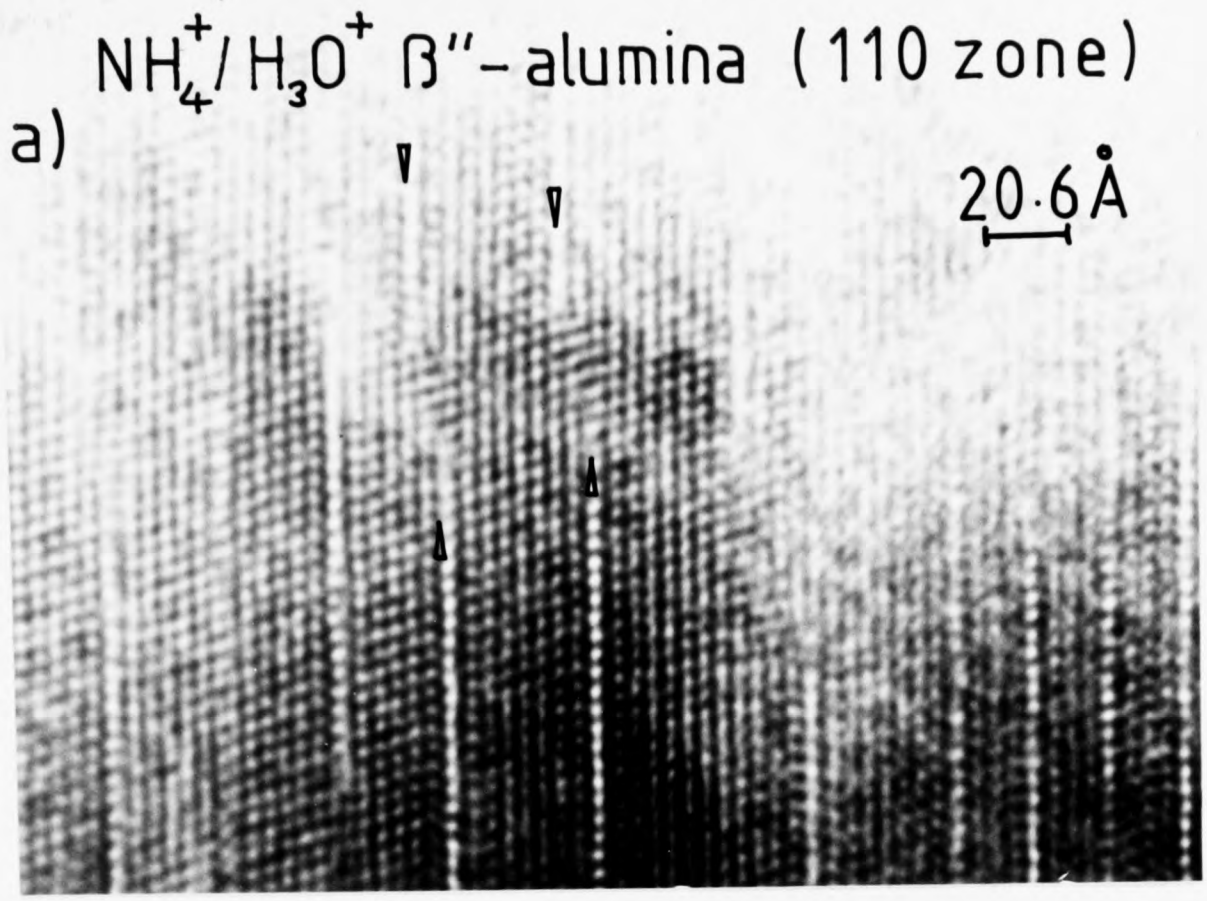

Fig. 4.5 Lattice images of a) NH_4^+/H_3O^+- and b) Na ß''-alumina - illustrating blocking defects (arrowed).

in figure 4.5a), and one in Na ß"-alumina in figure 4.5b).

4.3 Extrusion of material under an electron beam.

In 1979, Bovin (1979b) reported the presence of small semi-hexagonal crystals which appeared on the surface of a Na ß"-alumina crystal after exposure to the electron beam. An electron diffraction pattern from these small islands showed them to be metallic sodium.

In this study an analysis has been made of diffraction patterns from various such islands. They were observed to grow on the surface of Na ß and ß"-alumina specimens under an electron beam, and then to disappear again. Their short-lived nature made detailed analysis difficult.

Usually more than one crystal formed on the ß-alumina surface, giving rise to a polycrystalline spotty ring pattern. The production of such islands of material has been denoted Mode I damage (Hull et al., 1983). A second mode observed in silver ß"-alumina (not seen so far in Na ß"-alumina) involved the very rapid loss of material from specific surface locations. Both Mode I and Mode II damage have been reported in silver ß-alumina by Roth (1971), and are illustrated in figure 4.6.

Analysis of spotty ring patterns from a large number of sodium ß"-alumina specimens showed that the islands consist of various sodium oxides and hydroxides. The compounds found were: Na_2O, Na_2O_2, NaOH, $Na_2O.8H_2O$, and $Na_2O.2H_2O$. Some of the ring patterns correspond only to Na_2O, whilst others correspond to a mixture of oxides and hydroxides. None of the ring patterns corresponded solely to

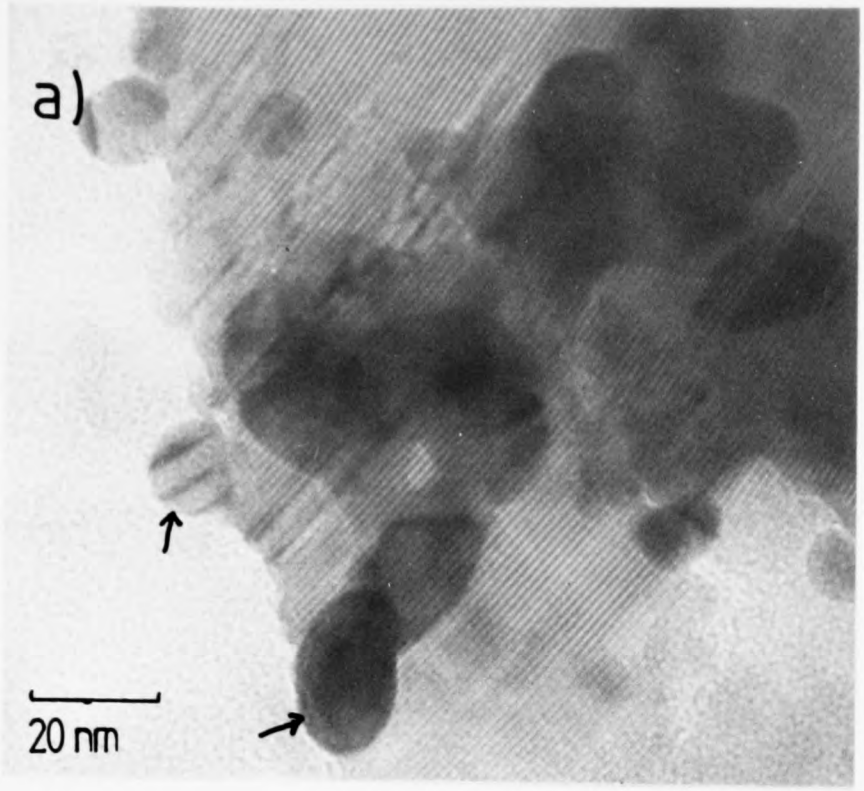

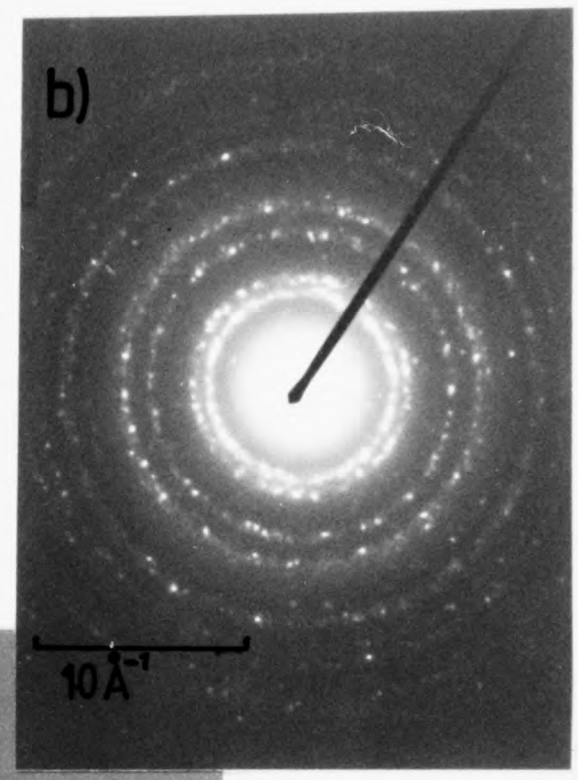

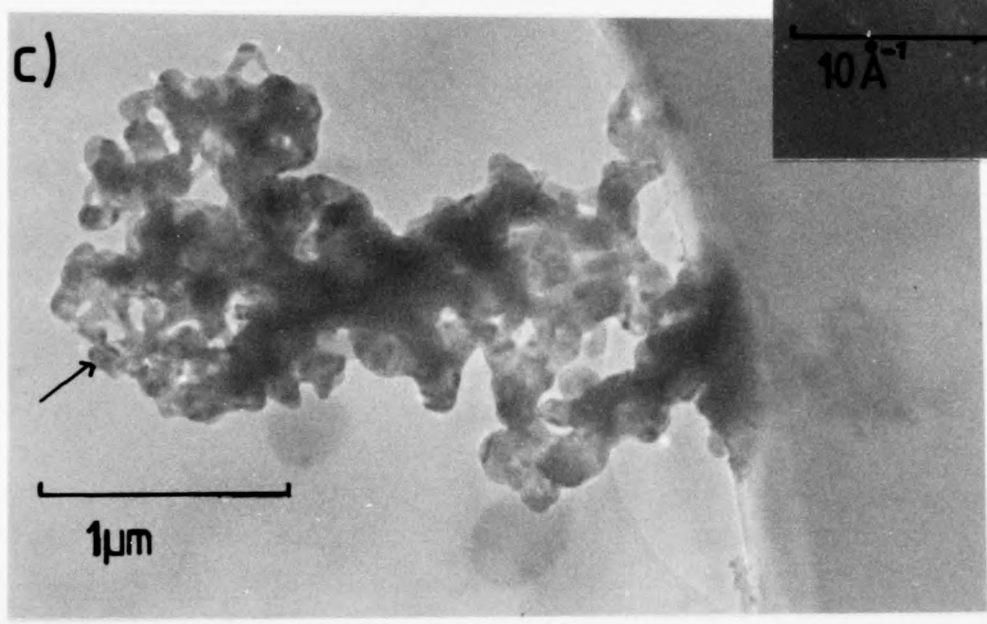

Fig. 4.6 a) Mode I extrusion in Ag ß-alumina (silver islands are arrowed).
b) Electron diffraction pattern from polycrystalline silver whiskers.
c) Mode II extrusion in Ag ß-alumina (silver whiskers are arrowed).

metallic sodium. Some examples of ring patterns and an image of islands are shown in figure 4.7 and the corresponding indices for the ring patterns in figure 4.8.

For each ring pattern an identifiable spot pattern was required for use as a calibration standard. Wherever possible a spot pattern on the same micrograph was used. In cases where this was not possible a calibration micrograph was taken immediately after the ring pattern, at the same camera length. In all cases the [110] ß or ß"-alumina spot pattern was used for calibration.

The ring diameter was measured parallel and perpendicular to the $\hat{c}^*$ direction of the calibration pattern. Once all the rings had been measured, an average radius and the corresponding lattice spacing for each ring was calculated. The experimental values were compared with the calculated values for Na ß and ß"-alumina and the various sodium compounds listed above. A best fit was then made, within experimental error, to both the lattice spacings and the calculated intensities. The most frequent match was found to be with Na_2O.

Two possible mechanisms for the formation of these islands are postulated:

1. The sodium leaving the conduction planes combines at the crystal surface with the conduction plane oxygen ions which have also left the crystal.

2. The sodium combines at the crystal surface with oxygen, hydroxide ions and/or water in the microscope vacuum.

At present it is not possible to determine which of these is the correct mechanism, although the second mechanism is also supported by work carried out in a CAMECA electron

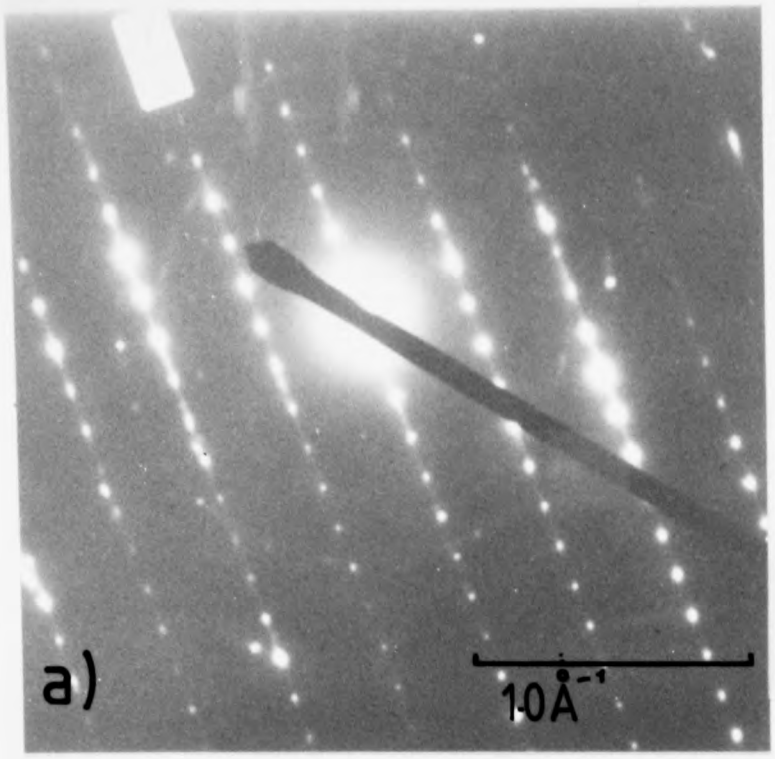

Fig. 4·7 a) Diffraction pattern from Na ß"-alumina showing ring pattern due to extruded material. See next figure for indexing of ring pattern.

b) Polycrystalline ring pattern from material extruded from Na ß"-alumina (see next figure for indexing of pattern).

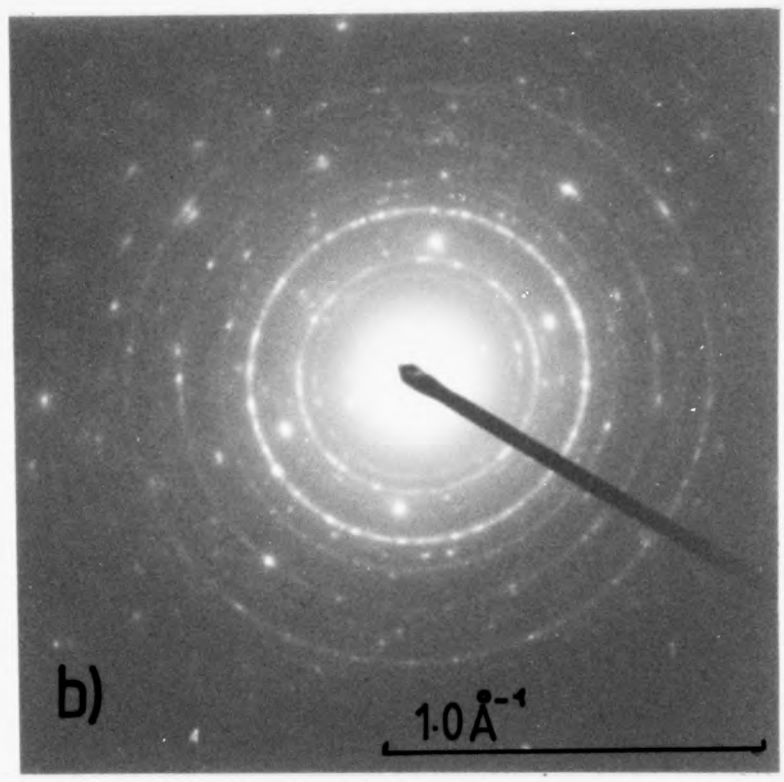

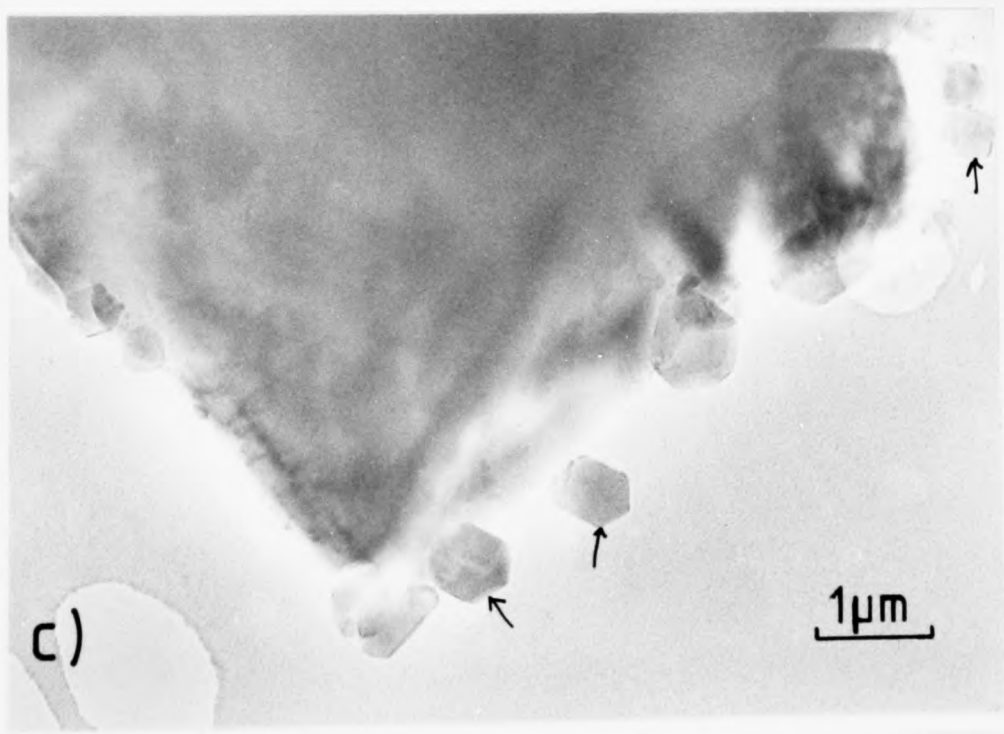

c) Mode I extrusion in Na ß"-alumina (extruded islands are arrowed).

Erratum

In Fig. 4.8 the column ´rings (a) corresponds to pattern (b) in Fig. 4.7, and vice versa.

Possible origins.

Ring radii in (Å) (a)	(b)	Material	Lattice spacing (Å)	hkl	X-ray intensity (see *)
3.59		$Na_2O_2.8H_2O$	3.55	-	30
3.12		Na_2O	3.19	111	40
		Na_2O_2	3.09	-	45
2.88		NaOH	2.85	040,120	20
	2.67	$Na_2O_2.8H_2O$	2.71	-	100
2.58		$Na_2O_2.8H_2O$	2.57	-	95
2.20		NaOH	2.20	-	60
2.02		NaOH	2.03	131	10
	1.95	Na_2O	1.95	220	100
		$Na_2O_2.8H_2O$	1.93	-	60
1.88		$Na_2O_2.8H_2O$	1.85	-	10
		Na_2O_2	1.90	-	50
	1.65	Na_2O	1.67	311	10
1.56		$Na_2O_2.8H_2O$	1.56	113,402	8
		Na_2O	1.60	222	20
	1.35	Na_2O	1.39	400	30
		NaOH	1.35	-	10
1.27		Na_2O	1.27	331	5
	1.10	Na_2O	1.13	422	30
		NaOH	1.11	-	10

* Relative X-ray intensity (strongest reflection = 100)

Fig. 4.8 Indexing of polycrystalline electron diffraction patterns shown in Fig. 4.7.

Erratum
In Fig. 4.8 the column ´rings (a) corresponds to pattern (b) in Fig. 4.7, and vice versa.

microprobe analyser (EMPA). In this case metallic sodium deposits form on the ß-alumina specimen surface under the electron beam; in the HREM only a small ß-alumina crystal is examined, and relatively few sodium ions are lost to the surface. The partial pressure of oxygen and water vapour in the HREM vacuum is large enough for each sodium ion to be oxidised on reaching the specimen surface by an ion from the surrounding atmosphere. In the EMPA however a bulk specimen is examined, and a large amount of sodium is produced. The partial pressure in this case is not high enough to allow oxidation of all the sodium extruded, resulting in the growth of a layer of metallic sodium on the specimen surface.

In the case of silver ß"-alumina, both Mode I and Mode II extrusion lead to deposits of polycrystalline metallic silver on the specimen surface. This is thought to be due to the fact that silver is much less reactive than sodium and so is reduced to form a metallic colloid of silver rather than reacting with the microscope gases.

4.4 Damage in sodium ß-alumina.

As mentioned in section 4.2vi above, conduction plane collapse is rarely seen in ß-alumina. The material is considerably more beam-stable than sodium ß"-alumina and exposure of a few minutes to a beam of high current density is required to cause beam damage to occur.

An experiment to observe beam damage in sodium ß-alumina was conducted using the Jeol 200CX HREM at Oxford. The condenser aperture was removed and a high current density beam was focused on the specimen. The ß-alumina did not lose conduction planes but the appearance of the crystal changed,

finally becoming amorphous. Figure 4.9 shows a damaging region of ß-alumina with associated diffraction patterns.

As can be seen from the diffraction patterns in figure 4.9b) and c), every fifth spot along the $\langle 001 \rangle$ ($\hat{c}^*$) direction is increased in intensity. This spot separation corresponds to a repeat distance of ~2.26Å along the c-axis - the separation of the close-packed oxygen layers in the lattice. This suggests that the electron beam damage is resulting in all the oxygen layers (spinel block and conduction plane) becoming equivalent and a breakdown in the long period order, although the mechanism by which this occurs is not understood. The other bright spots appear to correspond to a rotation of the lattice about the $\bar{c}$-axis.

4.5 Further damage modes observed in ammonium/hydronium ß"-alumina.

Two further damage modes have been observed in heat treated NH_4^+/H_3O^+ ß"-alumina which have not been seen in any of the other materials examined. Figure 4.10 illustrates the first of these; small light patches which increase in number and size as the electron irradiation continues. They correspond to regions of decreased density or thickness in the specimen. They are thought to be due to knock-on damage caused by the protons in the conduction planes. An incident electron displaces a proton within a conduction plane. The displaced protons can then act as an ion beam causing further displacement damage in the surrounding material. This is a very efficient damage mechanism since conservation of energy and momentum equations show that an electron beam can transfer much more energy to an atom via a proton than acting

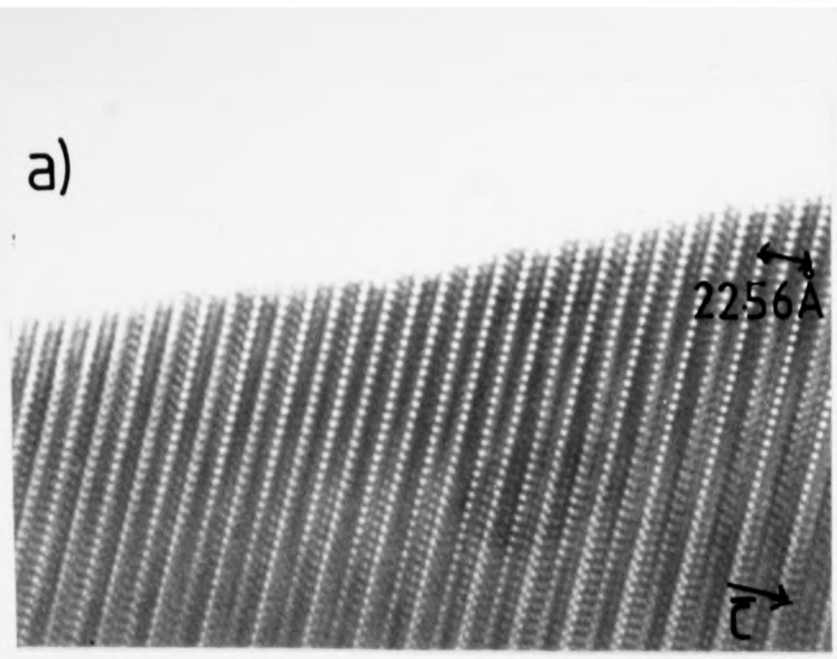

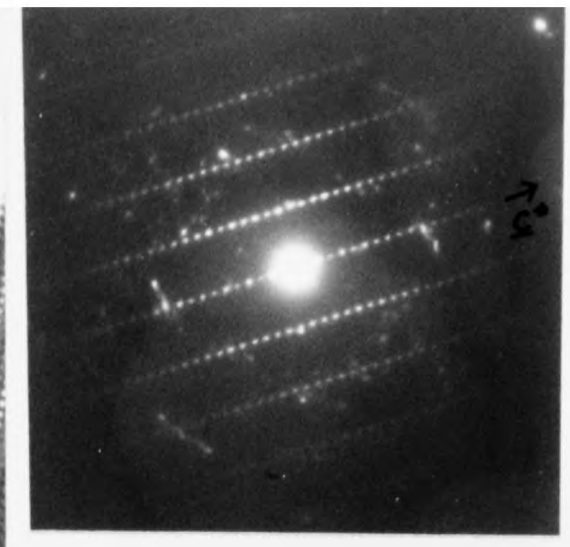

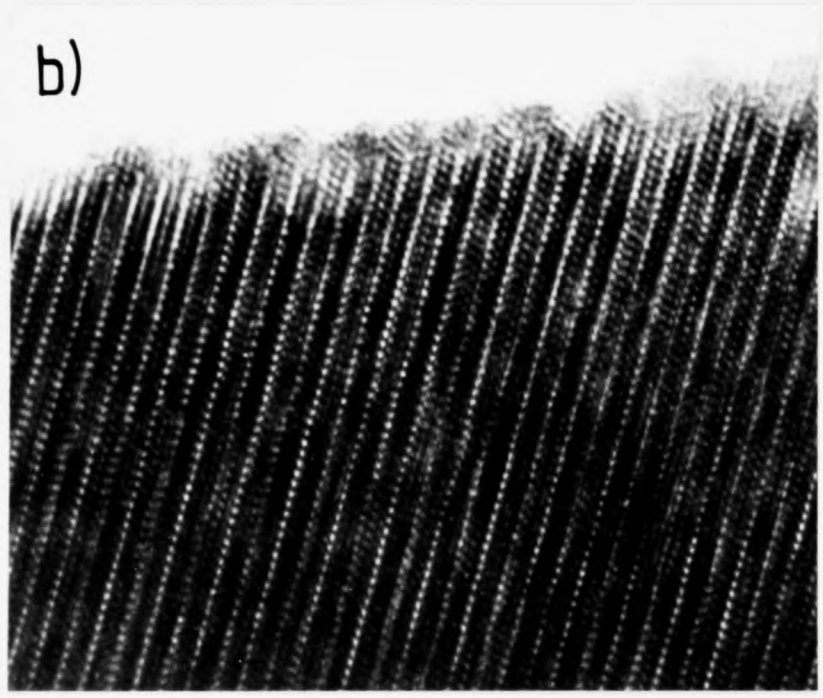

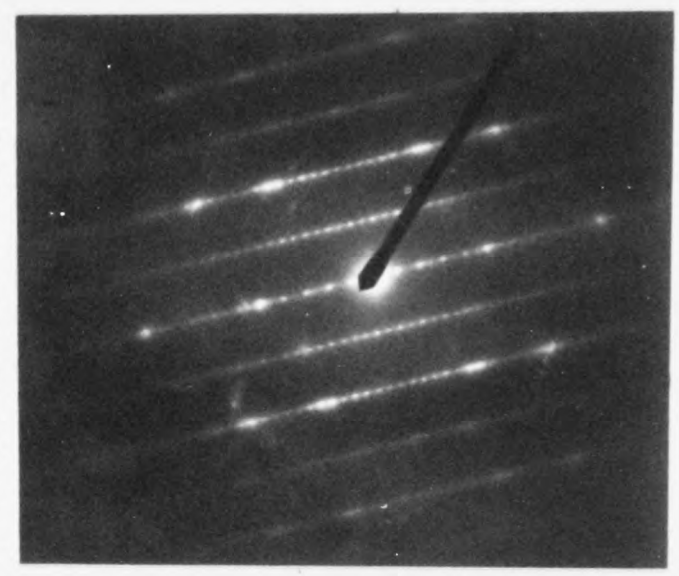

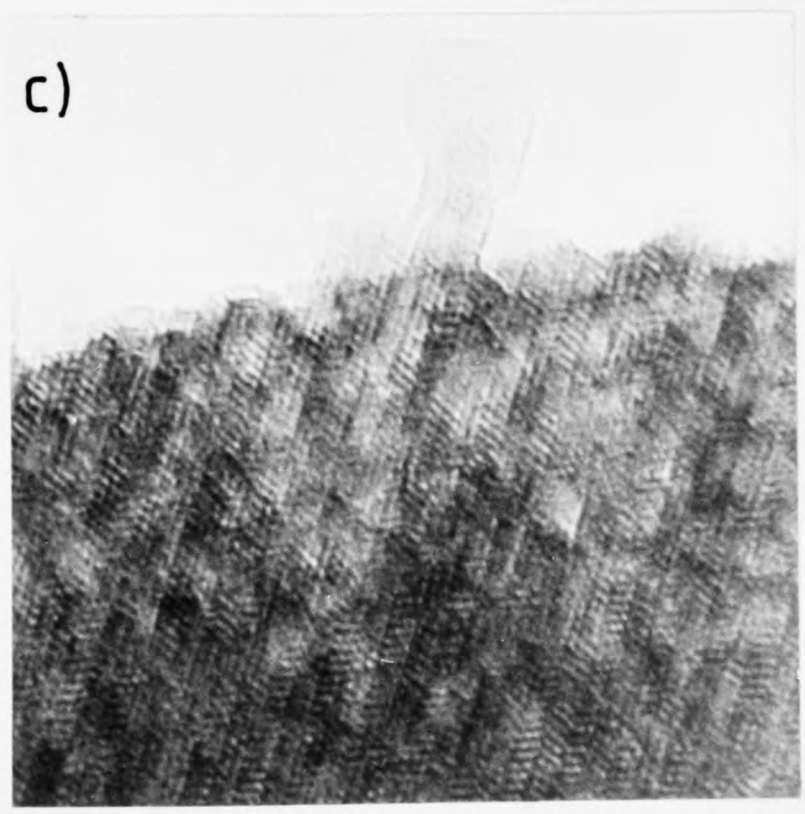

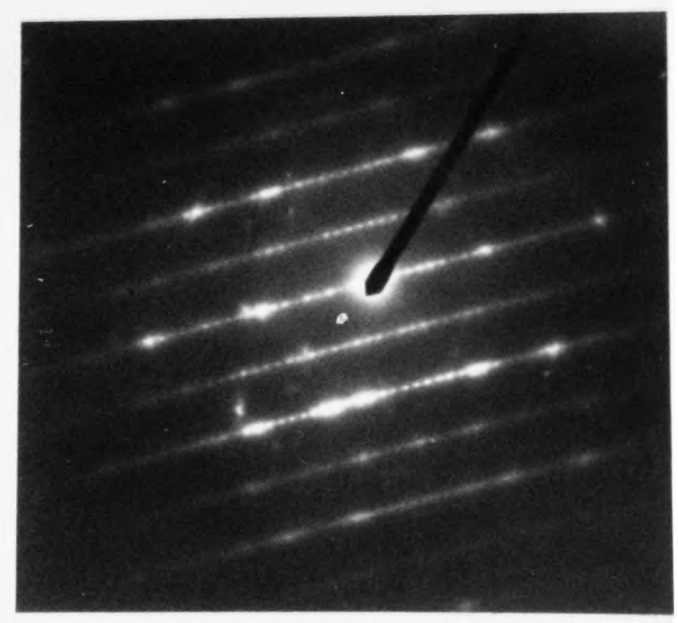

Fig. 4.9 a), b) and c) Lattice images of the same region of a crystal of Na ß-alumina taken at time intervals of a few minutes during exposure to an intense electron beam in the Jeol 200CX HREM. The corresponding electron diffraction pattern shows in each case the change in intensity and streaking of the diffraction spots due to beam damage [also see text]. Electron beam along $\langle 11\bar{2}0 \rangle$.

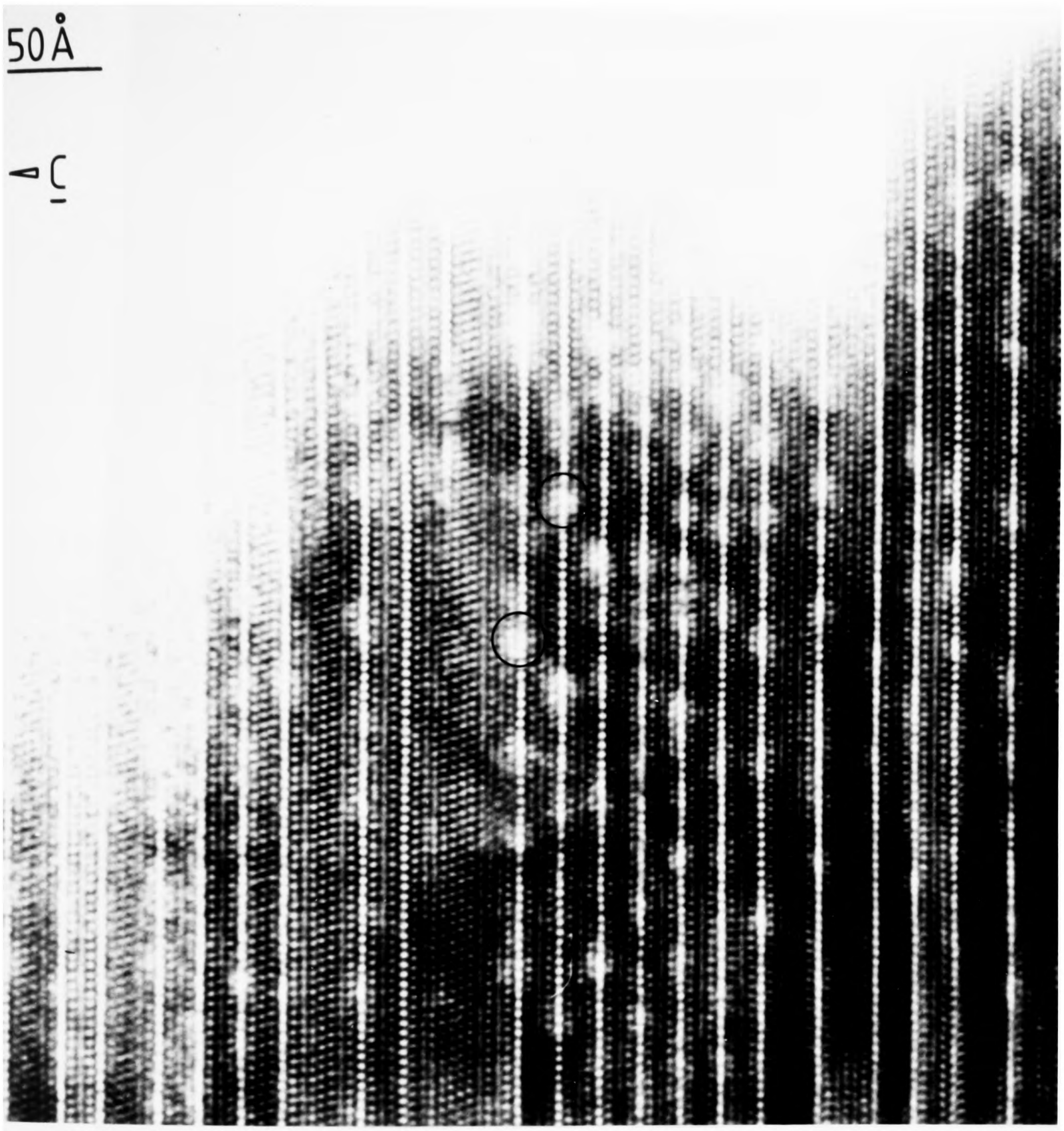

Fig. 4.10 Lattice image of ammonium/hydronium β''-alumina showing defects due to knock-on damage caused by protons in the conduction planes. Examples of defects are circled. Beam along $\langle 11\bar{2}0 \rangle$

alone.

This hypothesis is supported by the fact that damage is always centred on a conduction plane, and by the fact that similar damage has not been observed in any of the other specimens examined. In all other cases the cations in the conduction plane are too heavy to be displaced by an incident electron and so are not free to cause further knock-on damage.

Figure 4.11 illustrates the second damage mode. The images shown in 4.11b) and c) were taken at time intervals after 4.11a). A defect present on the left-hand side of the image in 4.11a) can be seen to grow as exposure to the beam continues, and a second similar defect has formed. The defects appear light in the image suggesting that they are of low density, and some structure is visible within them which is similar to that of the spinel blocks. It is suggested that these defects are ammonia bubbles which increase in size as radiation continues. The proposed defect growth mechanism is as follows:

1. A conduction plane starts to collapse from both edges of the crystal, with loss of ammonia, resulting in the formation of a closed length of conduction plane with broad spinel blocks at either end.

2. A few layers of atoms at the top and bottom surfaces of the crystal collapse so that a sealed "disc" of conduction plane is left.

3. Further electron irradiation causes reduction of NH_4^+ ions in the conduction plane to form ammonia gas molecules. The pressure exerted by the gas molecules on the walls of the "bubble" causes it to grow, deforming the surrounding

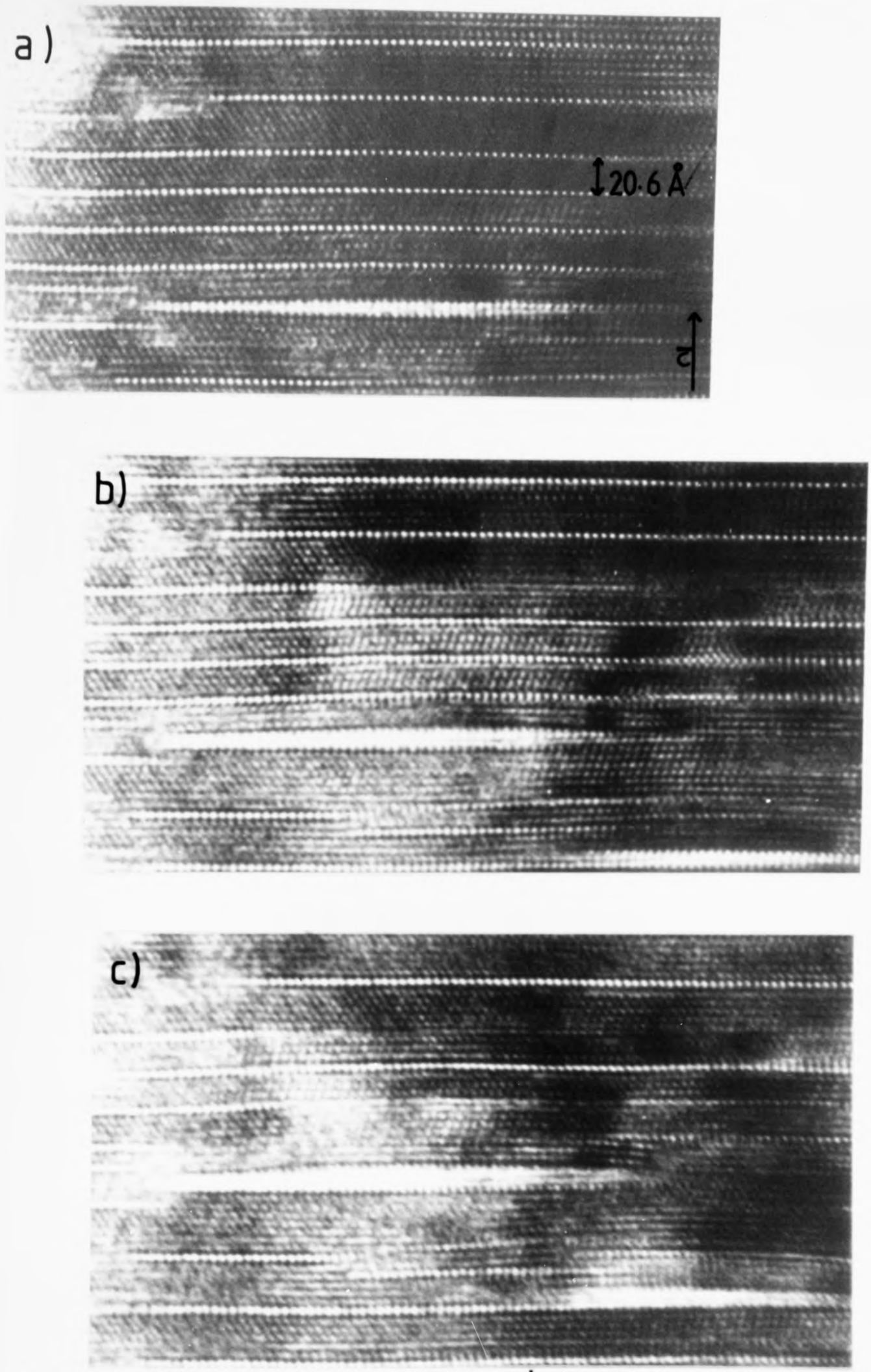

Fig. 4.11 Lattice image of NH_4^+/H_3O^+ β″-alumina showing formation and growth of NH_3 bubbles under the electron beam in the Jeol 200CX HREM. a), b) and c) were taken at time intervals of ~30 s. See text for growth mechanism. Electron beam along $\langle 11\bar{2}0 \rangle$.

a) viewed down [110] (in direction of beam)

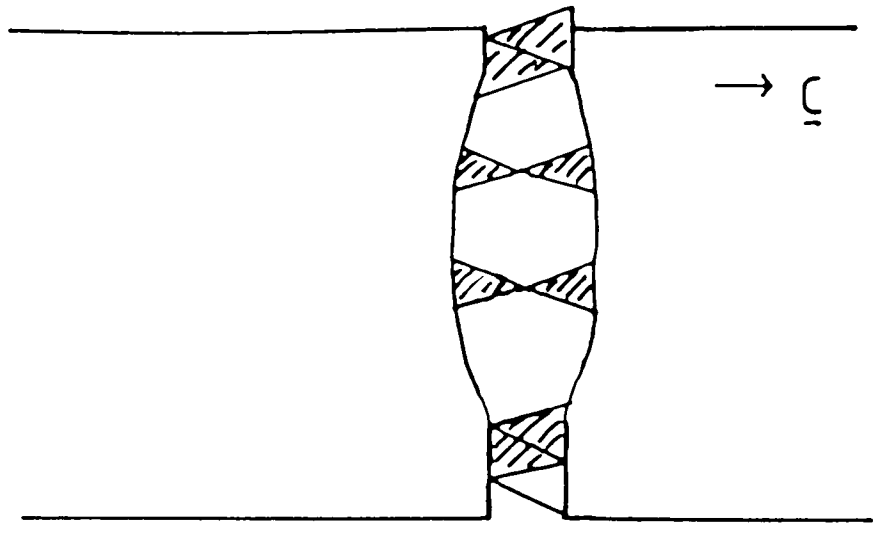

Conduction plane collapses at both faces of crystal

b) Beam ↓ view perpendicular to beam

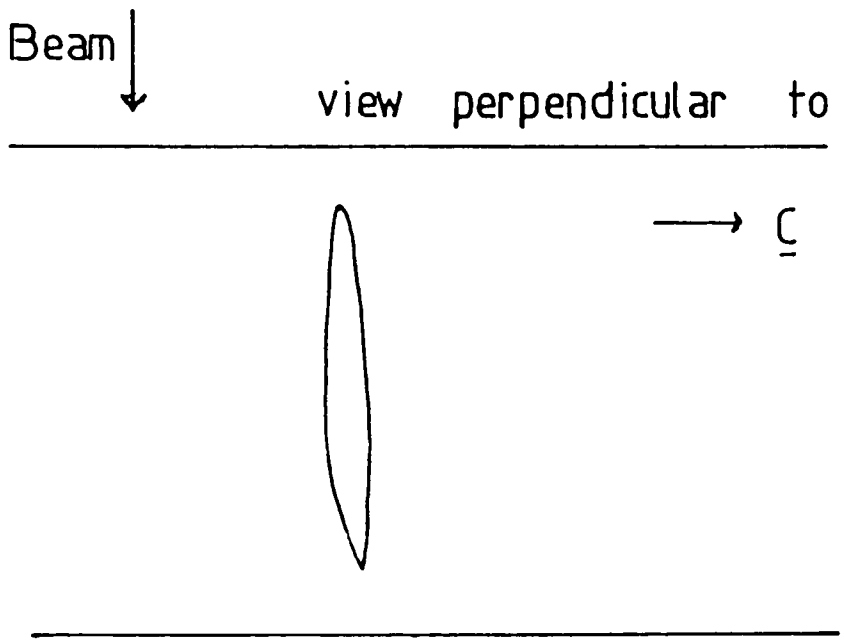

A few planes at top & bottom faces of crystal collapse to form a sealed "disc" of cation containing conduction plane

c) view down [110]

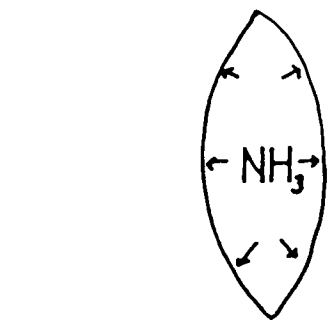

Defect grows due to pressure exerted by NH_3 gas produced in defect by electron beam

Fig. 4·12 Schematic representation of bubble growth mechanism in NH_4^+ / H_3O^+ β″-alumina.

lattice. This mechanism is illustrated in figure 4.12.

This mechanism is supported by the following evidence:

a) The defects only occur in conduction planes which are sealed off from the surface at both edges of the crystal.

b) The defects are of low density , but have some structure - this would be true of a gas bubble with a few layers of spinel above and below.

c) The defects contain material and are not cracks, as growth of empty cracks occurs to relieve stress in the lattice, whereas growth of these defects deforms the lattice further.

d) As mentioned in chapter 3, ammonia gas is known to be produced when the conduction planes collapse.

4.6 Electron beam hole drilling in ß and ß"-alumina.

Mochel et al. (1983) found that a focused, very high current density, electron beam (in a Vacuum Generators HB5 STEM) would rapidly drill small holes and cut fine lines through a number of metal ß and ß"-aluminas, on a 20Å scale. Once cut the ß-alumina was stable and the holes and lines did not degrade on exposure to air. Various other materials have also been tested, and recently some have been found (eg. CaF_2) in which hole drilling occurs.

The drilling rate depends on crystal thickness but does not appear to depend on crystal orientation. Further work is being done in this area and more quantitative data is being obtained.

4.7 Damage in the electron microprobe analyser (EMPA).

When bulk specimens of electrolyte tube material (mixed sodium ß and ß"-alumina) are examined in an EMPA, the EDX spectrum shows an aluminium peak, and a sodium peak which grows rapidly as irradiation continues, finally cutting out the aluminium signal. This is due to the fact that the beam draws sodium from the bulk material to the surface of the specimen, resulting in the build-up of a layer of sodium on the surface. The sodium layer grows very rapidly, making quantitative chemical analysis of the material impossible. If the specimens could be cooled to liquid nitrogen temperatures, the sodium ions would probably no longer be mobile, and a quantitative analysis could be made.

Growth of the sodium layer can be slowed down if a film of amorphous carbon is deposited on the specimen surface prior to analysis, although this does not completely solve the problem.

Chapter 5. Conduction mechanisms in the ß-aluminas.

5.1 Introduction

The conduction mechanisms in the ß-aluminas (of which sodium ß and ß" have been most extensively studied) are very complex and are not yet fully understood. Many workers have contributed to the research in this field, and some of their results are discussed in this chapter. The conduction plane structure and conduction mechanism are closely connected and are usually studied together.

Due to the layered structure in the ß-aluminas the conductivity is two-dimensional, with the ionic motion parallel to the $\overline{c}$-axis being virtually zero. Standard conductivity measurements are made with the electric field parallel to the $\overline{a}$ and $\overline{b}$ axes.

5.2 Basic conduction mechanisms.

Ion conduction in solids is due to the diffusion of ions under an applied voltage. For an ion to be able to move there must be sites available in the lattice between which it can move, and there must be sufficient energy to enable the ions to move. High ionic conductivity cannot occur for solids in which all sites are occupied, and is therefore associated with the presence of defects. For example, in ß"-alumina approximately 17% of the available mobile cation sites are vacant, compared with most solids in which less than 1 in 10^4 sites are vacant.

Ion movement in solids can occur by one of three main methods: the interstitial mechanism, the interstitialcy

mechanism or the vacancy mechanism.

i) The interstitial mechanism - An ion in an interstitial position can jump into a neighbouring interstitial site and thus move through the lattice.

ii) The interstitialcy mechanism - An ion in an interstitial site pushes a lattice site ion into an interstitial position and then replaces it. This is illustrated in figure 5.1. As can be seen, it requires the cooperative motion of two ions making up an interstitial pair, with the ion removed from the lattice site acting as an interstitial for a second lattice site ion.

iii) The vacancy mechanism - An ion can jump into a neighbouring vacant site. This type of diffusion can be regarded as the motion of vacancies through the solid.

As stated in chapter 3, ß-alumina generally contains a large number of sodium interstitials, amd so the interstitial or interstitialcy mechanism would be expected. Potential energy models such as that of Wang et al. (1975) have been used to obtain values for activation energies, vibrational frequencies and equilibrium positions for the mobile ions. These calculations show that the formation of interstitial pairs in ß-alumina reduces the barrier height for ion motion compared with that for single ions. For example the activation energy for a single ion is ~2eV compared with 0.14eV for an ion pair (in good agreement with the observed value). Thus the interstitialcy mechanism for ion transport is preferred in ß-alumina. In ß"-alumina however a large number of vacant sites are present, and thus the vacancy mechanism operates in sodium ß"-alumina.

The diffusion of ions through materials such as

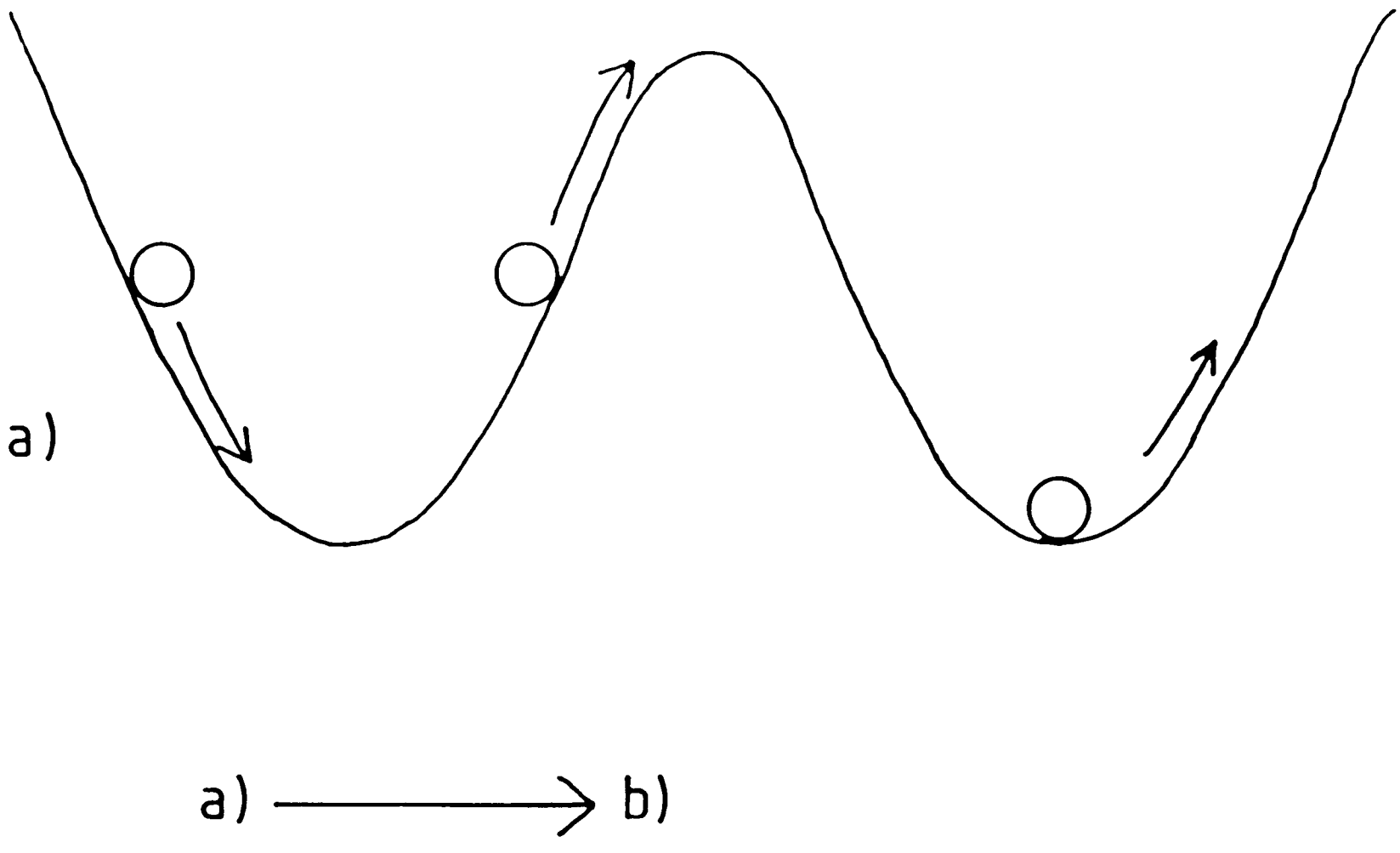

Fig,5·1 Schematic diagram illustrating the interstitialcy mechanism. One of the ions falls into a lattice site, while the other forms a new interstitial pair with an ion that moves out of a lattice site. This lowers the barrier for ionic motion.

ß-alumina is a thermally activated process and can be treated as the jumping of a particle between potential wells. The jump frequency, ν, of the ions is given by

1 $\quad \nu = \nu_0 \exp(-E/kT)$ $\quad$ E = activation energy

k = Boltzmann's constant

T = absolute temperature

where ν_0 is the frequency with which the particle approaches the barrier - the attempt frequency.

Using the random-walk concept, the diffusion coefficient is given by:

2 $\quad D = l^2 \nu_0 \exp(-E/kT)$ $\quad$ l = separation of potential wells

If l and ν_0 are constants then D has the Arrhenius form

3 $\quad D = D_0 \exp(-E/kT)$

Combining this with the simple Nernst-Einstein equation,

4 $\quad \sigma = \dfrac{nq^2 D}{kT}$ $\quad$ σ = conductivity

q = effective charge on each ion

n = number of ions per unit vol.

gives an expression for the temperature dependence of the ionic conductivity

5 $\quad \sigma T = \sigma_0 \exp(-E/kT)$ $\quad$ where: 6 $\quad \sigma_0 = nq^2 D_0/k$

Values of E and σ_0 are obtained experimentally from the slope and intercept, respectively, of a plot of $\log(\sigma T)$ versus 1/T. Thus high ionic conductivity requires a low activation energy (barrier height), E, and a high mobile ion density, n.

The above equations show how the conductivity is related to microscopic properties of the lattice. The activation energy depends on the ion type and arrangement around the mobile ions, and thus on the lattice structure. The jump distance, l, depends on the structure, and the

attempt frequency, ν_o, is related to a particular vibrational mode of the mobile ion; it is therefore important to have knowledge of the structure and dynamics of the material to understand the mechanics of fast ion transport in solids.

Equation 5 shows that the graph of $\log(\sigma T)$ versus $1/T$ will be linear if the activation energy and σ_o are constant. This is the case for ß-alumina and for most other ionic conductors, but for various ß"-aluminas (including sodium ß"), the graphs are curved at temperatures above about 200°C. This behaviour is associated with the presence of superlattice ordering of the mobile cations and vacancies in ß"-alumina due to the high number of these mobile defects. The formation of this superlattice - with unit cell of dimensions $\sqrt{3}a \times \sqrt{3}a$ - has been discussed in chapter 3. The curve in the $\log(\sigma T)$ graph is due to a rapid decrease in the superlattice correlation length and hence in the activation energy at a temperature of about 200°C. Both these variables approach constant values at high temperature.

The activation energy at low temperatures is larger than expected due to the ordering of the vacancies. The ordered vacant sites can be considered as special positions for which the binding energy is greater than at other sites. More energy is therefore required to move a vacancy from one of these sites than if no superlattice were present. As the temperature increases, thermal motion of the ions disorders the superlattice, removing the contribution to the activation energy arising from the vacancy ordering. At high temperatures the activation energy in sodium ß"-alumina is about 0.03eV (close to that calculated from potential energy models), and rises to 0.33eV near room temperature (Bates et

al., 1982).

5.3 Dependence of conductivity in sodium ß and ß"-alumina on composition and structure.

The ionic conductivity in ß-alumina has been measured using a.c. impedance techniques (Hooper, 1977) with blocking electrodes, as this overcomes electrode polarisation problems associated with d.c. methods. D.c. measurements also only give values for the total resistance, whereas a.c. measurements can distinguish between grain boundary and bulk contributions.

The ionic conductivity of single crystal sodium ß"-alumina is generally an order of magnitude greater than that of single crystal Na ß-alumina at 300°C. This can be understood in terms of the conduction plane structure: in ß-alumina the aBR sites cause a bottleneck for sodium ion motion where the spinel block oxygen above and below the conduction planes are only 2.0Å apart (diameter of a sodium ion = 1.94Å). In ß"-alumina the 120° rotation between adjacent spinel blocks results in the smallest gap coming at the mO site (~2.8Å).

The conductivity of single crystals of the ß-aluminas depends on the mobile ion concentration, n, and therefore on composition. The table in figure 5.2 gives values of σ_o and E for various compositions of Na ß and ß"-alumina. Undoped ß-alumina has the highest ionic conductivity for a sodium excess of ~25% above the stoichiometric value. The decrease in conductivity for increasing sodium content suggests that the additional charge-compensating oxygen interstitials act as local barriers to ion motion. ß-alumina doped with Mg

Phase	Stoichio-metry (x)	$\sigma_o(\Omega^{-1}cm^{-1}K^{-1})$	E(eV)	Reference
ß	0.00	-	0.62	a)
ß(i)	0.25	$2.2x10^3$	0.16	b)
ß	0.40	$4.8x10^3$	0.20	c)
ß(i)	1.00	-	0.30	d)
ß(Mg)	0.66	$8.0x10^3$	0.17	e)
ß"(Mg)	0.66	$1.2x10^5$	0.17(T>250°C)	e)
		$3.0x10^4$	0.22(T<250°C)	e)

(i) = compensated by oxygen interstitials.

(Mg)= compensated by Mg^{2+} ions in spinel block.

References a) Hayes et al., 1980 b) Whittingham and Huggins, 1971 c) Allen et al., 1978 d) Bourke et al., 1980 e) Baffier et al., 1981

Fig. 5.2 Conductivity of sodium ß and ß"-aluminas as a function of excess soda content.

MgO content (wt. %)	Soda content with maximum conductivity (wt. %)	Soda content for exact charge compensation (wt. %)	Ionic conductivity at 25°C $(\Omega cm)^{-1}$
1	6.8	6.85	$3.5x10^{-3}$
2	7.4	7.6	$8.0x10^{-3}$
4	9.5	9.1	$4.44x10^{-3}$

Reference Kennedy and Sammells, 1972

Fig. 5.3 Variation of maximum ionic conductivity with magnesia doping level in Na ß-alumina.

shows a higher ionic conductivity as the charge-compensating defects in this material lie in the spinel blocks and do not affect the motion of the mobile ions. Stoichiometric ß-alumina has no interstitials and so shows a very low ionic conductivity.

Composition will also affect the conductivity of sodium ß"-alumina, although in this case changes in superlattice correlation length have the greatest influence on the conductivity.

The conductivity of polycrystalline material is highly dependent on the grain size. As mentioned above, a.c. measurements can be used to ascertain the grain boundary contribution to the electrolyte resistance. Material with a fine grain structure will show a greater grain boundary resistance (R_{GB}) than a coarse grained material. Hooper (1977) found a bulk conductivity at 25°C of $0.78 \times 10^{-2} \Omega^{-1} cm^{-1}$ with an activation energy of 0.15eV. The overall (bulk plus grain boundary) conductivity at 25°C was found to be $0.12 \times 10^{-2} \Omega^{-1} cm^{-1}$ with an activation energy of 0.27eV. The grain boundary contribution falls rapidly as the temperature increases, becoming negligible above 250°C. The specimens analysed by Hooper contained both ß and ß" with grains typically 100µm x 20µm. A ratio of 2/3 - known as the tortuosity factor - for the absolute conductivities of single crystal and polycrystalline material with truly random grain orientation is observed. This factor is associated with the mismatch in conduction plane directions between grains. Hooper (1977) found a tortuosity factor of 1/3 - 1/5 suggesting that a preferred grain orientation is present in the material.

May and Hooper (1978) found the resistivity of the

polycrystalline material to be a function of the proportions of the ß and ß" phases present, the composition and the grain size.

Virkar et al. (1978) measured the resistivity of lithia stabilised polycrystalline ß"-alumina for fine and coarse-grained material. The resistivity for coarse-grained material (average grain size = 100µm) was 2.81Ωcm at 300°C with an activation energy of 0.16eV, whilst that for the fine-grained ß" was 4.80Ωcm at 300°C with E=0.19eV.

Kennedy and Sammells (1972) investigated the relationship between conductivity and soda content for various magnesium dopant levels. Their results showed that for a given magnesium content, the maximum ionic conductivity occured for a soda content at which the number of excess sodium ions were exactly balanced by the number of Mg^{2+} ions substituted in the Al(2) sites (see table in figure 5.3).

Ormrod and Kirk (1977) found that the conductivity of polycrystalline ß"-alumina depends on the dopant used, with lithia stabilised material having a higher conductivity than magnesia/lithia stabilised material.

5.4 The dependence of ionic conductivity on mobile cation species.

The substitution of various monovalent and divalent cations for sodium in ß-alumina was first studied by Yao and Kummer (1967). They also studied the diffusion rates of the different mobile species. Since the study of Yao and Kummer, many papers have been published concerning the conductivity of substituted ß and ß"-alumina. As can be seen from the table in figure 5.4, the conductivity of the monovalent ß and

(a) β-alumina

Cation	Cation radius (Å)	c-lattice parameter (Å)	Activation energy (eV)	Conductivity ($\Omega^{-1}cm^{-1}$)	ref
Li	0.60	22.642	0.24	3.7×10^{-3} (298K)	a)
Na	0.95	22.560	0.16	1.4×10^{-2} (298K)	f)
Ag	1.26	22.498	0.18	1.3×10^{-2} (298K)	c)
K	1.33	22.729	0.23	1.6×10^{-4} (298K)	c)
NH^{4+}	1.48	22.888	0.50	1.0×10^{-6} (298K)	b)

(b) β"-alumina

Li	0.60	-	0.30	5.0×10^{-3}	c)
Na	0.95	33.850	0.18	1.8×10^{-1} (298K)	g)
			0.10	2.2 (598K)	g)
Ag	1.26	33.420	0.19	4.0×10^{-3}	c)
K	1.33	34.030	0.18	1.4×10^{-1} (298K)	c)
NH^{4+}/	1.48	34.378	0.30	1.0×10^{-3} (298K)	b)
H_3O^+		-	-	1.0×10^{-2} (473K)	b)
Eu^{2+}	1.10	33.25	0.80	1.1×10^{-8} (293K)	e)
			0.60	4.7×10^{-2} (673K)	e)
Gd^{3+}	0.94	33.134	0.82	8.0×10^{-5} (673K)	d)
Eu^{3+}	0.95	33.50	-	1.0×10^{-12} (293K)	e)
			-	1.0×10^{-5} (673K)	e)

References a)Briant & Farrington, 1981 b)Thomas & Farrington, 1983 c)Bates et al., 1982 d)Dunn & Farrington, 1983 e)Ghosal et al., 1983 f)Whittingham & Huggins, 1971 g)Farrington & Briant, 1979.

Fig.5.4 Conductivity and activation energy for various ion-exchanged a) β-aluminas and b) β"-aluminas.

ß"-aluminas decreases with increasing cation size, with the exception of the lithium material. As the cation size increases, the activation energy increases as it becomes more difficult for the ions to move through the conduction plane. In ß-alumina the bottleneck caused by the oxygens above and below the aBR sites makes the motion of large ions especially difficult. The conductivity of the lithium material is lower than might be expected as the lithium ions have a high charge to radius ratio and are therefore more polarising than the other alkali ions. They relax away from the conduction plane towards the oxygen ions above and below the BR sites and bond covalently with these oxygen ions, thus increasing the activation energy for conduction. This was confirmed by the study of Tofield and Farrington (1979) who found lithium ions displaced from the centre of the conduction plane.

The ß"-aluminas all show a temperature dependent activation energy, probably due to the formation of a superlattice as described in section 5.2 above, which becomes disordered at high temperatures.

The divalent and trivalent ß"-aluminas show much lower conductivities than the monovalent materials. This is probably enhanced by the very high degree of superlattice ordering which occurs in these materials. It also seems likely that ion-exchange processes will damage the material (usually with the loss of conduction planes) which again will lower the conductivity.

Briant and Farrington (1981) studied the conductivity of mixed Li/Na ß-alumina compared with that of the pure Li material. They observed that the mixed material had a higher conductivity than the lithium material and postulated that

this was due to a co-ionic effect, similar to that postulated by Hendrickson and Bray (1972) for mixed alkali glasses. The conductivity of mixed ß-alumina does not vary linearly, but was found to pass through a minimum at a lithium content of ~75%, with the activation energy passing through a maximum for the same lithium content.

The theory of Hendrickson and Bray explains the mass dependence of the co-ionic effect and accounts for the non-linearity observed: they consider each ion as an oscillating dipole with a resonant frequency characteristic of a particular ion species. Different alkali ions will then have different frequencies and so unlike neighbouring ions will have a negative interaction energy (zero for like neighbours). The potential wells of a mixed ion pair will thus be deeper and the activiation energy for ion motion will be higher.

In non-stoichiometric ß-alumina many cells will contain interstitial ion pairs, for which the activation energy for motion is much lower than that for single ion motion (see section 5.2 above). In Li/Na ß-alumina many such pairs will consist of unlike pairs, with a higher activation energy, with the proportion of unlike pairs changing as the relative lithium and sodium proportions change. A maximum in activation energy will thus occur for the composition at which the maximum number of interstitial pairs are formed from unlike ions.

Chapter 6. Macroscopic damage modes in sodium ß/ß"-alumina electrolyte tubes.

6.1 Introduction

The most common cause of failure in the sodium/sulphur cell is breakdown of the ß-alumina electrolyte. The failure modes can be divided into electrical breakdown, thermal breakdown and mechanical shock, although in reality these are closely related, with the end result being mechanical collapse of the material. Electrical breakdown can result from internal short-circuiting due to the presence of metallic sodium "paths" through the electrolyte tube; usually accompanied by a change in colour of the tube from white to grey, brown or blue. Two mechanisms have been proposed to account for this damage mode: one involving the formation of sodium-filled cracks (dendrites), initiating at imperfections in the face of the electrolyte tube in contact with the sodium electrode, which propagate by a Poiseuille pressure mechanism, and the second involving the internal deposition of sodium colloids of ~1µm diameter due to the internal reduction of the sodium ions. These two models will be discussed later in the chapter. Electrical breakdown can also arise due to an excessive applied voltage, and this damage mode will be discussed in section 6.5 in this chapter.

The models proposed for the various damage modes are discussed more fully below.

6.2 The formation of sodium-filled cracks (Poiseuille

pressure mechanism).

As mentioned above, the sodium-filled cracks (dendrites) are initiated at the exit (sodium) face of the electrolyte tube, and are associated with the charging rather than the discharging of a cell.

Two mechanisms have been proposed to account for crack propagation, both of which depend on the cracks concentrating the current, thus causing a Poiseuille pressure in the crack due to sodium flow.

The critical fracture model (Armstrong et al., 1974) proposes that crack extension can occur when the stress intensity at the crack tip reaches a critical value, K_{Ic}. This critical value can be reached if sodium ions passing through the electrolyte tube are focused towards the sodium-filled crack. This can occur as sodium ions travelling to the sodium/electrolyte interface via a sodium filled crack encounter a lower resistance than if they travel through the electrolyte bulk.

A continuous flow of sodium ions into the crack will be set up, at a rate dependent on the current density and crack dimensions resulting in the increase of pressure within the crack. As the pressure increases, so the stress intensity at the crack tip increases. If K_{Ic} is reached, the crack will extend by a small amount, the pressure will drop and the process will start again. Thus the crack extends gradually through the electrolyte.

The second model (Richman and Tennenhouse, 1975) is a stress corrosion model in which crack propagation can occur at stress intensities below the critical value. The model proposes the stress-induced dissolution of the ceramic

electrolyte in liquid sodium at the crack tip. This has not however been observed in ß-alumina, suggesting that the critical stress mechanism is more directly applicable.

A study by Virkar (Virkar et al., 1980) has provided experimental confirmation of the current focussing concept, and has also shown that such cracks are tip-fed. Worrel and Redfern (1978) have carried out acoustic emission studies on ß-alumina electrolytes, and have confirmed that microcracking can lead to electrolyte failure.

Shetty et al. (1977) have evaluated the crack shape under the action of the Poiseuille pressure and have derived an expression for i_{cr}, the critical current density where

1 $i_{cr} = A/\eta l$ A = constant dependant on the elastic properties of the electrolyte

η = viscosity of sodium

l = crack length

A study by Virkar and Viswanathan (1979) has shown that the value of i_{cr} is lower below the melting point of sodium than above it, confirming the validity of the above expression

A more recent study by Brennan (1980) takes into account various factors previously ignored:

a) The sodium under pressure in the crack develops a back-emf which will reduce the current flowing into the crack. The increased pressure is due to an excess of sodium ions in the crack above that in the bulk. This excess charge will make the entry of further sodium into the crack more difficult - resulting in an effective back-emf.

b) Changes in the electrode/electrolyte surface resistance with time can result in previously sub-critical cracks

becoming critical.

A semiquantitative model has been developed by Brennan for the effects of current focusing. Brennan's study suggests that cracking does not occur slowly throughout the life of the electrolyte tube, but rather that an incubation period occurs initially during which various surface flaws can become critical, followed by rapid crack propagation. Brennan therefore suggests that the two main factors contributing to electrolyte failure are an increase in interface charge transfer resistance and high local current densities at the surface. Regions of high local current density can arise at the boundaries of non-wetted areas of the electrolyte surface by the sodium electrode, with a very high contact resistance in the non-wetted area. Various studies (Virkar et al., 1980; Singh and Lewis, 1983) have been made dealing with this problem.

Virkar and Viswanathan (1983) have developed a three-dimensional semiquantitative model for crack formation due to the above factors, which includes the effect of microstructure, and this appears to agree fairly well with experimental observations.

Degradation by rapid crack propagation has been termed Mode I failure (De Jonghe et al., 1981).

6.3 Chemical colouration of the electrolyte tube leading to internal sodium deposition.

De Jonghe et al. (1981) observed a second type of degradation - termed Mode II degradation - involving the propagation of a dark layer through the electrolyte starting at the sodium/electrolyte interface. Mode II damage was

observed only in cycled cells and is therefore associated with charge transfer. De Jonghe observed this damage mode in cells with total charge transfer ranging from 23 to 706Ahcm^{-2}. This darkening was found to be due to the internal deposition of metallic sodium. Optical observation at high magnification by De Jonghe (in the above study) of the darkened layer revealed the presence of subsurface microcracks filled with metallic sodium, and proposed that Mode II degradation involves electron conduction from the sodium electrode/ß-alumina interface, followed by Na^{+}/e^{-} recombination in the bulk of the electrolyte. In order for internal sodium deposition to be possible, the electronic conductivity of the material must be increased over its intrinsic value; recombination can only lead to microfracture if the process is driven by the applied voltage or current during charging - allowing a large enough sodium deposit to form under pressure to cause cracking. This will only occur if the electrolyte is not in equilibrium with the electrodes (ie. a gradient in electron conductivity is present).

De Jonghe suggests that the rapid colouration (as opposed to Mode II damage) observed by many other workers (for example Kirk and Ormrod, 1977) could be associated with a mechanism for internal sodium deposition. This darkening is associated with prolonged static contact with molten sodium metal, and it is not a function of cell charge/discharge. Various colours have been observed - brown, grey or black. Bourke (Bourke et al., 1980) noted that the colouration was accompanied by an increase in resistivity, although in other cases (Armstrong et al., 1982) no decrease in cell performance was observed.

Transmission electron microscopy of discoloured ß-alumina has failed to reveal any defect attributable to the chemical colouration (De Jonghe et al., 1981) suggesting that the colour change is due to point defects. The same study by De Jonghe noted that the colouration is associated with the loss of oxygen from the electrolyte.

A further study (De Jonghe and Beuchele, 1982) showed that chemically darkened material (as opposed to material showing Mode II damage) could be bleached again if reheated in air or oxygen suggesting that the bleaching process involves reoxidation of the ß-alumina. We have also observed this phenomenon. Bleached material examined in the HREM appeared damaged with many lost conduction planes. De Jonghe suggests that the chemical colouration is due to the injection of oxygen vacancies, $V_O^{\cdot\cdot}$, compensated by electrons. The colouration appears to proceed mainly through the spinel blocks, in single crystals, and along grain boundaries in polycrystalline material, and the bleaching proceeds through the conduction planes. The colouration reaction is as follows:

$$2Na + O \rightarrow Na_2O + V_O^{\cdot\cdot} + 2e^-$$

electrode electrolyte at electrolyte in electrolyte

This model has been developed further by Nicholson (1983) who suggests that more sodium ions are focused into feeder grains near to flaws at the sodium/electrolyte interface than can be transmitted by these grains. This supersaturation leads to local oxidation of the O(5) ions to give sodium atoms and colour centres (electrons trapped at oxygen vacancies from which the O(5) ions have been lost).

The sodium atoms can coalesce into colloids, possibly resulting in microcracking.

The colouration reaction proposed is:

$$Na^{*} + O(5) \rightarrow Na + O + V'_{Na} + (e);$$

Na vacancy trapped e- on O(5) site

In high vacuum the oxygen can be lost from the conduction plane, leading to collapse of the structure as described in chapter 4.

Degradation of the sulphur face of the electrolyte has also been observed (De Jonghe et al., 1981) due to the "imprinting" effect of the graphite current collector.

In this study we examined some cycled and uncycled specimens for macroscopic damage, (see next chapter for a fuller discussion). All the cycled specimens showed some darkening at the sodium/electrolyte interface, with the layer in the most heavily cycled specimen (635 charge transfer cycles) being approximately 150μm thick. The material appeared dark grey in this region. In this same specimen some darkening of the sulphur/electrolyte interface was observed with the ß-alumina appearing pale grey to a depth of approximately 70μm (see figure 6.1). No observations were made on uncycled specimens which had been held in contact with molten sodium metal.

The scale of sodium colloids expected (approximately 0.1μm thick) was too small to be resolved in the acoustic or optical microscope, and so it was not possible to ascertain whether the darkening was due to Mode II damage or to the initial chemical colouration. No cracks of the type associated with Mode I damage were observed in any of the

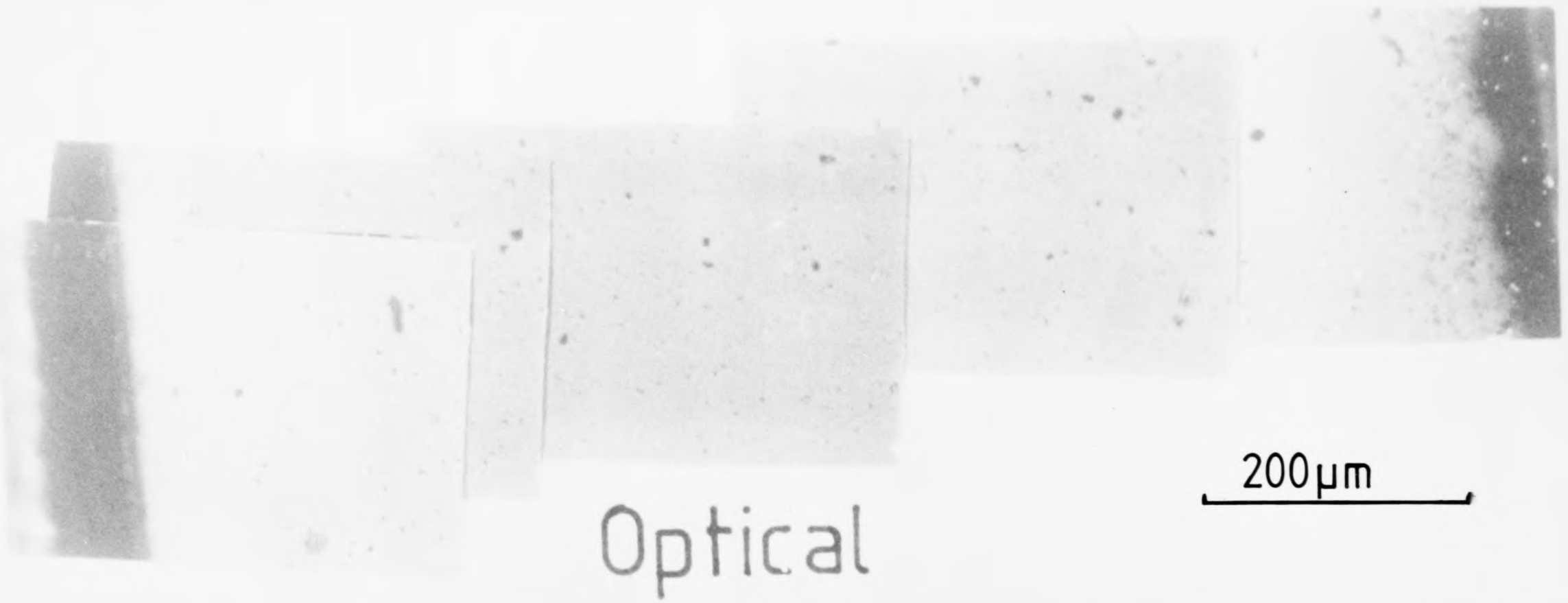

Fig. 6.1 Optical microscope image of cross-section through sodium β-alumina electrolyte tube showing dark layers at both sodium and sulphur electrode/electrolyte interfaces due to cell cycling. "Na" denotes surface of electrolyte in contact with the sodium electrode, and 'S' denotes that in contact with the sulphur electrode.

cycled specimens examined. It should be noted that none of the specimens had been cycled to failure.

HREM of cycled + uncycled specimens allowed some grain boundaries to be imaged. No obvious intergranular material was observed (see figure 6.2) although obviously the specimen preparation technique will break up the material into individual grains preventing analysis of grain boundaries. The specimens imaged in both figures 6.2a) and 6.2b) were prepared from uncycled magnesium doped electrolyte tube material.

6.4 The effect of microstructure and impurities on electrolyte degradation.

The electrolyte degradation rate has been found to depend heavily on microstructure (De Jonghe et al., 1982). This study showed that Mode I degradation was initiated preferentially at (00.1) grain boundary facets of large grains. These grain facets were found to be mechanically weak and to favour current flow along the boundary. Large grains were found to be weaker than small grains and therefore more prone to degradation.

Colouration was also observed to proceed preferentially along grain boundaries, resulting in increased grain boundary electronic conduction. As mentioned previously (section 6.3) Bourke et al.(1980) also noticed an increase in ionic resistivity associated with colouration. This will lead to an electron transport number gradient, suggesting that Mode II degradation will also involve grain boundaries.

The composition of the ß-alumina electrolyte will

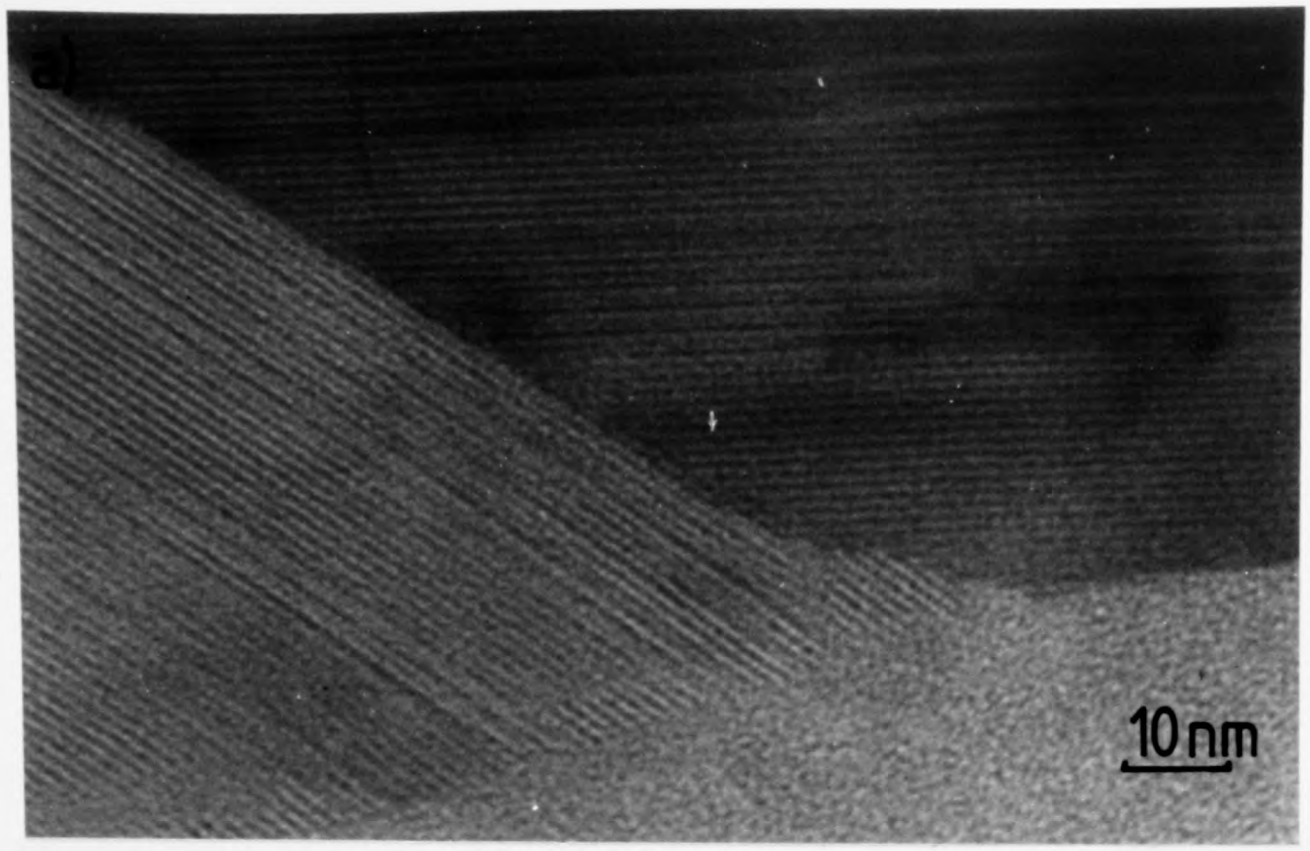

Fig. 6.2 a) Lattice image of grain boundary between two grains of sodium ß''-alumina. Both grains are oriented such that the electron beam is close to $\langle 11\bar{2}0 \rangle$.

Fig. 6.2 b) Lattice image showing boundaries between grains of sodium ß and ß''-alumina. The grain of Na ß-alumina marked 'A' is aligned such that the electron beam is close to $\langle 11\bar{2}0 \rangle$.

also affect the degradation rate (Tennenhouse et al., 1975) - a high soda content will result in greater ion focusing at flaws leading to degradation. Increased lithia content can lead to resistance rise and degradation (Brennan. 1980).

May and Tan (1979) noted that degradation could occur as the result of ion exchange with impurities in the electrodes leading to increased resistivity (see chapter 5).

Some improvement to electrolyte life can be achieved by the addition of partially stabilised zirconia (finely dispersed metastable tetragonal ZrO_2 in a matrix of cubic ZrO_2) to lithia stabilised electrolyte material, without greatly affecting the ionic conductivity (Viswanathan et al., 1983). The toughening effect is due to the fact that the metastable tetragonal zirconia particles convert to the monoclinic form in the near stress field of a propagating crack thus absorbing much of the energy needed for crack propagation and preventing the crack from advancing.

6.5 Voltage breakdown

It has been shown by Hooper (1980) that for a particular temperature a threshold voltage exists, above which the electronic insulating properties of the electrolyte are lost and gross physical damage occurs. The study by Hooper examined electrolytes with blocking electrodes. When non-blocking electrodes were used, damage did not occur. The voltage limit is of the order of a fewx10 volts. A model has been suggested, in which the applied voltage causes a layer of electrolyte close to the positive (sulphur) electrode to become depleted of sodium ions; the resistivity of this layer is increased. The majority of the applied

voltage will be dropped across the resistive layer leading to dielectric breakdown as the electrolyte decomposes.

Although the charging voltage for a single cell may be 2-3V, a battery of several cells will require a higher total over-voltage (several tens of volts). If one cell in the battery should become fully charged before the others, a high voltage will be dropped across this one cell leading to voltage breakdown.

6.6 Mechanical breakdown

Macrocracking of the electrolyte tube can be due to stresses grown in during manufacture, to stresses due to cell assembly, or to an externally applied shock. A crack through the electrolyte tube will allow liquid sodium and sulphur to mix, resulting in an increase in temperature. This can lead to further cracking and ultimately to electrolyte disintegration. Macrocracking will tend to occur preferentially at weak points on the tube such as gross defects, or in the region of the glass seal.

As tubes are cycled, the mechanical strength can often decrease, and it is therefore important to subject cycled cells, as well as new cells, to mechanical tests.

6.7 Thermal breakdown

There are three effects that can lead to thermal breakdown (Dell and Moseley, 1981/82).

i) A mismatch in the thermal expansion coefficients of the ß-alumina tube and the glass seal - this can lead to cracking in the region of the seal if the cell is heated or cooled too rapidly.

ii) Thermal shock due to a sudden rise in temperature leading to electrolyte disintegration. This can be triggered by primary mechanical breakdown.

iii) The change in volume of the electrodes on heating and cooling due to phase changes of the sodium and sulphur. Slow heating and cooling are required through the temperature range over which melting and solidification occur.

6.8 Water uptake

When Na ß-alumina is exposed to air it tends to pick up moisture, resulting in an increase in resistivity. This effect is influenced by a number of factors. A coarse grain structure and rough tube surface will aid water uptake, as can the presence of a high lithia content. Heavens (1982) noted the formation of a thin (approximately 5µm) hydrated layer at the surface of tubes exposed to water. The examination in this study of electrolyte specimens which had been exposed to moisture in the air for a number of months revealed a change in surface appearance - possibly due to the formation of such a layer. This is discussed more fully in the next chapter.

Harbach (1983) studied the relative effect of water uptake on fully and partially stabilised ß"-aluminas, and noted that fully stabilised ternary ß"-alumina was less prone to water damage than partially stabilised material.

These results suggest that tubes which are produced commercially should be stored in a dry atmosphere to prevent deterioration in mechanical strength with time.

6.9 Conclusion

The following conclusion outlines a few conditions which could increase the lifetime of an electrolyte tube. This will be divided into manufacturing conditions, storage conditions (ie. before cycling), and cycling conditions.

a) Conditions for manufacture

The tube material should be composed of small grains with a composition such that maximum conductivity is obtained whilst maintaining a low degradation rate (25 - 30% excess soda above the stoichiometric weight percent for Na ß"-alumina). A high proportion of the ß" phase is necessary to give a high conductivity, and if possible this should be fully stabilised to lower the degradation due to water uptake. The level of impurities not associated with charge compensation (eg. Ca and Fe) should be kept as low as possible. The electrode materials (molten sodium and sulphur) should also be kept free of impurities to prevent ion-exchange during cycling.

b) Conditions for storage

The ß-alumina tubes should be stored in a dry atmosphere to prevent surface degradation by water uptake, and should not come into contact with molten sodium until they are required for use, as this may in some cases lead to chemical colouration and an associated rise in resistivity. This suggests that cells should not be assembled until they are ready to be sold/used. Mechanical testing of cells is important at various stages during storage.

c) Conditions for use

The cells should not be subjected to rapid heating or

cooling during use. The charging current should be kept below the critical value, and care must be taken that the charging voltage does not exceed the threshold value above which voltage breakdown will occur.

The next chapter discusses the results obtained from an examination of bulk specimens of Na ß-alumina electrolyte tubes - both cycled and uncycled. The macroscopic defects observed using acoustic, optical and scanning electron microscopy are shown and some chemical analysis results are also given.

Chapter 7 Examination of macroscopic defects in sodium ß/ß"-alumina using acoustic microscopy and chemical analysis.

7.1 Scanning acoustic microscope (SAM) theory.

The reflection SAM consists of a hemispherical sapphire lens to which a transducer is fixed. The lens is connected to the specimen by way of a coupling fluid eg. water. The transducer both sends acoustic waves to the specimen and picks up the returning waves (see figure 7.1); it then transforms the acoustic signal to a voltage. The lens is scanned in a raster and the voltage at each point is recorded in a frame store. An image of a region can then be displayed on a monitor, with the sample signal at each point modulating the brightness. As the specimen to lens distance (z) alters so the signal, V, changes. Thus at focus on an isotropic material, contrast is obtained due to surface roughness.

The variation of V with z (the V(z) curve) has a characteristic periodicity dependent on the material being examined (see figure 7.2a). The material dependence of the V(z) curve when the lens is defocused is due to the interference of beams A and B (see figure 7.1). Beam B is incident on the specimen at such an angle as to excite surface Rayleigh waves which travel across the specimen surface with a velocity dependent on the elastic properties of the material examined. The interference between beams A and B for a given z will thus be different for different materials or for different orientations of an anisotropic material.

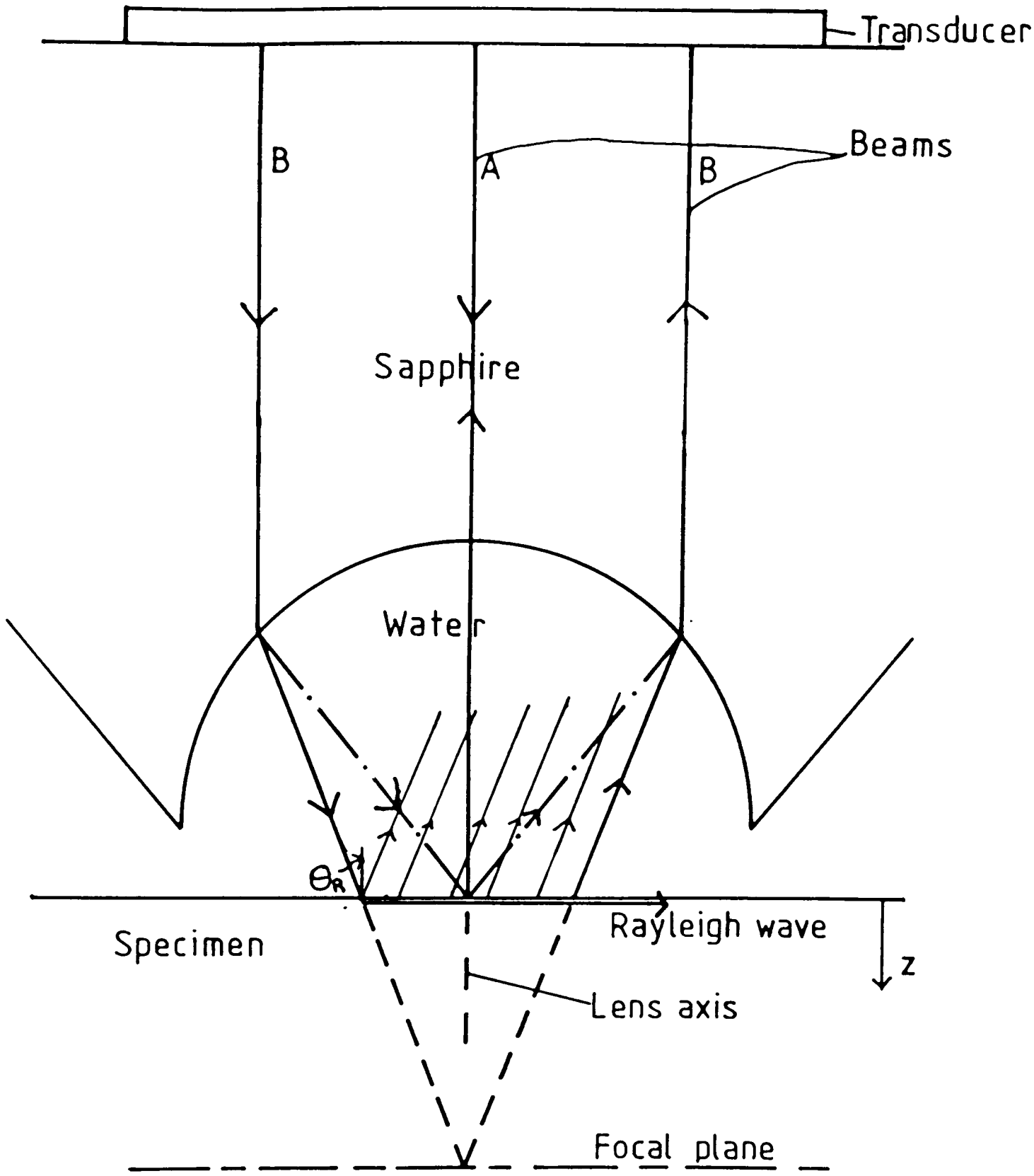

Fig. 7.1 Schematic diagram of acoustic lens in reflection scanning acoustic microscope (SAM).

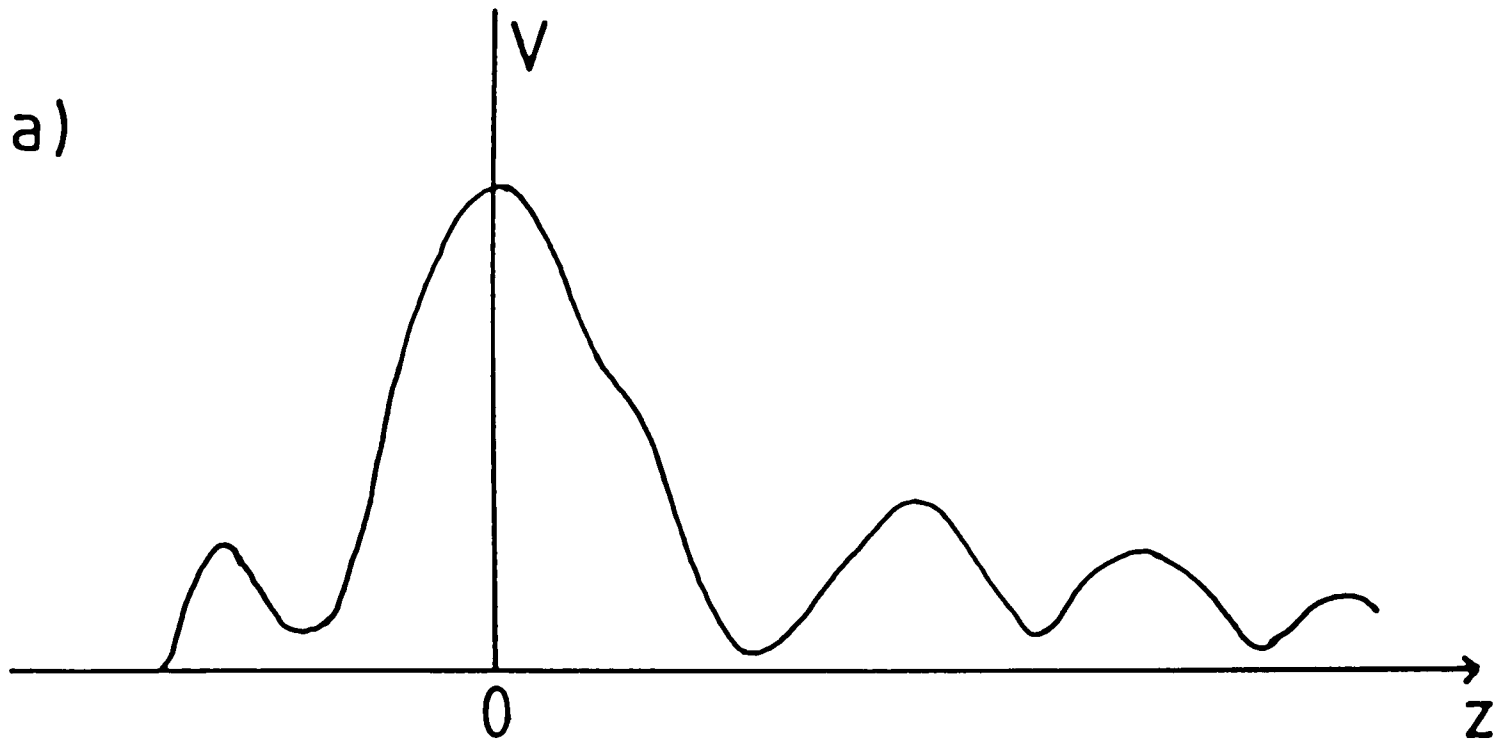

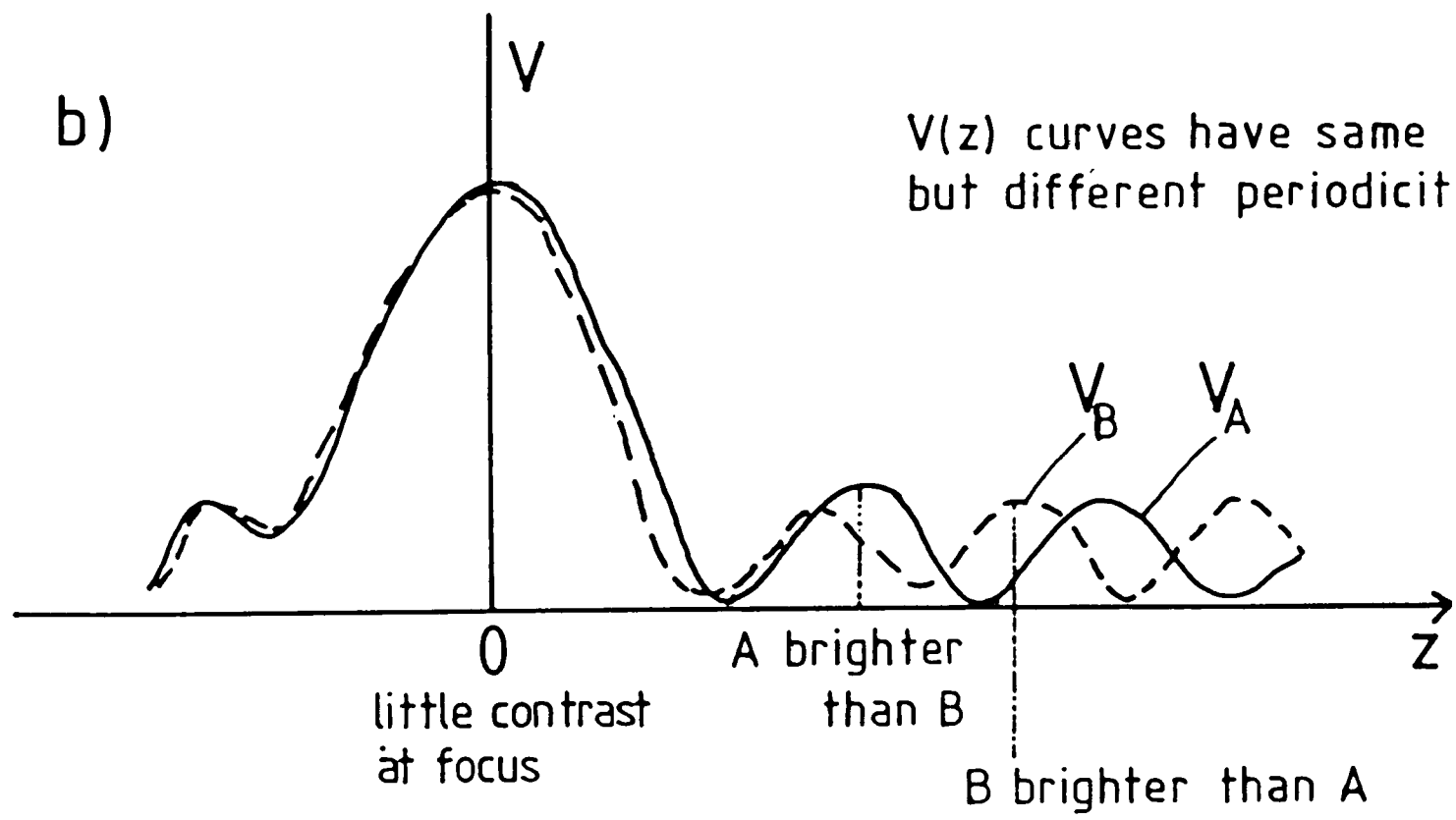

V(z) curves have same focus
but different periodicities

Fig. 7.2 V(z) curves a) for a single material, and
b) for two different materials A and B.

As previously mentioned, the image contrast depends on V (large V = bright image) and so two materials with different values of V for a given value of z will show different contrast at that defocus (see figure 7.2b).

It should be noted that the contrast due to surface roughness is much stronger than that due to differences in elastic properties so that images are best obtained from polished, flat surfaces.

Measurement of the periodicity of the V(z) curve for a particular specimen can give an idea of the material from which the specimen is made:

$$1\ \Delta z = \frac{v_L}{2f(1-\cos\theta_R)}$$

Δz = periodicity of the V(z) curve

$\sin\theta_R = v_L/v_R$

v_L = velocity of sound in coupling liquid ($v_{water} = 1550 ms^{-1}$)

v_R = velocity of Rayleigh waves on solid surface

The SAM used for this work operates at 730MHz giving a lateral surface resolution of 1-2μm and sampling to a depth of ~4μm.

From examination of the V(z) curves it can be seen that contrast between materials with different elastic properties in a sample is enhanced as one defocuses the lens towards the specimen.

The SAM can provide information about grain structure, cracks and intergrowths or impurities on the few μm scale.

The defocused SAM can also provide some information about structure under the surface. The depth to which

information can be obtained depends on the ratio of v_L and v_R:

$$2 \qquad \frac{\text{depth of image}}{\text{defocus}} = \frac{v_L}{v_R} \approx \frac{1}{4} \qquad \text{for most materials}$$

Ie. a defocus of -16μm results in structures up to 4μm depth influencing the image.

7.2 Practical acoustic microscopy

The reflection SAM is set up so that the acoustic lens can be interchanged with an optical objective lens attached to an optical microscope. Thus both optical and acoustic images can be recorded from the same region, for comparison.

The images are recorded on 35mm film from the flat-face TV screen onto which they are projected from the frame store. The scanned area is ~500μm x 500μm at a magnification of x100. In some cases more than one stored image at different defoci could be added together to increase the contrast, although this may produce artefacts in the image.

As mentioned in section 7.1 the specimens must be polished, with a surface roughness less than the resolution of the microscope (dependent on the interference between the Rayleigh wave and the wave normal to the surface). A surface roughness of 1μm or less is adequate.

The specimens must be at least 50μm thick so that effects due to reflection at the bottom surface of the specimen can be ignored.

The samples of ß-alumina examined were cut from cycled and uncycled electrolyte tubes of wall thickness

~1.5mm. Specimens 4x2x2mm were cut, both perpendicular and parallel to the length of the tube. The sections were set in perspex blocks with one of the 4x2mm faces uppermost, and these faces were polished using 1μm Dialap paste.

For each specimen a series of bright field and dark field optical plus focused and defocused acoustic images were taken so that an image of an entire cross-section (sodium electrode interface to sulphur electrode interface) could be compiled.

7.3 Acoustic microscope images from cycled and uncycled electrolyte tubes.

The reason for examining the sodium ß-alumina electrolyte tube samples in the SAM was to gain information about porosity, grain structure and defects of the order of 1 - 100μm, both at the surface and just below. The optical microscope will yield information about porosity but the contrast in the images tends to be low unless the specimen is etched, for example in hot phosphoric acid (McNamee and Ashurst, 1982). A scanning electron microscope (SEM) could provide information about surface defects, but, as mentioned in chapter 4, the electron beam draws sodium to the surface of a specimen and thus causes permanent damage as well as obscuring the specimen surface.

Acoustic images were taken at focus and with the microscope underfocused by a few microns. Optical images were also taken. Figure 7.3a) and b) show optical and SAM images from a cycled and an uncycled electrolyte tube. The broad dark and light bands at the edges of the acoustic images are due to the sensitivity of the SAM to curvature of

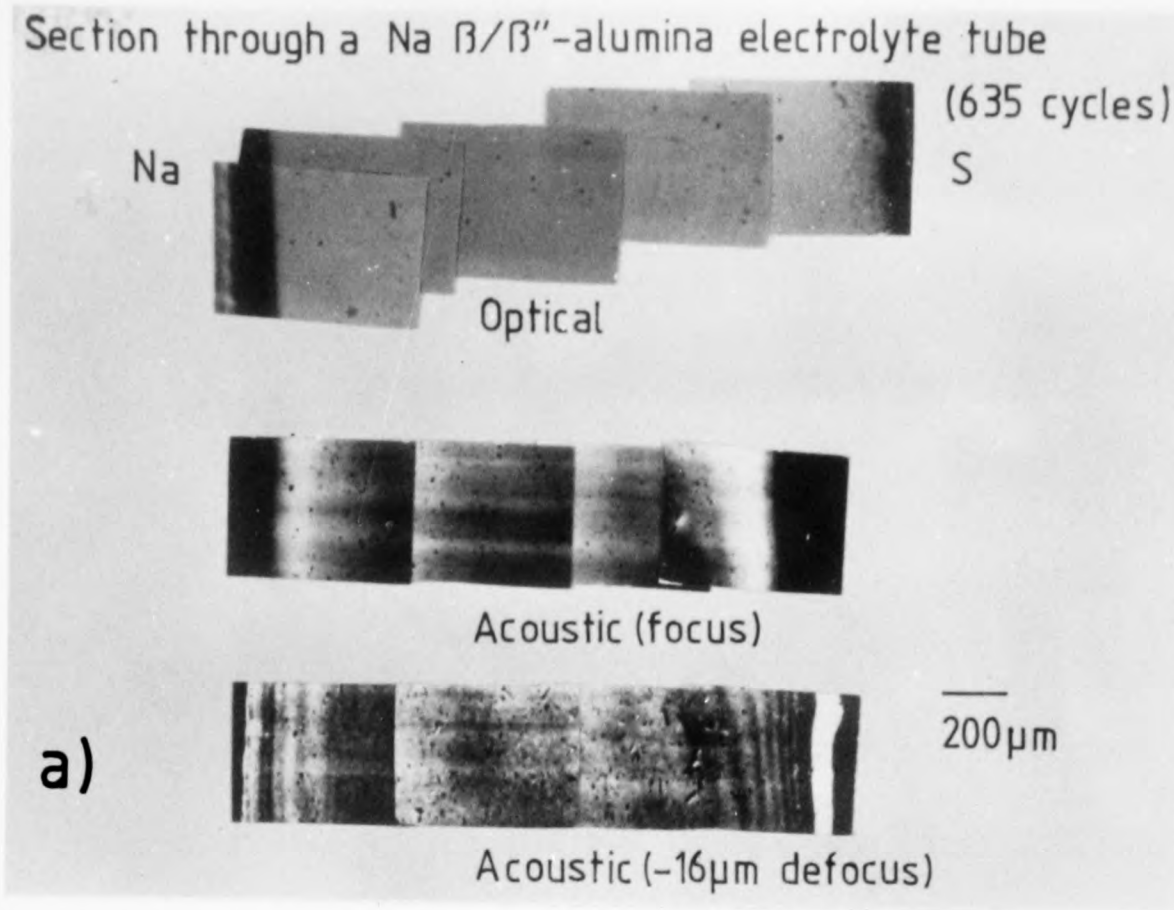

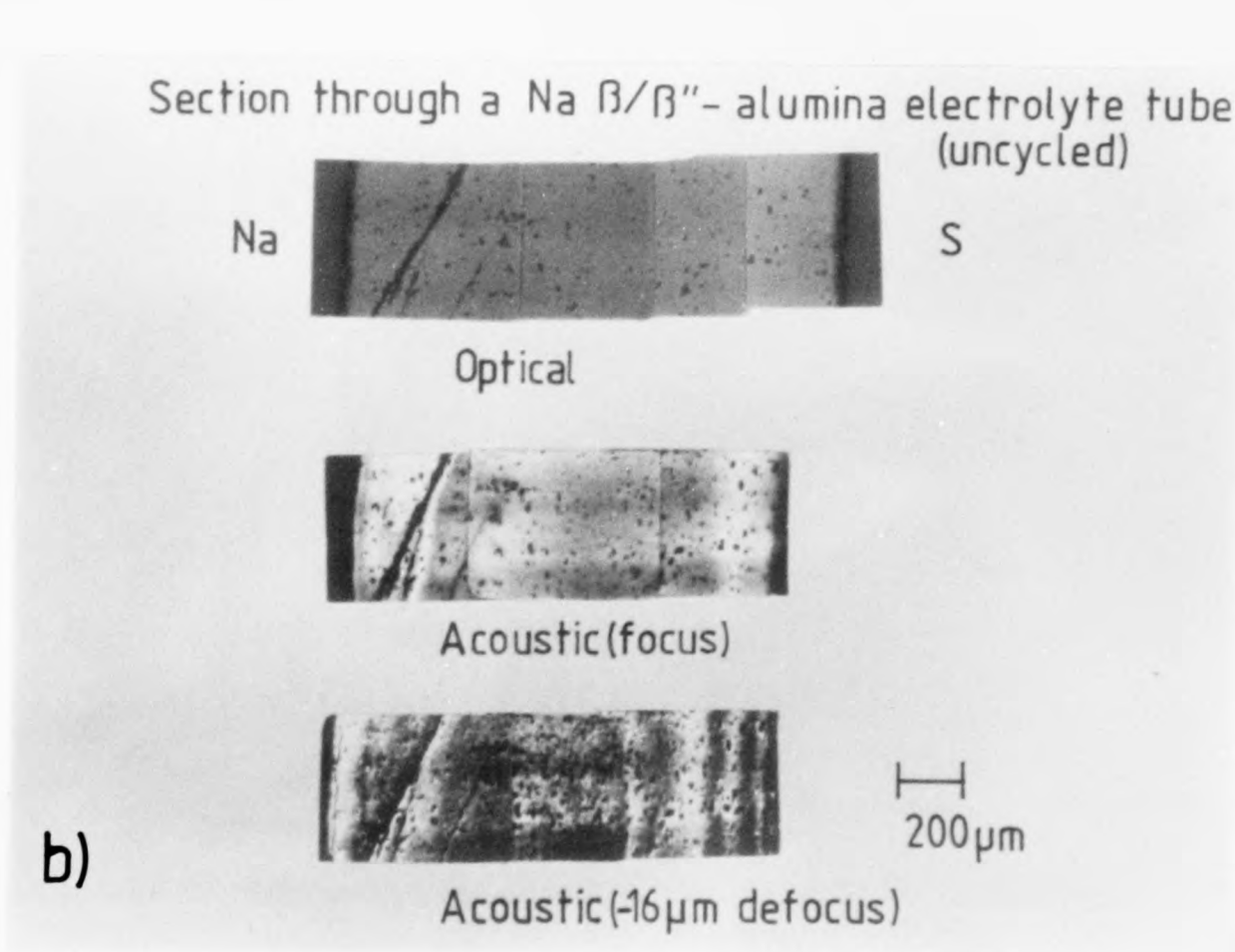

Fig. 7.3 Optical and scanning acoustic images from a) an electrolyte tube subjected to 635 charge/discharge cycles, and b) an uncycled electrolyte tube.

the specimen surface away from the lens. The small scale dappling indicates contrast due to grains in different orientations, with the grain boundaries visible in some regions as narrow dark lines surrounding paler regions. The black spots visible in the SAM and optical images correspond to pits and pores in the surface of the specimen (ie. throughout the bulk of the electrolyte tube). The dark rectangles visible only in the defocused acoustic images are features with elastic properties different from those of the small grain Na ß-alumina matrix. The fact that they are not visible in the acoustic image at focus confirms that the contrast of these features is due to their elastic properties rather than their topography

At defocus the SAM image of a small feature tends to be larger than the feature itself. Thus the rectangular features are likely to be slightly smaller than they appear in the image.

Note that the contrast in the SAM images is much better than that in the optical images.

7.4 Analysis of the rectangular features observed in the SAM (obelisks).

It was considered important to determine the nature of these features as they could act as weak spots in an electrolyte tube and could lead to early cell failure. The long straight edges of the features would be likely to act as preferential sites for Mode I degradation (see chapter 6) and if the features are cracks or non-conducting particles they will affect the conductivity of the electrolyte tube.

No chemical information can be obtained from the SAM

and so further analysis of the obelisks was carried out using a Camebax electron microprobe analyser (EMPA). To minimise electron beam damage the specimens were coated in a thin layer of carbon to provide electron conduction away from the beam area. Figure 7.4 shows energy dispersive x-ray (EDX) spectra taken on the matrix material and on an obelisk. A back-scattered electron (BSE) image is shown in figure 7.5. The BSE image was taken on a specimen which had undergone 635 charge/discharge cycles, and is of part of the region imaged acoustically in figure 7.3a.

The increased sodium count at the obelisk site leads to one of the following hypotheses:

1. the obelisks are small cracks which are filled with sodium,

2. the obelisks are small cracks which fill with sodium under the influence of the beam,

3. the obelisks are rod-shaped second phase particles. The excess sodium is due to the ease with which sodium can reach the specimen surface along the matrix/second phase particle interface,

4. the obelisks are second phase particles with an increased sodium content.

5. the obelisks are large grains of ß"-alumina with the conduction planes perpendicular to the surface, thus allowing easy loss of sodium to the specimen surface.

The obelisks were observed in both cycled and uncycled material suggesting that they are included in the tubes during the manufacturing process. This, together with their morphology, pointed to their being small second-phase particles or large ß"-alumina grains rather than cracks.

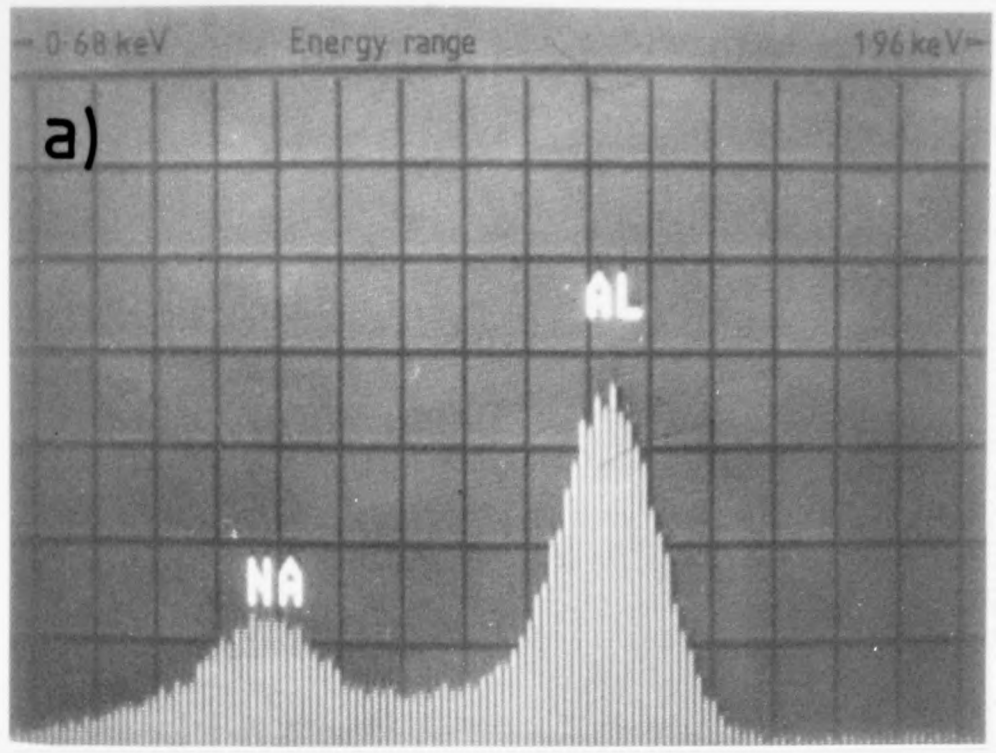

Fig. 7.4 a) Energy dispersive x-ray (EDX) spectrum taken on sodium ß-alumina electrolyte tube [spectrum from matrix material].

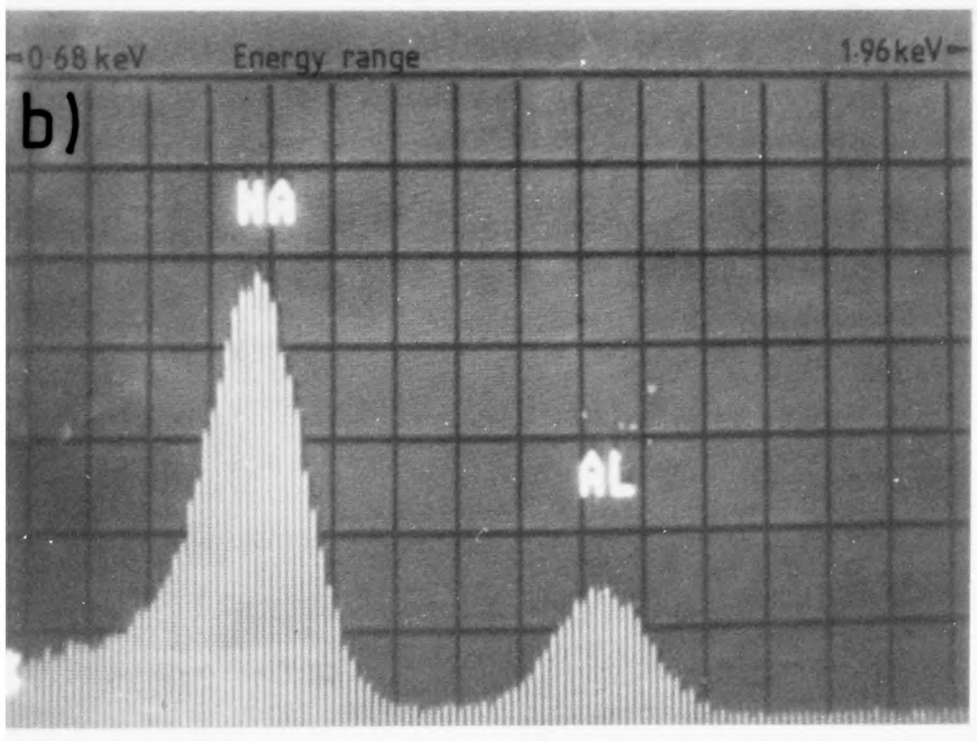

b) EDX spectrum taken on 'obelisk' on surface of same specimen as above. The same count time was used in both cases.

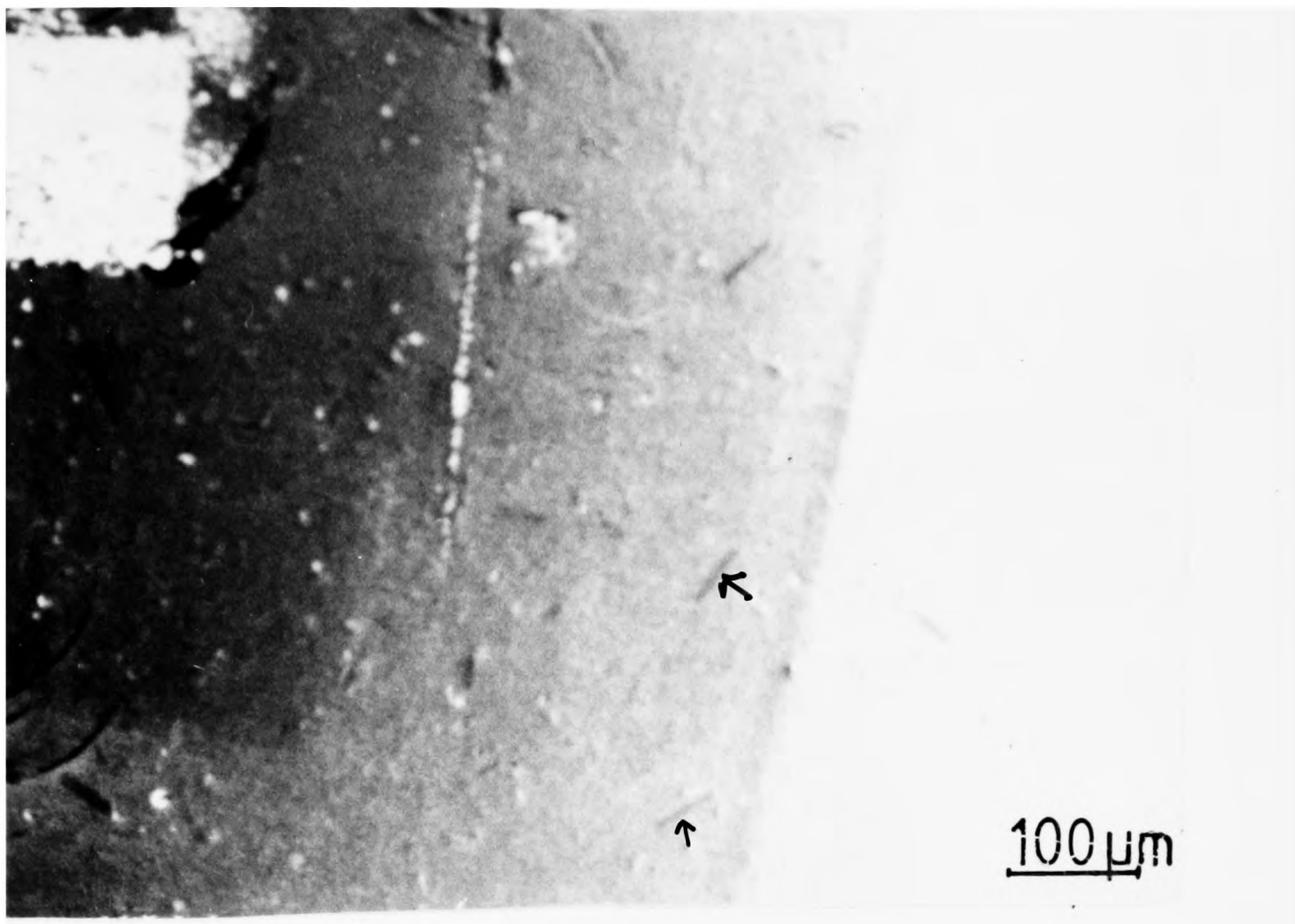

Fig. 7·5 Scanning electron microscope (SEM) image of Na ß-alumina electrolyte tube showing obelisks (arrowed). The bright region in the top left-hand corner of the image is due to the build-up of a layer of sodium on the specimen surface after extended exposure to the electron beam.

Examination using an optical Nemaski lens (which detects relief) did not reveal the features which again pointed to their being particles rather than cracks. Cracks have been observed in β -alumina electrolyte tubes (see chapter 6), but only after cell cycling. No correlation between density of features and number of cycles was observed in this analysis. An examination of obelisks in various uncycled specimens revealed some inverse correlation between porosity of the β-alumina tube and the density of obelisks present. The low porosity specimens appeared to contain many more of the particles than the high porosity specimens (see figure 7.6). As can be seen from figure 7.6a, the distribution of the obelisks within the tube, and their orientation, appears to be random.

The obelisks are not thought to be artefacts of the polishing process; the specimens were mounted in groups of five in one perspex block and were therefore subjected to exactly the same grinding and polishing conditions. Obelisks were not observed in all the specimens as would be expected if they were present due to the specimen preparation technique.

A fracture surface (as opposed to a polished surface) was also imaged (see figure 7.7). As expected the elastic contrast normally present in the acoustic images is completely dominated by contrast due to the surface roughness, and could only be seen if images taken at a number of different defoci were summed. However in this case the features were observable optically - especially in dark field - suggesting that fracture has either removed the particles leaving a pit, or has left particles above the level of the

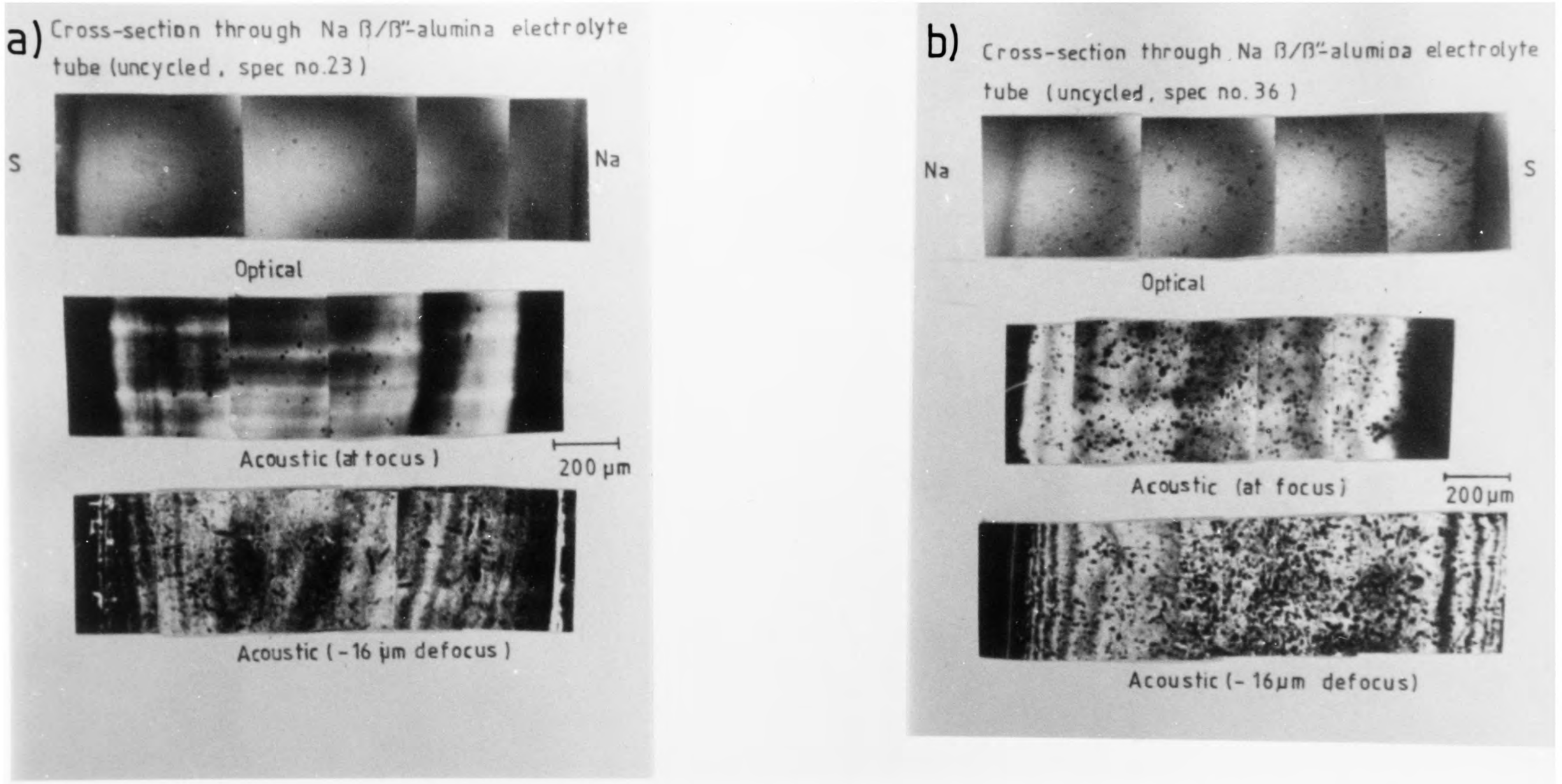

Fig. 7.6 Optical and acoustic images of Na ß-alumina electrolyte tubes a) with low porosity and b) with higher porosity - showing correlation between porosity and density of obelisks.

a) 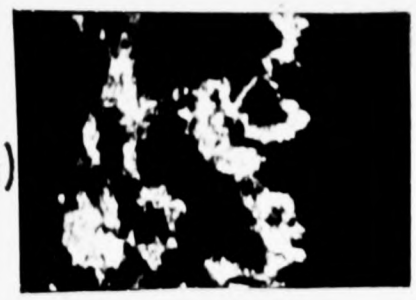

Fig. 7·7 a) Acoustic image at focus of fracture surface of Na β-alumina electrolyte tube. Surface roughness dominates the image contrast.

b) 

b) Acoustic image at a defocus of −2 µm, summed with an image at a defocus of −4 µm.

c) 

c) Summation of acoustic images at defoci of −6, −7, −8 and −9 µm.

d) 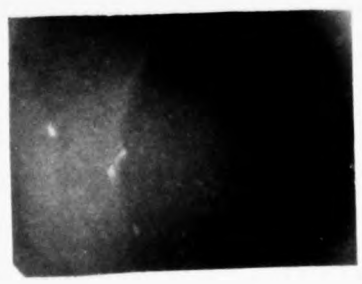

d) Bright field optical image. An obelisk appears to be visible in bright contrast at the left of the image.

e) 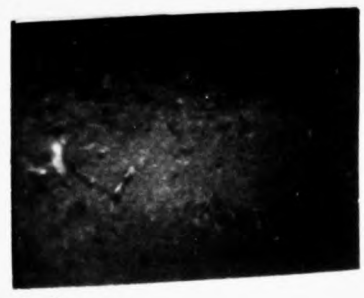

e) Dark field optical image. The contrast is greater than in the bright field revealing many rectangular features.

200µm

All images are of the same specimen area.

surrounding material. The specimen was examined immediately after fracture showing that the obelisks are not initially caused by exposure to the atmosphere.

The obelisks have an average length of 40μm with a variation in length between 15μm and 80μm.

The specimens were now left for several months at atmospheric pressure and room temperature.

On further examination of one of the uncycled specimens, using the optical microscope, the rectangular features previously observed were found to have increased in size from an average length of 40μm to an average length of 70μm with a corresponding increase in width. They were now visible optically in the polished specimens, but with poor contrast (see figure 7.8). The edges of the features were clearly visible along their entire length in most cases. Hexagonal features with similar contrast to the rectangular obelisks were also visible. These would not have been obvious previously as they would produce a very similar image to surface pores. A number of the rectangular features show some surface structure as can be seen in figure 7.8. The obelisks did not seem to have increased in number.

A chemical and morphological analysis of the enlarged obelisks was now carried out using the EMPA. Figure 7.9 shows the accretion of sodium (visible as white blobs) on the surface of the ß-alumina during exposure to the electron beam (images taken on uncycled specimen 23). The large hexagonal region free from surface sodium is an obelisk seen end-on, and the rectangular region partially covered with sodium is an obelisk seen in the projection more normally observed. EDX spectra were obtained from the matrix and from the larger

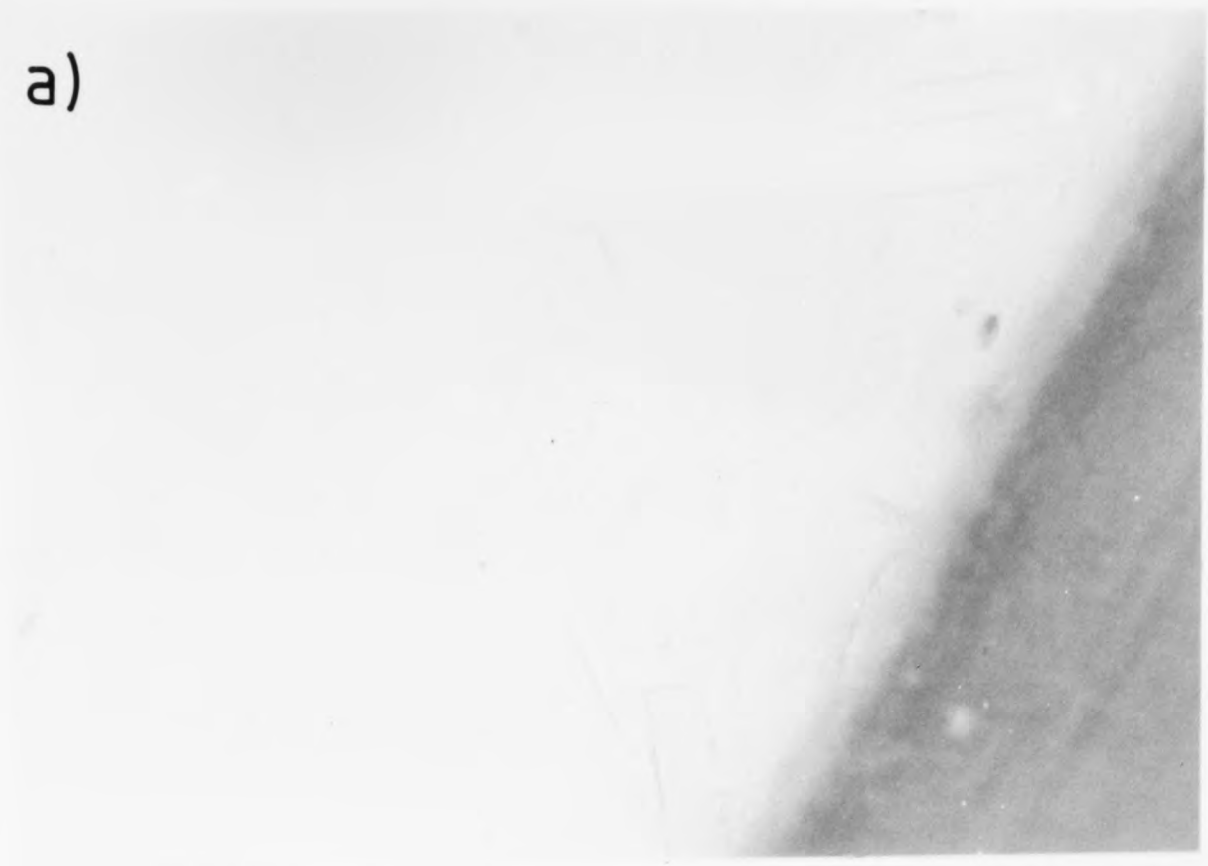

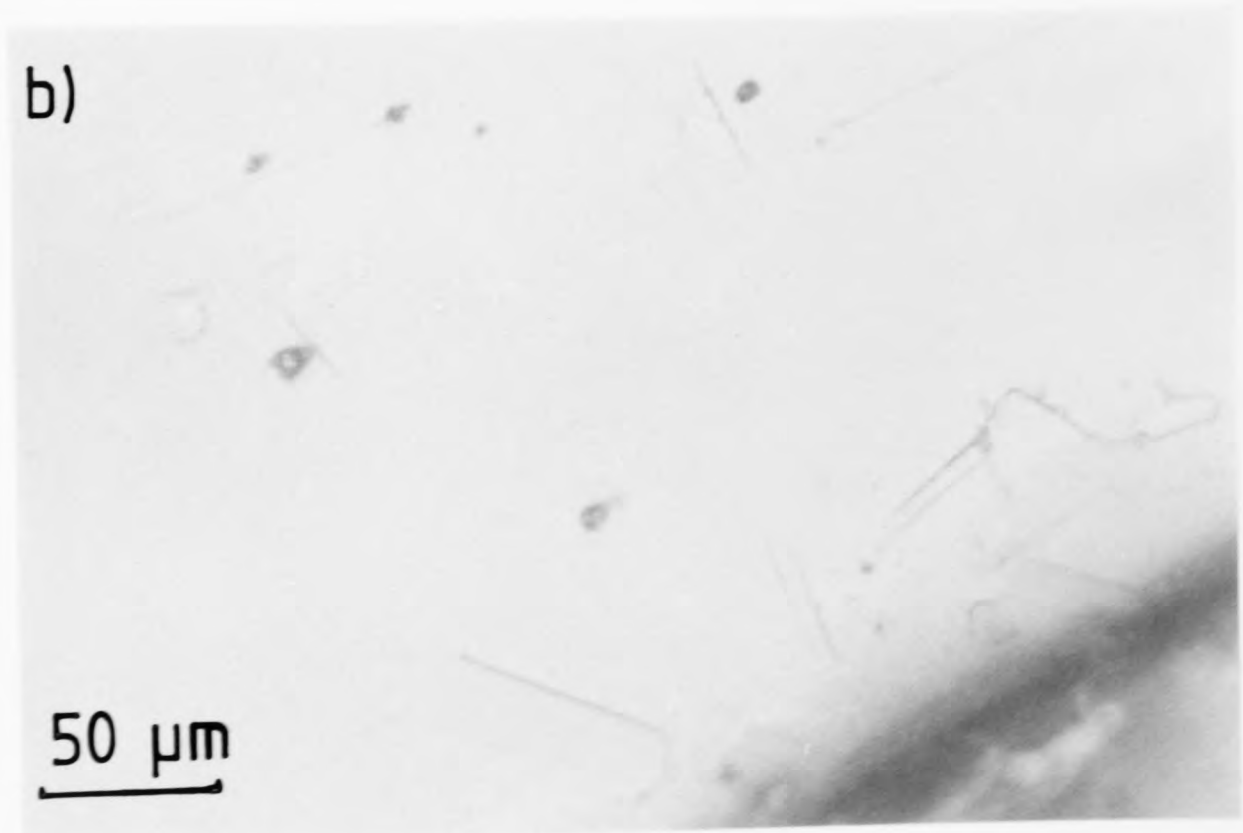

Fig. 7.8 a) and b) Optical images of sodium β-alumina electrolyte tube - taken several months after initial analysis - showing increase in size of obelisks (previously not visible optically in this specimen - specimen no. 23.

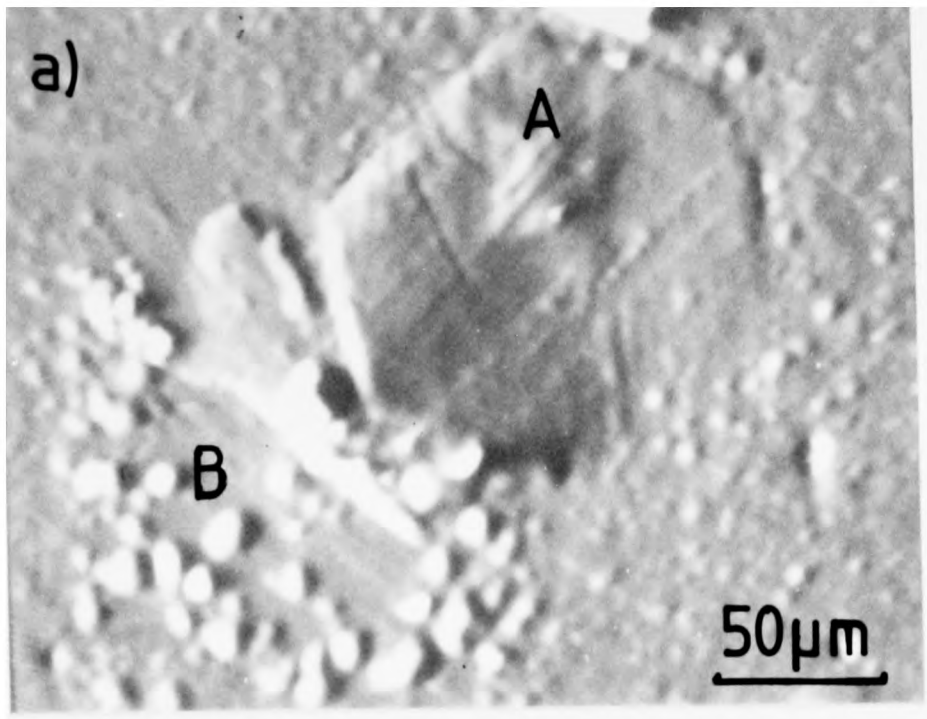

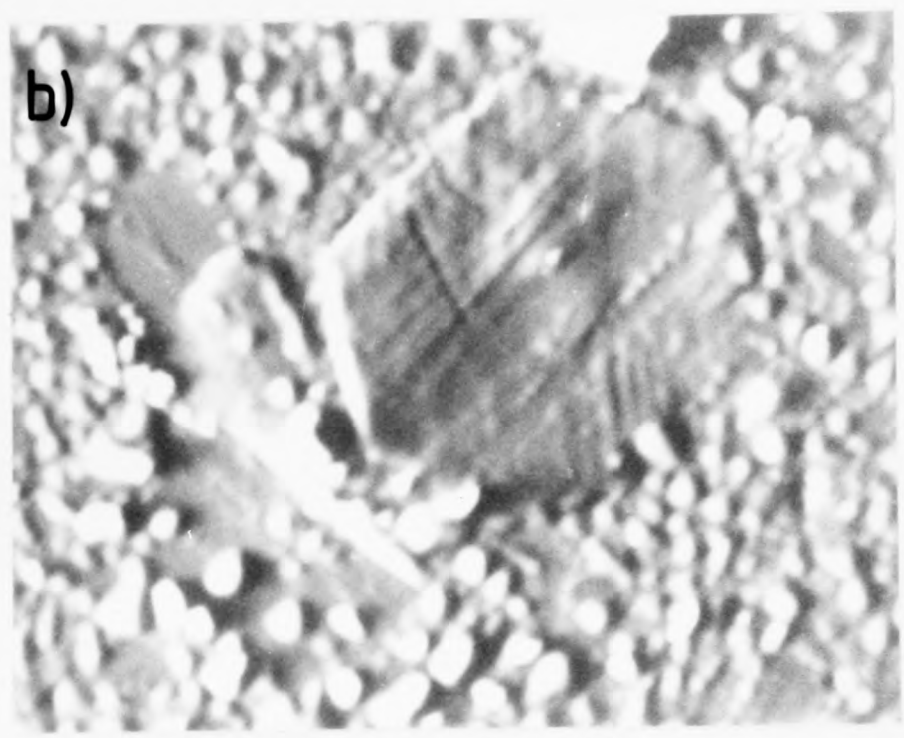

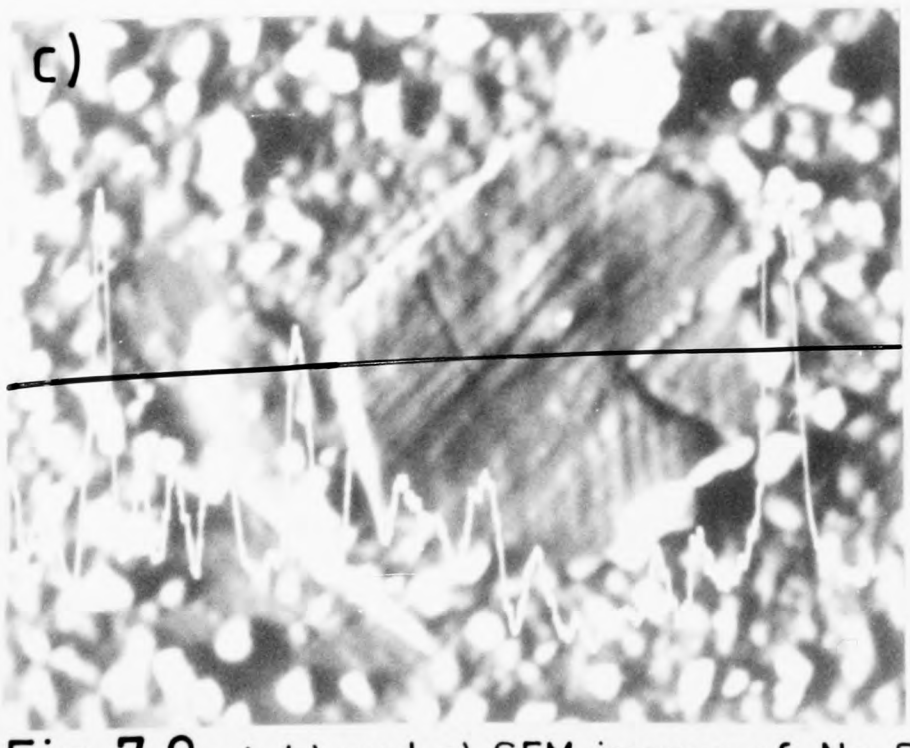

Fig. 7.9 a), b) and c) SEM images of Na ß-alumina electrolyte tube showing the build-up of sodium on the specimen surface during exposure to the electron beam. Figures a), b) and c) were taken at intervals of ~4 minutes, with the beam brightness kept low between photographic exposures. The bright regions are the sodium deposits, and regions 'A' &'B' are obelisks. c) also shows a line trace of the sodium x-ray count.

obelisks and examples are shown in figure 7.10. Large obelisks were chosen so that the spectrum would contain as little information from the surrounding electrolyte material and interface as possible. As can be seen, the obelisk shows a reduced sodium count compensated by an increased aluminium count. The appearance of the obelisks, and the reduced sodium count obtained, is consistent with the proposal that the obelisks are second-phase particles present in the ß-alumina which have grown during exposure to the atmosphere. These observations are also consistent with the proposal that the obelisks are large grains of ß"-alumina; obelisks seen "end-on" (hexagonal) would show a low sodium count as sodium is unable to reach the surface by passing upwards through a spinel block, but must travel along the conduction plane (parallel to the surface) to the edge of the grain and hence to the surface. Obelisks seen in the normal rectangular projection (conduction planes perpendicular to the surface) might well also show a low sodium count if they are ß"-alumina due to the ease with which Na could reach the surface, allowing the grain to undergo ion-exchange with atmospheric moisture during storage.

Aluminium and sodium were the only elements identified in the EMPA analysis of the obelisks. A quantitative analysis of the Al counts, compared with a standard of Al_2O_3, showed a match with an error of about 15%. This 15% error in the match is likely to be due to the effects of sodium x-rays from the matrix and the interface which were not counted. The x-ray trace on figure 7.10c) was taken using sodium x-rays and shows a definite dip in the region of the large obelisk.

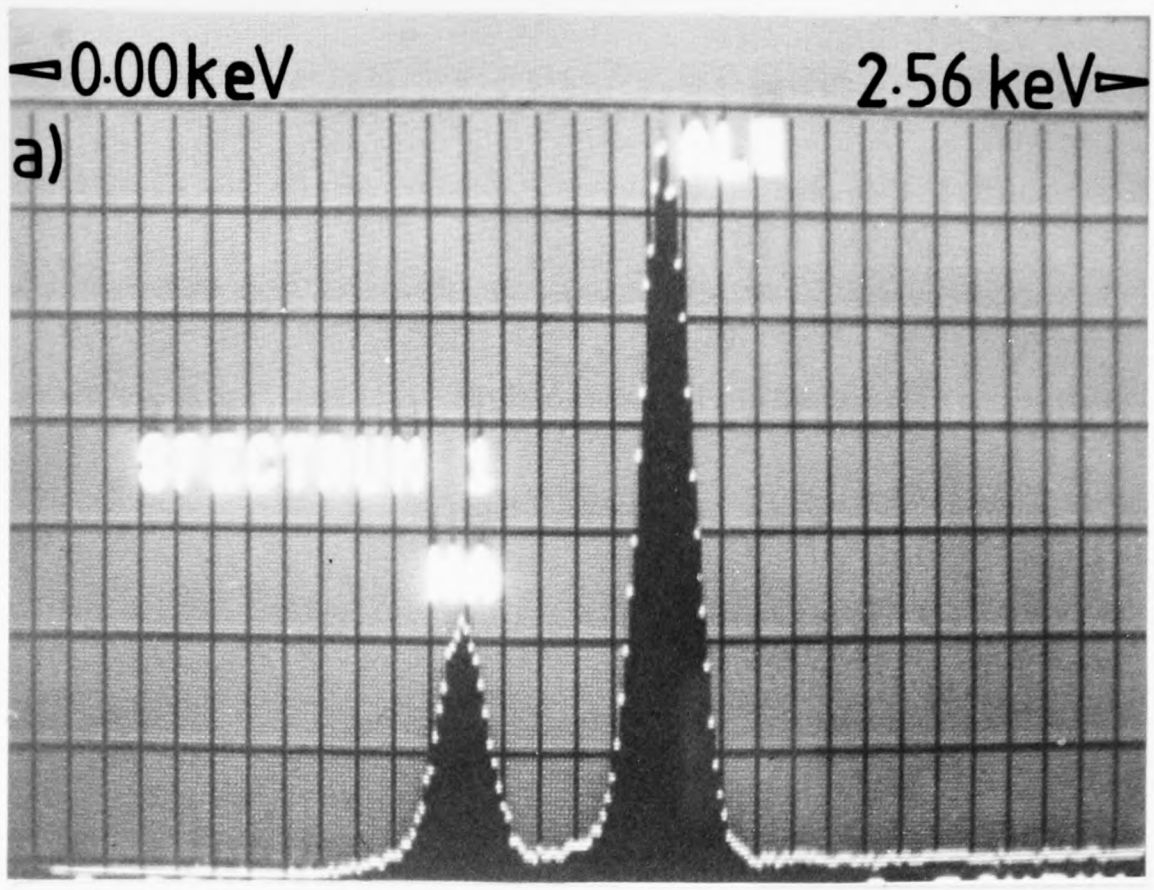

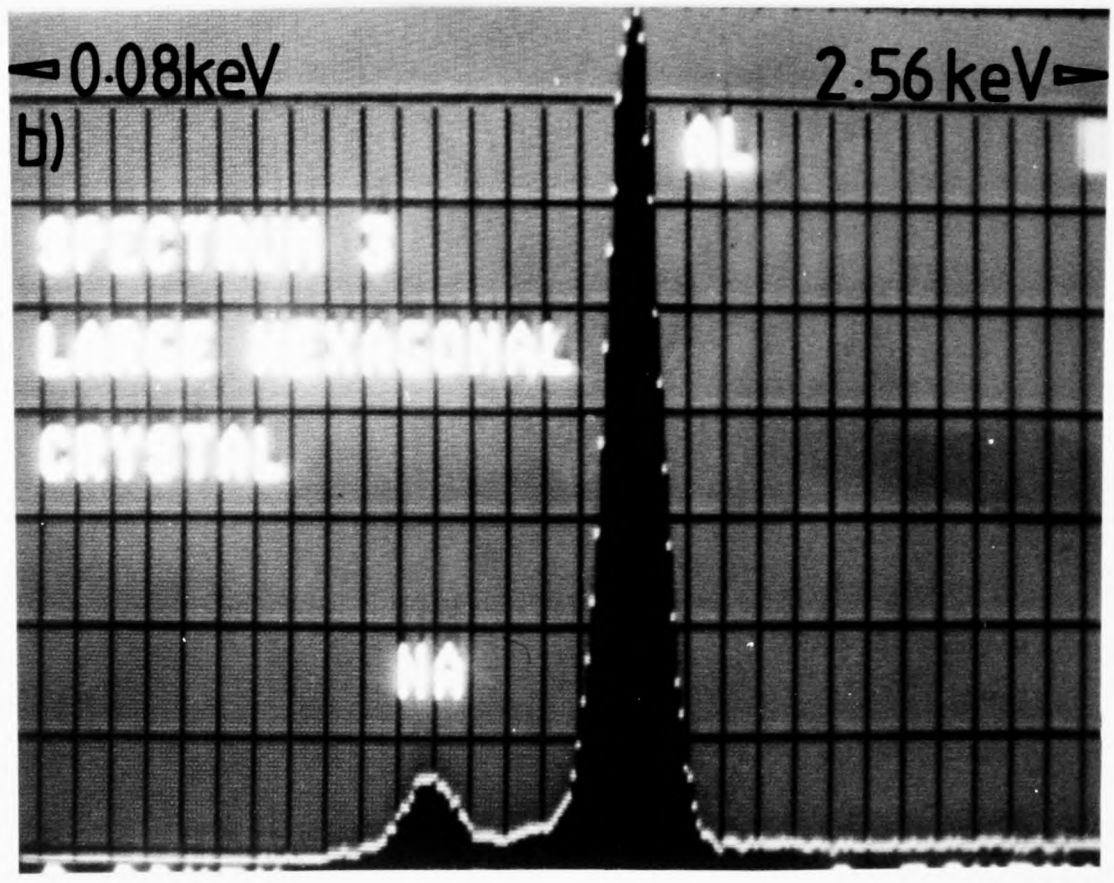

Fig. 7.10 a) EDX spectrum taken on matrix of Na ß-alumina electrolyte tube (specimen no. 23).
b) EDX spectrum from specimen no. 23 - taken on large hexagonal obelisk imaged in fig. 7.9

Further analysis in the acoustic microscope revealed the obelisks more clearly than previously (see figure 7.11) - both long edges were now visible, with the bulk of the obelisk showing contrast slightly different from that of the surrounding sodium ß-alumina, although the slight contrast difference suggests that the obelisks are of a similar material to ß-alumina. The slight difference in contrast would also be expected if the obelisks were large grains of ß"-alumina as the contrast from the surrounding material will be an average over many grains in different orientatins. ß and ß"-alumina are acoustically anisotropic, with different acoustic wave velocities parallel and perpendicular to the c-axis. The SAM images do not reveal any internal structure, suggesting that the obelisks are single crystal second-phase particles.

The SEM images clearly show the surface topography visible optically, again suggesting that the obelisks have hexagonal symmetry with a large c/a ratio.

One of the uncycled specimens which had undergone a very long anneal (300 hours) and had previously contained few obelisks, (and showed a high porosity) now showed a very different surface structure when examined acoustically - as can be seen in figure 7.12. The entire surface appeared to be changed, and it is suggested that this could be a similar effect to that observed by Heavens (1982) in which the surface of the sodium ß-alumina had reacted with atmospheric moisture giving rise to a thin layer of H_3O^+ ß-alumina. This layer is prominent due to an increase in lattice parameter which distorts the lattice. The fact that this surface layer

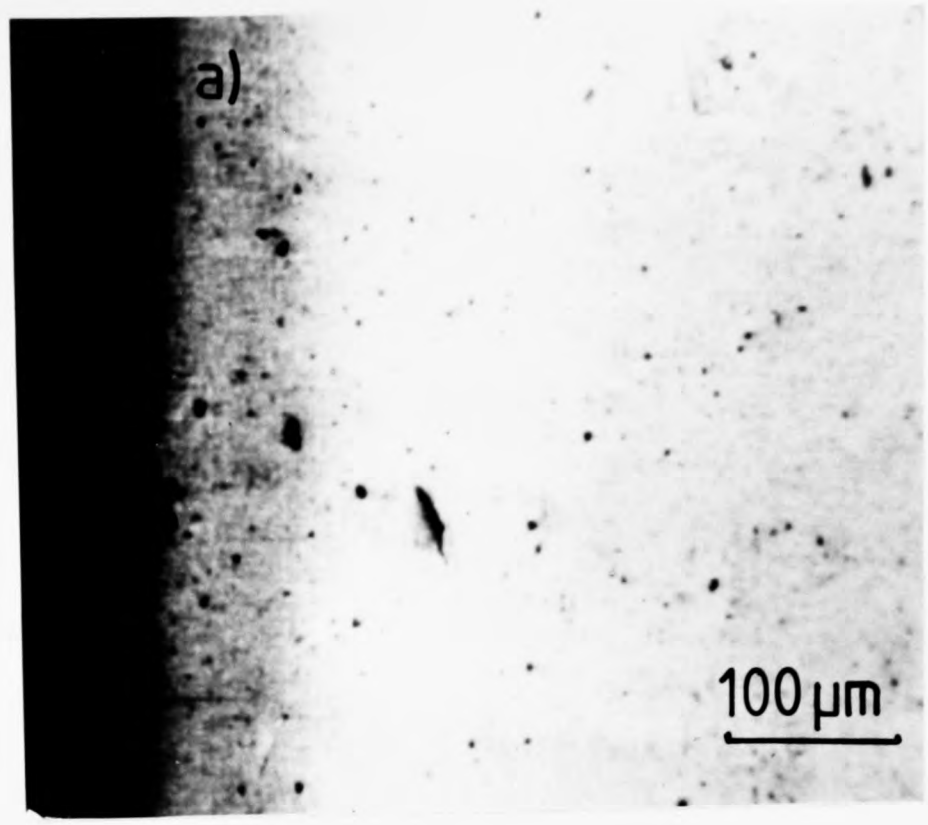

Fig. 7·11 Acoustic images a) at focus, and b) at a defocus of -13µm, of specimen 23. The obelisks have increased in size, and some are visible at focus.

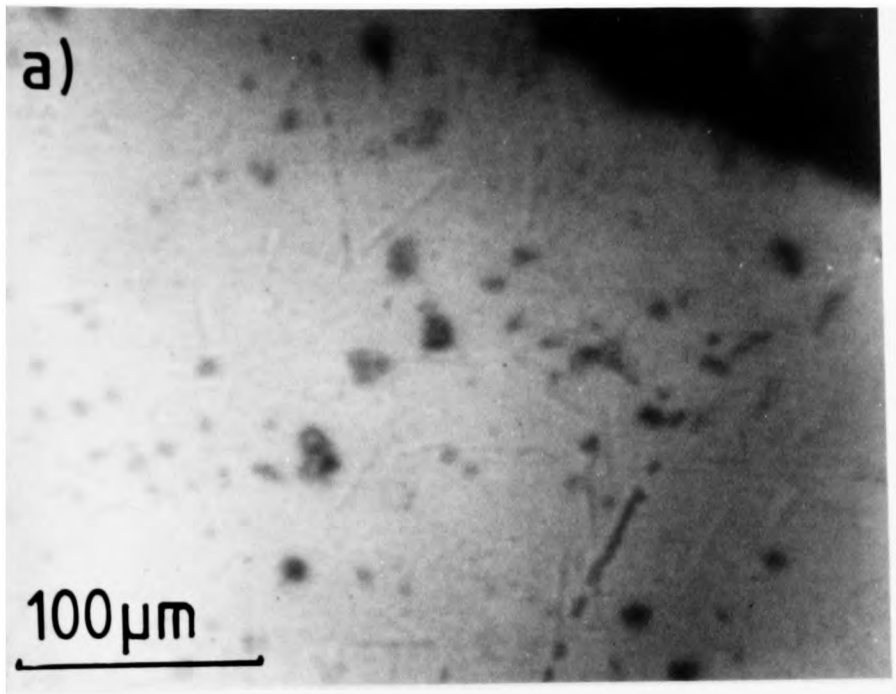

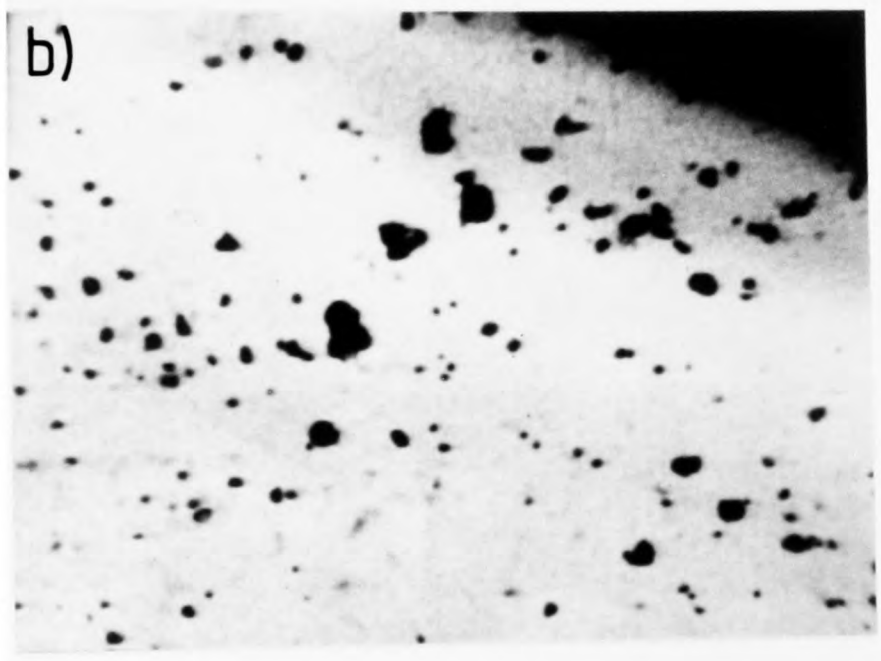

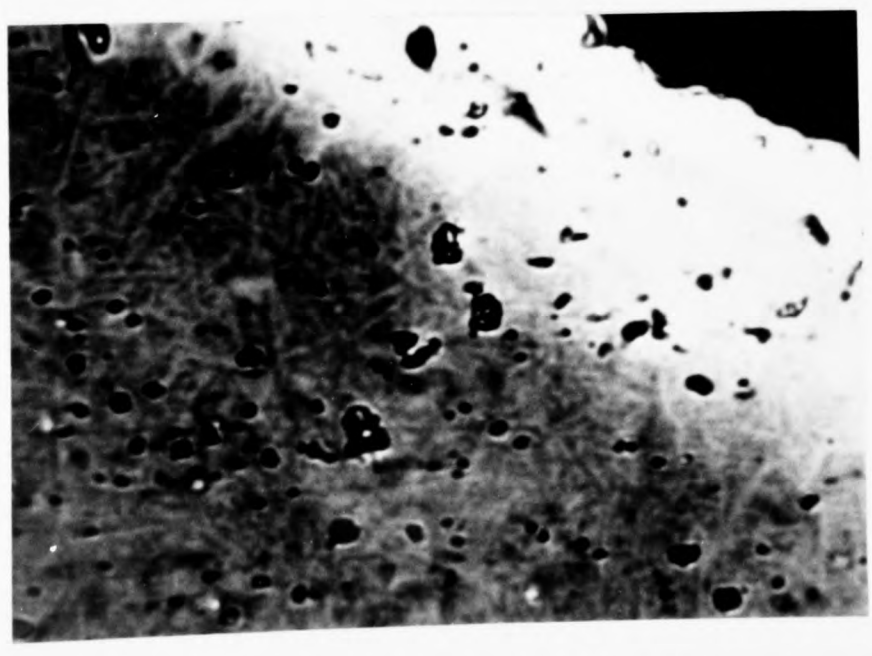

Fig. 7.12 a) Optical image, b) acoustic image at focus, and c) acoustic image at a defocus of -6 µm of specimen 36 showing surface layer.

only appears to have formed on this particular specimen suggests that the long anneal has made it more prone to attack from atmospheric moisture, since all the uncycled specimens had been stored under the same conditions.

The cycled specimens previously analysed had been coated with carbon for examination in the SEM, and this coating had not been removed before storing. When these specimens were reexamined optically, the rectangular features were not visible, and the acoustic images showed that they had not increased in size (see figure 7.13). The fact that the features have not increased in size suggests either that the carbon coating has prevented reaction with moisture in the atmosphere, or that the excess sodium present in the specimens due to cycling has replaced any sodium lost to the surface - preventing any phase change, or that the sodium at the particle/matrix interface has prevented growth of the particle. Further examination of these specimens after storage with the carbon film removed should clear up this ambiguity, but unfortunately this work will not be possible in this study.

As previously mentioned (see section 7.1) V(z) curves can be taken on a specimen to give some indication of the type of material present. V(z)s were taken both on the ß-alumina matrix and on the rectangular features. Examples of each are shown in figure 7.14. As can be seen the V(z) from the matrix shows many periods whilst on the obelisk the periodic structure is quickly damped. The periodic repeat distance is similar both on and off an obelisk indicating that the particles are composed of a material with a similar acoustic wave velocity (similar elastic properties) to that

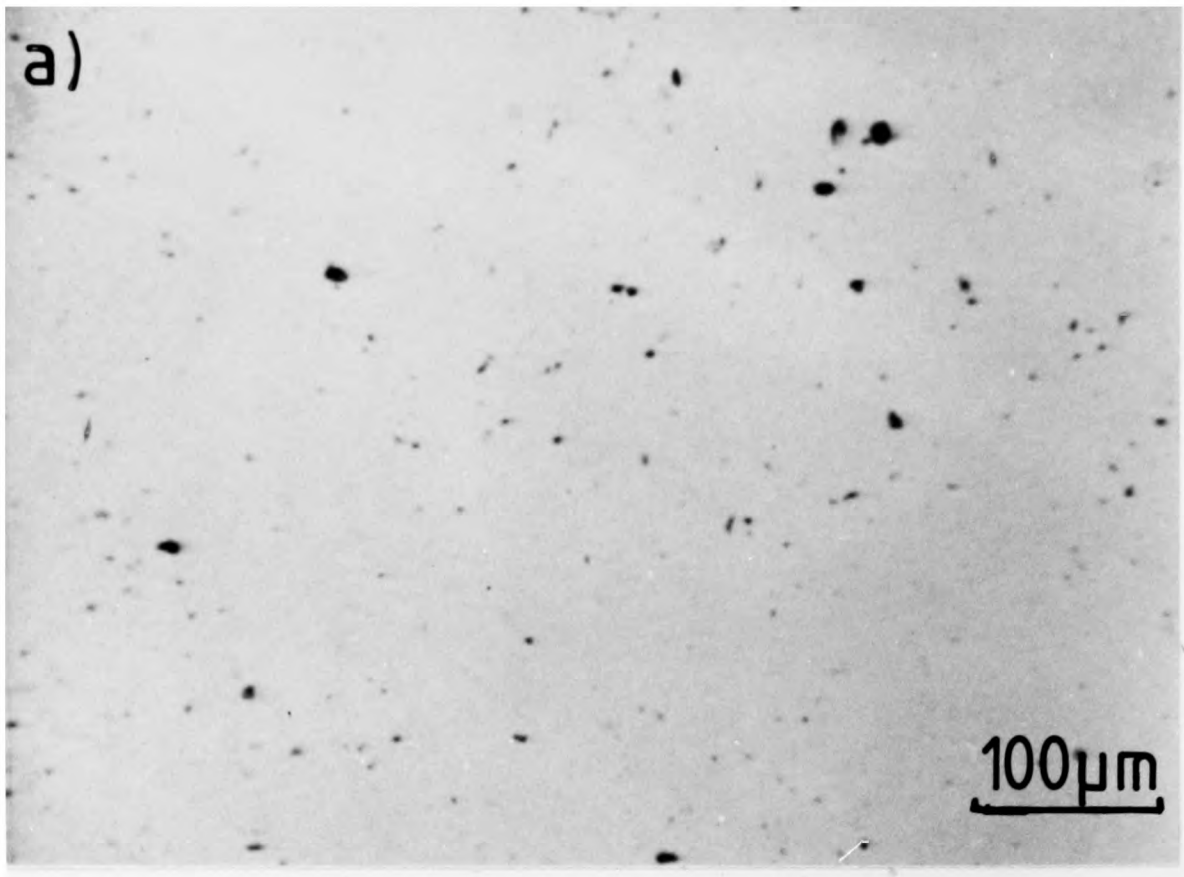

Fig. 7·13 Acoustic images a) at focus, and b) at a defocus of -12 µm of cycled electrolyte tube (635 cycles) after storage under a thin carbon film. Obelisks can be seen but do not appear to have increased in size.

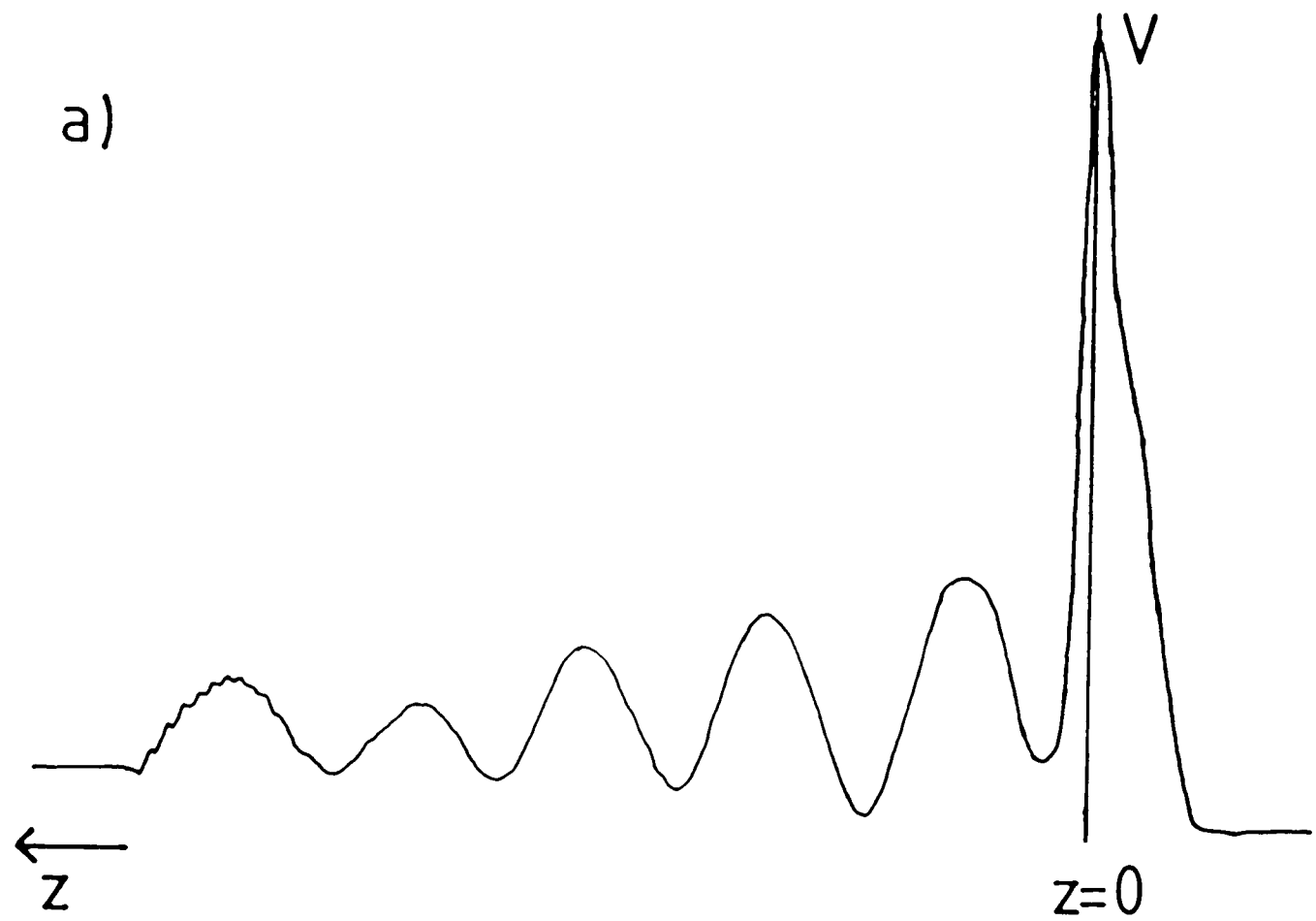

Fig. 7.14 V(z) curves taken a) on a ß/ß'' electrolyte tube, and b) on an obelisk on the surface of the same specimen.

of ß-alumina. It should be noted that ß-alumina is a very anisotropic material and so any value for the acoustic wave velocity calculated from the V(z) curve will be an average over many grains in different orientations, and so if the obelisks are large grains of ß"-alumina the V(z) curves would appear different from those taken on the matrix. Twinning and strain in the obelisks could also change the appearance of the V(z) curve, although the theory of acoustic V(z) curves is not yet well enough developed for such effects to be quantified.

The EMPA work suggests that the particles are some form of alumina, or an aluminium compound whose other constituents have atomic masses too low to produce detectable characteristic x-rays using EDX. α-alumina is one of the starting materials used in the manufacture of ß-alumina electrolyte tubes and small unreacted particles of this material could be present in the tubes after manufacture. The morphology of the particles (hexagonal cross-section rods) also agrees with that of α-alumina, or ß"-alumina.

The V(z) curves however point to the obelisks being a material other than α-alumina. A V(z) curve was also taken on a specimen of pure synthetic sapphire (α-alumina). This is shown in comparison with the V(z) curve from an obelisk in figure 7.15, both taken under similar conditions. As can be seen the two V(z)s are qualitatively quite different. It is rather surprising that the V(z) curve from the obelisk is so quickly damped as this implies that the Rayleigh waves are quickly lost in the material - unusual for a single crystal. It would be more usual for a material composed of small grains (such as the ß-alumina matrix) to give rise to a lossy

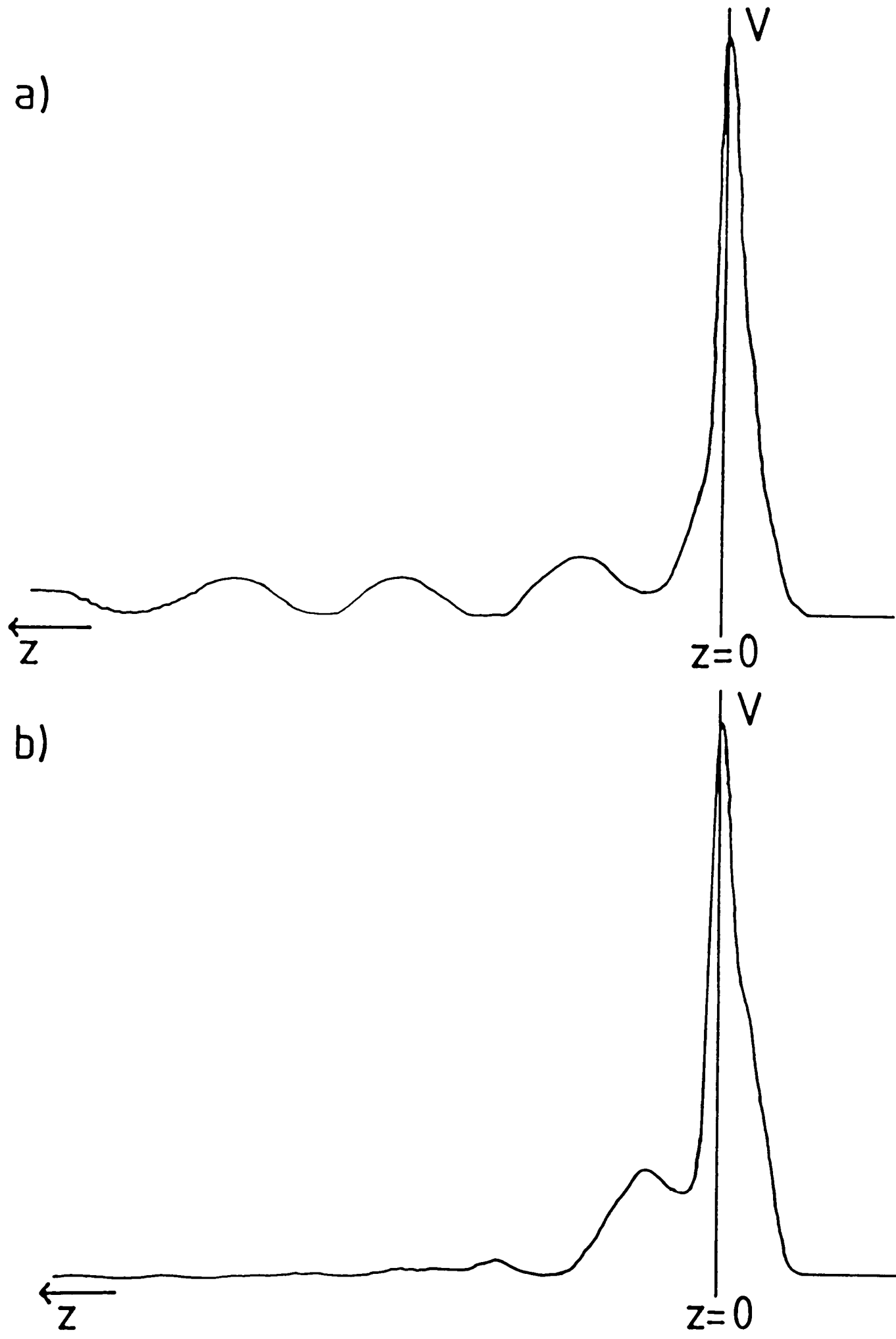

Fig. 7·15 V(z) curves taken on a) a single crystal of synthetic sapphire (α-alumina), and b) an obelisk on the surface of a β/β'' electrolyte tube specimen.

V(z) curve.

X-ray diffraction carried out at AERE Harwell on the uncycled specimens - both those containing large obelisks and that having a surface layer - revealed no peaks due to α-alumina - only those due to β and β"-alumina. This is consisent with the obelisks being large grains of β"-alumina, although if they consist of α-alumina the peaks due to the particles may be too small to be distinguished from the background, or may be dominated by the β and β"-alumina peaks. Examples of the x-ray diffraction spectra are shown in figure 7.16.

7.5 Summary

The results obtained suggest that the obelisks are either large grains of β"-alumina, which have become soda depleted due to ion-exchange with atmospheric moisture, or are second-phase particles composed of some other form of alumina.

The apparent increase in size of the particles after prolonged exposure to the atmosphere may well be due to etching of the specimen surface by acidic moisture in the atmosphere. The etching will preferentially attack the small, high surface area grains, leaving the large grains exposed to a greater degree. If an obelisk is at an angle to the surface such that part of it is below the depth to which the SAM can image, then removal of a surface layer by etching may bring the buried section close enough to the surface to be imaged, or even expose it at the surface.

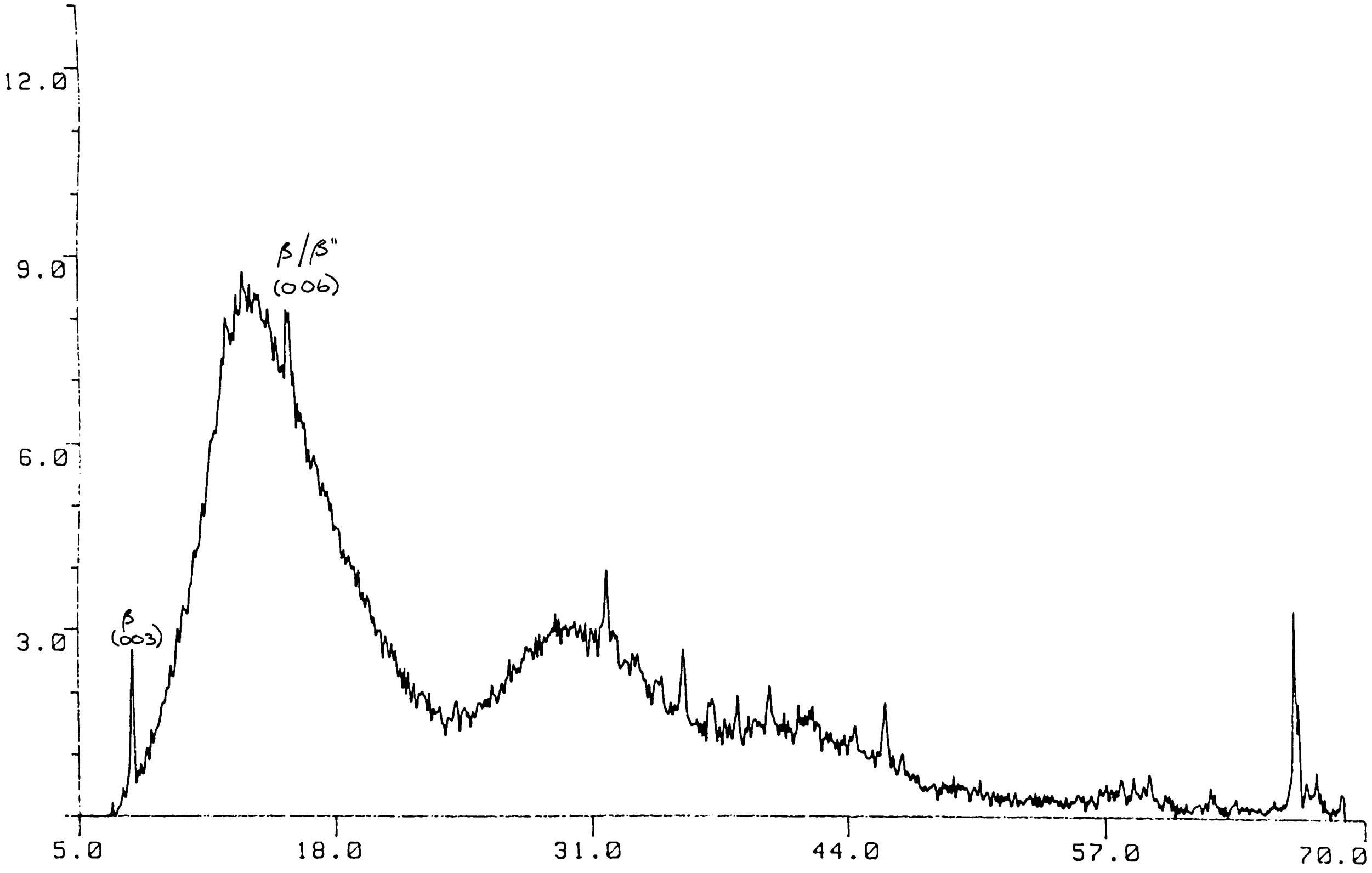

Fig. 7·16 a)

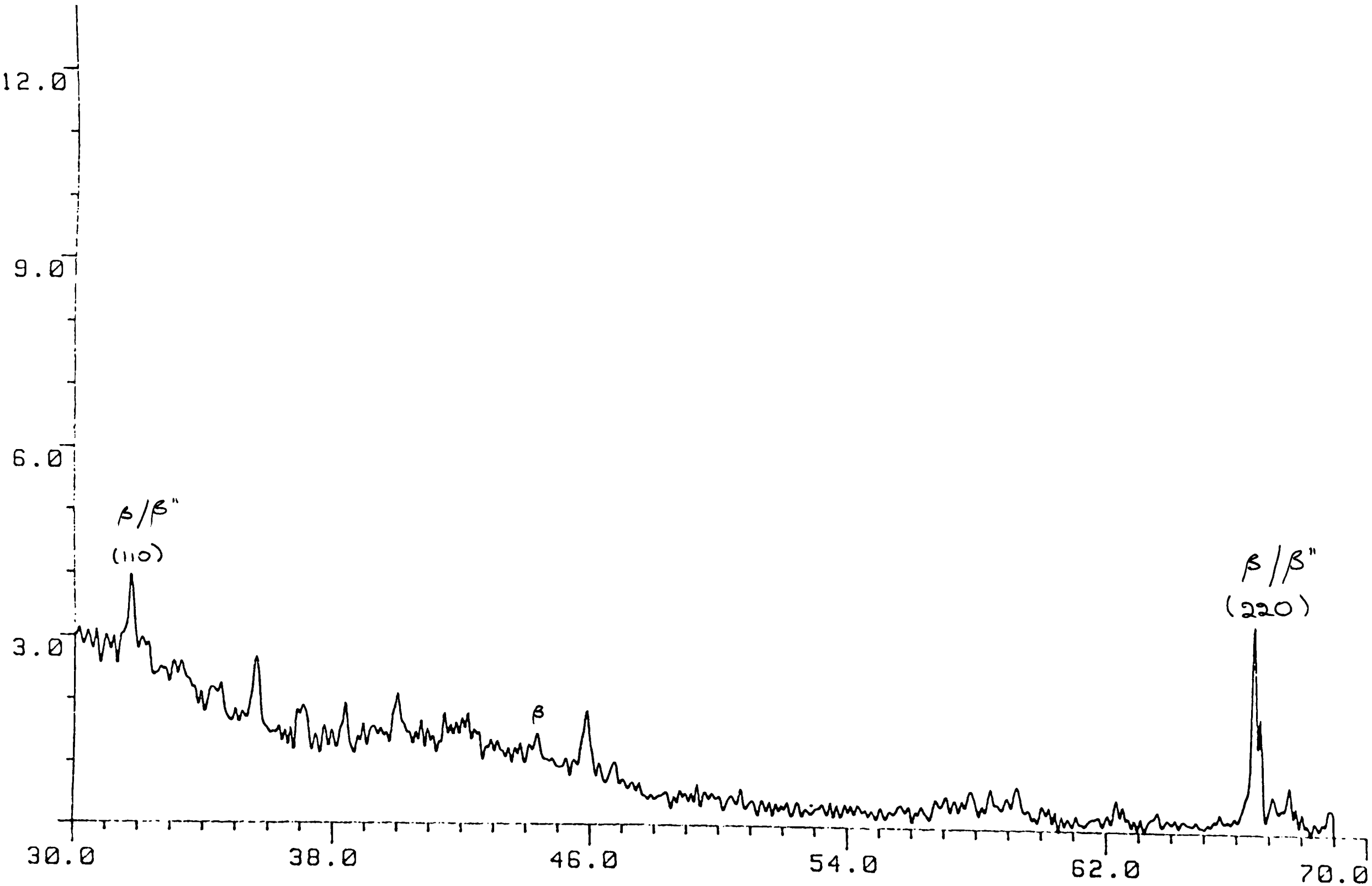

Fig. 7·16 b)

Chapter 8 Conclusions and suggestions for further work.

8.1 Conclusions

a) High resolution electron microscopy

HREM has been used to provide information about the structure and properties of various ß-alumina superionic conductors. Sodium ß and ß"-alumina specimens prepared from electrolyte tubes were examined initially, but results are also presented on several ion-exchanged ß"-aluminas not previously examined using HREM (NH_4^+/H_3O^+, Gd^{3+}, Eu^{2+} and Eu^{3+}). New long-period structures in the sodium material were also observed, as were intergrowths of sodium ß and ß"-alumina on the scale of a few spinel blocks (few x10Å).

Electron beam damage was found to result in various modes of damage - the most prominent in all the ß"-aluminas examined being loss of the mobile ion- containing planes leading to collapse and shear of the structure to form broad spinel blocks. A model previously proposed for the collapse vectors in sodium ß"-alumina was found to fit the experimental results obtained for collapse in ammonium/hydronium ß"-alumina.

The rate of conduction plane loss did not appear to depend on the conductivity (ionic mobility). Eu^{2+} ß"-alumina was found to be the most beam stable of the ß"-aluminas examined, with a specimen of ammonium/hydronium ß"-alumina which had had no heat-treatment after ion-exchange, being the least stable. The Eu^{2+} material could be exposed to the beam for several minutes with no loss of planes, whereas the NH_4^+/H_3O+ material would start to lose planes as soon as the

electron beam was focused on it, with the loss of approximately half of the visible planes within a few x10 seconds. The material appeared to reach a stable form with every alternate conduction plane lost. Observations were made on a specimen prepared from the same ion-exchanged crystal and then subjected to heat-treatment. These showed that the heat-treatment had also resulted in conduction plane loss with the most dominant repeat distance being 20.6Å (ie. every alternate conduction plane missing). The results obtained suggest that NH_4^+/H_3O^+ ß"-alumina prefers to exist in a form in which alternate planes have been lost leading to 20.6Å spinel blocks. The protonic conductivity of the material is likely to be affected if only half as many conduction planes as expected are available.

In the case of Eu, Gd and NH_4^+/H_3O^+ ß"-aluminas, the HREM results produced in this study were able to explain several anomalous results obtained using x-ray and neutron diffraction. For example anomalous cation site average occupancies were explained by the fact that some conduction planes had been lost - resulting in a disordered structure. Thus HREM has shown that care must be taken when calculating structure models of the ß-aluminas using techniques that average over a bulk specimen.

Two further electron beam damage modes were observed in ammonium/hydronium ß"-alumina which had not previously been reported in the ß-aluminas. Knock-on damage caused by the protons in the conduction plane, and the formation of NH_3 bubbles within regions of conduction plane sealed from the surface of the crystal. Mechanisms for these two damage modes were proposed.

Sodium ß-alumina was found to damage in the beam by the extrusion of islands of material onto the crystal surface. These were analysed and found to consist of various sodium oxides and hydroxides, with the most common component being Na_2O. Extended exposure to an intense beam also resulted in a structural change of the ß-alumina crystals - this appeared to result in all the oxygen layers perpendicular to the c-axis becoming equivalent. Silver ß-alumina was also seen to damage by the extrusion of islands to the crystal surface, and also by the rapid extrusion of quite large amounts of material from specific surface sites. The extruded material was found to be metallic silver.

Superlattice ordering was observed in gadolinium, Eu^{3+} and Eu^{2+} ß''-aluminas. The superlattice cells in the gadolinium and Eu^{3+} materials appears to be similar, although the ordering was much more extensive in the Eu^{3+} material. The superlattice cell in both cases has dimensions 3a x 3a x5c/3. The superlattice in the Eu^{2+} ß''-alumina has dimensions 2a x 2a x c.

b) Scanning acoustic microscopy and chemical analysis work

Acoustic microscopy has been used to obtain results on bulk Na ß/ß''-alumina electrolyte tube specimens. The SAM revealed the presence of large particles with an initial average length of 40µm. The particles appeared rod-shaped, and increased in size during prolonged exposure to the atmosphere (a few months) to an average length of 70µm. Hexagonal particles showing the same contrast were also observed and are thought to be rods viewed along the c-axis.

Chemical analysis using a Cameca EMPA was also carried out and SEM images of the particles were obtained.

V(z) curves were taken on the matrix and on the obelisks, and a comparison made between these curves and ones taken on a specimen of pure synthetic sapphire (α-alumina).

X-ray diffraction data was obtained from the surfaces of the specimens and showed only peaks corresponding to ß and ß"-alumina.

We suggest that the particles are either large grains of ß"-alumina which appear to grow due to etching of the surrounding material, or second-phases particles of some other type of alumina.

8.2 Further work

The following suggestions are intended to illustrate directions for further research in the fields of electron microscopy, acoustic microscopy and chemical analysis. They are not intended to be comprehensive, and the use of other techniques not discussed here will obviously be needed to gain a complete picture of the structures and properties of the ß-aluminas.

Much more HREM and computer simulation needs to be carried out on the divalent and trivalent ß"-aluminas in which superlattices are observed, so that the exact supercell dimensions and a refined model for the cation sites can be produced. The weak beam technique, using one of the superlattice reflections, could prove useful for investigating the presence of microdomains in these ordered materials. Electron diffraction with the beam along the $\bar{c}$-axis of the ß"-alumina could also prove useful - again in detecting the presence of microdomains.

The computer simulation used to model the Eu^{3+}

ß"-alumina superlattice used a 3a x 3a x c supercell, and although this gives a good match perpendicular to the c-axis, the relationship between adjacent conduction planes is not correctly modelled. The c superlattice parameter needs to be changed, and this modelling will require extensive work.

It would be useful to prepare ion-beam thinned specimens of a complete cross-section through a Na ß/ß"-alumina electrolyte tube for examination in the Jeol 200CX HREM. This would give an indication of whether the density of defects observed, such as lost conduction planes and intergrowths, was a function of the distance of a particular grain from the electrode/electrolyte interface. With the present specimen preparation technique there is no way of telling where a particular grain was originally positioned in the tube. This would also provide more information concerning grain boundaries, and in cycled material should reveal internal sodium colloids, microcracks and point defects leading to chemical colouration.

This research has shown that in the case of ion-exchanged ß-aluminas (eg. NH_4^+/H_3O^+ ß"-alumina) the exchange process and subsequent treatment affects the quality of the crystal. Further HREM studies of crystals prepared under different exchange conditions could lead to a correlation between preparation and defect density. This is important in the case of materials which are of commercial interest, as the specimen quality must be kept at a reasonable level. For example - a preparation technique needs to be established for the production of stable NH_4^+/H_3O^+ ß"-alumina crystals with as few lost conduction planes as possible so as to maintain a high conductivity.

Chemical analysis of the ß-aluminas using an EMPA could provide useful information concerning the composition of these materials. In order to obtain quantitative results, the work should be carried out at a temperature which is low enough to "freeze" the mobile ions into the lattice. Liquid nitrogen temperatures should prove adequate.

The cycled electrolyte tube specimens which had been stored under a carbon film, and have now had the film removed, should be examined (after a few months) optically and in the SAM to discover whether or not the obelisks have increased in size. If they have, then it is the presence of the carbon film which prevented previous growth; if not then it is likely that the excess sodium present due to cycling has prevented the particles from increasing in size. Information regarding the optimum storage conditions for the tubes is required and this work could be helpful.

Further analysis of the so-called obelisks is needed to ascertain their exact nature, and electron diffraction could be used to advantage in this area.

If the obelisks do turn out to be large grains of ß"-alumina, further acoustic work on electrolyte tubes which have been cycled to failure could show whether a correlation exists between the presence of large grains and preferential electrolyte degradation after cell cycling. This is important as it could help determine the levels of grain growth which are acceptable in Na ß/ß"-alumina electrolytes.

REFERENCES.

References with * are to chapter 1.

Allen S.J., Cooper A.S., De Rosa F., Remeika J.P. and Olasi S.K. - Phys. Rev. B17, 1978, p.4031.

Anderson J.S. and Hyde B.G. - J. Phys. Chem. Sol. 28, 1967, p.1393.

Armstrong R.D., Dickenson T. and Turner J. - Electrochim. Acta 19, 1974, p.187.

Armstrong R.D., Sellick D.P. and Tan S.R. - Sol. Stat. Ionics 6, 1982, p.203.

Baffier N., Badot J.C. and Colomban J.C. - Mat. Res. Bull. 16, 1981, p.259.

* Bagotzky and Skundin - Chemical Power Sources, 1980.

Bates J.B., Wang J.C. and Dudney N.J. - Physics Today, July 1982, p.46.

Beevers C.A. and Ross M.A.S. - Z.Krist. (A) 97, 1937.

Bettman M. and Peters C.R. - J. Phys. Chem. 73 no.6, 1969, p.1774.

Bevan D.J.M., Hudson B. and Moseley P.T. - Mat. Res. Bull. 9, 1974, p.1073.

Boilot J.P., Collin G., Comes R., Thery J., Collongues R. and Guinier A. - Superionic Conductors (ed Mahon and Roth) 1977.

Boilot J.P., Colomban Ph., Collin G. and Comes R. - Fast Ion Transport in Solids (ed Vashishta, Mundy and Shenoy), 1979, p.243.

Boilot J.P., Thery J., Collongues R., Comes R. and Guinier A. - Acta Cryst. A32, 1976, p.250.

Bourke M.A.M., Hooper A., Moseley P.T. and Taylor R.G.. - Sol. Stat. Ionics 1, 1980, p.367.

Bovin J-O. - Acta Cryst. A35, 1979, p.572.

Bovin J-O. - Fast Ion Transport in Solids (eds Vashishta, Mundy and Shenoy), 1979b, p.315.

Bovin J-O. and O'Keeffe M. - J. Sol. Stat. Chem. 33, 1980, p.37.

Bragg W.L., Gottfried C. and West J. - Zeitschrift fur Kristallographie 77, 1931.

Brennan M.P.J. - Electrochim. Acta 25, 1980, p.621.

Briant J.L. and Farrington G.C. - J. Electrochem. Soc. 128

no.9, 1981, p.1830.

Carrillo-Cabrera W., Thomas J.O. and Farrington J.C. - Sol. Stat. Ionics 9 and 10, 1983, p.245.

Collin G., Colomban Ph., Boilot J.P. and Comes R. - Fast Ion Transport in Solids (ed Vashishta, Mundy and Shenoy), 1979, p.309.

Cowley J.M. - "The principles of high resolution electron microscopy" in "Principles and Techniques of Electron Microscopy", 1974, ed Hayat M.D..

De Jonghe L.C. - Interim Report prepared for Electric Power Research Institute, 1975.

De Jonghe L.C. - J. Mat. Sci. 12, 1977, p.497.

De Jonghe L.C. - Mat. Res. Bull. 12, 1977, p.667.

De Jonghe L.C. and Beuchele A. - J. Mat. Sci. 17, 1982, p.885.

De Jonghe L.C., Beuchele A. and Armand M. - Sol. Stat. Ionics 9 and 10, 1983.

De Jonghe L.C., Beuchele A. and Yoon K.H. - Lawrence Berkeley Laboratories Report no.LB1-14150.

De Jonghe L.C., Feldman L. and Beuchele A. - J. Mat. Sci. 16, 1981, p.780.

Dell R.M. and Moseley P.T. - J. Power Sources 7, 1981/1982, p.45.

Duncan G.K. and West A.R. - Sol. Stat. Ionics 9 and 10, 1983.

Dunn B. and Farrington G.C. - Sol. Stat. Ionics 9 and 10, 1983, p.223.

Farrington G.C. and Briant J.L. - Science 204, 1979, p.1371.

Farrington G.C., Dunn B. and Thomas J.O. - Appl. Phys. A32, 1983, p.159.

Fast Ion Transport in Solids - ed. Vashishta, Mundy and Shenoy, 1979 (North Holland).

Frase K.G., Thomas J.O. and Farrington G.C. - Sol. Stat. Ionics 9 and 10, 1983, p.307.

Ghosal B., Mangle E.A., Topp M.R., Dunn B. and Farrington G.C. - Sol. Stat. Ionics 9 and 10, 1983, p.273.

Harbach F. - J. Mat. Sci. 18, 1983, p.2437.

Hayes W., Holden L. and Tofield B.C. - Sol. Stat. Ionics 1, 1980, p.373.

Heavens S.N. - J. Mat. Sci. 17, 1982, p.965.

Hendricks S.B. and Pauling L. - Z. Krist. 64, 1927.

Hendrickson J.R. and Bray P.J. - Phys. Chem. Glasses 13, 1972. p.107.

Hirsch P., Howie A., Nicholson R.B., Pashley D.W. and Whelan M.J. - Electron Microscopy of Thin Crystals (Robert E. Krieger Publishing Company, Inc., N.Y.).

Hooper A. - J. Phys. D: Appl. Phys. 10, 1977, p.1487.

Hooper A. - Trans. J. British Ceram. Soc. 79, 1980, p.136.

✳House of Lords Report - Select Committee on Science and Technology (Electric Vehicles), 1980.

Hull R., Cherns D., Humphreys C.J. and Hutchison J.L. - Proceedings of EMAG 1981.

Hull R., D.Phil. Thesis, Oxford, 1983.

Hull R., Petford A.K., Humphreys C.J. and Smith D.J. - Sol. Stat. Ionics 9 and 10, 1983, p.181.

Humphreys C.J. and Spence J.C.H. - Optik 58, 1981, p.125.

Ilett C. - Private Communication, 1983.

✳Jones I.W., Reasbeck P. and Steele B.C.H. in Prospects for Industrial Electrochemistry. Royal Society discussion 1981 p.121-156.

Jorgensen J.D., Rotella F.J. and Roth W.L. - International Conference on Fast Ion Transport in Solids, 1981.

Kennedy J.H. and Sammells A.F. - J. Electrochem. Soc. 119 no.12, 1972, p.1609.

Kirk D.L. and Ormrod S.E. - Phys. Stat. Sol.(a) 44, 1977, p.643.

Matsui Y. and Horiuchi S. - Acta Cryst. A37, 1981, p.51.

May G.J. and Hooper A. - J. Mat. Sci. 13, 1978, p.1480.

May G.J. and Tan S.R. - Electrochim. Acta 24, 1979, p.755.

McNamee M. and Ashurst J.G. - Metallography 15, 1982, p.281.

McWhan D.B., Dernier P.D., Vettier C., Cooper A.S., and Remeika J.P. - Phys. Rev. 17B, 1978, p.4043.

Mochel M.E., Humphreys C.J., Eades J.A., Mochel J.M. and Petford A.K. - Appl. Phys. Lett. 42(4), 1983, p.392.

Murphy and Christian - Science 205, no.4407, 1979.

*NATO meeting on Intercalation Electrodes, 1979.

Newsam J.M. - Sol. Stat. Ionics 6, 1982, p.129.

Newsam J.M. and Tofield B.C. - J. Phys. C: Sol. Stat. Phys. 14, 1981, p.1545.

Nicholson P.S. - J. Mat. Sci. 18, 1983, p.1597.

Ormrod S.E. and Kirk D.L. - J. Phys. D: Appl. Phys. 10, 1977, p.1769.

Peters C.R., Bettman M., Moore J.W. and Glick M.D. - Acta Cryst. B27, 1971, p.1826.

Reidinger F., La Placa S.J. and Roth W.L. - Fast Ion Transport in Solids (eds Vashishta, Mundy and Shenoy), 1979.

Richman R.H. and Tennenhouse G.J. - J. Am. Ceram. Soc. 58(1-2), 1975, p.63.

Roth W.L. - General Electric Technical Information Series no. 71-C-328, 1971.

Roth W.L. - J. Sol. Stat. Chem. 4, 1972, p.60.

Roth W.L., Anne M., Tranqui D. and Heidemann A. - Fast Ion Transport in Solids (eds Vasahishta,Mundy and Shenoy), 1979.

* Roth W.L., Reidinger F. and La Placa S.J. - Superionic Conductors (eds. Mahon and Roth) 1977 (Plenum Press).

Sato H. and Hirotsu Y. - Mat. Res. Bull. 11, 1976, p.1307.

Scherzer O. - J. Appl. Phys. 20, 1949, p.20.

Shetty D.K., Virkar A.V. and Gordon R.S. - in Fracture Mechanics of Ceramics 4, (eds Bradt, Hasselmann and Lange), 1979, p.651.

Singh R.N. and Lewis N. - Sol. Stat. Ionics 9 and 10, 1983.

Skarnulis A.J. - J. Appl. Cryst. 12, 1979, p.636.

Spence J.C.H. - Experimental High Resolution Electron Microscopy, 1981, (Oxford University Press).

Stevens R. - J. Mat. Sci. 9, 1974, p.801.

Stevens R. and Miles L.J. - J. Mat. Sci. 11, 1976, p.1911.

Tennenhouse G.J., Ku R.C., Richman R.H. and Whalen T.J. - Ceram. Bull. 54 no.5, 1975, p.523.

Thery J. and Briancon D. - Compt. Rend. 254, 1962, p.2782.

Thomas J.O. and Farrington G.C. - Acta Cryst. B39, 1983, p.227.

Thomas J.O., Frase K.G., McIntyre G.J. and Farrington G.C. - Sol. Stat. Ionics 9 and 10, 1983, p.1029.

Tofield B.C. and Farrington G.C. - Nature 278, 1979, p.438.

Virkar A.V. and Viswanathan L. - J. Am. Ceram. Soc. 62, 1979, p.528.

Virkar A.V. and Viswanathan L. - J. Mat. Sci. 18, 1983, p.1202.

Virkar A.V., Viswanathan L. and Biswas D.R. - J. Mat. Sci. 15, 1980, p.302.

Virkir A.V., Miller G.R. and Gordon R.S. - J. Am. Ceram. Soc. 61 no.5-6, 1978, p,250.

Viswanathan L., Ikuma Y. and Virkar A.V. - J. Mat. Sci. 18, 1983, p.109.

Wang J.C., Gaffari M. and Choi Sang-Il - J. Chem. Phys. 63 no.2, 1975, p.772.

West A.R. - Mat. Res. Bull. 14, 1979, p.441.

White D.R., Chen S., Harrison H.R. and Sato H. - Sol. Stat. Ionics 9 and 10, 1983, p.255.

Whittingham M.S. and Huggins R.A. - J. Chem. Phys. 54, 1971, p.414.

Worrel C.A. and Redfern B.A. - J. Mat. Sci. 13, 1978, p.1515.

Yamaguchi G. and Suzuki K. - Bull. Chem. Soc. of Japan 41, 1968, p.93.

Yao Y.Y. and Kummer J.T. - J. Inorg. Nucl. Chem. 29, 1967, p.2453.